The Effects of Residual Stress on the Material Characterisation of Individual Nanowires

A thesis presented to the University of Dublin, Trinity College

for the degree of

Doctor of Philosophy in Chemistry

2017

Shaun Mills

Under the supervision of Prof. John J. Boland

School of Chemistry & CRANN

Trinity College Dublin

DECLARATION

I, the undersigned, declare that this work has not previously been submitted as an exercise for a degree at this, or any other University, and that unless otherwise stated is my own work. Elements of this work that have been carried out jointly with others or by collaborators have been duly acknowledged in the text.

I agree to deposit this thesis in the University's open access institutional repository or allow the library to do so on my behalf, subject to Irish Copyright Legislation and Trinity College Library conditions of use and acknowledgement.

Shaun Mills

Date

SUMMARY

Huge emphasis has been placed on the use of nanowires in a range of devices, due to their ease of fabrication, flexibility, transparency and low cost. In order to incorporate nanowires into functional devices it is imperative that their mechanical properties are widely understood. Throughout the literature, different techniques have been used to measure the mechanical properties of nanowires. However, in the majority of cases prior to the mechanical measurement, the initial stress state of the nanowire is unknown. Nanomaterials are sensitive to external stimuli and the deposition and manipulation of these materials often involves multiple processing steps. The aim of this thesis is to demonstrate for the first time the importance of the initial stress state of nanowires prior to mechanical testing.

Using an atomic force microscope (AFM) lateral manipulation technique, the adhesion of silver and silicon nanowires (~ 60 nm in diameter) to a SiO_2 substrate was investigated when they were deposited with and without a solvent processing step. It was observed that when polymer coated silver nanowires were solvent deposited, solvent-polymer interactions resulted in a strong adhesion to a SiO_2 surface. Furthermore, when these AgNWs were dropcast over a trench, clamped and manipulated using a 3-point bending procedure, it was observed that they were affected by an initial residual stress. When these wires were deposited without solvent affects, they were weakly adhered to the surface and were not affected by a residual stress. The adhesion of SiNWs to a SiO_2 surface was weak regardless of the deposition method used because no solvent interactions occur with the native oxide coating on these wires. When wires are mobile on the surface, they cannot be affected by a residual stress as they are free to relax.

Occasionally, the SiNWs adhered to the substrate upon solvent deposition. However, they were not affected by an initial residual stress. This indicates that interactions between the solvent and polymer coating on the AgNWs is the likely reason for the observed residual stress. The same adhesion characteristics were observed for AuNWs (~ 60 nm in diameter) which contained a surfactant surface coating. These wires were also affected by a residual stress when solvent deposited indicating further that the surface coatings on nanowires have the potential to induce stress in a nanowire by swelling in the presence of a solvent. An estimation of the potential swelling of the polymer coating on these nanowires indicated that

strains of up to 0.33% could be induced in a nanowire which was comparable to strains measured experimentally.

This thesis also informs the science community of the caution that is required when analysing the Young's modulus of nanowires in a doubly-clamped beam configuration affected by a residual stress. Adaptions made to the (zero-residual stress) model developed by Heidelberg *et al*. to account for residual stresses have been shown to be problematic. The problems arise due to experimental noise in the 3-point bending experiment. This results in developed models being unable to separate the contributions of Young's modulus and residual stress. This is an important result as it warns against the incorrect application of models that are currently in use.

To remove residual stress from silver nanowires they were sectioned using a focused ion beam. This allows Euler-Bernoulli cantilever beam analysis to be used to extract the Young's modulus of stress free nanowires. These cantilever beam measurements were used as a benchmark to compare the Young's modulus values extracted on an individual wire using both the doubly-clamped and cantilever beam methods. It was found that for two SiNWs that were not affected by a residual stress, the Young's moduli obtained by the doubly-clamped beam method using the Heidelberg (zero-residual stress) model were in agreement with the Young's moduli extracted from the cantilever beam measurements. Again, the model used to account for residual tension was shown to provide ambiguous results.

Finally, using a previously developed electromechanical technique, the effects of electrical charge flow on the Young's modulus of NWs was investigated. The Young's modulus of single crystal pentagonally twinned silver and gold nanowires was observed to increase by $\sim 70\%$ with current densities $> 10^9$ A/m^2, however the stiffening was permanent indicating a change in microstructure of the nanowires. This stiffening effect had not been observed in polycrystalline nanowires and is attributed to the unique pentagonal twin structure of these nanowires. Further work is required to determine the exact mechanism behind the stiffening effect and will be addressed in future work.

Acknowledgements

First and foremost, I would like to thank my supervisor Professor John Boland for his constant help and guidance throughout the course of my PhD. Every time I left John's office was with a new found sense of clarity and purpose. I would also like to thank Professor John Sader for all his help and valuable input over the years. The 8am Skype calls were always worth it for the insight that he provided. Of course none of this work would have been possible without the generous support of the Naughton Foundation and SFI. I owe a great debt to both.

Over the past 4 and a half years I've had the privilege of working with some wonderful people. To the members of the Boland group both past and present, your help over the years has proved invaluable. Particular mention goes to Eoin, Allen, Curtis, Jessamyn, David, Hugh, Sam, Prabhava, Fabio and Peter. Special mention goes to Eoin and Hugh for proof reading this thesis. Thanks also to all the staff in CRANN and the AML who have helped over the years. If I was to mention each of you individually, this might become one of the longest sections of my thesis.

On a personal note, I am eternally grateful for the love and support of my parents Ollie and Anna. They taught me the values of hard work and perseverance and made any goal seem possible. I would like to thank my brother, Darren, and sisters, Laura and Áine, for keeping my feet on the ground and not letting me get ahead of myself. Last but by no means least, words cannot express the gratitude I feel for my girlfriend, Orla. You have the patience of a saint for supporting and encouraging me over the years. You were always there for me and for that I'll be forever grateful.

TABLE OF CONTENTS

LIST OF FIGURES

LIST OF TABLES

LIST OF ABBREVIATIONS

0D	0-Dimensional
1D	1-Dimensional
2D	2-Dimensional
AFM	Atomic Force Microscope
AgNW	Silver Nanowire
AuNW	Gold Nanowire
CNT	Carbon Nanotube
CTAB	Cetyltrimethylammonium bromide
EBID	Electron Beam Induced Deposition
EBL	Electron Beam Lithography
EM	Electron Microscopy
F-d	Force-displacement
FEG	Field Emission Gun
FIB	Focussed Ion Beam
GIS	Gas Injection System
HMDS	Hexamethyldisilazane
ICP	Inductively Coupled Plasma
IPA	Isopropanol
MEMS	Micro Electromechanical Systems
MMA	Methyl Methacrylate
NEMS	Nano Electromechanical Systems
NiNW	Nickel Nanowire
NW	Nanowire
PDMS	Poly (dimethylsiloxane)
PDOS	Projected Density of States

PMMA	Poly (methyl methacrylate)
PVP	Polyvinylpyrollidone
RIE	Reactive Ion Etching
SEM	Scanning Electron Microscope
SiNW	Silicon Nanowire
TEM	Transmission Electron Microscope
UV	Ultraviolet
VLS	Vapour-Liquid-Solid

LIST OF PUBLICATIONS

Alan P. Bell, Jessamyn A. Fairfield, Eoin K. McCarthy, Shaun Mills, John J. Boland, Guillaume Baffou, David McCloskey, "*Quantitative Study of the Photothermal Properties of Metallic Nanowire Networks*", ACS Nano, **2015**, 9 (5), 5551-5558.

Agostino Galanti, Oxana Kotova, Salvador Blasco, Chloe J. Johnson, Robert D. Peacock, Shaun Mills, John J. Boland, Martin Albrecht, Thorfinnur Gunnlaugsson, *Exploring the Effect of Ligand Structural Isomerism in Langmuir-Blodgett Films of Chiral Luminescent* Eu^{III} *Self Assemblies"*, Chemistry A European Journal, **2016**, 22, 9709-9723

Amir S. Esmaeily, Shaun Mills, John Coey, "*Amorphous Alumina Nanotubes; Magnetic Hard Anodization and Mechanical Properties*", Nanoscale, **2017**, 9, 5205-5211.

Shaun Mills, John E. Sader, John J. Boland, "*The Effects of Residual Stress on the Material Characterisation of Doubly-Clamped Nanowires"*, Nanotechnology, **2017**, 28, 1-8.

1

INTRODUCTION

> "The principles of physics, as far as I can see, do not speak against the possibility of manoeuvring things atom by atom. It is not an attempt to violate any laws; it is something, in principle, that can be done; but in practice, it has not been done because we are too big". - Richard P. Feynman, 1959[1].

The above words of Richard P. Feynman, revered by many as the father of nanoscience, were delivered at the 1959 meeting of the American Physical Society entitled "There's Plenty of Room at the Bottom"[1]. In his lecture, Feynman considered the possibility of manipulating and controlling materials on an atomic scale. He envisioned being able to write the whole of the *Britannica Encyclopedia* on the head of a pin. Feynman also envisioned that at an atomic level, there are "new kinds of forces and new kinds of possibilities, new kinds of effects". It is these endless possibilities that have led to the ever growing field of nanotechnology, a term which was originally coined in 1974 by Norio Taniguchi and popularised by Eric Drexler[2] in 1981.

Nanotechnology describes any technology or device whose operation or functionality is dependent on nanosized objects. Through the exploration of the mechanical behaviour of nanoscale objects, this thesis aims to further advance the collective knowledge of this field.

Nanoscience is a multidisciplinary subject encompassing areas of Physics, Chemistry, Biology and Engineering. The term nanomaterial refers to any material that has one of its dimensions confined to 100 nm in length (10^{-9} m). Nanomaterials can be divided into three categories based on their dimensions. A one-dimensional (1D) nanomaterial has two dimensions smaller than 100 nm and one dimension of macroscopic size. These include materials such as carbon nanotubes[3,4] (CNTs) and nanowires[5]. Two-dimensional (2D) nanomaterials refer to materials that have only one dimension smaller than 100 nm and are macroscopic in the other two. Graphene is a prime example[6]. A zero-dimensional (0D)

nanomaterial is one in which all its dimensions are less than 100 nm making it essentially zero-dimensional. Nanoparticles[7] and quantum dots[8] are examples of zero dimensional nanomaterials.

What makes nanomaterials so exciting is that as a material's size decreases into the nanoscale regime the properties of materials do not scale linearly. Therefore, nanomaterial properties may differ greatly to those of their bulk counterparts[9]. The most intuitive 'nano-size' effect is produced as a result of the dominance of surface atoms in nanomaterials. The surface atoms contain dangling bonds or a dis-ordered atomic arrangement on its outermost surface. For bulk surfaces the number of surface bonds will be in the minority compared to the number of bulk bonds, therefore the properties of the bulk bonds dominate. However, as the size of a material decreases to the nanoscale, the ratio of surface bonds to bulk bonds increases, Figure 1.1. At certain lengthscales the surface bonds will begin to influence the properties of the material. Theoretical calculations and experiments have determined that these size effects are observed when the dimensions decrease below 100 nm[10]. This makes them ideal for use in areas where surface to volume ratio plays a critical role such as in catalysis[11]. Furthermore, the electrical properties of nanomaterials can vary from that of the bulk due to quantum confinement effects[12]. This occurs when the wavelength of electrons is comparable to any dimensions of the material. Devices such as solar cells, lasers and p-n junctions have been designed to exploit these unique nanomaterial properties.

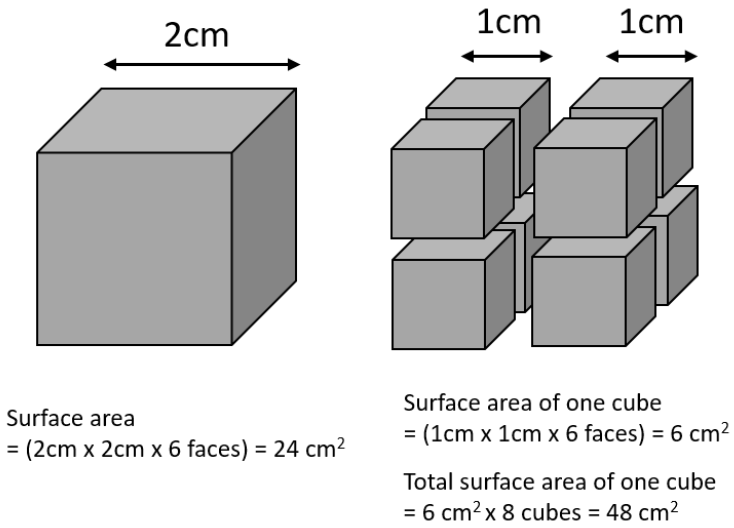

Figure 1.1: Schematic showing increased surface area as the size of materials are scaled towards the nanoscale.

Numerous studies have reported that nanostructures possess ultrahigh mechanical strengths, close to the theoretical limits[13,14]. In the past decade, mechanical properties of uni-axial loaded microstructures have shown promising size effects, - so called 'smaller is stronger'[15], even at sizes greater than 100 nm[16-18]. Upon further miniaturisation into the nano regime where surface effects become dominant (< 100 nm), 1D nanomaterials have received much interest. Nanotubes (NTs), nanowires (NWs) and nanobelts (NBs) exhibit unique thermal[19], electrical[20], optical[21] and mechanical[22,23] properties. Indeed nanowires are used in a plethora of nanoscale devices such as transistors[24,25], memory devices[26], actuators[27], nano-electromechanical devices[28,29] (NEMs), interconnects[30] and sensors[31] to name but a few.

However, although mechanical properties of bulk materials can be routinely measured, difficulties arise when attempting to probe the mechanical properties of 1-dimensional materials such as nanowires. This next section will focus on the relevant material properties that are measured in bulk materials. Following this, the challenges involved in determining these same material properties on the nanoscale will be discussed.

1.1 Mechanical Properties

To incorporate nanomaterials into functional devices it is important that the fundamental properties of these materials are understood. Due to the small sizes of nanomaterials, it is equally important that the effects of external factors on the measured mechanical response of nanomaterials are investigated.

One of the main aspects investigated in this work is how the observed mechanical properties of nanowires can be affected by the techniques used to deposit them on surfaces. The three fundamental properties which govern the mechanical properties of a material are their stress, strain and strength;

I. The *stress* applied to a material is the force per unit area applied to the material. The maximum stress a material can withstand before it breaks is called its ultimate tensile stress.

$$\sigma = \frac{F}{A_0} \tag{1.1}$$

II. *Strain* is the ratio of the extension of a material over its initial length.

$$\varepsilon = \frac{\Delta l}{l_0} \tag{1.2}$$

III. *Strength* is the ability of a material to resist deformation. A material's strength has three definitions;

(a) *Yield Strength* is the stress at which material starts to deform inelastically. Prior to the yield point the material will return to its original shape after deformation.

(b) *Ultimate Tensile Strength* is the stress that a material can withstand prior to failure.

(c) *Fracture Strength* of a material is the stress at which a material fractures or fails.

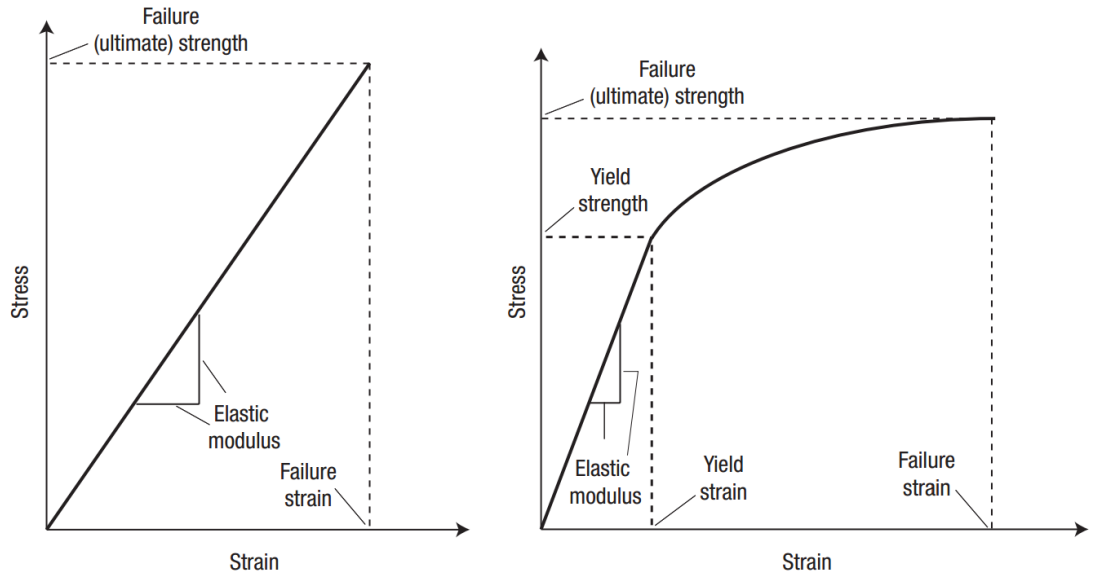

Figure 1.2: Schematic stress-strain curve for a brittle material (left) and a plastic material (right) showing how the elastic modulus and other mechanical properties of a material can be determined[32].

On a macroscopic scale, one of the easiest ways to measure the mechanical properties of a material is to conduct a tensile experiment. A specimen is deformed, to fracture, with a gradually increasing tensile load that is applied uni-axially along the long axis of the specimen. An important observation to make here is that the strength of a uni-axially loaded specimen is related to its cross-sectional area. This is because the strength arises from the number of chemical bonds connecting one cross section with the adjacent one, where each bond has a certain stiffness and strength. In contrast, increasing the length of the specimen will not make it stronger (in fact it is more likely to decrease the strength because, from a statistical perspective the specimen has a greater chance of containing a strength-reducing defect).

Deformation in which the stress and strain are proportional (Figure 1.2) is called elastic deformation and is governed by the relationship known as Hooke's Law;[33]

$$\sigma = E\varepsilon \tag{1.3}$$

where the constant of proportionality *E* is the modulus of Elasticity, or *Young's Modulus*. The slope of the stress-strain curve corresponds to Young's modulus. The modulus may be thought of as the stiffness of a material or a material's resistance to elastic deformation. As shown by the stress-strain curve, elastic deformation is reversible meaning that the material relaxes to its original shape upon the removal of the applied stress. The main focus of the work presented in this thesis involves measuring nanowires solely in the elastic regime and so it is important to establish when an applied load results in inelastic deformation. This can be recognised by a sharp drop in force which indicates fracture of the material, or by a change in the stress-strain slope which indicates plastic deformation of the material[34].

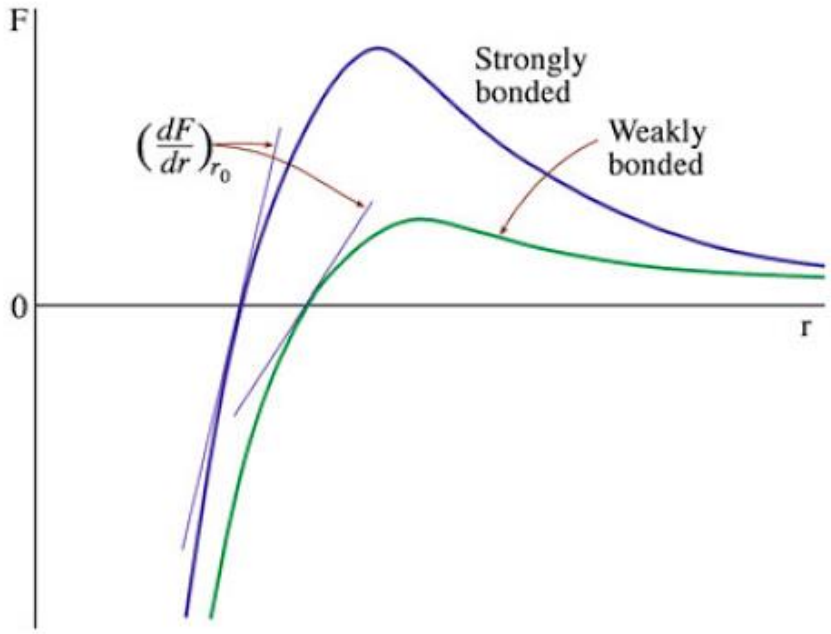

Figure 1.3: Force versus interatomic separation for weakly and strongly bonded atoms. The magnitude of Young's Modulus is proportional to the slope of each curve at the equilibrium interatomic separation r_0[35].

At an atomic level, changes in the interatomic spacing and the stretching of interatomic bonds occur as a result of macroscopic strain. The interatomic bonding forces govern the magnitude of Young's modulus because it is a measure of the resistance to separation of adjacent

atoms/ions/molecules. Young's modulus is proportional to the slope of the interatomic force-separation curve at the equilibrium spacing;[35]

$$E \propto \left(\frac{dF}{dr}\right)_{r_o} \tag{1.4}$$

Figure 1.3 shows the force - separation curves for materials having both strong and weak interatomic bonds; the slope at r_0 is indicated for each. Differing modulus values between metals, ceramics and polymers is a result of the different types of atomic bonding that exists for the material types.

Measuring mechanical properties at a bulk level is relatively straightforward. Tensile testing has fully standardised testing procedures to determine Young's modulus, yield strength, tensile strength and the ultimate strength of a material. Additionally, the failure of a material, whether ductile or brittle, can be easily observed. However, force measurements are much more complicated at the nanoscale.

1.2 Mechanical Properties of 1-Dimensional Nanomaterials

The mechanical properties of nanomaterials have been shown to vary significantly at the nanoscale. These include the ultra-high strength of carbon nanotubes[36,37], size-induced weakening[38] and increasing Young's modulus of materials as their dimensions are decreased[39,40]. Indeed there have been several excellent reviews on the measurement of the mechanical properties of 1D materials[41-43]. Measuring the mechanical properties of 1D nanomaterials such as nanowires is extremely challenging due to their miniscule size. However, with advances in electron and scanning probe microscopies, experimental measurements became feasible and reliable.

The main challenges involved in measuring the mechanical properties of 1D nanostructures are; (i) manufacturing and positioning specimens with nanometre accuracy, (ii) application and measurement of forces with nanonewton (nN) accuracy and (iii) the measurement of deformation with nanometre accuracy.

1.2.1 Manipulation and Positioning of Specimens

To measure the mechanical properties of 1D nanostructures, it is necessary to position the specimen in such a way that its properties can be measured. The degree of difficulty involved in the positioning will depend on the technique being used to conduct the mechanical

measurement. For example, for tensile testing experiments both ends of the specimen must be clamped to the measurement stage[44]. Alternatively, for nanoindentation experiments, positioning may not be critical because the nanoindenter can often be moved to locate the position of the specimen[45]. The main deposition methods used are outlined below.

1.2.1.1 Random Dispersion

One of the most facile methods of depositing 1D nanomaterials is by dispersion in a volatile solvent, followed by pipetting a small volume of the dispersion onto a substrate. Evaporation of the dispersing solvent results in a random dispersion of the nanomaterials on the surface, Figure 1.4 (a). Substrates can be pre-fabricated with trenches[46] or holes[23] to suspend the specimen. This is most suitable for nanoindentation and atomic force microscopy (AFM) experiments. The specimen is usually clamped either side of the trench/hole using metal assisted electron beam induced deposition (EBID) to fix the specimen to the substrate. Similarly, specimens can be deposited using a dry transfer method where a soft polymer can be used to transfer specimens from their growth substrate to their target substrate[47]. For these types of measurements, if an array of trenches or holes are used, statistically, some of the nanostructures will be oriented suitably for mechanical measurement.

1.2.1.2 Nanomanipulation

For in-situ electron microscopy (EM) experiments, the positioning of the specimen is more crucial. Tensile experiments based on multi-axes piezo strain stages require the specimen to be fixed to both ends of the strain stage. Generally, a micromanipulator is used to ‘pick and place’ the specimen to the chosen position and EBID is used to deposit metal or carbon deposits to fix the specimen in place, Figure 1.4 (b). These methods are quite laborious and throughput is low however, EM techniques do allow for powerful in-situ imaging of the specimen during mechanical deformation.

1.2.1.3 Direct Growth

Rather than manipulating and aligning nanostructures after their synthesis, researchers have examined methods to control their growth. This is very promising for nanomechanical measurements as it removes the requirement for additional fixation of the specimen using EBID, eliminating the possibility of contamination of the nanostructure by foreign atoms. This type of growth has been demonstrated for carbon nanotubes[48,49]. The technique involves patterning a catalyst in an array, which controls the growth of the CNTs between two specific

sites, Figure 1.4 (c). Additionally, arrays of vertically grown nanowires can often be measured as grown[50,51], Figure 1.4 (d).

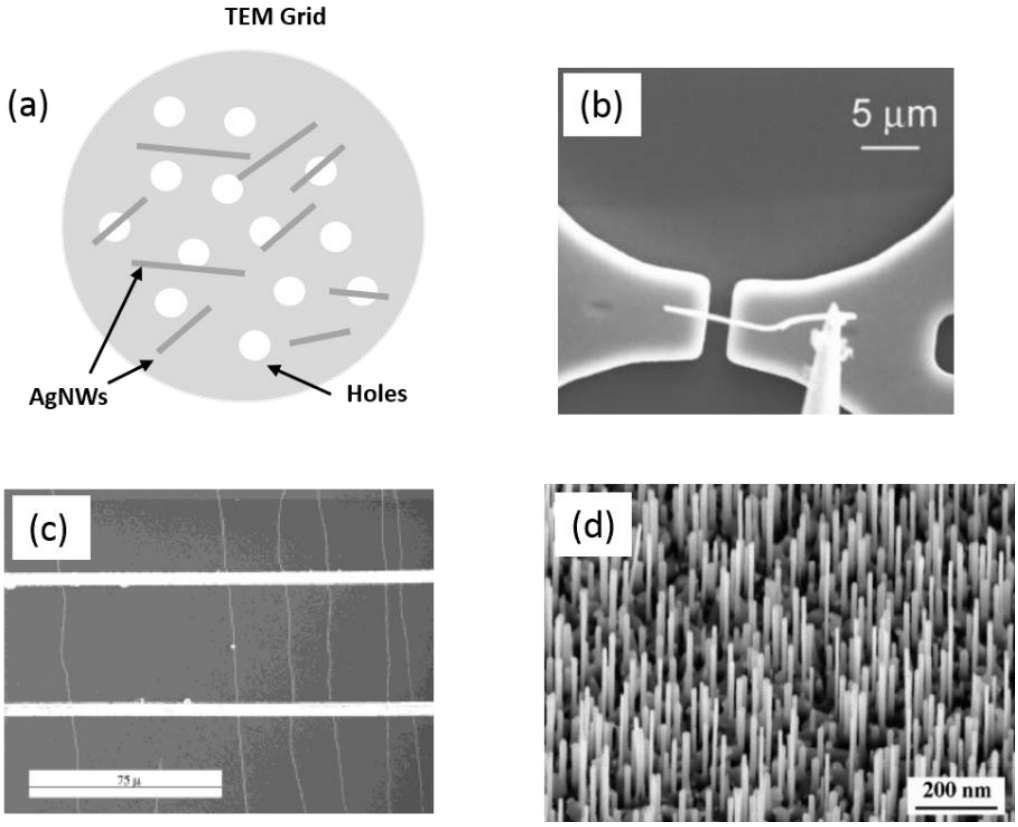

Figure 1.4: (a) Schematic showing random deposition of silver nanowires on a TEM grid with holes. (b) Nanomanipulation of a palladium nanowire onto a MEMs test structure[53]. (c) SEM image of aligned growth of carbon nanotubes over two trenches (bright areas of image)[52]. (d) SEM image of vertically aligned ZnO nanowire array on a sapphire surface[50].

1.2.2 High Resolution Displacement and Force Measurements

Electron microscopy and surface probe microscopy techniques have been used extensively in the characterisation of materials. Techniques such as scanning electron microscopy (SEM), transmission electron microscopy (TEM) and AFM, have been widely used to measure dimensions and deformations on the nanoscale. SEM is capable of 1 nm resolution, and conventional TEM is capable of 0.5 - 1 nm resolution. The imaging capabilities of these microscopes can be used to measure the deflection of beams with nanometre resolution which can in turn be used to measure forces. Microelectromechanical systems (MEMs) devices[53] have also been shown to measure forces with nN resolution and these can be adapted to allow operation within the chambers of electron microscopes.

Electron microscopes are used for imaging only whereas an AFM is also an instrumental testing tool. AFM works on the principle of a sharp probe attached to a cantilever

that is driven by a piezoelectric scanner. The instrument resolution is a function of the cantilever stiffness and optical detection system used. Once the cantilever spring constant is known, the AFM tip can be used as a powerful force sensor[54,55] with nanonewton resolution. This is achieved by recording the cantilever deflection whilst displacement can also be measured with sub nanometre resolution. These electron and probe microscope techniques are the basis behind nanomechanical measurements on the nanoscale.

1.3 In-situ Electron Microscopy Techniques

Typically, there are two types of in-situ transmission electron and scanning electron microscopy methods used to determine the mechanical properties of 1D nanomaterials; thermal and electrostatic actuation, and tensile measurements.

1.3.1 Thermal and Electrostatic Actuation

One of the first in-situ EM experiments was conducted in 1996 by Treacy *et al*.[56] In these measurements the Young's modulus of carbon nanotubes was determined by analysing the thermal actuation of a singly-clamped carbon nanotube, see Figure 1.5 (a). The amplitude of the thermal oscillations was measured as a function of temperature and the relationship between the two then used to extract Young's modulus using;

$$\sigma^2 \approx 0.4243 \frac{L^3 kT}{E(a^4 - b^4)} \tag{1.5}$$

where σ is the root-mean-square vibration amplitude, L is the clamped length of the CNT, k is Boltzmann's constant, T is the temperature, E is Young's modulus and a and b are the outer and inner radii of the CNT respectively. The average Young's modulus of the CNTs was found to be 1.8 TPa, however the value fluctuated from 0.4 to 4.15 TPa, therefore these initial results could only be used as an estimate. However, this method did pioneer the way for the improvement of this technique.

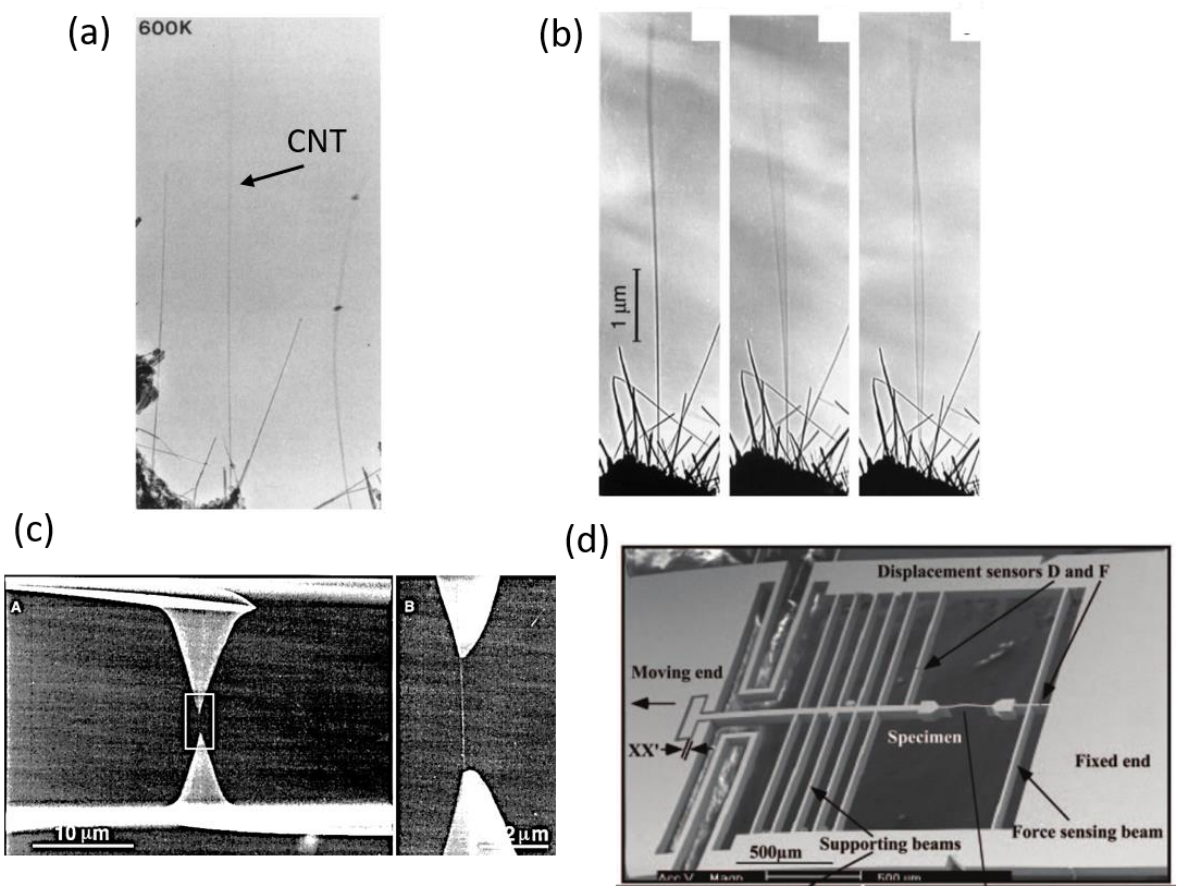

Figure 1.5: (a) Thermal Actuation: bright-field TEM image showing thermal oscillation of a free standing carbon nanotube at 600 K[56]. (b) Electrostatic Actuation: response of a carbon nanotube to resonant alternating applied potentials, left to right, no resonance, resonance of the fundamental mode of vibration, resonance of the second harmonic[57]. (c) Tensile Testing: an individual MWCNT mounted between two opposing AFM tips, attached using e-beam deposition of carbonaceous material[36]. (d) MEMs stage: SEM image of MEMs nano-stressing stage including a co-fabricated thin film and force sensor. An external piezoelectric actuator is used to conduct the tensile test[58].

In an attempt to improve on the uncertainties that occur when measuring thermal vibrations, Poncharal *et al.*[57] fabricated an electromechanical holder that contained a counter electrode, so that carbon nanotubes could be electrostatically deflected, Figure 1.5 (b). The deflection could be accurately measured in the TEM and the deflection was found to be proportional to V_s^2, where V_s was the voltage applied to the counter electrode. Using Euler-Bernoulli analysis of cantilevered beams, Young's modulus could be determined[57];

$$v_j = \frac{\beta_j^2}{8\pi}\frac{1}{L^2}\sqrt{\frac{(D^2 + D_i^2)E_B}{\rho}} \tag{1.6}$$

where D and D_i are the tubes inner and outer diameter respectively. L is the length, ρ is the density, E_B is the bending modulus, v_j is the frequency for the jth harmonic and β_j is a constant for that harmonic. In these measurements, it was determined that the Young's modulus for individual CNTs was large ($\sim$ 1 TPa) for diameters < 10 nm, but the Young's modulus dropped to ($\sim$ 100 GPa) for tubes of larger diameters. Although these measurements are conducted inside a TEM where high resolution imaging of the structure of the nanotubes is available, these measurements do not provide any in-situ observation of the specimen deformation history or details about defect propagation. To address these issues researchers explored the use of in-situ tensile testing stages.

1.3.2 In-situ Tensile Testing

In 2000, Yu *et al*.[36] used a "nano-stressing" stage consisting of two AFM probes to perform tensile tests on multiwalled carbon nanotubes (MWCNTs) inside an SEM (Figure 1.5 (c)) to observe nanotube failure in-situ. The AFM probes provide sharp ends for picking and mounting each NT, and also act as force sensors. It was observed that the MWCNTs broke in the outermost layer ("sword-in-sheath" failure), and the tensile strength of the outer layer ranged from 11 to 63 GPa for 19 MWCNTs measured. In-situ microelectromechanical systems (MEMs) have been developed for use as tensile stages.

In 2004 Haque *et al*.[58] developed a stage (Figure 1.5 (d)) where the force load on a specimen is applied by external piezo-actuators and monitored by beam deflection measurements. One shortcoming of this technique is that this sensing approach prevents simultaneous sample imaging at high magnification because the deflection of a beam needs to be imaged in order to determine specimen displacement. In 2005, Zhu *et al*.[53,59] developed a MEMs stage that incorporated a capacitive sensor that allows the force load to be measured electrically. This facilitates the continuous observation of the specimen during deformation and failure.

Although in-situ observation of mechanical deformation is promising for imaging the mechanical failure of a material and changes to its crystal structure, there are disadvantages. The effects of high-energy electron beams on the elastic properties of materials must be taken into consideration. It has been shown that electron beams have no obvious effect on the mechanical properties of metallic bonds[60], however electron beam irradiation can increase the temperature of NWs. It can also significantly enhance diffusion and dislocation mobility, which may lead to the observed increased ductility in in-situ TEM experiments for silicon

nanowires[61], NaCl nanowires[62] and carbon nanotubes[63]. Therefore, it is important to explore techniques that do not require the use of an electron beam during the measurement of a material's mechanical properties.

1.4 Nanoindentation/AFM Techniques

Nanoindentation techniques generally involve the use of an indenter combined with an AFM. The nanoindenter tip can be used as the "AFM tip" to locate a specimen on the surface of a substrate and then to indent the sample where the force resolution can be measured to 1 nN and the displacement to ~ 0.2 nm[64]. If an AFM tip is to be used as an indenter the force response will be a convolution of the wire indentation and the movement of the AFM tip, therefore the spring constant and stiffness of the AFM tip must be calibrated[65].

1.4.1 Nanoindentation/AFM Nanoindentation

In 2003, Li *et al*.[45] determined the hardness and elastic modulus of a silver nanowire 42 nm in diameter using a Hysitron nanoindenter in conjunction with a Veeco Dimension AFM. Silver nanowires were randomly dispersed on a glass slide, imaged with the indenter and then indented with the indenter, as in Figure 1.6 (c). From the measured load versus displacement curve (Figure 1.6 (d)), the indentation hardness, *H*, could be determined;

$$H = \frac{P_{max}}{A} \tag{1.7}$$

where P_{max} is the peak load and *A* is the projected contact area. The nano-indentation elastic modulus was calculated using the Oliver-Pharr data analysis procedure[66];

$$E = 2\beta \sqrt{\frac{A}{\pi} E_r} \tag{1.8}$$

where β is a constant that depends on the geometry of the indenter and E_r is the reduced elastic modulus that accounts for the fact that elastic deformation occurs in both the sample and the indenter[45]. Oliver-Pharr analysis is used because during nanoindentations with a nanoindenter the NW sample is likely to undergo plasticity. The Young's modulus depends on the shape of the nano-indenter tip, and so models have been developed to account for the tip shape to allow the Young's modulus of the wires to be determined. It was found that the silver nanowires

had hardness and Young's modulus values comparable to that of bulk silver. Nanoindenters can also be used in combination with in-situ electron microscopy compression studies where the failure of nanopillars is observed while a nanoindenter is simultaneously subjecting them to compression tests[67,64].

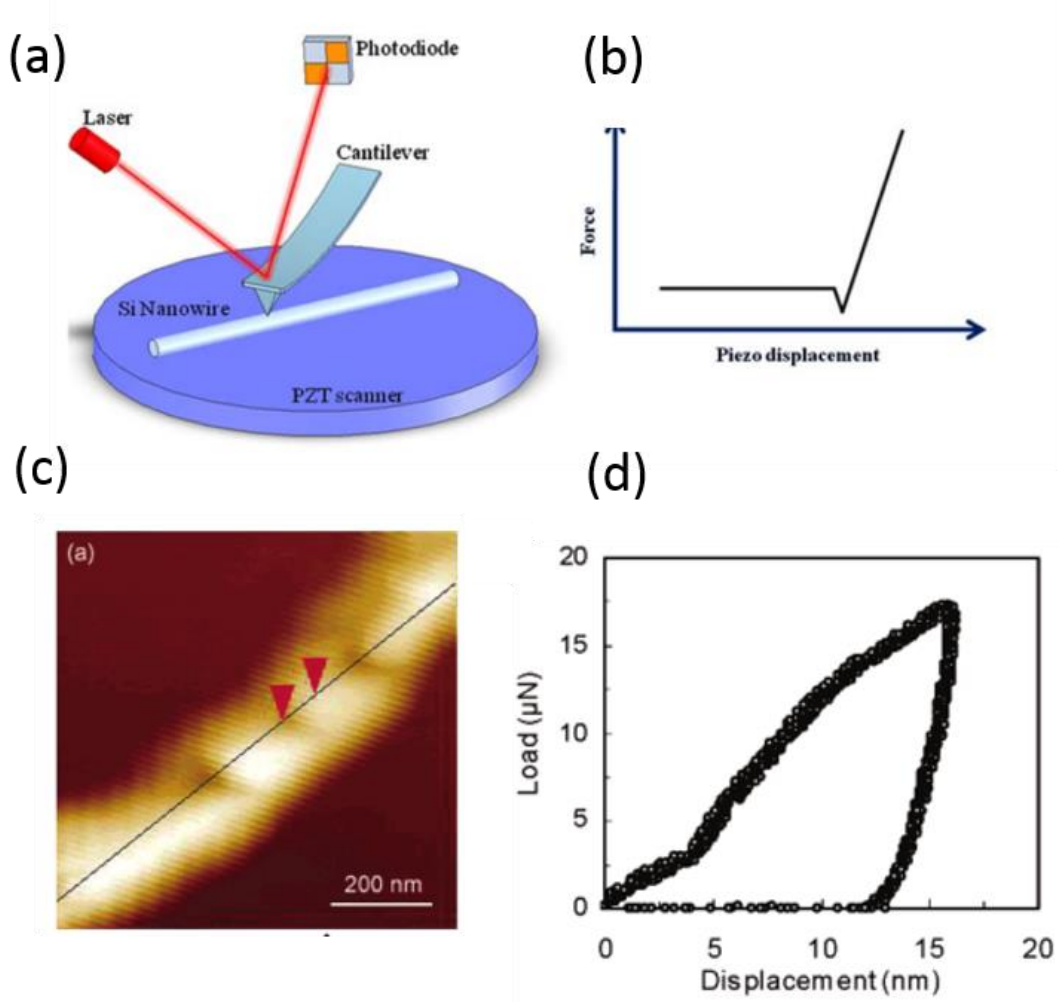

Figure 1.6: (a) Schematic illustration of AFM nanoindentation of a silicon nanowire. A laser beam is used to measure the cantilever bending deflection during nanoindentation[68]. (b) Schematic of a typical force-displacement response for an indentation experiment. (c) AFM images of indents in a silver nanowire. (d) A representative nanoindentation load-displacement curve[45].

An AFM tip can also be used as a nanoindenter by mechanically loading a NW with a set-point force and measuring the resultant deformation in the NW, as shown in Figure 1.6 (a) and (b). In 2009 Sohn *et al.*[68] used an AFM nanoindenter to measure the Young's modulus of silicon nanowires with diameters between (100 - 600 nm). Hertz theory was applied to determine the Young's modulus. Hertz theory is the preferred model used for AFM nanoindentation because the indentation is generally elastic due to the lower controlled force

of the AFM tip compared to a nanoindenter. According to Hertz contact theory, the applied force *F* is related to the indentation displacement, *d*, by;

$$F = \frac{4}{3} E^* R^{\frac{1}{2}} d^{\frac{3}{2}} \tag{1.9}$$

where E^* is the reduced Young's modulus whereby the indentation in both the NW and the AFM tip needs to be considered, *R* is the AFM tip radius. This method is based on several assumptions[69]; (i) Hertz contact theory is assumed, which is applicable to elastic half space but may not be applicable to very thin NWs, (ii) The substrate is assumed to be much more rigid than the NWs which might not be correct for very stiff nanowires, (iii) The radius of the AFM tip is assumed to be spherical and (iv) The NWs are assumed to be isotropic[68].

When dimensions of NWs are reduced, the potential errors associated with nanoindentation experiments increase. Additionally, AFM tip/NW slippage becomes an issue as the NW dimensions decrease.

1.4.2 AFM Techniques

An AFM tip is a powerful measurement tool capable of sensitive force resolutions ~ 0.1 nN and accurate force displacements ~ 0.1 nm, therefore AFM has been widely utilised to measure the mechanical response of nanomaterials. It is capable of being operated in several different modes such as contact mode, lateral force mode and force microscopy mode.

In 2005, Song *et al.*[50] measured the elastic properties of individual vertically aligned zinc oxide (ZnO) nanowires. By imaging the vertically aligned nanowires in contact mode and simultaneously recording the lateral force deflection as the AFM tip passed over the NWs (Figure 1.7 (d)), the elastic modulus of the NWs could be determined. This technique allows the measurement of NWs of different heights as the AFM tip adjusts its height to maintain a user setpoint force. Another benefit of this method is that NWs can be measured directly from their growth wafer and so no additional deposition and specific NW placement steps are required.

When a vertical NW experiences a lateral force, f, parallel to the AFM tips scanning direction, the displacement of the NW under the small deflection approximation can be expressed as[50];

$$EI \frac{d^4 x}{dy^4} = (f_o + f)\delta(y - L) \tag{1.10}$$

where f_0 is the projected component of the friction force between the tip and the NW parallel to the tip scanning direction, E and I are the Young's modulus and moment of inertia of the NW respectively, x is the lateral displacement perpendicular to the NW, y is the height from the fixed end of the NW to the point where the lateral force is applied, which is approximated as the tip of the NW. The contact is assumed to be a point contact, and L is the length of the NW. Expressing Young's modulus as a function of the spring constant, K, for a hexagonal cross section NW, the Young's modulus is given by;

$$E = \frac{16L^3K}{15(3^{1/2})a^4} \tag{1.11}$$

where a is the side length of one of the hexagonal sides, which for a regular hexagon is equal to the radius.

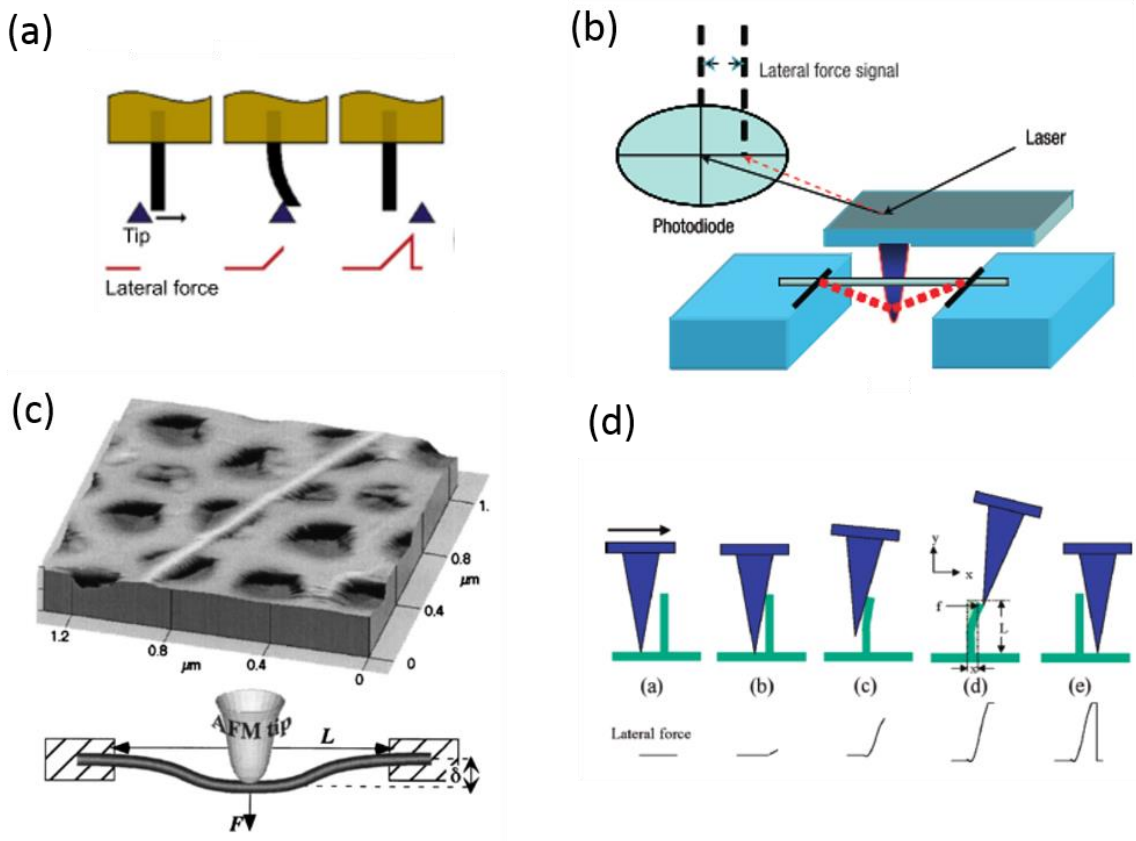

Figure 1.7: (a) Schematic of beam bending with an AFM tip for a silicon carbide rod pinned at one end. The tip moves in the direction of the arrow and the lateral force is indicated by the red trace at the bottom[70]. (b) Schematic 3-point lateral bending technique for a NW suspended over a trench fixed in place with EBID clamps[22]. (c) Top: AFM image of a CNT rope suspended over a hole in a polished alumina ultrafiltration membrane, Bottom: Schematic of vertical 3-point bending technique performed on the nanotube resulting in a vertical deflection of the AFM tip[23]. (d) Lateral force technique used to measure the Young's modulus of vertically aligned ZnO nanowires[50].

In lateral force microscopy mode two methods of sample configuration and loading procedures have been used. The first method was implemented by Wong *et al.*[70] where silicon carbide (SiC) nanorods (NRs) were randomly dispersed on a low friction substrate (MoS_2). Silicon oxide (SiO) pads were then used to clamp the NRs at one end. The NRs were laterally manipulated (Figure 1.7 (a)) at various positions along their length resulting in an array of force-displacement curves. Using conventional Euler-Bernoulli beam mechanics, the Young's modulus and strengths of the NRs could be determined. The general response of a beam to a force *F* applied at a distance *a* (along the x-axis) from the fixed pinning point (x = 0), for a cylindrical wire is given by[70];

$$k(x) = \frac{3\pi r^4}{4x^3} E \tag{1.12}$$

where $k(x) = dF/dy$, *r* is the radius of the wire, *x* is the load position along the length of the wire measured from its fixed end and *E* is its Young's modulus. One major advantage of this technique is that because *k(x)* is determined at multiple positions along the length of the NW, it is possible to obtain a reliable measure of *E* without knowledge of the exact pinning point[70]. Determination of the clamping points is one of the major sources of experimental error for singly or doubly-clamped measurements that rely on a single loading location on a NW. Caution needs to be exercised when using EBID clamps to ensure they don't impact the mechanical properties being measured[71,72]. This is discussed in greater detail in chapter 3.

This technique, however cannot eliminate wire/substrate friction effects (friction coefficients can be studied using a similar method[73,54]) so another method was used to either selectively etch the substrate under the NW[74] or deposit the NW over a substrate with pre-fabricated holes[75], Figure 1.7 (c), or trenches[46], Figure 1.7 (b). The NWs are then fixed in place using EBID deposited clamps unless surface adhesion[76] to the substrate is strong enough to prevent movement of the nanostructure. This doubly-clamped configuration is widely used throughout this thesis, therefore it will be discussed in greater detail.

1.5 Young's Modulus of a Doubly-Clamped Beam

This doubly-clamped beam configuration has been widely used to analyse the mechanical properties of nanowires[23,76-78,22]. The Young's modulus for the first measurements of this type was normally obtained from a measurement of the beam displacement as a function of load.

For a doubly-clamped beam the resulting force-displacement response is described by the well-known equation[79];

$$F_{centre} = \frac{192EI}{L^3}\Delta z_{centre} \tag{1.13}$$

where F_{centre} is the load applied to the centre of the beam, Δz_{centre} is the resulting displacement of the beam at the load point, E is the Young's modulus of the beam, I is the areal moment of inertia for the beam ($I = \pi R^4/4$, assuming a cylindrical beam), and L is the length of the beam. This model accounts only for elastic Euler-Bernoulli beam bending and is only valid for displacements less than the radius of the NW that is being measured. Indeed, linear force-displacement (*F-d*) curves (Figure 1.8 (a)) have been reported for CNTs[70,75], MoS_2 ropes[76] and even lithographically defined silicon beams[80].

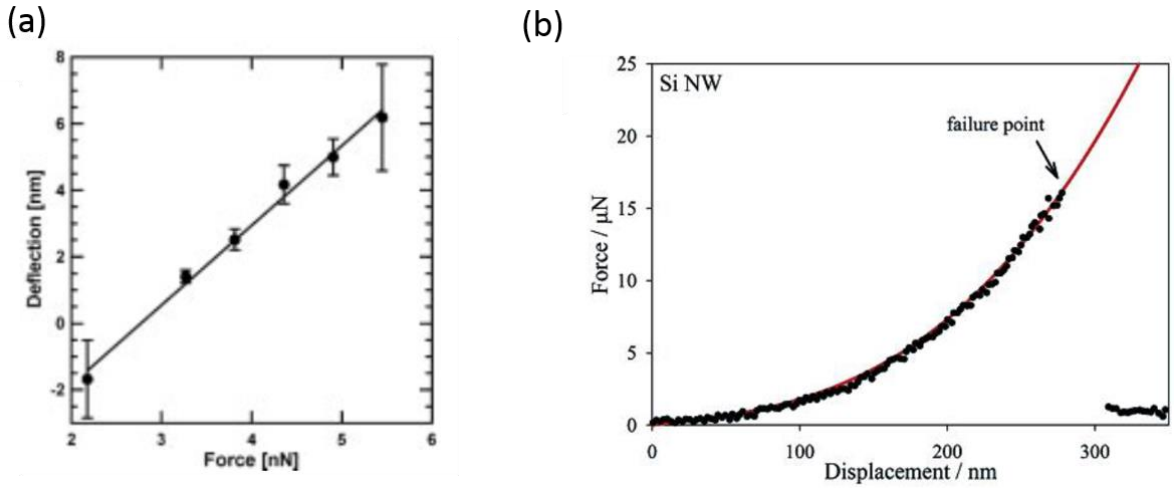

Figure 1.8: (a) Linear deflection vs force curve obtained for a 12 nm diameter CNT under varying normal load[76]. (b) Non-linear *F-d* curve for a 150 nm diameter silicon nanowire laterally loaded using an AFM tip[81].

At displacements greater than the radius of the wire under investigation, non-linear force-displacement responses are observed, as in Figure 1.8 (b). Non-linear *F-d* curves have also been observed for carbon nanotubes[74,82,83] and glass nanofibers[84]. However, initial models used to analyse these *F-d* curves were either exclusively linear or non-linear. In the 2006 work of Heidelberg *et al.*[81] the model described by equation (1.13) was expanded to account for tensile stresses that are induced in a beam at displacements larger than the beam's radius. This adaption provides a full description of the elastic properties of doubly-clamped beams over the entire elastic regime. The model uses a single closed-form analytical description which

can extract linear material constants such as Young's modulus (*E*) but can also be used to describe the entire elastic range and identify the yield points for different systems[81].

Equation (1.13) is valid only for displacements that are smaller than the radius of the beam under investigation as it accounts only for the elastic bending of the beam. When the beam is displaced further than its diameter the response becomes increasingly non-linear as an axial force is induced due to the stretching of the beam. Equation (1.13) does not capture this. This force affects the total stress in the beam and results in an enhancement of its rigidity[79]. Accounting for this we get the equation;[81]

$$F_{centre} = \frac{192EI}{L^3} f(\alpha)\Delta z_{centre} \tag{1.14}$$

where $f(\alpha)$ is a function of the wire dimensions;

$$f(\alpha) = \frac{\alpha}{48 - \frac{192\tanh(\sqrt{\alpha}/4)}{\sqrt{\alpha}}} \tag{1.15}$$

where α is related to the displacement Δz_{centre} of the wire by;

$$\alpha = \frac{6\epsilon(140+\epsilon)}{350+3\epsilon}, \qquad \epsilon = \left(\frac{2\Delta z_{centre}}{R}\right)^2, \tag{1.16}$$

The function $f(\alpha)$ may be approximated so that the force F_{centre} comprises two terms; (i) a bending term that is linear in the displacement Δz_{centre} and (ii) a tensile term that is cubic in the displacement Δz_{centre}. Equation (1.14) becomes;[81]

$$F_{centre} = \frac{192EI}{L^3}\Delta z_{centre}\left(1 + \frac{A}{24I}\Delta z_{centre}^2\right) \tag{1.17}$$

This is only an approximate solution which has been obtained by superimposing small and large deflection limits. It is used here for the purpose of simplicity. The full generalised model described by equations (1.14), (1.15) and (1.16) is used to extract the mechanical data in this thesis unless otherwise stated. The full derivation can be found in the appendix (A1). In the approximated form of the model in equation (1.17), the term which is linear in the displacement accounts for elastic beam bending whereas the cubic dependence accounts for tensile stresses induced along the length of the beam. It is important to note, for reasons that

will become apparent in subsequent chapters, that the model presented here assumes that the beam is under no initial stresses prior to manipulation. This model has been used to analyse the full spectrum of mechanical properties of nanowires[81,46,85].

As outlined, there is an array of different techniques that can be used to determine the mechanical properties of 1D nanostructures. The advantages and disadvantages of these techniques are summarised in table 1.1. However, in the techniques outlined, it is assumed that when NWs are fabricated, deposited and manipulated, they are not being subjected to any additional forces except for the force subjected by the force measurement technique that is being used. When working with nanomaterials, every step of the deposition and fabrication process must be considered in relation to the potential parasitic effects that can be incorporated into the NWs. These effects may be incorrectly measured and documented as an inherent property of that material. In the work presented in this thesis, we analyse how significant differences in the initial stress state of a NW deposited on a surface can be observed, depending on whether NWs are deposited with or without the influence of a solvent drying step. Furthermore, the effects that variations in the NWs initial stress state have on the determination of the Young's modulus of doubly-clamped beams will be explored.

Table 1.1: Advantages and disadvantages of electron microscope (EM) and AFM nanomechanical measurements.

	Advantages	Disadvantages
EM Methods	• Atomic resolution imaging throughout deformation process • Crystallographic information	• High electron beam irradiation • Low sample throughput • Difficult sample preparation • Limited to nanostructures > 100 nm in diameter
AFM Method **- Nanoindentation**	• Experiment is relatively simple • Extremely sensitive (0.2 nN force resolution) • No specimen damage during imaging • Simple NW deposition methods used	• Data extraction is complicated • Tip "slippage" • Substrate effects • Unable to visualise specimen deformation in real time
AFM Method **- AFM Bending**	• No tip slippage • Simple NW deposition methods used • Extremely sensitive (0.2 nN force resolution) • No specimen damage during imaging • Ability to measure nanowires < 20 nm in diameter • Can be adapted for electromechanical measurement	• Complex substrate fabrication required • Reliability of clamps • Arduous tip calibration required • Unable to visualise specimen deformation in real time

1.6 Electromechanical Measurements

The 3-point lateral bending measurement technique was chosen for the work of this thesis because with minor modification, it can be used to measure the electromechanical properties of nanowires. In 2014, McCarthy *et al.*[86] measured the Poisson's ratio of individual metallic nanowires. A lateral force microscopy technique was used to elastically load metallic nanowires and measure the resistance change in the NW as the wire was manipulated, as

shown in Figure 1.9. The mechanical manipulation used is similar to that used in previous works[22,46,85].

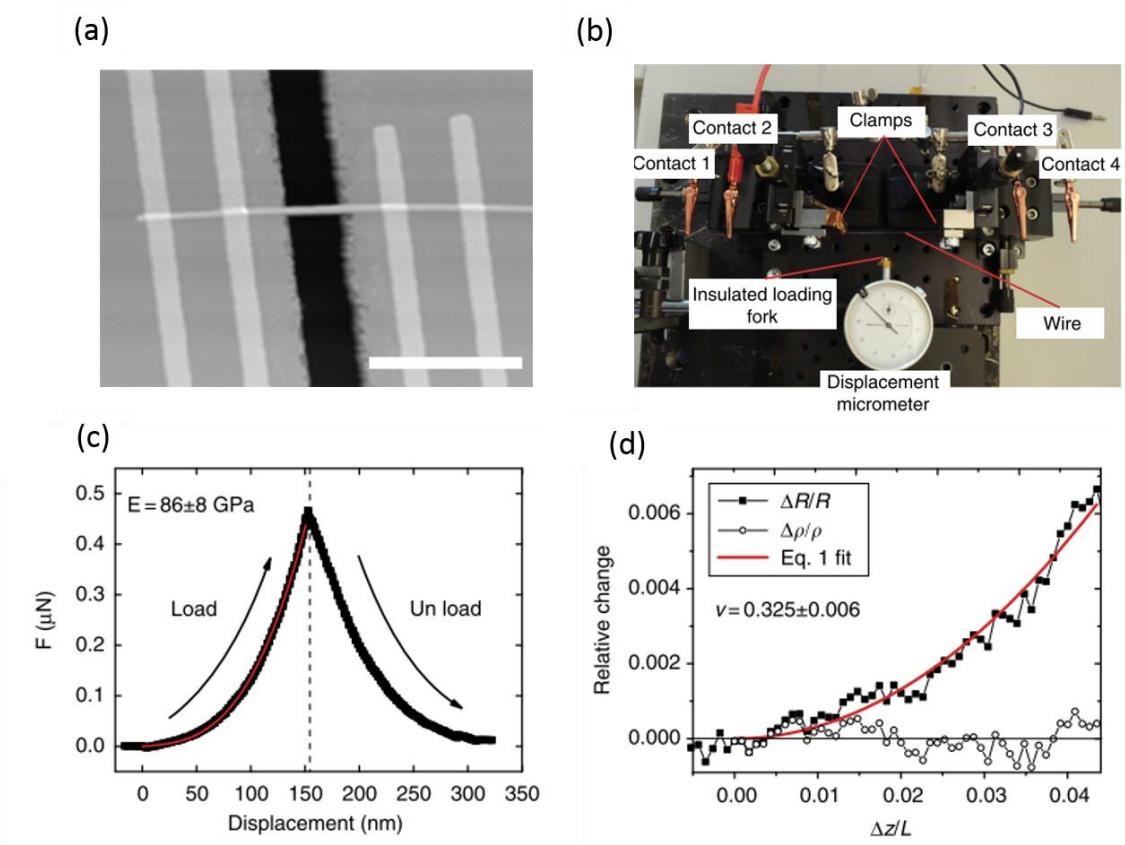

Figure 1.9: (a) AFM image of an individual suspended 80 nm diameter AgNW with four contact-electrodes prior to 3-point bending experiment, scale bar 5μm. (b) Photograph of the macroscopic experiment of the 3-point bending experiment with four electrical contacts. (c) Force-displacement response for loading and unloading the AgNW in (a), the loading curve can be used to determine Young's modulus. (d) Relative change in resistance as a function of the ratio of the displacement to the clamped length, from which Poisson's ratio can be determined[86].

A model was also developed that allowed Poisson's ratio to be determined from the relative change in resistance. *Poisson's ratio*, *v*, is a dimensionless material property that relates the lateral strain in a material to the longitudinal strain[33]. The same measurement was repeated using macroscopic nanowires and a macroscopic measurement set-up (Figure 1.9 (b)). It was found that the Poisson's ratio of macroscopic nanowires and nickel nanowires were comparable to bulk values. However, the Poisson's ratio for silver nanowires measured deviated from that of bulk silver. It was proposed that the variation in silver nanowires was due to differences in their pentagonally twinned structure, which is known to produce significant internal stress[87].

Towards the end of the thesis this electromechanical technique will be used to analyse the effects that current flow can have on the mechanical properties of pentagonally twinned AgNWs. Previously, the most common type of electromechanical measurements performed were piezoresponse force microscopy measurements (PFM) measurements[88-90]. Additionally, MEMs tensile testing stages were developed to facilitate electromechanical measurements[91-93]. In order to use the technique developed by McCarthy *et al*.[86] careful consideration is required when making electrical measurements on NWs.

1.7 Electrical Properties of 1-Dimensional Nanomaterials

The electrical properties of 1D nanomaterials are also difficult to measure on the nanoscale. Like mechanical properties, connections to the specimen are required to probe their electrical properties. This is generally achieved using lithographically defined metallic contacts, as in Figure 1.9 (a).

Electrical conduction occurs as a result of an external electro-motive force which causes charge to flow predominantly in the direction of the applied electric field. While it is well known that electrical properties of a material can be altered via doping, strain is also known to dramatically affect electron scattering mechanisms and hence a material's electrical conductivity. Electromechanical measurement provides an opportunity to directly explore the effects of perfect uniaxial strain on 1D wire systems.

The most common method to measure a material's electrical properties is current-voltage (*IV*) analysis. This generally involves sweeping a voltage across the material and measuring the resulting current, or *vice versa*. From measuring the *IV* response of a material several material electrical properties can be determined such as resistance (R), resistivity (ρ), current density (j) and conductivity (σ).

Electrical current is the rate at which charge flows past a given point. The current flow through a material can be determined if the quantity of charge Q passing through a cross section of the material in a time, t, can be measured. Put simply, the current is the ratio of the quantity of charge and time;

$$I = \frac{dQ}{dt} \tag{1.18}$$

where I is the current, Q is charge and t is time. The units are coulombs/second (C/s) more commonly known as Amperes (A). The ease at which a solid material transmits an electric

current is one of the most important electrical characteristics. *Ohm's Law* relates the current, *I*, to the applied voltage;

$$V = IR \tag{1.19}$$

where *R* is the *resistance* of the material to current flow. It is important to note that not all conductors follow Ohm's law. It generally holds true for metals but it does not hold true for semiconductors. The unit of resistance is the *Ω*. The resistance of a material is affected by the geometry of the material through which a current is passing. The *resistivity* (ρ) of a material is independent of geometry and so it can be used as a direct comparison between different materials. It is related to *R* as follows;

$$\rho = \frac{RA}{l} \tag{1.20}$$

where l is the distance between the two points where the voltage is applied and *A* is the cross-sectional area of the material perpendicular to current flow.

The *electrical conductivity* is the reciprocal of the resistivity and demonstrates the ease with which a material can conduct an electric current;

$$\sigma = \frac{1}{\rho} \tag{1.21}$$

The *current density* is the ratio of the electric current flowing at a particular point in a conductor to the cross-sectional area of the conductor taken perpendicular to the current flow at that point. It is measured in units of A/m^2;

$$j = \frac{I}{A^2} \tag{1.22}$$

There are certain considerations when making electrical measurements on nanomaterials compared to their bulk counterparts[94];

I. Nanoscopic particles will in general not support the same current levels as macroscopic devices. Therefore, careful control of the current levels is required when interrogating a specimen.

II. Owing to their small masses, nanoscopic devices are more prone to electric fields from nearby components. Therefore, attention to the applied voltages is required. Care is also required when handling devices as static charge build-up can cause significant damage to the material of interest.

III. Again, due to their small size, parasitic inductance and capacitance of nanoscopic devices tend to be small. Therefore, instrumentation used for characterising their *IV* curves must be capable of measuring low currents at a short reaction time.

Two types of measurement techniques are generally used for measuring the electrical properties of a nanomaterial; a 2-point or 4-point measurement. In a 2-point measurement the current and voltage is measured over the same two contacts where the voltage is sourced. This results in significant error because the contact resistance between the leads and the nanomaterial can be many magnitudes greater than that of the material itself. A 4-point measurement gives a true resistance measurement of the material. In this scenario, the voltage is sourced across the outer two contacts while the current is measured across the inner two. This prevents the measurement of the contact resistance between the leads and the material. Figure 1.10 shows a schematic of both methods.

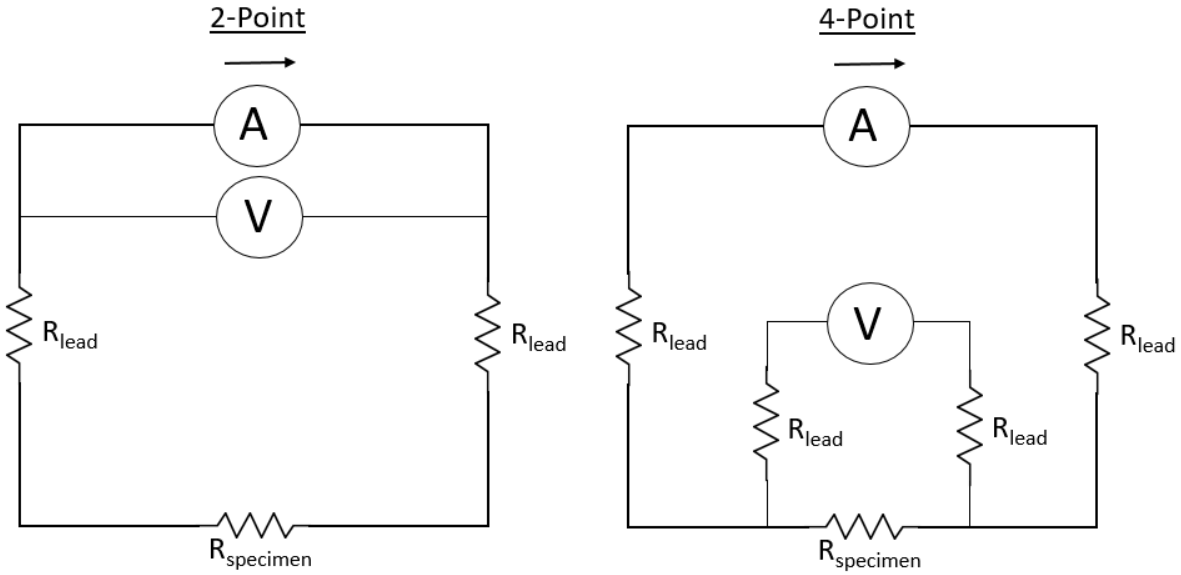

Figure 1.10: Equivalent circuits demonstrating both 2-Point and 4-Point measurements. By measuring the voltage drop across the specimen of interest, the contact resistance is removed from the measurement.

By carefully measuring the 4-point electrical properties of nanowires, along with the technique developed in the work of McCarthy[95,86], the measurement of the effects of current

flow on the mechanical properties of nanowires can be investigated. This is an area which, to date, has seen little research due to the measurement difficulties involved.

1.8 Thesis Outline

This thesis demonstrates for the first time the importance of the initial stress state of NWs prior to mechanical testing. The origins of the different observable mechanical responses for solvent and dry deposited NWs are investigated, with particular emphasis on the resulting stress state of the material. This chapter has discussed the motivation for this work, and has provided a detailed review on the current methods used to deposit NWs and measure their mechanical properties. In chapter 2, the equipment and methods used to conduct the experiments presented in this thesis are discussed. The work presented in chapter 3 analyses the different adhesion characteristics observed between silver and silicon nanowires and SiO_2 substrates, including a determination of the initial residual stress state of these NWs.

Chapter 4, provides an analysis of the validity of different models currently being used to extract the Young's modulus of doubly-clamped beams affected by a residual stress. Differences between theoretical predictions and experimental data are discussed, and it is concluded that caution must be exercised when analysing doubly-clamped wires affected by residual stress. In chapter 5, cantilever beam measurements on NWs are used to determine the Young's modulus of NWs which are not affected by residual stress. These cantilever beam measurements are used as a benchmark to compare results of Young's modulus values obtained from doubly-clamped wires affected by a residual stress. In chapter 6, the origin of the residual stress in silver nanowires is explored. Chapter 7 outlines a unique irreversible stiffening effect that occurs when current is passed through pentagonally twinned silver nanowires. Final remarks and conclusions are then presented in chapter 8.

1.9 References

(1) Feynman, R. P. There's Plenty of Room at the Bottom. *J. Microelectromechanical Syst.* **1992**, *1*, 60–66.

(2) Drexler, K. E. *Engines of Creation: The Coming Era of Nanotechnology*; Doubleday, **1986**.

(3) Baughman, R. H.; Zakhidov, A. A.; de Heer, W. A. Carbon Nanotubes --- the Route toward Applications. *Science (80-.).* **2002**, *297*, 787–792.

(4) Bernholc, J.; Brenner, D.; Nardelli, M. B.; Meunier, V.; Roland, C. Mechanical and Electrical Properties of Nanotubes. *Annu. Rev. Mater. Res.* **2002**, *32*, 347–375.

(5) Kuno, M. An Overview of Solution-Based Semiconductor Nanowires: Synthesis and Optical Studies. *Phys. Chem. Chem. Phys.* **2008**, *10*, 620–639.

(6) Geim, A. K.; Novoselov, K. S. The Rise of Graphene. *Nat. Mater.* **2007**, *6*, 183–191.

(7) Mayoral, A.; Barron, H.; Estrada-Salas, R.; Vazquez-Duran, A.; José-Yacamán, M. Nanoparticle Stability from the Nano to the Meso Interval. *Nanoscale* **2010**, *2*, 335–342.

(8) Valizadeh, A.; Mikaeili, H.; Samiei, M.; Farkhani, S. M.; Zarghami, N. Quantum Dots : Synthesis , Bioapplications , and Toxicity. *Nanoscale Res. Lett.* **2012**, *7*, 1–14.

(9) Binns, C. *Introduction to Nanoscience and Nanotechnology*; Desurvire, E., Ed.; Wiley, **2010**.

(10) Siegel, R. W. Nanostructured Materials -Mind over Matter-. *Nanostructured Mater.* **1994**, *4*, 121–138.

(11) Singh, S. B.; Tandon, P. K. Catalysis : A Brief Review on Nano-Catalyst. *J. Energy Chem. Eng.* **2014**, *2*, 106–115.

(12) Mohammad, S. N. Understanding Quantum Confinement in Nanowires: Basics, Applications and Possible Laws. *J. Phys. Condens. Matter* **2014**, *26*, 423202.

(13) Zhu, T.; Li, J. Ultra-Strength Materials. *Prog. Mater. Sci.* **2010**, *55*, 710–757.

(14) Suresh, S.; Li, J. Deformation of the Ultra-Strong. *Nature* **2008**, *456*, 716.

(15) Maaß, R.; Van Petegem, S.; Ma, D.; Zimmermann, J.; Grolimund, D.; Roters, F.; Van Swygenhoven, H.; Raabe, D. Smaller Is Stronger: The Effect of Strain Hardening. *Acta Mater.* **2009**, *57*, 5996–6005.

(16) Greer, J. R.; De Hosson, J. T. M. Plasticity in Small-Sized Metallic Systems: Intrinsic versus Extrinsic Size Effect. *Prog. Mater. Sci.* **2011**, *56*, 654–724.

(17) Uchic, M. D.; Dimiduk, D. M.; Jeffrey, F. N.; Nix, W. D. Sample Dimensions Influence Strength and Crystal Plasticity. *Science (80-.).* **2004**, *305*, 986–989.

(18) Uchic, M. D.; Shade, P. A.; Dimiduk, D. M. Plasticity of Micrometer-Scale Single Crystals in Compression. *Annu. Rev. Mater. Res.* **2009**, *39*, 361–386.

(19) Li, D.; Wu, Y.; Kim, P.; Shi, L.; Yang, P.; Majumdar, A. Thermal Conductivity of Individual Silicon Nanowires. *Appl. Phys. Lett.* **2003**, *83*, 2934–2396.

(20) Wilder, J. W. G.; Venema, L. C.; Rinzler, A. G.; Smalley, R. E.; Dekker, C. Electronic Structure of Atomically Resolved Carbon Nanotubes. *Nature* **1998**, *391*, 59–62.

(21) Bell, A. P.; Fairfield, J. A.; McCarthy, E. K.; Mills, S.; Boland, J. J.; Baffou, G.; McCloskey, D. Quantitative Study of the Photothermal Properties of Metallic Nanowire Networks. *ACS Nano* **2015**, *9*, 5551–5558.

(22) Wu, B.; Heidelberg, A.; Boland, J. J. Mechanical Properties of Ultrahigh-Strength Gold Nanowires. *Nat. Mater.* **2005**, *4*, 525–529.

(23) Salvetat, J.-P.; Briggs, G.; Bonard, J.-M.; Bacsa, R.; Kulik, A.; Stöckli, T.; Burnham, N.; Forró, L. Elastic and Shear Moduli of Single-Walled Carbon Nanotube Ropes. *Phys. Rev. Lett.* **1999**, *82*, 944–947.

(24) Larrieu, G.; Han, X.-L. Vertical Nanowire Array-Based Field Effect Transistors for Ultimate Scaling. *Nanoscale* **2013**, *5*, 2437–2441.

(25) Guerfi, Y.; Larrieu, G.; Park, D.; Yeo, K.; Suk, S.; Li, M.; Yeoh, Y.; Cho, K.; Hong, K.-H.; Yun, S.; *et al.* Vertical Silicon Nanowire Field Effect Transistors with Nanoscale Gate-All-Around. *Nanoscale Res. Lett.* **2016**, *11*, 210.

(26) O'Kelly, C.; Fairfield, J. A.; Boland, J. J. A Single Nanoscale Junction with Programmable Multilevel Memory. *ACS Nano* **2014**, *8*, 11724–11729.

(27) Berdichevsky, Y.; Lo, Y. H. Polypyrrole Nanowire Actuators. *Adv. Mater.* **2006**, *18*, 122–

125.
(28) Loh, O. Y.; Espinosa, H. D. Nanoelectromechanical Contact Switches. *Nat. Nanotechnol.* **2012**, *7*, 283–295.
(29) Duraffourg, L.; Arcamone, J. *Nanoelectromechanical Systems*; Baptist, R., Ed.; Wiley, **2015**.
(30) Xu, W. H.; Wang, L.; Guo, Z.; Chen, X.; Liu, J.; Huang, X. J. Copper Nanowires as Nanoscale Interconnects: Their Stability, Electrical Transport, and Mechanical Properties. *ACS Nano* **2015**, *9*, 241–250.
(31) Cui, Y.; Wei, Q.; Park, H.; Lieber, C. Nanowire Nanosensors for Highly Sensitive and Selective Detection of Biological and Chemical Species Cited by Me. *Science (80-.).* **2001**, *293*, 1289–1292.
(32) Stach, E. Nanotubes Reveal Their True Strength. *Nat. Nanotechnol.* **2008**, *3*, 586–587.
(33) Hibbeler, R. C. *Mechanics of Materials*; 8th Edition; Pearson Educational, **2011**.
(34) W.D. Callister Jr. *Materials Science and Engineering: An Integrated Approach*; 2nd Edition; John Wiley and Sons, **2005**.
(35) Carter, C. B.; Norton, M. G. *Ceramic Materials: Science and Engineering*; 2nd Edition; Springer Science & Business Media, **2013**.
(36) Yu, M.; Lourie, O.; Dyer, M. J.; Moloni, K.; Kelly, T. F.; Ruoff, R. S. Strength and Breaking Mechanism of Multiwalled Carbon Nanotubes Under Tensile Load. *Science (80-.).* **2000**, *287*, 637–640.
(37) Cuenot, S.; Demoustier-Champagne, S.; Nysten, B. Elastic Modulus of Polypyrrole Nanotubes. *Phys. Rev. Lett.* **2000**, *85*, 1690–1693.
(38) Jang, D.; Greer, J. R. Size-Induced Weakening and Grain Boundary-Assisted Deformation in 60 Nm Grained Ni Nanopillars. *Scr. Mater.* **2011**, *64*, 77–80.
(39) Zhu, Y.; Qin, Q.; Xu, F.; Fan, F.; Ding, Y.; Zhang, T.; Wiley, B. J.; Wang, Z. L. Size Effects on Elasticity, Yielding, and Fracture of Silver Nanowires: In Situ Experiments. *Phys. Rev. B - Condens. Matter Mater. Phys.* **2012**, *85*, 1–7.
(40) Xu, F.; Qin, Q.; Mishra, A.; Gu, Y.; Zhu, Y. Mechanical Properties of ZnO Nanowires under Different Loading Modes. *Nano Res.* **2010**, *3*, 271–280.
(41) Zhu, Y.; Ke, C.; Espinosa, H. D. Experimental Techniques for the Mechanical Characterization of One-Dimensional Nanostructures. *Exp. Mech.* **2007**, *47*, 7–24.
(42) Han, X.; Zhang, Z.; Wang, Z. L. Experimental Nanomechanics of One-Dimensional Nanomaterials By in Situ Microscopy. *Nano* **2007**, *2*, 249–272.
(43) Wang, W.; Li, S.; Zhang, H.; Lu, Y. Recent Developments in Testing Techniques for Elastic Mechanical Properties of 1-D Nanomaterials. *Recent Pat. Nanotechnol.* **2015**, *9*, 33–42.
(44) Yu, M.-F.; Files, B. S.; Arepalli, S.; Ruoff, R. S. Tensile Loading of Ropes of Single Wall Carbon Nanotubes and Their Mechanical Properties. *Phys. Rev. Lett.* **2000**, *84*, 5552–5555.
(45) Li, X.; Gao, H.; Murphy, C. J.; Caswell, K. K. Nanoindentation of Silver Nanowires. *Nano Lett.* **2003**, *3*, 1495–1498.
(46) Wu, B.; Heidelberg, A.; Boland, J. J. Microstructure-Hardened Silver Nanowires. *Nano Lett.* **2006**, *6*, 468–472.
(47) Li, H.; Wu, J. M. T.; Huang, X.; Yin, Z. Y.; Liu, J. Q.; Zhang, H. A Universal, Rapid Method for Clean Transfer of Nanostructures onto Various Substrates. *ACS Nano* **2014**, *8*, 6563–6570.
(48) Dai, H. Controlling Nanotube Growth. *Phys. World* **2000**, *13*, 43–47.
(49) Hong, G.; Chen, Y.; Li, P.; Zhang, J. Controlling the Growth of Single-Walled Carbon Nanotubes on Surfaces Using Metal and Non-Metal Catalysts. *Carbon N. Y.* **2012**, *50*, 2067–2082.
(50) Song, J.; Wang, X.; Riedo, E.; Wang, Z. L. Elastic Property of Vertically Aligned Nanowires. *Nano Lett.* **2005**, *5*, 1954–1958.
(51) Hoffmann, S.; Utke, I.; Moser, B.; Michler, J.; Christiansen, S. H.; Schmidt, V.; Senz, S.; Werner, P.; Gŏsele, U.; Ballif, C. Measurement of the Bending Strength of Vapor-Liquid-Solid Grown Silicon Nanowires. *Nano Lett.* **2006**, *6*, 622–625.
(52) Huang, S.; Woodson, M.; Smalley, R.; Liu, J. Growth Mechanism of Oriented Long Single Walled Carbon Nanotubes Using “Fast-Heating” Chemical Vapor Deposition Process. *Nano*

Lett. **2004**, *4*, 1025–1028.
(53) Zhu, Y.; Espinosa, H. D. An Electromechanical Material Testing System for in Situ Electron Microscopy and Applications. *Proc. Natl. Acad. Sci. U. S. A.* **2005**, *102*, 14503–14508.
(54) Stan, G.; Krylyuk, S.; Davydov, A. V.; Cook, R. F. Bending Manipulation and Measurements of Fracture Strength of Silicon and Oxidized Silicon Nanowires by Atomic Force Microscopy. *J. Mater. Res.* **2011**, *27*, 562–570.
(55) Ni, H.; Li, X.; Gao, H. Elastic Modulus of Amorphous SiO_2 Nanowires. *Appl. Phys. Lett.* **2006**, *88*, 43108.
(56) Treacy, M. M. J.; Ebbesen, T. W.; Gibson, J. M. Exceptionally High Young's Modulus Observed for Individual Carbon Nanotubes. *Nature* **1996**, *381*, 678–680.
(57) Poncharal, P.; Wang, Z. L.; Ugarte, D.; de Heer, W. A. Electrostatic Deflections and Electromechanical Resonances of Carbon Nanotubes. *Science (80-.).* **1999**, *283*, 1513–1516.
(58) Haque, M. A.; Saif, M. . T. A. Deformation Mechanisms in Free-Standing Nanoscale Thin Films: A Quantitative in Situ Transmission Electron Microscope Study. *Proc. Natl. Acad. Sci. U. S. A.* **2004**, *101*, 6335–6340.
(59) Zhu, Y.; Corigliano, A.; Espinosa, H. D. A Thermal Actuator for Nanoscale In Situ Microscopy Testing: Design and Characterization. *J. Micromechanics Microengineering* **2006**, *16*, 242–253.
(60) Gu, X. W.; Jafary-Zadeh, M.; Chen, D. Z.; Wu, Z.; Zhang, Y. W.; Srolovitz, D. J.; Greer, J. R. Mechanisms of Failure in Nanoscale Metallic Glass. *Nano Lett.* **2014**, *14*, 5858–5864.
(61) Han, X.; Zheng, K.; Zhang, Y.; Zhang, X.; Zhang, Z.; Wang, Z. L. Low-Temperature in Situ Large-Strain Plasticity of Silicon Nanowires. *Adv. Mater.* **2007**, *19*, 2112–2118.
(62) Moore, N. W.; Luo, J.; Huang, J. Y.; Mao, S. X.; Houston, J. E. Superplastic Nanowires Pulled from the Surface of Common Salt. *Nano Lett.* **2009**, *9*, 2295–2299.
(63) Huang, J. Y.; Chen, S.; Wang, Z. Q.; Kempa, K.; Wang, Y. M.; Jo, S. H.; Chen, G.; Dresselhaus, M. S.; Ren, Z. F. Superplastic Carbon Nanotubes. *Nature* **2006**, *439*, 281.
(64) Bhushan, B.; Li, X. Nanomechanical Characterisation of Solid Surfaces and Thin Films. *Int. Mater. Rev.* **2003**, *48*, 125–164.
(65) Furmanchuk, A.; Isayev, O.; Dinadayalane, T. C.; Leszczynska, D.; Leszczynski, J. Mechanical Properties of Silicon Nanowires. *Wiley Interdiscip. Rev. Comput. Mol. Sci.* **2012**, *2*, 817–828.
(66) Oliver, C.; Pharr, M. An Improved Technique for Determining Hardness and Elastic Modulus Using Load and Displacement Sensing Indentation Experiments. *Journal of Materials Research*, **1992**, *7*, 1564–1583.
(67) Zou, Y.; Ma, H.; Spolenak, R. Ultrastrong Ductile and Stable High-Entropy Alloys at Small Scales. *Nat. Commun.* **2015**, *6*, 1–8.
(68) Sohn, Y.-S.; Park, J.; Yoon, G.; Song, J.; Jee, S.-W.; Lee, J.-H.; Na, S.; Kwon, T.; Eom, K. Mechanical Properties of Silicon Nanowires. *Nanoscale Res. Lett.* **2010**, *5*, 211–216.
(69) Zhu, Y. Experimental Mechanics of Crystalline Nanowires. *Appl. Mech. Rev.* **2016**, *69*, 1–24.
(70) Wong, E. W.; Sheehan, P. E.; Lieber, C. M. Nanobeam Mechanics: Elasticity, Strength, and Toughness of Nanorods and Nanotubes. *Science (80-.).* **1997**, *277*, 1971–1975.
(71) Murphy, K. F.; Chen, L. Y.; Gianola, D. S. Effect of Organometallic Clamp Properties on the Apparent Diversity of Tensile Response of Nanowires. *Nanotechnology* **2013**, *24*, 1–8.
(72) Qin, Q.; Xu, F.; Cao, Y.; Ro, P. I.; Zhu, Y. Measuring True Young's Modulus of a Cantilevered Nanowire: Effect of Clamping on Resonance Frequency. *Small* **2012**, *8*, 2571–2576.
(73) Conache, G.; Gray, S. M.; Ribayrol, A.; Fröberg, L. E.; Samuelson, L.; Montelius, L.; Pettersson, H. Comparative Friction Measurements of InAs Nanowires on Three Substrates. *J. Appl. Phys.* **2010**, *108*, 1–5.
(74) Walters, D. A.; Ericson, L. M.; Casavant, M. J.; Liu, J.; Colbert, D. T.; Smith, K. a.; Smalley, R. E. Elastic Strain of Freely Suspended Single-Wall Carbon Nanotube Ropes. *Appl. Phys. Lett.* **1999**, *74*, 3803–3805.
(75) Salvetat, J.-P.; Kulik, A. J.; Bonard, J.-M.; Briggs, G. A. D.; Stöckli, T.; Méténier, K.; Bonnamy, S.; Béguin, F.; Burnham, N. A.; Forró, L. Elastic Modulus of Ordered and

Disordered Multiwalled Carbon Nanotubes. *Adv. Mater.* **1999**, *11*, 161–165.
(76) Kis, A.; Mihailovic, D.; Remskar, M.; Mrzel, A.; Jesih, A.; Piwonski, I.; Kulik, A. J.; Benoît, W.; Forró, L. Shear and Young's Moduli of MoS_2 Nanotube Ropes. *Adv. Mater.* **2003**, *15*, 733–736.
(77) Kis, A.; Kasas, S.; Babić, B.; Kulik, A. J.; Benoît, W.; Briggs, G. A. D.; Schönenberger, C.; Catsicas, S.; Forró, L. Nanomechanics of Microtubules. *Phys. Rev. Lett.* **2002**, *89*, 248101.
(78) Namazu, T.; Isono, Y.; Tanaka, T. Evaluation of Size Effect on Mechanical Properties of Single Crystal Silicon by Nanoscale Bending Test Using AFM. *J Microelectromech S* **2000**, *9*, 450–459.
(79) Landau, L. D.; Lifshitz, E. M. *Theory of Elasticity*; Ltd., P. P., Ed.; J.W. Arrowsmith Ltd., **1959**.
(80) Sundararajan, S.; Bhushan, B.; Namazu, T.; Isono, Y. Mechanical Property Measurements of Nanoscale Structures Using an Atomic Force Microscope. *Ultramicroscopy* **2002**, *91*, 111–118.
(81) Heidelberg, A.; Ngo, L. T.; Wu, B.; Phillips, M. A.; Sharma, S.; Kamins, T. I.; Sader, J. E.; Boland, J. J. A Generalized Description of the Elastic Properties of Nanowires. *Nano Lett.* **2006**, *6*, 1101–1106.
(82) Tombler, T.; Zhou, C.; Alexseyev, L.; Kong, J.; Dai, H.; Liu, L.; Jayanthi, C.; Tang, M.; Wu, S. Reversible Electromechanical Characteristics of Carbon Nanotubes under Local-Probe Manipulation. *Nature* **2000**, *405*, 769–772.
(83) Minot, E. D.; Yaish, Y.; Sazonova, V.; Park, J.-Y.; Brink, M.; McEuen, P. L. Tuning Carbon Nanotube Band Gaps with Strain. *Phys. Rev. Lett.* **2003**, *90*, 156401.
(84) Bellan, L. M.; Kameoka, J.; Craighead, H. G. Measurement of the Young's Moduli of Individual Polyethylene Oxide and Glass Nanofibres. *Nanotechnology* **2005**, *16*, 1095.
(85) Ngo, L. T.; Almecija, D.; Sader, J. E.; Daly, B.; Petkov, N.; Holmes, J. D.; Erts, D.; Boland, J. J. Ultimate-Strength Germanium Nanowires. *Nano Lett* **2006**, *6*, 2964–2968.
(86) McCarthy, E. K.; Bellew, A. T.; Sader, J. E.; Boland, J. J. Poisson's Ratio of Individual Metal Nanowires. *Nat. Commun.* **2014**, *5*, 1–7.
(87) Sun, Y.; Ren, Y.; Liu, Y.; Wen, J.; Okasinski, J. S.; Miller, D. J. Ambient-Stable Tetragonal Phase in Silver Nanostructures. *Nat. Commun.* **2012**, *3*, 1-6.
(88) Wang, Z. L.; Song, J. Piezoelectric Nanogenerators Based on Zinc Oxide Nanowire Arrays. *Science (80-.).* **2006**, *312*, 242–246.
(89) Minary-Jolandan, M.; Bernal, R. A.; Espinosa, H. D. Strong Piezoelectricity in Individual GaN Nanowires. *MRS Commun.* **2011**, *1*, 45–48.
(90) Zhao, M. H.; Wang, Z. L.; Mao, S. X. Piezoelectric Characterization Individual Zinc Oxide Nanobelt Probed by Piezoresponse Force Microscope. *Nano Lett.* **2004**, *4*, 587–590.
(91) Yong, Z.; Xinyu, L.; Changhai, R.; Yan Liang, Z.; Lixin, D.; Yu, S. Piezoresistivity Characterization of Synthetic Silicon Nanowires Using a MEMS Device. *Microelectromechanical Syst. J.* **2011**, *20*, 959–967.
(92) Bernal, R. A.; Filleter, T.; Connell, J. G.; Sohn, K.; Huang, J.; Lauhon, L. J.; Espinosa, H. D. In Situ Electron Microscopy Four-Point Electromechanical Characterization of Freestanding Metallic and Semiconducting Nanowires. *Small* **2014**, *10*, 725–733.
(93) Murphy, K. F.; Piccione, B.; Zanjani, M. B.; Lukes, J. R.; Gianola, D. S. Strain- and Defect-Mediated Thermal Conductivity in Silicon Nanowires. *Nano Lett.* **2014**, *14*, 3785–3792.
(94) James Niemann (Keithley Inc.). Electrical Measurements On Nanoscale Materials. **2005**.
(95) McCarthy, E. K. The Electromechanical Properties of Individual Nanowires, Trinity College Dublin, **2013**.

2

EQUIPMENT AND METHODS

2.1 Introduction

To investigate the properties of nanoscale materials, special microscopy and fabrication tools are required. These are necessary to image materials for characterisation purposes, manipulate materials into specific positions and to make contacts to nanomaterials. This allows fundamental material properties such as their electrical, mechanical and optical properties to be investigated. In this chapter I will discuss the fabrication and microscopy tools that were used throughout the work in this thesis, furthermore the experimental procedures involved will be outlined.

2.2 Electron Microscopy

Electron microscopes were developed due to the fundamental limitations involved with conventional optical microscopes. The resolving power of optical microscopes is limited by the wavelength of light, this results in an achievable resolution that is on the order of half the wavelength of light ~ 250 nm. This is not enough to observe nanomaterials which are less than 100 nm in one if not more dimensions. To achieve this resolution, microscopes which use electrons rather than light were invented. Louis de Broglie theorised that electrons have a wave like nature in 1924 which was verified experimentally in 1927 by electron diffraction experiments[1]. The first electron microscopes were reported in 1931. They were based on de Broglie's equation where the wavelength of an electron went as $\lambda = 1.23/E^{1/2}$ with λ in nm and E in eV.

Electron microscopes generally operate between 0.5 and 300 kV, so at the highest accelerating voltages resolutions up to 0.2 nm can be achieved. However, due to imperfections in the lenses that make up the microscope these resolutions are almost unachievable. Resolution is the most important property of a microscope as it allows the user to resolve

objects that are very close to one another. Another benefit of electron microscopes over optical microscopes is that they have a much higher depth of field which allows the user to see objects as apparent in 3 dimensions. This again is due to the short wavelength of electrons. There are many different types of electron microscopy such as scanning electron microscopy, transmission electron microscopy and there are also microscopes which use focused ion beams such as gallium or helium ions for imaging as well as applications such as milling.

2.2.1 Scanning Electron Microscopy

The basic principle of the scanning electron microscope (SEM) was developed by Knoll in 1935[2], however, early SEM's suffered from deficiencies in the collection and amplification of the signal from the specimen. It was Charles Oatley in 1965[3] that developed scanning electron microscopes as we know them today.

SEM works on the principle whereby a beam of electrons (with energies from a few hundred eV to tens of keV) is focussed at the surface of a specimen and scanned across it in a raster pattern. The beam is generated by an electron gun that is composed of three components (Figure 2.1) 1) a filament or cathode made of tungsten wire, Lanthanum Hexaboride crystal (LaB_6) or Field Emission Gun (FEG) materials, 2) A Wehnelt cylinder that controls the flow of electrons, 3) and a positively charged anode plate which attracts electrons down the electron column towards the specimen. The brightness of the source is related to the current density and ultimately determines the contrast, resolution and signal to noise ratio of the microscope.

FEGs have higher brightness values $\sim 10^{12}$ A/m^2sr at 100 kV compared to Tungsten which has a brightness of $\sim 10^{10}$ A/m^2sr at the same accelerating voltage. The reason being that the emission current for FEG sources occurs within a very small source size. The beam exits the gun from this source, which is on the order of nanometres compared to a few microns for the other source types. However, these FEG sources come at a much greater cost which must be taken into account when considering the resolution and application required. The gun must be kept under ultra-high vacuum ($< 10^{-9}$ mbar) otherwise the filament would burn out. Additionally, the chamber needs to be kept under high vacuum ($< 10^{-6}$ mbar) otherwise the electron beam would be scattered because of interactions with molecules in the chamber before reaching the specimen.

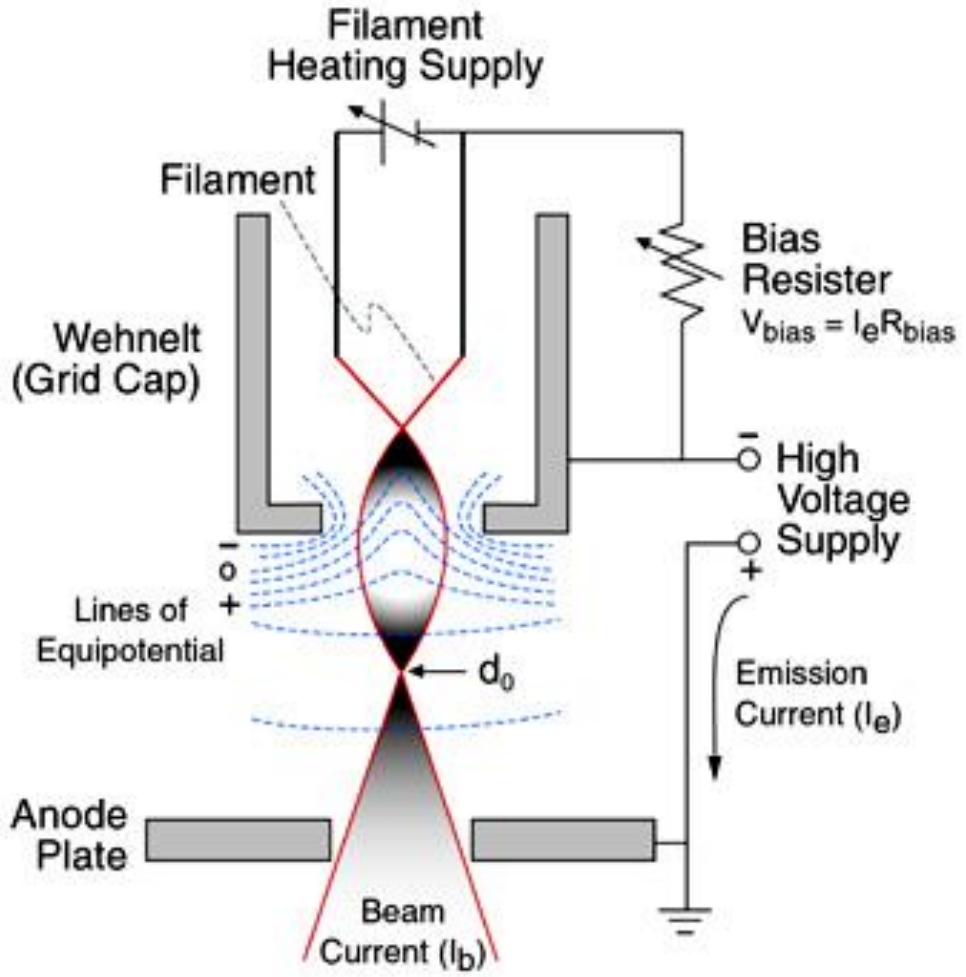

Figure 2.1: Schematic illustration of the setup of the gun of an SEM[4].

The electron beam is accelerated down the column and passes through a series of electromagnetic lenses and apertures (see Figure 2.2), which are used to produce a small focused beam of electrons on the specimen. Signal detection begins when the beam electron, known as the primary electron, enters the specimen. A primary electron will travel some distance into a material before scattering occurs, due to collisions with other atoms in the material. There are several different scattering events that can occur and the interaction volume where all the scattering processes occurs is depicted in Figure 2.3. The volume of the interaction volume depends on the atomic density, topography of the specimen and the acceleration voltage of the incident primary electron beam.

The interactions can be either elastic or inelastic. *Backscattered electrons* arise due to elastic collisions between the incident beam and the nucleus of the target atom. The incident electrons are backscattered with little or no loss in energy and can be scattered to angles between 0 - 180°. *Secondary electrons* are generated by inelastic scattering of the primary

electron beam. An inelastic collision can result in the outermost electrons being dislodged from the specimen atom. These secondary electrons have energies generally < 50 eV. Due to the low energy, only electrons which are close to the surface (2-5 nm) have enough energy to escape. The secondary electron current is representative of a very small region on the specimen surface and so is used in high-resolution surface imaging. When electrons are dislodged from specific orbits of an atom in the specimen, x-rays are emitted. With an energy dispersive detector (EDS) these x-rays can be detected to give elemental information about the atom from which they originated due to the energy and wavelength of the x-ray. In this thesis, a suite of Carl Zeiss SEM's was used including the Zeiss Supra, Ultra and Auriga.

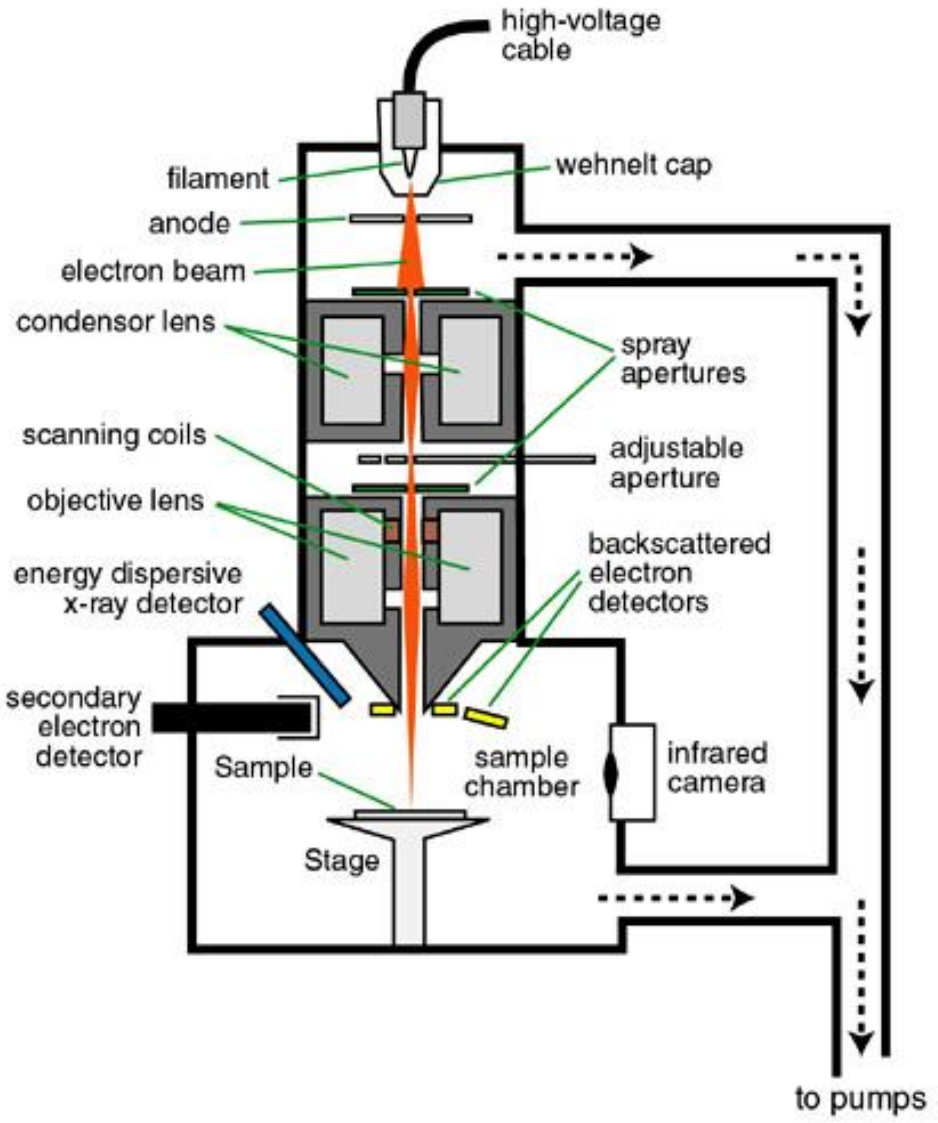

Figure 2.2: Schematic illustration of the inside of an SEM column[4].

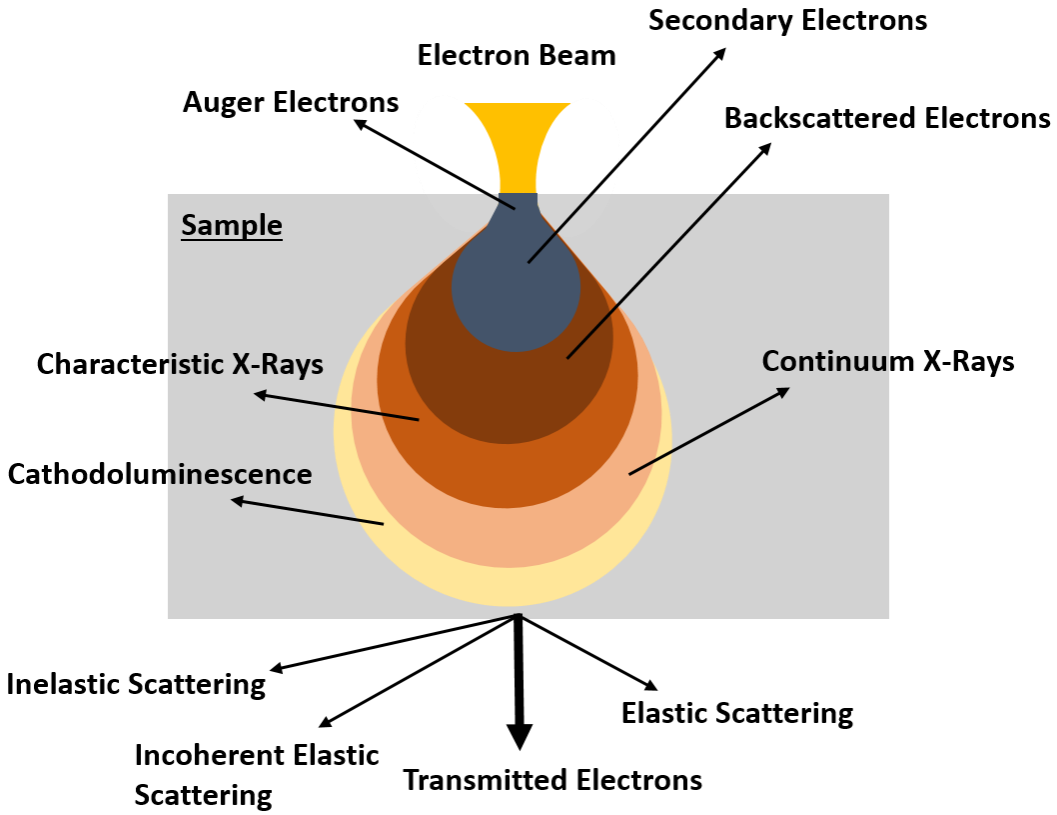

Figure 2.3: Schematic showing various incident beam interactions with a sample.

2.2.2 Transmission Electron Microscopy

The first transmission electron microscope (TEM) was developed in 1931 by Ruska and Knolls[5]. It was the first electron microscope to be invented. TEM is fundamentally different from SEM in that rather than using backscattered and secondary electrons, it relies on transmitted electrons to build up an image. For electrons to be able to pass through a specimen, it must be very thin (< 100 nm thick). Detectors on the opposite side of the specimen collect these electrons which contain information about the specimen. A specimen must often be removed from a supporting substrate to be examined. If the specimen of interest can be suspended in a solvent, it can be dropcast onto a TEM grid or it may have to be prepared by lamella preparation. This involves the use of a focused ion beam to cut out a section of a sample and thinning techniques to reduce its thickness down to less than 100 nm. The resolution of the final image is related to how the electron beam interacts with the sample and how much transmits through to the detector. This can be affected by sample thickness,

accelerating voltage, atomic number of the atoms in the sample, crystallinity and sample density. Generally, accelerating voltages used are between 50 keV and 300 keV.

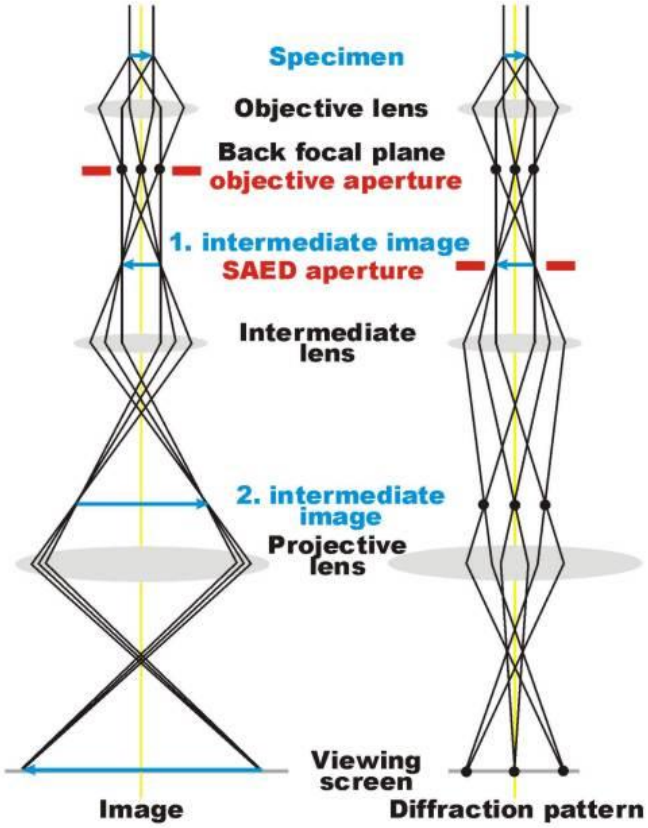

Figure 2.4: Schematic set up of a TEM in two different imaging modes (a) Imaging (b) Diffraction[6].

Increasing the accelerating voltage can improve the resolution but it also increases the risk of the beam damaging the specimen. Therefore, sample preparation is crucial to ensure an adequate resolution is achieved. The ultimate resolution of TEMs is determined by the quality of the electromagnetic lenses and their ability to interact with the beam. Figure 2.4 shows a schematic of the column of a TEM. There are two main operating modes of the TEM; imaging and diffraction.

To create an image, a beam of electrons is generated at the electron gun and is focused into a small, thin, coherent beam by the condenser aperture which excludes high angle electrons. By changing the strength of the intermediate lens and adding or removing the objective aperture it is possible to change between imaging mode and diffraction mode. By inserting the selected area diffraction (SAD) aperture a specific part of an image can be chosen from which to generate a diffraction pattern. This diffraction pattern can be used to examine

crystal orientations or crystal defects. Furthermore, it is particularly useful for examining a crystal orientation from a specific area of a sample and when characterising nanowires (NWs) which have considerably small sizes. Diffraction imaging is a powerful tool when characterising crystalline samples. It is analogous to x-ray diffraction but is unique in that it can image areas as small as several hundred nanometres, whereas x-ray diffraction is generally from much larger areas. This allows the crystal structure of a few grains within a sample, separated by a couple of nanometres, to be resolved using SAD.

The principle advantage of TEM over other electron microscopy techniques is its resolution. By applying classic Rayleigh criteria for a 100 kV accelerating voltage, the wavelength is 4 pm so theoretically a resolution of 2 pm should be achievable. However, as previously mentioned, this is not possible due to imperfections in the lenses. There have been huge advances in this field over the past few years due to breakthroughs in spherical and chromic aberration corrected TEMs. This has increased the resolution capabilities of TEMs leading to the development of High Resolution TEM (HRTEM)[7].

2.3 Electron Beam Lithography

In order to pattern surfaces with contacting features to nanomaterials, electron beam lithography (EBL) is used. Unlike conventional UV lithography which uses UV light to irradiate a resist, EBL uses electrons to irradiate the resist. In conventional UV lithography, a hard mask with a pattern is needed to define features. However, with EBL a computer software program such as Raith can be used to direct an SEM to irradiate a pattern on the resist. EBL was invented in the 1960s[8] and allowed microelectronics to be reduced down to nanoscale dimensions.

The sample is coated with an electron sensitive resist which, when sufficiently dosed by an electron beam, changes its chemical composition allowing it to be removed by a developer while the unexposed area of the resist remains. Further metal deposition steps can then be undertaken to produce a metallised pattern as desired. There are two different types of resist; positive photo resist, where the area irradiated by the electron beam is removed; or negative photoresist, where the areas that haven't been irradiated by the electron beam are removed. EBL is generally used in conjunction with SEM's that have been altered to contain beam blanking plates and a special software that allows the control of the electron beam such as Raith. Raith is a CAD package which saves designs in the GDSII format. It is a software

specially developed for lithographic applications and it allows for the alignment of drawn patterns to alignment marks on a substrate.

One of the most commonly used resists is poly(methylmethacrylate) (PMMA) which is a positive tone resist. When the resist is exposed to an electron beam polymer chains undergo scission which enables them to be dissolved more easily in a developer than longer unexposed chains. Hydrogen silsesquioxane (HSQ) is a negative tone resist where exposure to an electron beam induces polymerisation via cross linking of the polymer chains making removal more difficult.

As mentioned earlier, the interaction of the electrons with the specimen is an important consideration, especially in EBL where both backscattered and secondary electron effects need to be considered. The extent to which electrons are scattered is highly dependent on the energy of the incident electron beam. As electrons pass through the resist there can be positive effects such as undercutting, which leads to better metal deposition. However, there are also negative effects such as over exposure, which can lead to features merging lowering the resolution. The inelastic collision cross section decreases with an increase in electron energy. This provides better resolution capabilities, however reduced forward scattering results in an increased exposure time to deliver a sufficient dose to induce the required changes in the resists. A trade-off is required to find the exposure time which can achieve the resolution needed in an acceptable time.

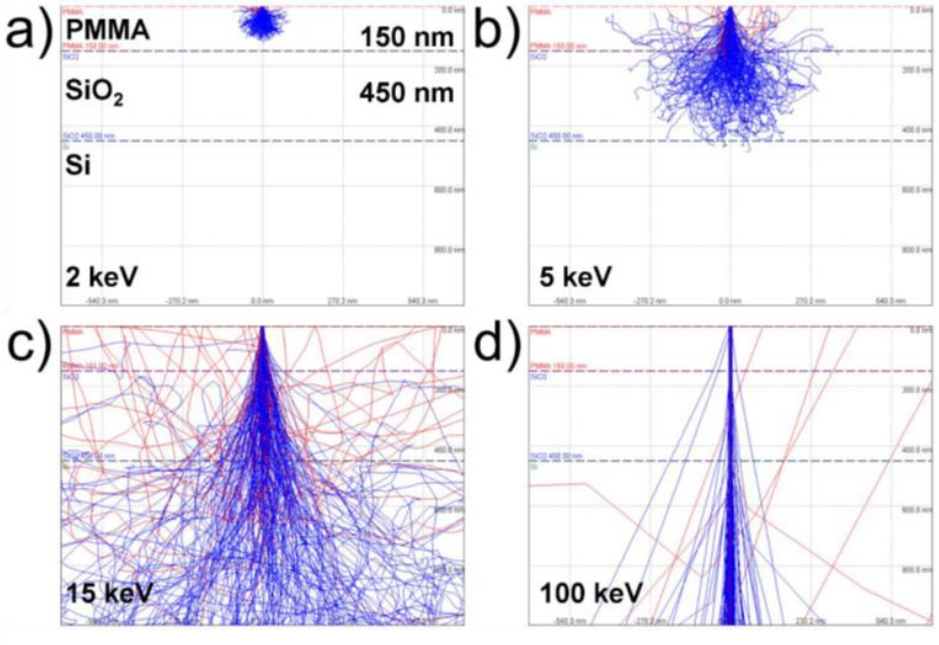

Figure 2.5: Electron trajectories through PMMA covered SiO_2/Si substrate using CASINO software[9]. (a) 2 keV accelerating voltage, (b) 5 keV acceleration voltage, (c) 15 keV acceleration voltage and (d) 100 keV acceleration voltage.

As shown in Figure 2.5 it is possible to simulate the interaction volumes of electrons and a resist using different acceleration voltages. At an accelerating voltage of 2 keV the beam does not interact fully with the resist making it unsuitable for EBL. At 5 keV the beam fully interacts with the resist but there are many scattering events which will lower the resolution achievable. At 15 keV the beam fully penetrates the resist with only a slight undercut at the PMMA/SiO_2 interface. This would make it a suitable accelerating voltage for EBL applications. EBL can be performed up to accelerating voltages of 100 keV where the beam passes linearly through the resist with minimal scattering events. This will allow the exposure of high-resolution features but it will also require a significant increase in the dwell time for the beam to expose the resist in the target region.

To expose an area completely a certain number of electrons must strike the sample within that area. The dose depends on the beam current, beam dwell time and step size. The beam current is defined by the accelerating voltage and aperture size. The step size is the distance from pixel to pixel which will increase the resolution achievable. The dose, beam current and step size are user defined and the dwell time for the exposure is calculated by the software.

In this work a Carl Zeiss Supra SEM modified for EBL applications with Raith software is used. The apertures used are 10 and 20 µm and the beam acceleration voltages used are 10 kV.

2.4 Electron Beam Induced Deposition

Electron Beam Induced Deposition (EBID) is a technique where the deposition of metal or insulator materials is achieved through the dissociation of an adsorbed pre-cursor gas on a surface[10]. The precursor gas is adsorbed through a gas injection system (GIS) which consists of a precursor that can be heated and cooled. This, is coupled to a fine capillary which can be brought in close proximity to the surface as shown in Figure 2.6 (b). When the electron beam interacts with the adsorbed molecules, they decompose to leave some materials on the surface while the volatile products enter the vacuum. For platinum (Pt) deposition, the organometallic precursor $C_5H_4CH_3Pt(CH_3)_3$ is introduced to the SEM chamber, which when struck by the electron beam, decomposes to leave Pt on the substrate as shown in Figure 2.6 (a). The area where the Pt deposits is controlled by the area where the electron beam is scanned. The thickness of Pt metal deposited is controlled by the accelerating voltage, beam current and the beam dwell time.

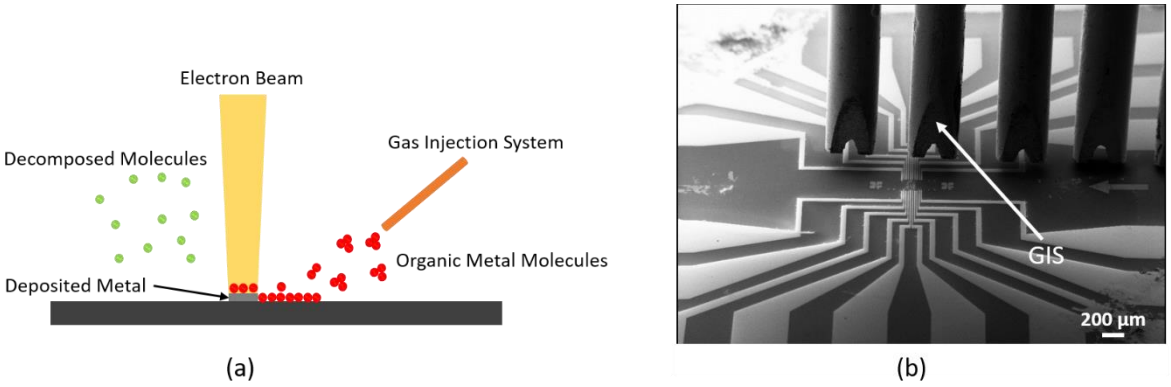

Figure 2.6: (a) Schematic of electron beam induced deposition. (b) SEM image of gas injection system (GIS) located 5 mm above sample surface.

2.5 Focused Ion Beam Milling

The Focused Ion Beam microscope (FIB) is similar to an SEM, except that the beam which is rastered over the sample is an ion beam rather than an electron beam. Ion beam techniques are used for an array of material science applications, from circuit editing to TEM sample preparation and failure analysis. In most commercial systems gallium (Ga) ions are used as their sputtering ability allows precise machining of samples. Unlike electron microscopes FIB is inherently destructive to the sample. This is due to the momentum possessed by the gallium ions as they strike the surface.

The interaction of an ion beam with a surface is more complicated than the equivalent interaction of an electron beam due to the greater momentum involved. There are many different interaction processes that can occur when an impingent Ga ion strikes the surface as depicted in Figure 2.7. When the high-energy ions strike the sample, they sputter atoms from the surface. There will also be implantation of gallium ions into the top few nanometres of the surface. Secondary electrons are also generated by the interaction of the ion beam with the surface which can be used for imaging. It can also be used to deposit material when used in conjunction with a gas injection system. The main use of FIB is the controlled removal of substrate material which allows features to be defined on a sub-micron scale. Most modern FIB instruments supplement the FIB column with an additional SEM column so that the instrument becomes a “dual-beam” platform for imaging, material removal, and deposition at length scales of a few nanometres.

In this work the FIB used was a dual beam Carl Zeiss Auriga with GIS control for metal deposition. For Pt deposition, the aperture used was 30 µm with a 5 kV accelerating voltage. For FIB cutting of NWs a beam current of 1 nA was used.

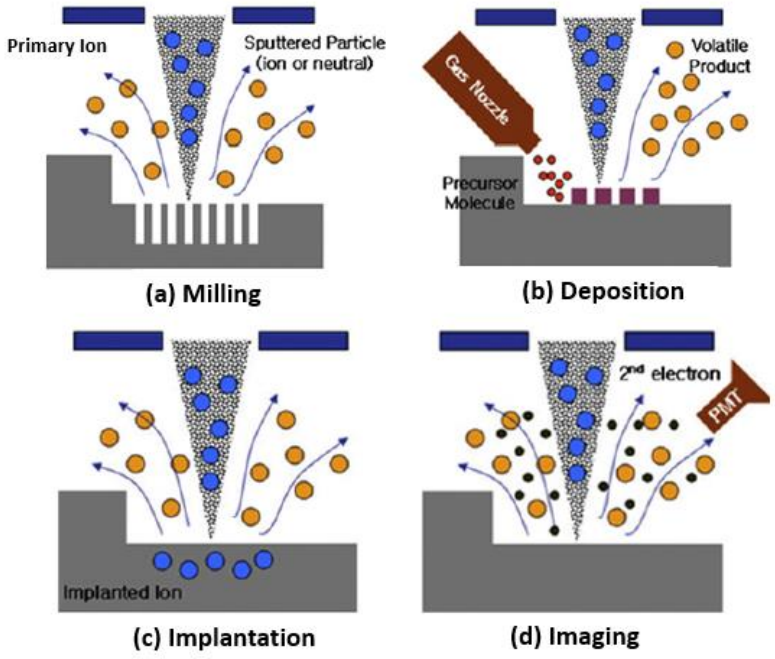

Figure 2.7: Four basic functions of FIB processing: (a) Milling, (b) Deposition, (c) Implantation, (d) Imaging[11].

2.6 Atomic Force Microscopy

Atomic Force Microscopy (AFM) is a type of surface probe microscopy (SPM) developed by Binnig and Rohrer in 1981[12]. The instrument was developed by modifying a Scanning Tunnelling Microscope (STM). STM works by monitoring the tunnelling current between a tip, which consists of a sharp metal wire and a conducting substrate. A feedback loop is utilised which keeps the tip close to the sample surface as it scans the surface in a raster pattern. Although STM was a fundamental advancement for scientific research it had limited applications as it only works on conducting substrates, this is due to the need for a constant measurement of the tunnelling current.

In 1986 Binnig, Quate and Gerber[13] published a paper where they replaced the STM tip with a lever containing a tiny diamond attached onto the end of a spring made of a thin strip of gold. This was the very first AFM. There have been major advancements in AFM from this very first AFM to where it is now today[14]. Today's AFM's operate by rastering a sharp tip very close to a surface, a laser diode is reflected off the back of the cantilever on to a four-quadrant photodiode which measures the change in the position of the tip as it passes over the surface topography as shown in Figure 2.8. A 2D profile is recorded during each pass which then builds to a 3D topography image upon completion of a scan. Unlike SEM where the resolution is limited by the imperfection in the lenses, the limiting factor for AFM's is the

sharpness of the tip. Thus, with very sharp tips (<1 nm) atomic resolution is readily achievable with AFM[15].

AFM does not have to be conducted under vacuum like electron microscopes therefore opening up a range of biological applications[16]. The AFM tip can also provide further probing capabilities such as conductive AFM[17] (C-AFM) where a bias can be applied between the tip and sample, kelvin probe force microscopy (KPFM) or it can probe the mechanical properties of numerous different systems whether they are biological[18], polymers[19], metals[20,21] etc. The modes used in this work are discussed below.

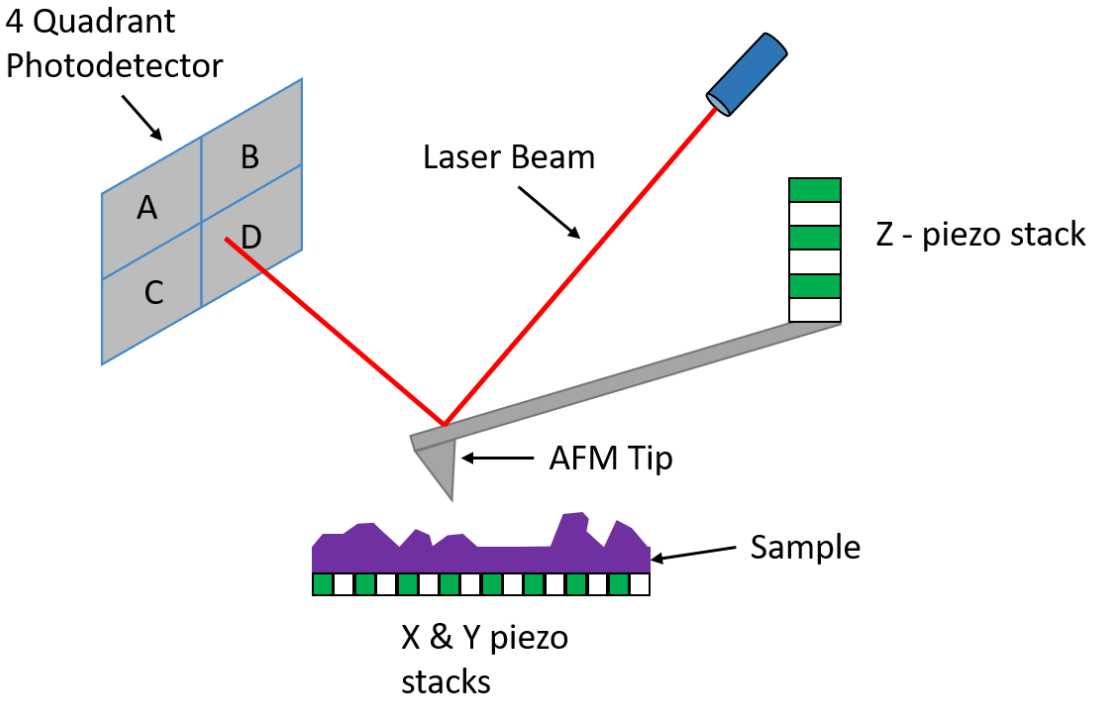

Figure 2.8: Schematic showing basic operation of an AFM. The AFM tip rasters across the surface where its position is captured by the reflection of a laser off the back of the cantilever to a photodetector. This information is translated into a topographical image of the surface.

2.6.1 Static AFM

The most commonly used AFM imaging mode is static mode, also known as contact mode, where the tip is in contact with the surface as it rasters across it. Contact mode was the first imaging mode developed for the AFM. It is the fastest topographic mode and capable of achieving high-resolution images. In order to explain how contact mode works it is important to discuss force-distance curves as shown in Figure 2.9. When the tip is far away from the surface it experiences no forces and so has zero deflection. As the tip approaches the surface,

it first experiences attractive van der Waals forces causing the tip to 'snap–in' to contact with the surface. As the tip is moved further towards the surface the tip enters the repulsive regime as it is now applying a force to the sample. It is within this repulsive regime that contact imaging occurs at a user defined set point force.

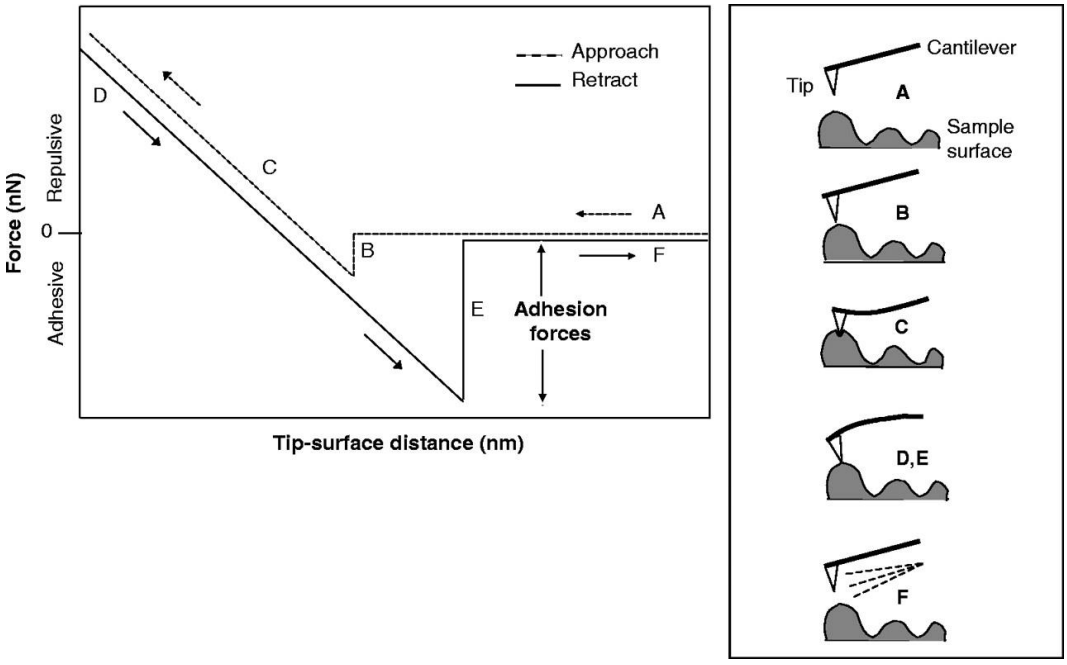

Figure 2.9: Idealized force-distance curve describing a single approach-retract cycle of the AFM tip, which is continuously repeated during surface scanning. The AFM tip is approaching the sample surface (A). The initial contact between the tip and the surface is mediated by the attractive van der Waals forces (contact) that lead to an attraction of the tip toward the surface (B). Hence, the tip applies a constant and default force upon the surface that leads to sample indentation and cantilever deflection (C). Subsequently, the tip tries to retract and to break loose from the surface (D). Various adhesive forces between the sample and the AFM tip, however, hamper tip retraction. These adhesive forces can be taken directly from the force-distance curve (E). The tip withdraws and loses contact to the surface upon overcoming the adhesive forces (F)[22].

As the tip is scanned across the surface the feedback loop maintains a constant tip – sample deflection force by adjusting the height of the AFM tip using the sensitive z-piezo elements. The forces applied by the probe on the surface can be estimated from Hooke's Law;

$$F = -k\,x\,D$$

Where k = probe force constant (N/m) and D = deflection distance (m). The main reason for the development of other imaging modes is the fact that the tip is in constant contact with the sample. The applied normal force also leads to a high lateral force as it scans which can become problematic when imaging soft samples or weakly adsorbed samples which could be damaged or removed by the tip.

2.6.2 Dynamic Mode Imaging

In dynamic/tapping mode imaging the AFM tip is oscillated at its resonant frequency. The tip gently taps across the surface and builds up a point-by-point topography of the surface. As the tip approaches the surface the oscillation changes due to the interaction between the tip and the force field from the sample. The effect causes the oscillation of the tip to be dampened. Due to the feedback loop of the AFM, the height of the tip is adjusted to maintain a constant amplitude. This feedback loop allows a constant tip – sample separation distance allowing a 3D topography of the image to be acquired. The table below lists some of the advantages and disadvantages of contact and tapping mode.

Table 2.1: Comparison of the advantages and disadvantages of AFM imaging modes, contact mode and tapping mode.

	Contact Mode	Tapping Mode
Advantages	• Atomic Resolution • High Scan Speeds • Electrical Measurements	• Less Destructive • Tips last longer
Disadvantages	• Can be destructive to sensitive samples • Image distortion due to shear forces • Piezo Hysteresis	• Slow scan speed • Piezo Hysteresis

2.6.3 AFM Probes

An important consideration when using AFM is the type of AFM probe used. The images or information you obtain from AFM are only as good as the tips used. For instance, the resolution you wish to achieve is determined by the apex of the AFM tip used. For atomic resolution imaging an atomically sharp tip needs to be used. Likewise, for conductive AFM (C-AFM) an AFM tip coated with a conductive metal needs to be used to allow current flow between tip and sample. Tips are also chosen depending on whether contact mode or tapping mode imaging is desired. They are generally chosen in relation to their resonant frequency, AFM tips for contact mode have resonant frequencies between 10 kHz to 75 kHz and tapping mode tips have resonant frequencies from 50 kHz to 400 kHz. The two most common materials used for AFM cantilevers are silicon nitride (Si_3N_4) and silicon (Si).

2.7 Etching Techniques

In order to fabricate microscale structures in devices it is often necessary to use etching techniques to remove some of the substrate material. There are two types of etching techniques; Wet etching, which involves dissolving a material that is soluble in some chemical medium; or by dry etching in which a material is sputtered or dissolved using reactive ions or a vapour phase etchant. In this work a dry etching technique called reactive ion etching is used to fabricate trenches in a SiO_2 substrate. The etcher used is an Oxford Instruments PlasmaLab system 100 plasma etcher.

2.7.1 Reactive Ion Etching

In reactive ion etching (RIE) a plasma is struck using a radio frequency (RF) power source inside a reactor where several gases can be introduced depending on the material to be etched. This breaks the gas molecules into ions where the negatively charged ions are then accelerated towards the substrate surface due to the presence of an electric field. If the ions possess a high enough energy they can knock atoms out of the material without any chemical reactions taking place. Selective etching is achieved by using a hardmask such as etch resistant photoresist to protect areas of the sample where etching is not desired.

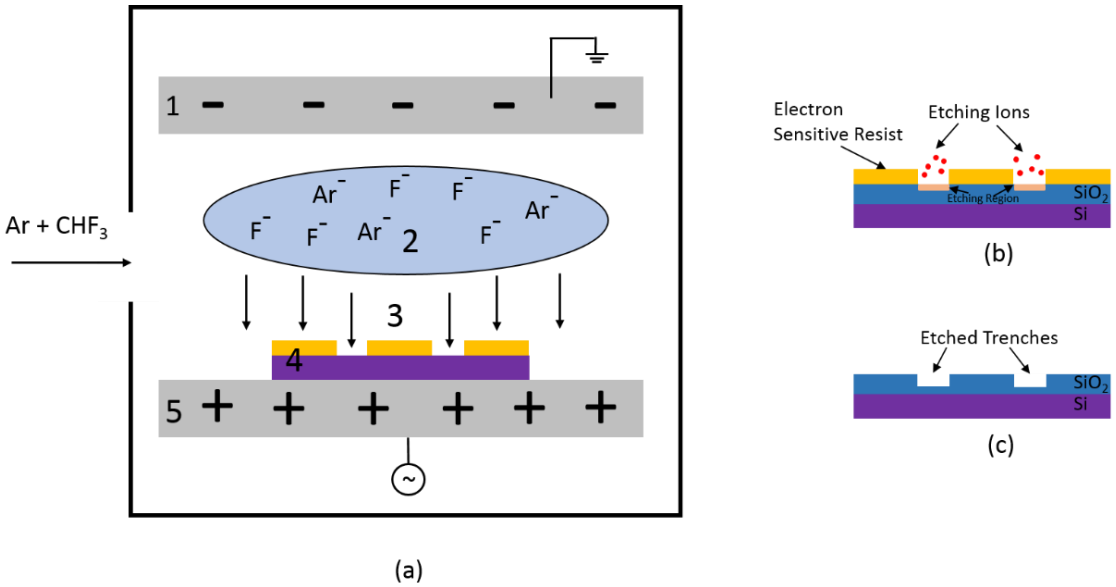

Figure 2.10: (a) Schematic of a common RIE setup, consisting of two electrodes (1 and 5) that generates an electric field (3) that bombards ions towards the sample surface (4). The area labelled (2) represents the generated plasma. (b) Schematic of electron sensitive resist mask on SiO_2 showing region where accelerated ions react with the surface. (c) Sample with etched features after removal of electron sensitive resist.

A schematic of the process can be seen in Figure 2.10. Plasma etching is generally preceded by a lithography step to define the area to be removed. In this work plasma etching is used to remove SiO_2 in order to fabricate trenches on a substrate over which NWs can be suspended. To etch SiO_2, argon and fluoroform (CHF_3) gases are used. The argon gas bombards the surface breaking the strong SiO_2 bonds. Then the fluorine ions react with the silicon and are removed as SiF by the chamber vacuum. The oxygen then reacts with carbon to be removed as CO_2. The etch rate of dry etching processes can be easily controlled and for the recipe used in this work the etch rate was 100 nm/min. Trenches were etched to a depth of 250 nm.

2.8 Nanowire Synthesis Methods

Nanowires are synthesised through various methods such as chemical vapour deposition (CVD) [23-25], vapour liquid solid (VLS) [26-28] methods and they can also be grown via solvent based synthesis[29-31]. In terms of specimen deposition, a facile method for depositing NWs onto a substrate is from a dispersion of the materials in a volatile solvent, such as isopropanol (IPA), followed by pipetting a small volume (5 µL) onto a target substrate. The solvent then evaporates leaving the NWs on the target substrate. This process is advantageous as it is time efficient and allows for careful control of the concentration of wires on the substrate. This is important when performing electrical measurements on single NWs, as a high concentration of wires will create difficulties in establishing reliable electrical contacts to individual wires and will increase the potential for unintended short circuits to occur. The NWs used in this thesis were silver, gold and silicon nanowires, which were synthesised by the methods detailed below.

2.8.1 Silver and Gold Nanowire Synthesis

The silver nanowires (AgNWs) used in these experiments were purchased from Seashell Technologies. They were synthesised using the solution based polyol synthesis method[32,33]. The polyol process is based on the reduction of an inorganic salt by a polyol at elevated temperature. The main aspects of the synthesis are detailed below.

Ethylene glycol (EG) is used as both a solvent and a reducing agent, poly(vinylpyrrolidone) (PVP) acts as a stabilising agent, and silver nitrate ($AgNO_3$) is used as a silver source. The reaction proceeds as follows;[34]

$$2HOCH_2CH_2OH \rightarrow 2CH_3CHO + H_2$$

$$2CH_3CHO+2Ag^{+}\rightarrow 2Ag^{0}+2H^{+}+CH_3COCOCH_3$$

The liberated Ag ions start to form Ag nanoparticles via homogeneous nucleation. The PVP then adsorbs onto the surface of the nanoparticles passivating the (100) facets of the wire which leaves the (111) planes active for NW growth along the [110] direction, as depicted in Figure 2.11. The PVP also serves to prevent the NWs from agglomerating and precipitating out of solution. The structure of the AgNWs has been analysed using high-resolution transmission electron microscopy (HRTEM) as shown in Figure 2.11 (c). The expected pentagonally twinned structure is clearly visible in this cross-sectioned NW.

The gold nanowires (AuNWs) used were purchased from Sigma Aldrich. They were synthesised via the polyol synthesis method similar to that of AgNWs. However, rather than using PVP to promote 1-dimensional growth and to stabilise the wires, cetyltrimethylammonium bromide (CTAB) is used due to its specific bonding on the AuNW surface.

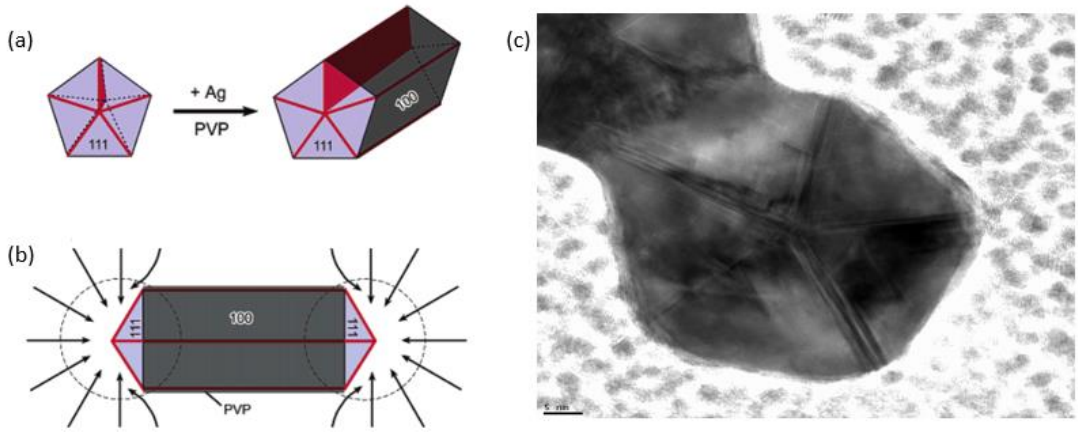

Figure 2.11: (a), (b) Schematics for the proposed formation of AgNWs via the polyol synthesis route[33]. (c) TEM cross section of a AgNW (60 nm in diameter) showing the 5-fold symmetry of the wire (TEM courtesy of Dr. Eoin McCarthy).

2.8.2 Silicon Nanowire Synthesis

The silicon nanowires (SiNWs) used in these experiments were synthesised in Prof. James Cahoon's group in the University of North Carolina (UNC), Chapel Hill. NWs were grown in a custom built chemical vapour deposition (CVD) system. Gold catalysts with diameters of 60 nm were used to control the wire diameter. The gold nanoparticles were immobilised on a Si/SiO_2 surface with polylysine (Sigma Aldrich) and cleaned in a UV–Ozone cleaner. The substrate was then inserted into a one inch diameter hot wall tube furnace (Lindberg Blue M) and heated to 650˚C. Silane (SiH_4, Voltaix) served as the source of Si with H_2 (Matheson

TriGas, 5N semiconductor grade) used as the carrier gas. Reactions were carried out at a total pressure of 20 Torr, with 0.5 sccm SiH_4. The flow of carrier gas varied between 180-200 sccm. All gas flow rates were controlled and measured using mass-flow controllers from MKS Instruments (model P4B). Figure 2.12 shows an SEM image of the SiNWs as grown on their growth wafer.

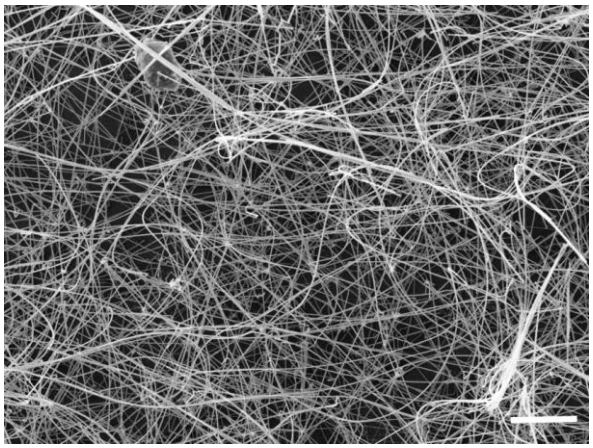

Figure 2.12: SEM image of SiNWs as grown via chemical vapour deposition on a silicon substrate, scale bar 2 μm.

2.9 Fabrication of Mechanical Devices

Fabrication of mechanical devices requires a complex multi-step process. For the devices fabricated in this work substrates were also fabricated with UV contacts so that electrical measurements on the NWs could be performed. Additionally, it also allowed for the potential of electromechanical investigations of wires.

2.9.1 Mechanical Measurement

2.9.1.1 UV Lithography

Substrates used for mechanical measurements are fabricated in such a way that they can be used to make electromechanical measurements. 1 mm thick Si wafers with a 1 μm thick thermally grown oxide were used as the substrate for these experiments. A protective layer of resist S1813 was spun on to a 6" silicon wafer at 2000 rpm and soft baked on a hotplate at 115° C for 75 seconds. The resist parameters here were not important as the sole purpose was to protect the wafer during dicing. The silicon wafer was diced into 2 cm x 2 cm pieces using a diamond disco dicing blade. Using a dicing saw reduces silicon fragments from the edges which can affect resolution achievable by the UV lithography process. The resist was removed and substrates cleaned by sonicating in acetone for 10 mins at 37 kHz followed by rinsing in isopropanol and drying under N_2 flow. UV Lithography was used to define the electrode

pattern as shown in Figure 2.13 using a custom designed hard mask. The process flow followed for UV lithography is outlined in table 2.2.

Table 2.2: UV Lithography process flow.

UV Lithography Recipe
1. Spin S1813 resist at 5000 rpm for 45 sec, with 5 sec ramp at 500 rpm.
2. Soft bake on hotplate at 115°C for 75 sec.
3. Expose at 365 nm for ~ 6 sec.
4. Develop in MF-319 for 45 sec. Rinse in H_2O.

The speed at which the resist is spun produces a film which is ~ 1.2 µm thick, the soft bake is required to remove the solvent from the resist prior to exposure. Once the sample is developed Ti/Au with thicknesses of 5/35 nm was evaporated onto the substrate, where Ti acts as an adhesion layer. The electron beam evaporation tool used was the Temescal FC-2000. After metal deposition, the substrates were left overnight in acetone to remove the remaining resist leaving only the desired metal pattern in a process known as 'lift–off'. The finished UV pattern can be observed in Figure 2.13 (b). The exposure parameters for UV lithography are important as an overexposure can cause blurring of features. If underexposed, it can result in difficulty during the lift-off process. A test exposure is carried out initially to determine the correct parameters and to ensure there is no beam intensity variation or sample tilt which can affect the quality of the lithography.

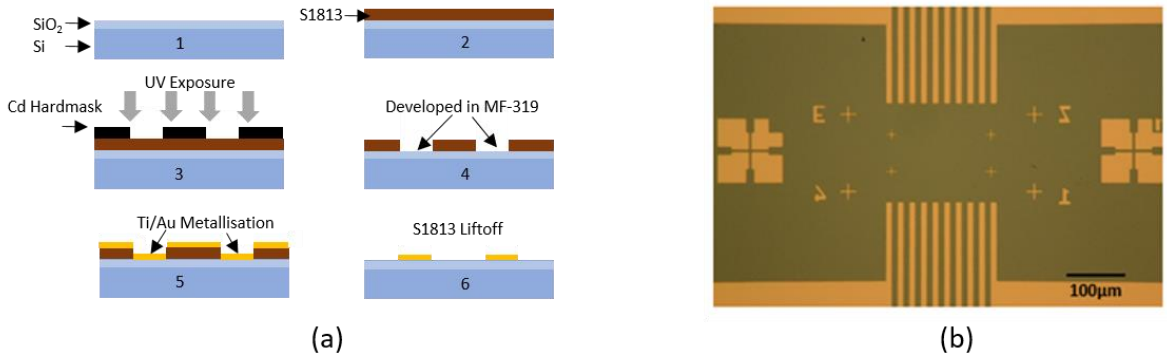

Figure 2.13: (a) Schematic showing fabrication of UV Lithography electrodes. (b) Optical Image showing electrode array fabricated by UV Lithography.

2.9.1.2 Electron Beam Lithography

Electron Beam Lithography is used to define trenches over which NWs are suspended in order to conduct the 3-point AFM bending experiment. The resist used for etching the trenches is ZEP-520A which is a positive tone resist with good etch resistance. Hexamethyldisilazane (HMDS) is used as an adhesion layer for the ZEP-520A. The process flow for resist spinning and EBL exposure is outlined in the table below. To determine the alignment of the trench pattern on the substrate relative to the UV contact pads, there are 3 steps necessary; compensating for the rotation of the sample, designating a (0,0) origin and defining all translations relative to that point, and finally aligning to an alignment feature on the substrate immediately prior to exposure. The Raith software then controls the beam by rastering it over the resist in pre-designed patterns created with the Raith software.

Table 2.3: Process flow for EBL step to define trench pattern in ZEP-520A resist.

EBL Lithography Recipe
1. Cover substrate in HMDS for 30 sec. Spin HMDS at 3000 rpm for 5 sec.
2. Spin ZEP 520-A resist at 3000 rpm for 45 sec, with 5 sec ramp at 500 rpm.
3. Soft bake on hotplate at 180˚C for 3 min.
4. Expose using the following parameters:
▪ Accelerating voltage: 10 kV
▪ Aperture: 10 µm
▪ Dose: 5 passes of 5 µC/cm^2, Total dose: 25 µC/cm^2
5. Develop in B.O.B. for 5 min, Rinse in IPA, Spin dry on spinner.

2.9.1.3 Reactive Ion Etching

Reactive ion etching (RIE) is used to etch trenches in the SiO_2. RIE was performed on the substrates which had trench features defined by EBL. A 40 sccm Ar gas mixture and 10 sccm CHF_3 was used to etch samples at a vacuum pressure of 6 mT. The inductively coupled plasma (ICP) power used was 1500 – 2500 W and RIE power of 70 – 250 W. A DC bias with an extraction voltage of -100 - -250 V with a 10 Torr He back pressure was used. The etch rate with these parameters is 100 nm/min. Samples were etched for 2.5 mins to give trenches 250 nm deep and 2 µm wide, where the width was defined by the EBL step. After RIE the ZEP resist was removed using 1165 resist remover at 80˚ C for 36 hours followed by sonication at 80 kHz for 60 mins. The substrates were then sonicated in isopropanol for 5 mins before being

dried under N_2 flow. This results in a metallised structure with 20 electrical contacts and 19 trenches as seen in Figure 2.14.

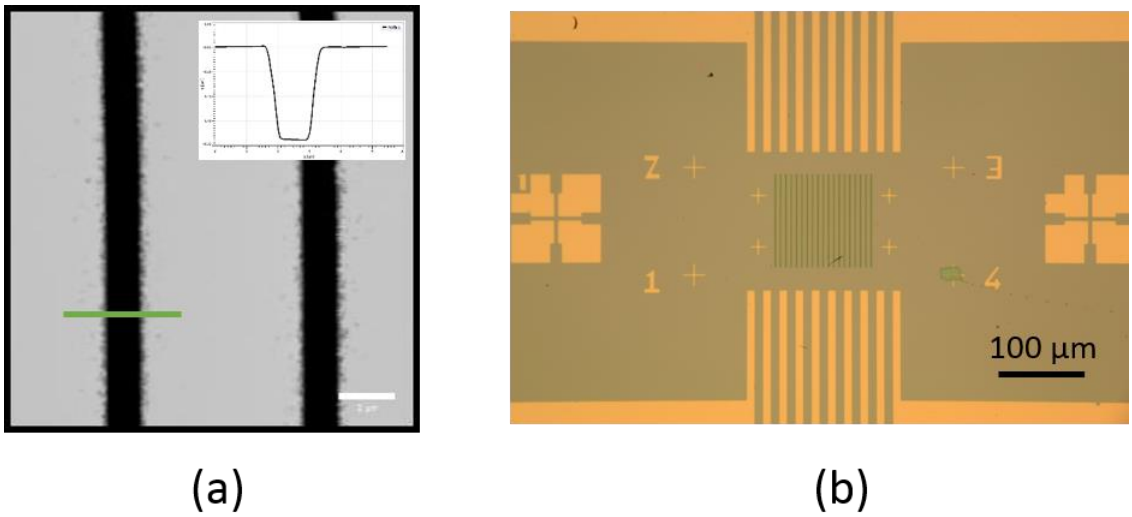

Figure 2.14: (a) AFM image of trenches fabricated in SiO_2 by RIE, with an inset line profile of one of the trenches, scale bar 2 µm. (b) Optical image showing electrodes fabricated by UV lithography plus array of 19 trenches at the centre of the pattern.

2.9.1.4 Nanowire Placement and Procedure for Electrically Contacting

There are different methods to transfer nanowires onto a pre-fabricated substrate. The most commonly used method is via dropcasting. This is made possible by dispersing NWs in a volatile solvent. The silver nanowires (AgNWs) used in these experiments were supplied by Seashell Technologies pre-dispersed in isopropanol. The silicon nanowires (SiNWs) were grown using a vapour-liquid-solid (VLS) method by our collaborators in UNC Chapel Hill[35] and were obtained vertically aligned on a Si growth wafer. To disperse these wires a piece of the growth wafer was placed in a small vial with a couple of drops of isopropanol. The wires were then sonicated at 80 kHz for 2-3 seconds until the wires were removed from the growth wafer. This is visually observed when the bare silicon wafer becomes visible indicating the removal of the SiNWs.

To solvent deposit the wires, 5 µL of the solution was dropcast onto the pre-patterned substrate. Using N_2 flow the solvent drop was blown perpendicularly across the trenches to preferentially align the wires perpendicularly across the trenches. The solvent evaporates leaving the wires fixed on the surface, Figure 2.15 (a). NWs were then located in an optical microscope at *x 50* mag and wires which were 1) perpendicular across a trench and 2) have

enough wire either side of the trench for mechanical clamping were identified for mechanical testing.

NWs were also deposited via a dry transfer method. To dry transfer the NWs a polydimethylsiloxane (PDMS) stamp was used. The PDMS was a mixture of silicone elastomer:resin (10:1) (Sylgard -184, Dow Corning). The mixture was degassed in a desiccator for 5 mins and placed on a glass slide where it was cured on a hotplate at 80° C. For AgNWs, 5 µL of a concentrated AgNW solution (2 mg/ml) was dropcast on a piece of unpatterned SiO_2. The PDMS stamp was then placed onto the SiO_2 to remove the NWs and transfer them to a substrate pre-patterned with trenches. A schematic for the transfer process can be seen in Figure 2.15 (b). The SiNWs were dry transferred directly from their growth wafer to the pre-patterned substrate using the PDMS stamp. NWs were optically inspected to identify wires that spanned trenches.

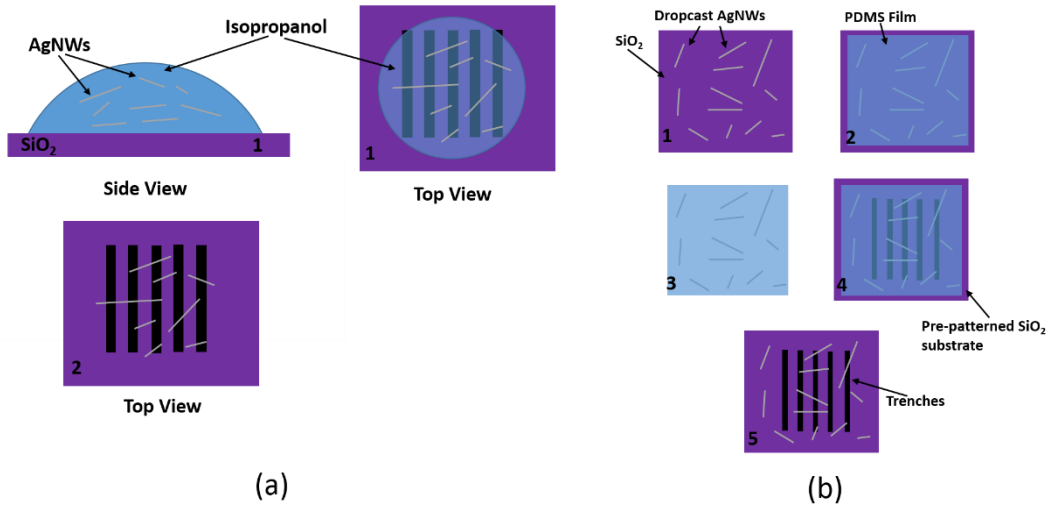

Figure 2.15: (a) Schematic of solvent deposition of AgNWs. (b) Schematic of dry deposition of AgNWs; 1. AgNWs are dropcast onto a blank SiO_2 wafer, 2. With a PDMS film on top, 3. PDMS with AgNWs adhered after peeling off from SiO_2, 4. PDMS film attached to pre-patterned SiO_2, 5. AgNWs deposited on pre-patterned SiO_2 after the removal of the PDMS film.

2.9.1.5 Electron Beam Induced Deposition of Mechanical Clamps

To clamp NWs either side of a trench, the substrate was loaded into a dual beam SEM/FIB electron microscope with a gas injection system (GIS). The reservoir containing the platinum organometallic compound was heated to 90° C. Due to the position of the GIS needles the stage was adjusted to a 54˚ angle to allow access for the needles to the substrate. The needles were positioned 5 mm above the substrate surface. The aperture used for deposition was 30

μm and an accelerating voltage of 5 kV was used. This was found to allow for sufficient Pt deposition in a reasonable time period.

Using the software on the SEM interface a rectangular box was drawn to define the area for the desired Pt deposition. When the box was positioned in the correct place, the capillary for the Pt reservoir was opened to allow the organometallic precursor $C_5H_4CH_3Pt(CH_3)_3$ to enter the chamber. Beam shift was used to counteract sample drift during deposition. Deposition times were roughly 20 – 30 seconds and produced Pt deposits ~ 200 nm in height. The electron beam was then blanked and the capillary closed. The beam was not switched back on until the pressure in the SEM chamber returned to its base level (3.8 $x10^{-5}$ – 8.7 x 10^{-6} mbar) which takes 1 – 2 minutes. This time allowed for any unreacted organometallic precursor to be removed from the chamber and to prevent any contamination of the wire through unwanted Pt deposition. Once the wire had been mechanically pinned to the substrate it was then ready for the AFM 3-point bending technique.

2.10 AFM Calibration for Mechanical Measurement

To obtain quantitative mechanical properties from the mechanical measurements of NWs, it is necessary to perform a full calibration on the sensitivities, both vertical and lateral of the AFM tip used. Furthermore, the dimensions of each individual tip used needs to be measured. The AFM tip is calibrated using the procedures outlined by Schwarz[36].

The lateral sensitivity of the tip is determined by laterally loading a trench wall of a silicon nitride calibration grid. It is important to calibrate the tip on a non-compliant surface otherwise the sensitivities would be a combination of the tip and surface sensitivities. The height at which the tip calibrates the grid is user defined by first taking a tapping mode image across the trench. The feedback loop is then switched off by choosing contact mode. This drives the tip in the manipulation path but the piezo does not adjust the tip height resulting in the tip laterally loading the grid. This is all done using the lithography suite of the Asylum MFP-3D. The signal is recorded on the photodetector and the lateral sensitivity (S_{lat}) is the slope of the loading curve in V/μm. The grid is loaded a minimum of three times to ensure consistent repeatable loading. Figure 2.16 (a) shows the lateral response of a 75 kHz AFM tip in V/μm.

To measure the vertical sensitivity of the tip, a force curve as shown in Figure 2.16 (b), is obtained. For this, contact mode is selected and a deflection setpoint of 0.2 V is chosen. It is important to choose a low setpoint force to avoid damaging the tip before the NW

manipulation experiments. Initially the tip is positioned approximately 1 µm away from the surface. A single force curve is executed which allows the tip to locate the surface. Then a second force curve is executed. The vertical sensitivity (S_{ver}) is the inverse of the slope of the repulsive section of the plot in nm/V. Figure 2.16 (b) illustrates how the approach and retraction curves are identical and there is no hysteresis. This verifies that the tip is pushing on a non–compliant surface. This measurement is repeated five times and an average value calculated.

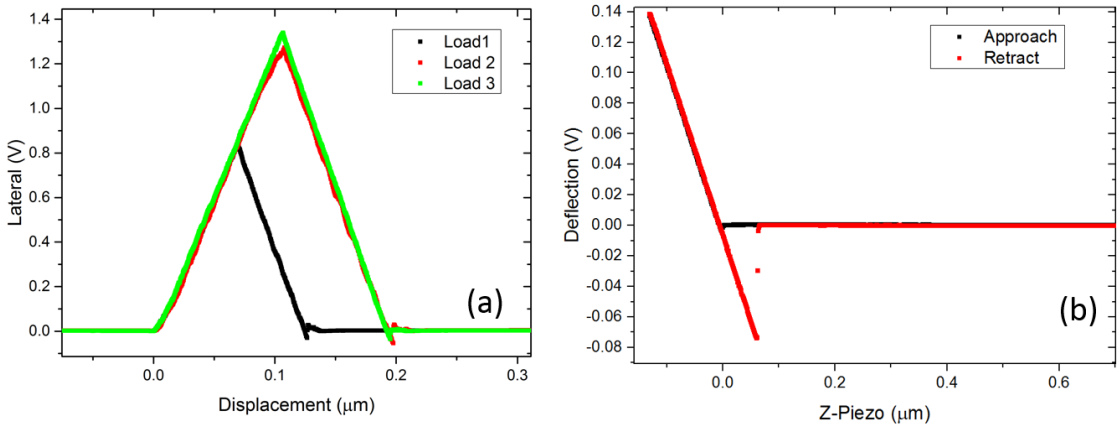

Figure 2.16: (a) Lateral deflection voltage vs displacement plot where an AFM tip is loaded against the side of a non-compliant trench to determine the lateral sensitivity of the tip in V/µm. (b) Vertical deflection used to calculate the vertical sensitivity of the AFM tip. The Approach (black) and Retrace (red) curves overlap demonstrating that the tip is pushing into a non-compliant surface otherwise hysteresis would be observed.

It is necessary to measure the dimensions of the AFM cantilevers, the width (w), thickness (t), length (L) and the tip height (l_{tip}). These are measured in an SEM with an optimum measuring angle achieved by tilting and rotating the AFM tip in the SEM, Figure 2.17. Approximately fifteen measurements of each of the dimensions is recorded and averaged.

Once all the dimensions are known, along with the lateral and vertical sensitivities the following well known equation can be used to convert the lateral signal in Volts (ΔU_{lat}) to a force in Newtons;[36]

$$F = \frac{Gwt^3}{4L^2 l_{tip}} S_{ver} \Delta U_{lat}$$

Where G is the shear modulus of the tip. The AFM measures the change in lateral voltage with respect to the piezo displacement. To determine how much a NW has been displaced the

lateral spring constant (k_c) of the AFM tip must be known. This is obtained with the known formula;

$$k_c = S_{lat} \frac{F}{\Delta U_{lat}}$$

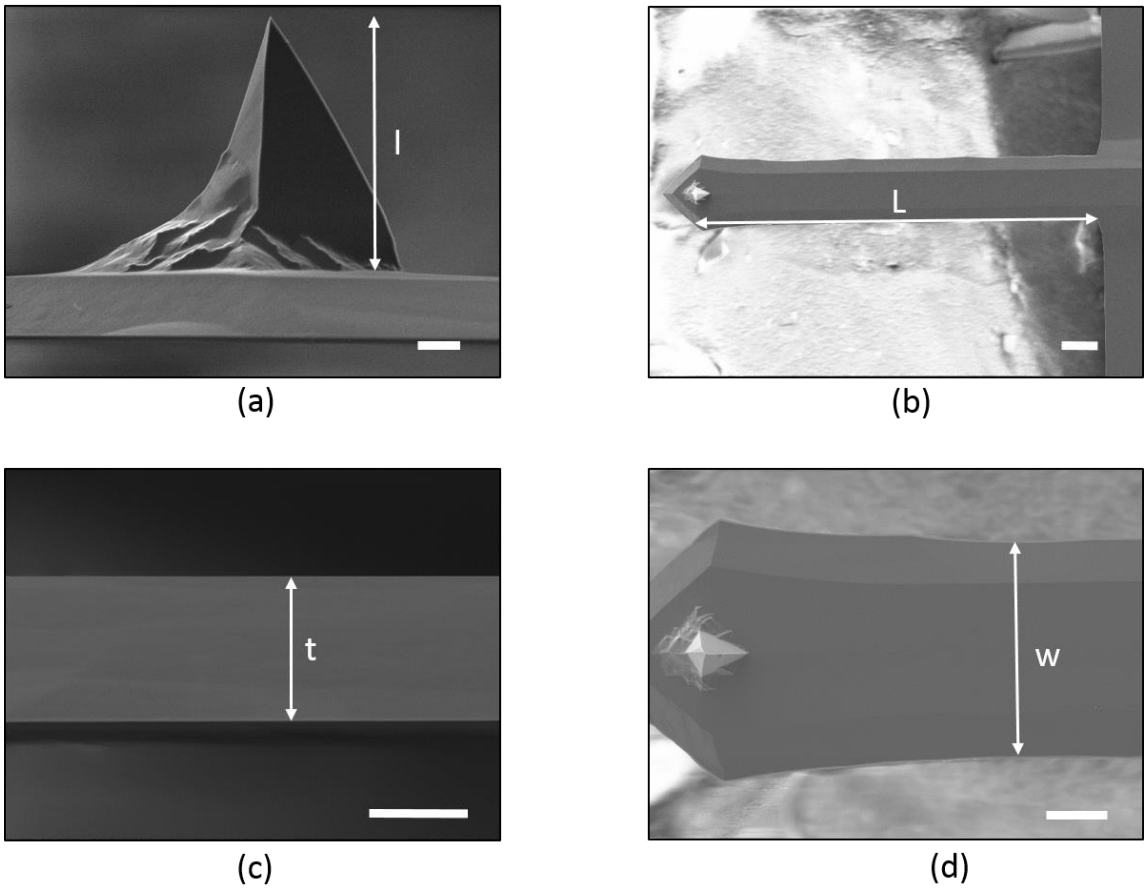

Figure 2.17: SEM images of a cantilever tip from which the dimensions are measured, (a) tip height (*l*), scale bar 2 µm, (b) cantilever length (*L*), scale bar 20 µm, (c) cantilever thickness (*t*), scale bar 2 µm, (d) cantilever width (*w*), scale bar 10 µm.

2.11 AFM 3-Point Bending of Nanowires

The method for the 3-point bending experiment for NWs is the same as for loading the calibration grid. The wire for manipulation is located with the AFM. It is important that the long axis of the NW is parallel to the long axis of the cantilever beam. This prevents the tip slipping during the manipulation. An AFM scan 3 µm x 3 µm around the manipulation area is acquired. This allows the user to easily identify the midpoint of the wire and repeatedly load the wire in the same position. A tapping mode image of the wire is taken along a user defined path as shown in Figure 2.18. This path can either be a "one shot" experiment, where

a wire is loaded to fracture, or can consist of a loading and unloading cycle where a wire is only loaded in its elastic regime to prevent an inelastic deformation occurring as shown in Figure 2.19.

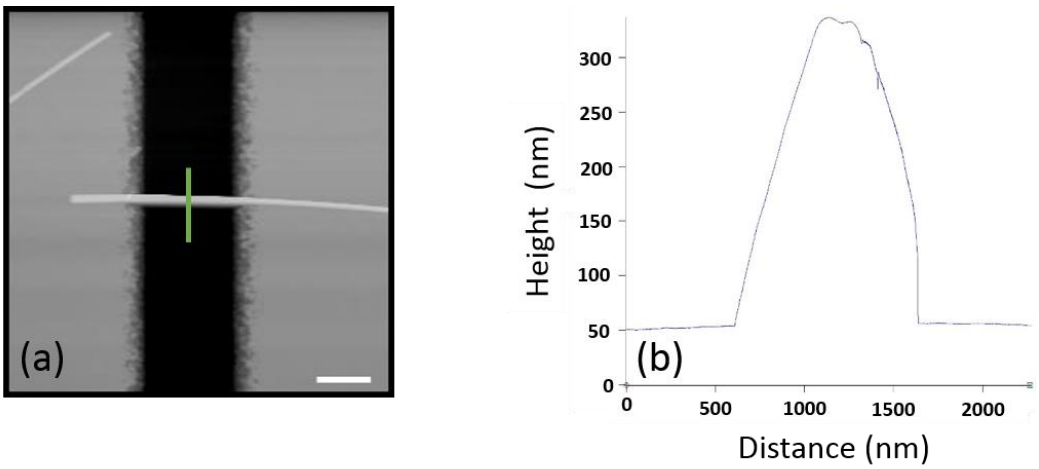

Figure 2.18: (a) AFM image of a AgNW suspended over a trench showing user defined tapping mode pre-scan, scale bar 1 μm. (b) Tapping mode pre-scan defined by green line in (a) where the tip height for the mechanical manipulation was fixed.

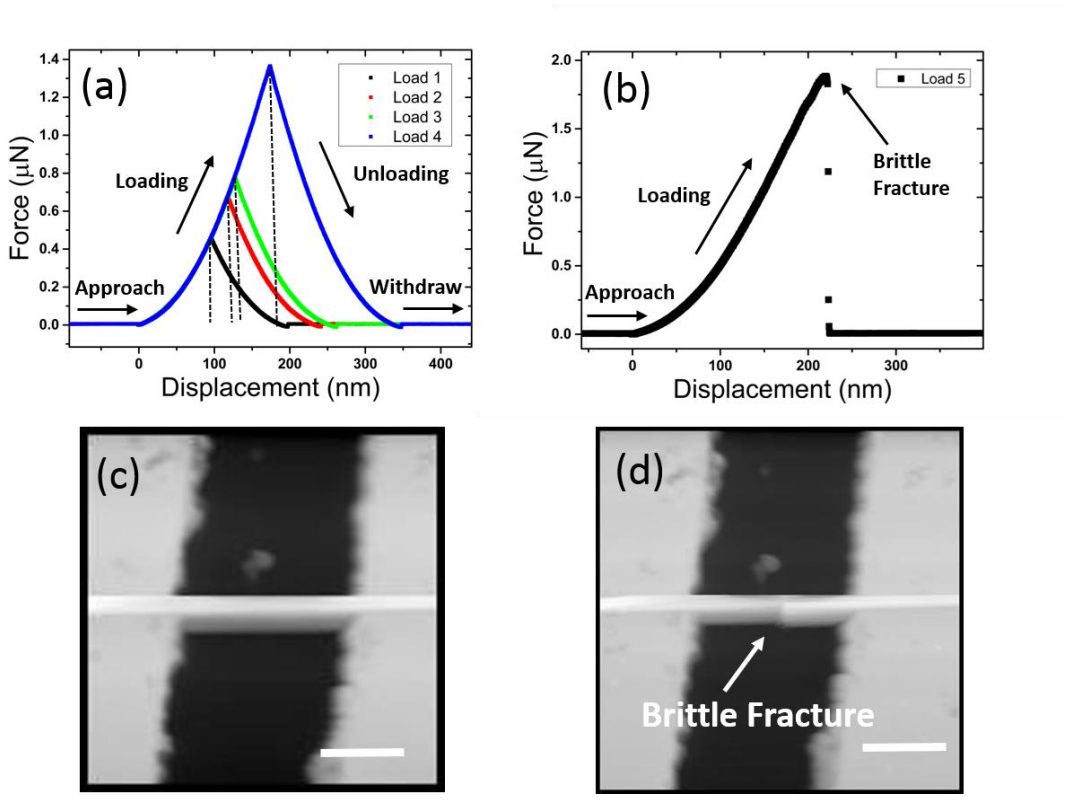

Figure 2.19: *F-d* responses for (a) Repeatable loading/unloading of an individual AgNW. The wire is kept in the elastic regime which can be seen from the symmetry of the curves around the direction of tip change. (b) One shot experiment where the AgNW is pushed to failure. In this case, the point of brittle fracture can be detected from the sharp reduction in force. (c), (d) AFM images of the AgNW before and after brittle fracture respectively, scale bar 1 μm.

It is crucial that the height defined for the NW load is at the same height for which the tip is calibrated. Once the tip height is set the feedback loop is disabled and the wire is manipulated. As outlined above the lateral force and piezo displacement is converted to a force vs displacement (*F-d*) plot as shown in Figure 2.19. After each loading cycle, it is necessary to re-image the area to inspect the NW for damage and to account for any drift in the sample before additional loads are performed. The initial region of the plot before 0 nm represents the baseline where the tip is approaching the wire. The lack of a force response also demonstrates that the tip is not in contact with the bottom of the trench. As the AFM tip contacts the wire at 0 nm, the tip starts to laterally load the NW which can be seen by the increasing force.

In the case of elastic loading, after loading to a user defined displacement, the AFM tip reverses direction and the force begins to decrease. This can be observed in Figure 2.19 (a) where the dashed line represents the reversal point for each of the individual loads. When the tip separates from the wire, the force returns to zero, its magnitude before the initial contact with the wire. Figure 2.19 (b) shows the *F-d* response for a NW loaded to fracture. In this case the AFM tip is only driven in one direction with the force response initially the same as in (a). However, in this case the AFM tip in-elastically loads the wire eventually resulting in brittle fracture. This can be seen from the sharp drop in force in the *F-d* curve. Once the tip breaks through the wire, the force on the tip returns to zero. AFM images of the NW before and after brittle fracture can be observed in Figure 2.19 (c) and (d).

2.12 Electrical Measurement

In order to perform electromechanical measurements on NWs they must be electrically contacted. This is achieved using an additional EBL step to connect the large UV contact pads to the NW. Patterns for the electrodes are designed using Raith software. The resist used is a bi-layer resist consisting of MMA (methyl methacrylate) and PMMA (poly methyl methacrylate). The purpose of the bi-layer resist is that the MMA layer provides an undercut which prevents deposited metal adhering to trench walls during metal lift-off (Figure 2.20 (a)) resulting in the coined term ‘rabbit ears’. The process flow for the process is outlined in table 2.4. Figure 2.20 (b) shows a single AgNW contacted with four Ag electrodes.

Table 2.4: Process flow for Bi-layer EBL step.

EBL Lithography Recipe - Bilayer Procedure
1. Cover substrate in MMA. Spin at 6000 rpm for 45 sec, with 5 sec ramp at 500 rpm. 2. Soft bake on hotplate at 180˚C for 2 min. 3. Cover Substrate in PMMA. Spin at 6000 rpm for 45 sec, with 5 sec ramp at 500 rpm. 4. Soft bake on hotplate at 180˚C for 3 min. 5. Expose using the following parameters: ▪ Accelerating voltage: 10 kV ▪ Aperture: 20 µm ▪ Dose: 120 µC/cm^2 6. Develop MIBK:IPA, Stop in IPA, N_2 dry. 7. Deposit 120 nm Ag metal followed by lift off in Acetone for 2 hours followed by IPA rinse, N_2 dry.

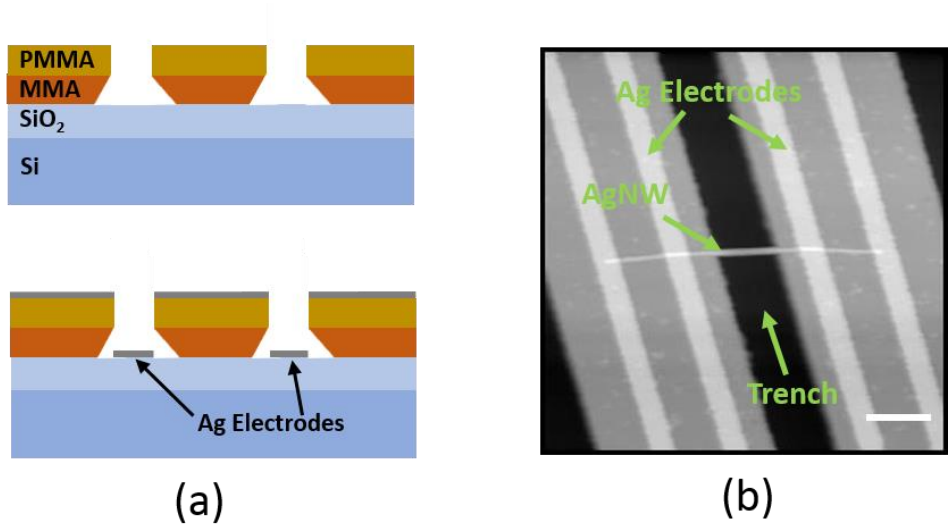

Figure 2.20: (a) Schematic of the MMA/PMMA bi-layer resist used for EBL step. (b) AgNW contacted by four Ag electrodes after EBL, metal deposition and "lift-off", scale bar 2 µm.

2.12.1 Electrical Testing of NWs

After "Lift-off" is complete the samples are optically inspected at *x 50* magnification to determine the success of the EBL step. It is important that the electrodes are only either side of the trench and not over the trench. If they are over the trench they will pull the NWs into the trench and make them mechanically unviable. The NWs are contacted in a 4-point configuration as discussed in chapter 1. This allows a direct measurement of the resistance of

the wire as it removes the effect of the resistance of the contacts from the measurement. Figure 2.21 (b) shows a comparison of a 2-point and 4-point current-voltage (*IV)* measurement on an individual AgNW. To probe the electrical properties of the NW a Keithley 4200 Semiconductor Characterisation System (SCS) was used to source current across the outer two electrodes and measure the voltage across the inner two as depicted in Figure 2.21 (b). A Karl Suss PM-8 probe station which houses four micropositioners (Cascade Microtech) is used to make electrical contact to the UV contact pads corresponding to the EBL contact pads connected to the NW. When a wire is deemed to have a suitable electrical contact, it can then be prepared for the electromechanical experiment.

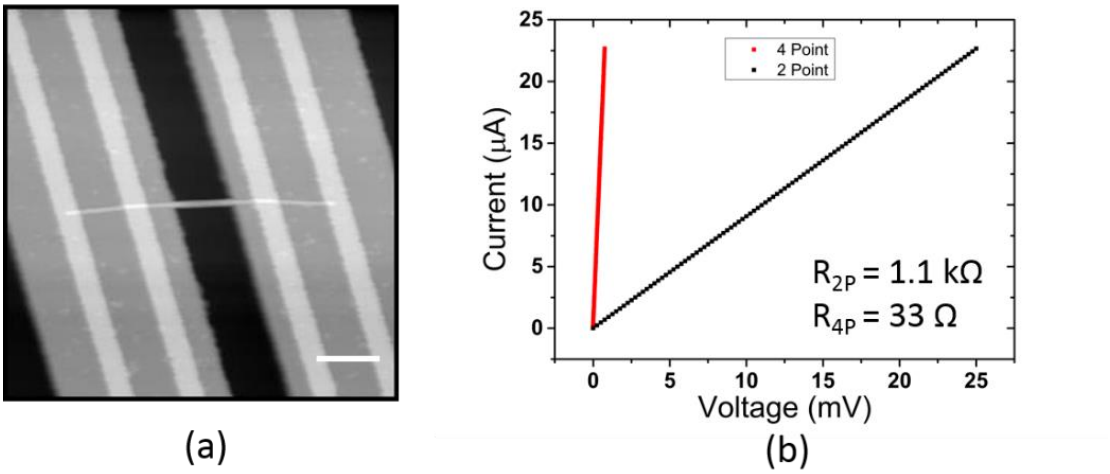

Figure 2.21: (a) AgNW suspended over a trench with four silver contacts for 4-point *I-V* measurement. Current is sourced between the outer two electrodes with the voltage drop across the inner two being recorded. (b) Difference between 2-point and 4-point electrical measurement. The 4-point measurement allows the correct resistance of the wire to be determined (33 Ω), the 2-point measurement is higher (1.1 kΩ) as the contact resistance between the metallic contacts and the wires is also measured in this configuration.

2.13 Electromechanical Measurement

Here the approach for electromechanical measurements is described. To apply an electrical bias to a sample whilst simultaneously probing its mechanical properties on the AFM, a homebuilt stage has been previously developed in the Boland group[37]. This homebuilt stage involves a chip carrier that is connected to two electrical switch boxes which are subsequently connected to two Keithley 2400 sourcemeters to apply a bias to the wire and to simultaneously record the voltage drop across the inner two electrodes. A schematic outline of the technique can be observed in Figure 2.22. The Keithleys are controlled by a LabView program which allows the voltage response to be recorded. To connect the sample to the chip carrier, the

substrate must be wire bonded to the carrier. The wire bonded pads must be located at least 5 mm away from the centre of the sample. This is to allow the cantilever access to the NW.

The resistance of the NW is then tested on the electromechanical set-up to ensure that the same resistance obtained on the 4200 SCS is obtained. For the electromechanical experiment, the mechanical 3-point AFM bending experiment is conducted as outlined above except that the wire under interrogation is simultaneously subjected to current flow.

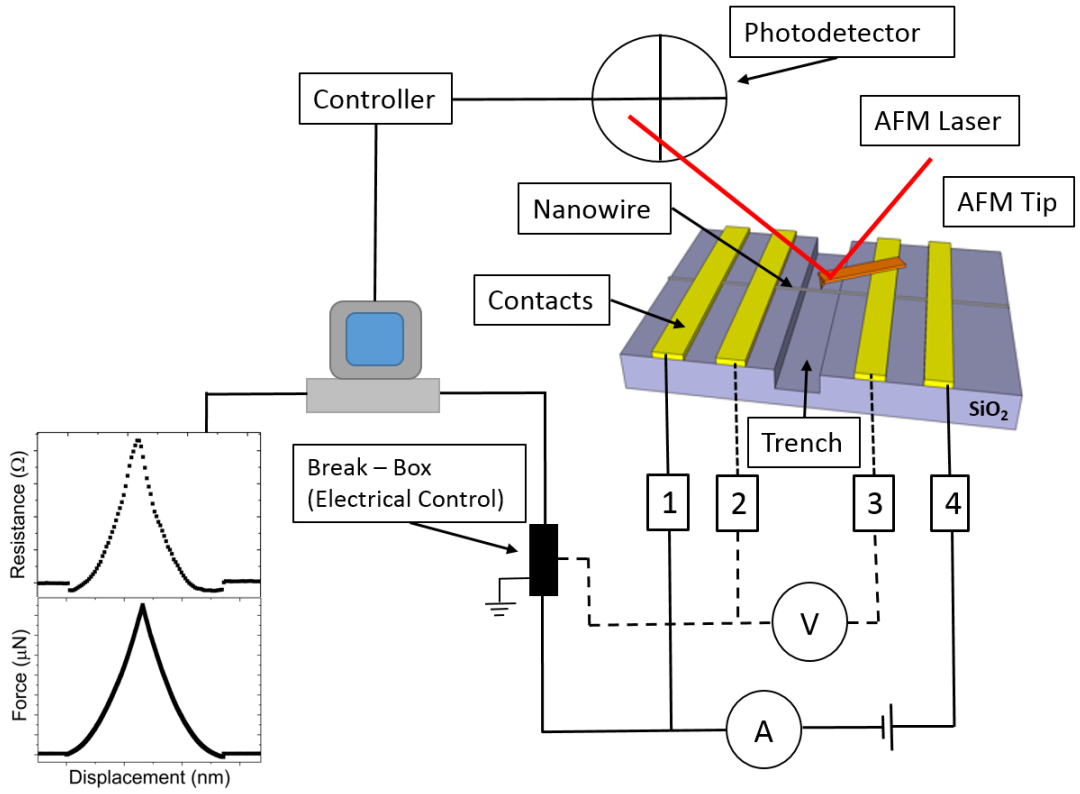

Figure 2.22: Schematic of the electromechanical experiment[37]. The mechanical measurement is performed by lowering a calibrated AFM tip below the xy plane of the NW which is suspended over a pre-fabricated trench. The AFM tip laterally loads the NW and the lateral deflection of the tip is recorded by the photodetector to allow the *F-d* response to be recorded. Simultaneously current is sourced between the outer two contacts 1 & 2, with the voltage drop between the inner two contacts 2 & 3 being measured. This allows the current dependent mechanical properties to be studied and *vice versa*. The current is sourced and measured using Keithley 2400 sourcemeters and the break-box allows each contact to the wire to be controlled individually.

2.14 Conclusion

In this chapter, the working principles of many of the techniques used have been described. These techniques allow the fundamental properties of these nano-sized materials to be probed. Without the constant advancement of the characterisation and fabrication tools discussed here the true potential of nanomaterials would never be realised. The methods used to fabricate

both mechanical and electrical contacts on single NWs have been described, as have the lateral AFM bending technique used extensively throughout this thesis and the electrical measurements used to allow electromechanical measurements to be performed on these NWs.

In chapter 3 which follows, the effects which deposition methods of NWs can have on their adhesion to a SiO_2 substrate are investigated. Subsequently, investigated are the effects different deposition methods have on NWs that are clamped in a doubly-clamped beam configuration.

2.15 References

(1) Davisson, C. J.; Germer, L. H. Reflections of Electrons by a Crystal of Nickel. *Proc. Natl. Acad. Sci.* **1928**, *14*, 317–322.
(2) Freundlich, M. M. Origin of the Electron Microscope. *Science* **1963**, *142*, 185–188.
(3) Oatley, C. W. The Early History of the Scanning Electron Microscope. *J. Appl. Phys.* **1982**, *53*, R1–R13.
(4) Wittke, J. H. SEM Overview http://saturno.fmc.uam.es/web/superficies/instrumentacion/Instrumentation.htm (accessed Nov 11, 2016).
(5) Ruska, E. The Development of the Electron Microscope and of Electron Microscopy. *Biosci. Rep.* **1987**, *7*, 607–629.
(6) Krumeich, F. Imaging and Diffraction in TEM http://www.microscopy.ethz.ch/TEMED.htm (accessed Nov 11, 2016).
(7) Smith, D. J. Development of Aberration-Corrected Electron Microscopy. *Microsc. Microanal.* **2008**, *14*, 2–15.
(8) Hatzakis, M. Electron Resists for Microcircuit and Mask Production. *J. Electrochem. Soc.* **1969**, *11*, 1033–1037.
(9) Hovington, P.; Drouin, D.; Gauvin, R. CASINO: A New Monte Carlo Code in C Language for Electron Beam Interaction - Part I: Description of the Program. *Scanning* **1997**, *19*, 1–14.
(10) Matsui, S.; Ichihashi, T.; Baba, M.; Satoh, A. Electron Beam Induced Selective Etching and Deposition. *Superlattices and Mcrostructures* **1990**, *7*, 295–301.
(11) Kim, C. S.; Ahn, S. H.; Jang, D. Y. Review: Developments in Micro/nanoscale Fabrication by Focused Ion Beams. *Vacuum* **2012**, *86*, 1014–1035.
(12) Binnig, G.; Rohrer, H.; Gerber, C.; Weibel, E. Tunneling through a Controllable Gap. *Appl. Phys. Lett.* **1982**, *40*, 178–180.
(13) Binnig, G.; Quate, C. F. Atomic Force Microscope. *Phys. Rev. Lett.* **1986**, *56*, 930–933.
(14) Giessibl, F. J. Advances in Atomic Force Microscopy. *Rev. Mod. Phys.* **2003**, *75*, 949–983.
(15) Giessibl, F. J. AFM's Path to Atomic Resolution. *Mater. Today* **2005**, *8*, 32–41.
(16) Frederix, P. L. T. M.; Bosshart, P. D.; Engel, A. Atomic Force Microscopy of Biological Membranes. *Biophys. J.* **2009**, *96*, 329–338.
(17) Nirmalraj, P. N.; Bellew, A. T.; Bell, A. P.; Fairfield, J. A.; McCarthy, E. K.; O'Kelly, C.; Pereira, L. F. C.; Sorel, S.; Morosan, D.; Coleman, J. N.; *et al.* Manipulating Connectivity and Electrical Conductivity in Metallic Nanowire Networks. *Nano Lett.* **2012**, *12*, 5966–5971.
(18) Vinckier, A.; Semenza, G. Measuring Elasticity of Biological Materials by Atomic Force Microscopy. *FEBS Lett.* **1998**, *430*, 12–16.
(19) Chen, J.; Bell, G. A.; Dong, H.; Du, P.; Lin, I.; Lu, H.; Attard, P.; Tranchida, D.; Kiflie, Z.; Acierno, S.; *et al.* Nanoscale Mechanical Characterization of Polymers by Atomic Force Microscopy (AFM) Nanoindentations : Viscoelastic Characterization of a Model Material. *Meas. Sci. Technol.* **2009**, *20*, 1–9.
(20) Wu, B.; Heidelberg, A.; Boland, J. J. Mechanical Properties of Ultrahigh-Strength Gold Nanowires. *Nat. Mater.* **2005**, *4*, 525–529.
(21) Wu, B.; Heidelberg, A.; Boland, J. J. Microstructure-Hardened Silver Nanowires. *Nano Lett.* **2006**, *6*, 468–472.
(22) Shahin, V.; Ludwig, Y.; Schafer, C.; Nikova, D.; Oberleithner, H. Glucocorticoids Remodel Nuclear Envelope Structure and Permeability. *J. Cell Sci.* **2005**, *118*, 2881–2889.
(23) Li, C.; Mizuta, H.; Oda, S. *Growth and Characterisation of Ge Nanowires by Chemical Vapour Deposition*; Hashim, A., Ed.; InTech, **2011**.
(24) Cai, X. M.; Ye, F.; Jing, S. Y.; Zhang, D. P.; Fan, P.; Xie, E. Q. CVD Growth of InGaN Nanowires. *J. Alloys Compd.* **2009**, *467*, 472–476.
(25) Hwang, N. M.; Cheong, W. S.; Yoon, D. Y.; Kim, D.-Y. Growth of Silicon Nanowires by Chemical Vapor Deposition: Approach by Charged Cluster Model. *J. Cryst. Growth* **2000**, *218*, 33–39.

(26) Pinion, C. W.; Nenon, D. P.; Christesen, J. D.; Cahoon, J. F. Identifying Crystallization and Incorporation Limited Regimes During Vapor-Liquid-Solid Growth of Si Nanowires. *ACS Nano* **2014**, *8*, 6081–6088.
(27) Choi, H.-J. *Semiconductor Nanostructures for Optoelectronic Devices*; Yi, G.-C., Ed.; Springer, **2006**; Vol. 6.
(28) Mohammad, S. N. Analysis of the Vapor – Liquid – Solid Mechanism for Nanowire Growth and a Model for This Mechanism. *Nano Lett.* **2008**, *8*, 1532–1538.
(29) Zhu, Y.; Qin, Q.; Xu, F.; Fan, F.; Ding, Y.; Zhang, T.; Wiley, B. J.; Wang, Z. L. Size Effects on Elasticity, Yielding, and Fracture of Silver Nanowires: In Situ Experiments. *Phys. Rev. B - Condens. Matter Mater. Phys.* **2012**, *85*, 1–7.
(30) Meng, F.; Jin, S. The Solution Growth of Copper Nanowires and Nanotubes Is Driven by Screw Dislocations. *Nano Lett.* **2012**, *12*, 234–239.
(31) Kuno, M. An Overview of Solution-Based Semiconductor Nanowires: Synthesis and Optical Studies. *Phys. Chem. Chem. Phys.* **2008**, *10*, 620–639.
(32) Coskun, S.; Aksoy, B.; Unalan, H. E. Polyol Synthesis of Silver Nanowires : An Extensive Parametric Study. *Cryst. Growth Des.* **2011**, *2*, 2–5.
(33) Sun, Y.; Mayers, B.; Herricks, T.; Xia, Y. Polyol Synthesis of Uniform Silver Nanowires: A Plausible Growth Mechanism and the Supporting Evidence. *Nano Lett.* **2003**, *3*, 955–960.
(34) Meléndrez, M. F.; Medina, C.; Solis-Pomar, F.; Flores, P.; Paulraj, M.; Pérez-Tijerina, E. Quality and High Yield Synthesis of Ag Nanowires by Microwave-Assisted Hydrothermal Method. *Nanoscale Res. Lett.* **2015**, *10*, 1–9.
(35) Pinion, C. W.; Nenon, D. P.; Christesen, J. D.; Cahoon, J. F. Identifying Crystallization and Incorporation Limited Regimes During Vapor-Liquid-Solid Growth of Si Nanowires. *ACS Nano* **2014**, 6081–6088.
(36) Schwarz, U. D.; Koester, P.; Wiesendanger, R. Quantitative Analysis of Lateral Force Microscopy Experiments. *Rev. Sci. Instrum.* **1996**, *67*, 2560–2567.
(37) McCarthy, E. K. The Electromechanical Properties of Individual Nanowires, Trinity College Dublin, **2013**.

3

DEPOSTION EFFECTS ON THE ADHESION AND RESIDUAL STRESS OF NANOWIRES

3.1 Introduction

As discussed in detail in chapter 1, various techniques have been used to measure the mechanical properties of nanomaterials, specifically one-dimensional nanoscale wires. These include nano-indentation techniques[1,2], in-situ SEM/TEM techniques[3,4] and lateral force microscopy techniques[5-7]. Nanomaterials often exhibit size dependent mechanical properties due to their dimensions[8,9]. These unique properties open the door for the use of nanomaterials in a range of applications that includes, nano-electromechanical-systems (NEMs), interconnects, sensors and actuators. What must also be understood, but which is not widely appreciated, is the potential influence fabrication and processing conditions may have on the mechanical properties of these materials.

Fabrication processes generally involve several steps, for instance, - material deposition, heat treatment, lithography, etching, metallisation steps and device testing. Indeed, during the fabrication of nanomaterials themselves, it is often necessary for the surfaces of the nanomaterials to be functionalised in order to prevent agglomeration or to promote growth along a desired direction[10]. It is important to ensure that these fabrication steps and growth conditions do not influence the fundamental properties of the nanomaterial whose properties are under investigation or required for successful device operation. It has already been established that surface functionalisation has a dramatic influence on the optical properties in nanomaterials as a result of modifying the rate of carrier recombination at surfaces. In the case of mechanical properties, it has been established that residual stresses can occur as a result of fabrication methods, which can strongly impact material and device performance.

3.2 Residual Stress

Residual stress is a stress that remains in a material after all external forces have been removed[11]. The scientific interest in residual stresses began as early as 1877 corresponding to the period when electrodeposition was first studied[12]. Residual stress is also very relevant in the deposition of thin films due to the inevitable mismatch in material properties between the substrate and film. Residual stresses may be desirable or undesirable. When materials are processed into functional structures or devices they are often trapped in a non-equilibrium state. These residual stresses remain in the structure when clamping or adhesion conditions allow for it, as in the case of a doubly–clamped beam. Examples of the effects of residual stress on nanomaterials include buckling of mechanical structures[13,14], extremely high Quality Factors (QF) in resonators[15-17] and the influence on the stiffness and hence the frequency dependence of resonators[18-20]. At times, residual stress can be beneficial for example, by enhancing the corrosion resistance of composite coatings[21]. In other instances, it leads to deteriorated or unpredictable performance.

Residual stresses can be categorised in two ways; intrinsic and extrinsic stresses. *Intrinsic stresses* reflect the internal composition of a material during its deposition. As nanowires (NWs) become miniaturised, the surfaces have an increasingly strong influence on the behaviour of the nanowire[22]. Indeed several different wire types such as silver[23,24], ZnO[25] and silicon[9] show varying mechanical properties such as Young's modulus and fracture stress due to enhanced surface effects at small dimensions (< 60 nm).

The second mechanism by which residual stresses can be generated in a material is through *extrinsic stresses.* Generally, extrinsic stresses are unintended factors such as temperature gradients or some other processing step which unintentionally causes the material to become strained.

3.2.1 Liquid Mediated Residual Stress

When incorporating beams into mechanical devices it is often necessary to use solvents as part of fabrication/cleaning steps. This liquid interaction can become problematic at the nanoscale when distances between nanoscale components are reduced. In NEMS devices, there are countless studies of adhesion related failure which is a major limitation for device integration. This generally occurs when a beam, doubly or singly clamped, is separated from the substrate by only a couple of microns or less. During the fabrication of a device it is often necessary to expose the device to a solution based process. When the device-to-substrate gap

is small, strong attractive capillary forces can develop during the evaporation of the solvent which can then cause the collapse and subsequent pinning of the beam[26,27]. It is also possible for the same collapse to occur if the device is exposed to high humidity conditions that results in capillary condensation[28]. This collapse can become permanent, as even after the solvent has evaporated the cantilever can remain pinned to the substrate, as shown in Figure 3.1. It is reasonable to think that a possible solution to this problem would be to increase the stiffness of the active component, so that the capillary forces are not large enough to collapse the beam. However, for devices such as actuators it is beneficial to minimise beam stiffness as the required actuation voltage scales with stiffness[29]. Although it may appear that the beam stiffness is the critical parameter for NEMs devices, it is essential to consider the impact of the fabrication processes on the mechanical properties and consequently on the device behaviour and performance.

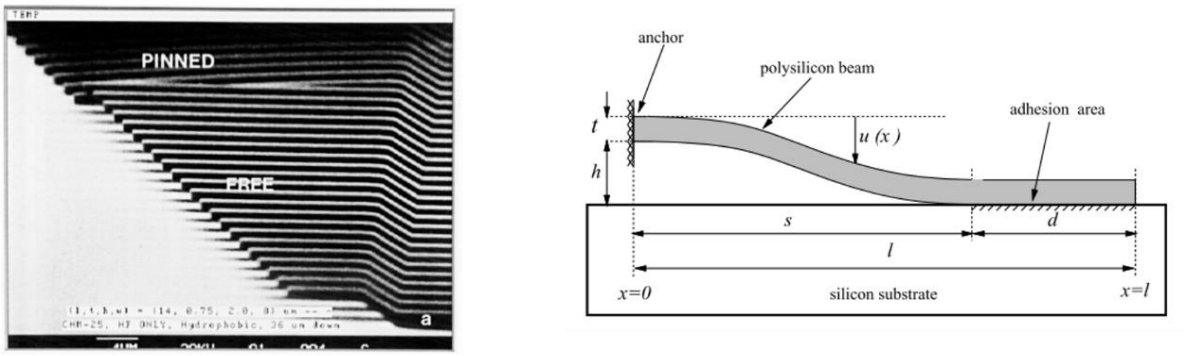

Figure 3.1: (a) After evaporation of solvent used in wet lithography, long cantilever beams remained pinned to the substrate. (b) Schematic of cantilever beam adhering to the substrate[30].

For nanomaterials such as NWs, different deposition methods are required to deposit the NWs into positions so that their mechanical properties can be investigated, as discussed in chapter 1. These deposition methods can cause unwanted residual stresses in materials. The deposition method used is often dictated by the technique used to synthesise the NWs. The techniques used to synthesis the nanowires used in these experiments has been described in chapter 2.

3.3 Nanowire Deposition

The AgNWs used in these measurements are received in a stock solution of isopropanol (20 mg/ml). The simplest method to deposit these wires is by dropcasting a 5 µL aliquot of a 0.02 mg/ml solution of NWs in IPA. AgNWs can also be transferred via a dry transfer process as

discussed in chapter 2. The method used to deposit SiNWs is via a direct dry transfer of the wires directly from the growth wafer (in the same manner used for AgNW dry transfer). SiNWs can also be solvent transferred using IPA as the dispersive solvent. To achieve solvent dispersal, the SiNWs are removed from their growth wafer via sonication at 80 kHz for 3 seconds in a small volume of IPA. This disperses the NWs in the solvent so that they can be subsequently dropcast. Through this, a comprehensive comparison of the adhesion and mechanical properties of both wire types on SiO_2 can be performed where they have been deposited with or without solvent interactions. As mentioned previously, liquid interactions can have dramatic effects on the operation of mechanical devices. Moreover, when NWs are deposited on a surface using a solvent, it is important that the interactions and forces involved during the solvent evaporation are considered.

3.4 Drying Effects on Solvent Deposited Nanowires

We've established that it is important to consider the possible effects that the solvent evaporation process has on dispersed NWs prior to being deposited. This includes directing the NWs final position on the substrate and inducing a residual stress on the NW. It has been reported that ring-shaped "coffee stains" are observed when a droplet of colloidal solution dries as illustrated in Figure 3.2 (a). This is caused by an outward capillary flow of solvent to compensate for solvent loss at the perimeter of the evaporating droplet. This effect draws the dispersed nanomaterial away from the centre of the solvent droplet, to the droplet periphery, resulting in a concentrated deposition of material at the edge of the droplet, along the 3-phase boundary line between the solvent-atmosphere-substrate, as seen in Figure 3.2 (c). In the case of NWs, this capillary flow will orientate the NWs along the radial direction[31]. As the solvent evaporates the pinning line retracts and wires that are close to the receding front "pin" to the substrate resulting in NW deposition as shown in Figure 3.2 (b), (c).

The drying effects of nanomaterials suspended in solvents has been previously exploited. For example, in the assembly of single colloidal particle lines[32] and in aligned NW electrode devices[33]. In this instance, capillary flow and drying effects are being exploited for fabrication purposes, therefore it is important to assess whether these drying effects can induce unwanted effects on the nanomaterials such as enhanced adhesion or straining of the devices.

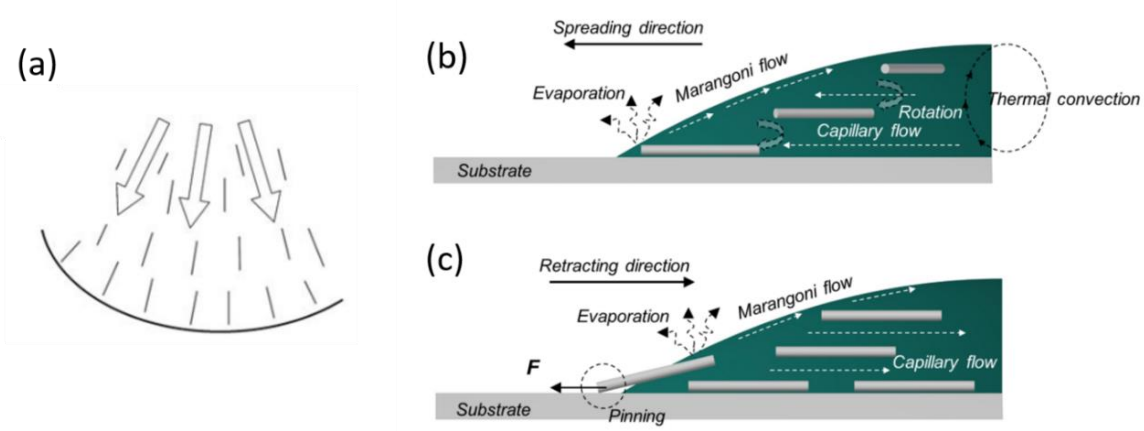

Figure 3.2: (a) Schematic showing how NWs are orientated radially at the edge of a drying droplet. The pinning contact line (black line) induces an outward capillary flow (arrows) to compensate for the loss of solvent at the perimeter due to evaporation. This flow aligns the NWs radially and carries them to the contact line, resulting in the "coffee stain" effect[31]. (b) Side-view of a NW suspension during deposition, showing the direction of capillary forces. (c) As the contact line retracts due to the solvent evaporation, NWs are pinned to the surface resulting in deposition[34].

In 2015, Liu *et al.*[35] demonstrated that by applying moisture onto a AgNW network, cold welding of the junctions could be achieved. This resulted in lower sheet resistances of their NW films due to the improved contact at the NW junctions as a result of solvent interactions. A schematic of the process can be observed in Figure 3.3 (a), water drops accumulate at the small gaps between the junctions, resulting in the formation of a capillary bridge. The capillary force between two identical spheres is estimated analytically using;[36]

$$F_{capillary} = -\frac{2\pi R\gamma cos\theta}{1 + (H/2d)} \tag{3.1}$$

where γ is the surface tension of the liquid, R is the radius of the sphere, θ is the contact angle, H is the separation distance between the two spheres and d is the immersion length between the two spheres. The authors estimate that the capillary force can increase to 10 nN when using the surface tension of water (72 mN/m) for particles with a radius of 50 nm. Solvent deposition is the preferred choice for the deposition of NWs due to its ease of use, cost effectiveness and large scale processibility. It is clear that solvent interactions can be complex on the nanoscale and caution must be exercised when processing with solvents. It is important

to analyse potential solvent processing phenomena and assess the potential impacts this may have on the mechanical response of NWs.

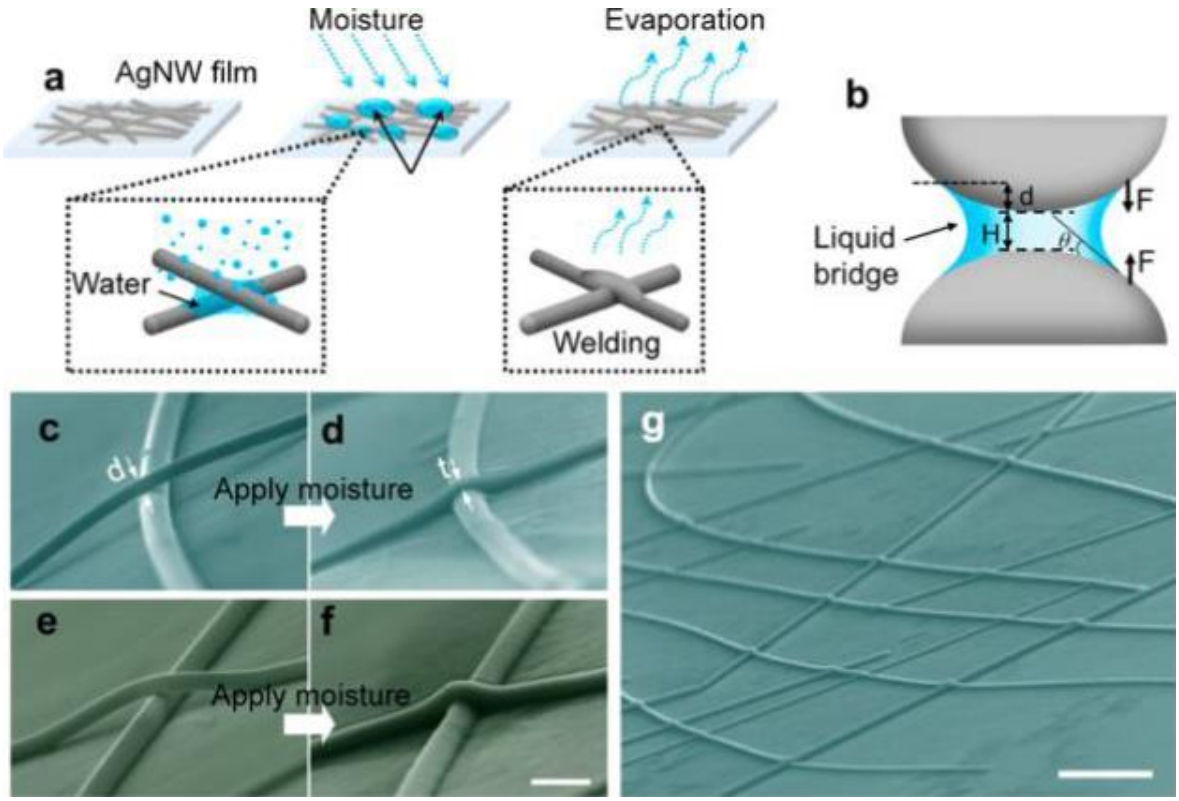

Figure 3.3: Capillary force induced welding of AgNWs. (a) Schematic of welding process under the presence of water moisture. (b) Schematic of liquid bridge formation between two spherical particles. (c,d/e,f) Two sets of AgNW junctions before and after moisture treatment, scale bar 200 nm. (g) SEM image of an array of cold welded AgNW junctions, scale bar 1 μm[35].

In this work, the mechanical properties of NWs were measured, using the lateral force microscopy technique outlined previously[7]. For these experiments, it is important to correctly define the boundary conditions of the doubly-clamped beam in order to ensure a mechanically robust system. This allows the determination of the correct Young's modulus by establishing a doubly-clamped beam of known length, *L*. The NWs are clamped using electron beam induced deposition of Pt metal (Pt-EBID). It is important to note that the purpose of these Pt-EBID clamps is to precisely define the NW-substrate clamp location while ensuring strong adhesion but without interfering with the measured mechanical response of the NWs themselves. For this reason, we now review the Pt-EBID clamping process in more detail.

3.5 Electron Beam Induced Depositions

It is imperative that when using EBID to clamp a NW that the clamping does not have an influence on the mechanical properties of the material being investigated. For example, in 2005 Ding *et al.*[37] showed how the resonance frequency of crystalline boron NWs was affected by EBID of carbonaceous material. The authors compared the resonance frequency of a wire, pinned only by adhesion forces, with the resonance frequency obtained when increasing depositions of carbon were deposited repeatedly at the point where the NW contacted the AFM tip used for the resonance measurement. As seen in Figure 3.4, their results suggest that there was a possibility that having a stronger attachment leads to an increase of resonance frequency. Additionally, the authors believe that the frequency increase could have been caused by a decrease of the effective beam length due to the build-up of EBID material.

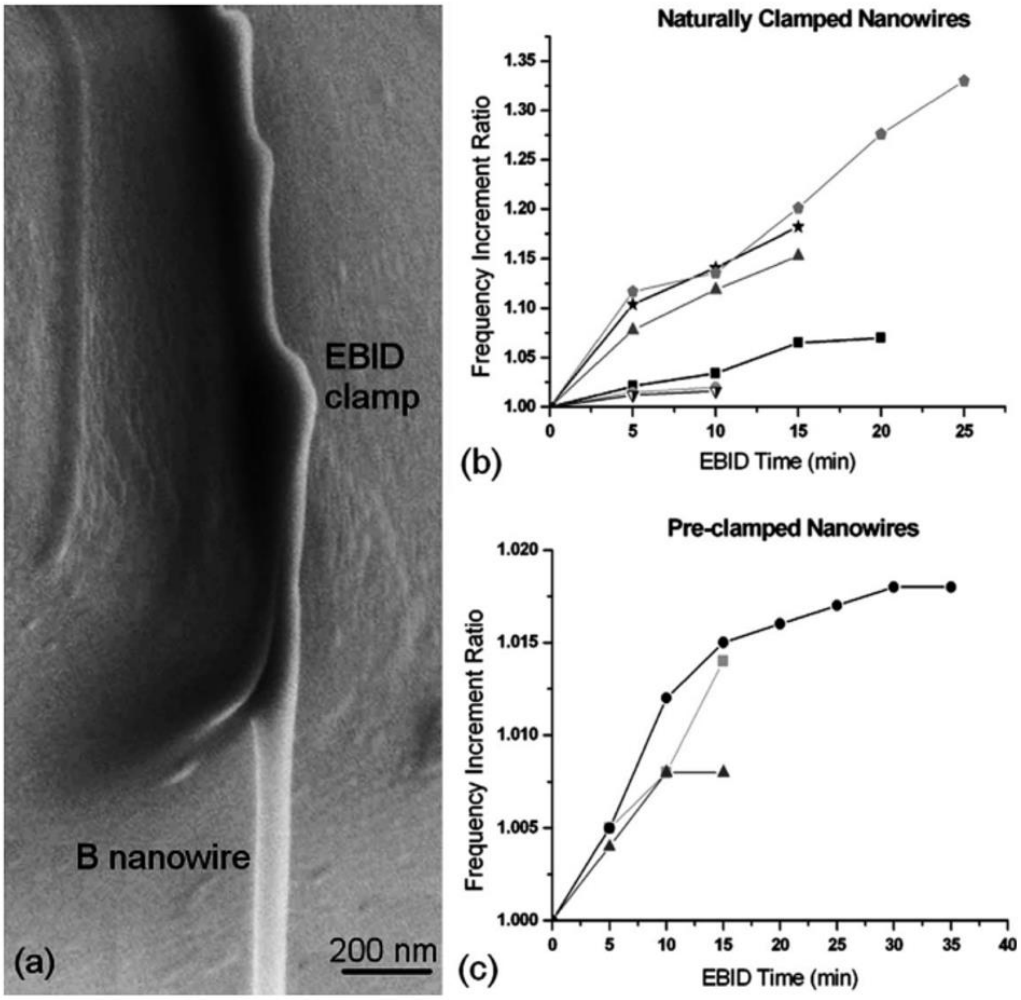

Figure 3.4: (a) SEM image of a boron NW being clamped to an AFM tip surface with EBID. (b) Frequency increment ratio vs EBID deposition time for six boron NWs that were initially held without EBID. (c) Frequency increment ratio for three pre-clamped boron NWs with increasing EBID deposition time[37].

It has been demonstrated that the resonance frequency of a micromechanical oscillator can be significantly affected by exposing it to a focused electron beam, this is because the electron beam induces local carbon deposition on the surface of the oscillator which results in an increase in the effective stress along the beam[38].

These examples illustrate how fabrication steps can incorporate unwanted stresses into the material systems of interest and can mask their true mechanical properties. In the case of doubly-clamped beams, there have been instances where fibers/nanowires have been fabricated with unintended residual stresses. In 2013, Hudson *et al.* conducted doubly-clamped beam measurements on spider silk fibers which were determined to have been subjected to an initial residual stress[39] as seen in Figure 3.5 (a). Initial strains corresponding to 0.06 GPa and 0.07 GPa were reported. The force-displacement (*F-d*) response of these fibers therefore did not fit the model described by Heidelberg *et al.*[40] The authors adjusted the Heidelberg model to account for this residual stress. However, the values extracted by this tension-adjusted model can prove problematic and will be discussed in more detail in chapter 4. Similarly in 2015, Calahorra *et al.*[41] fabricated SiNWs in a doubly-clamped beam configuration. Due to fabrication processes, residual stresses were also incorporated into the NWs as shown in Figure 3.5 (b). Initial stresses between -0.3 - +0.45 GPa were reported. In both cases either fabrication processes or inherent residual stresses were cited as the most likely cause of the incorporation of residual stresses.

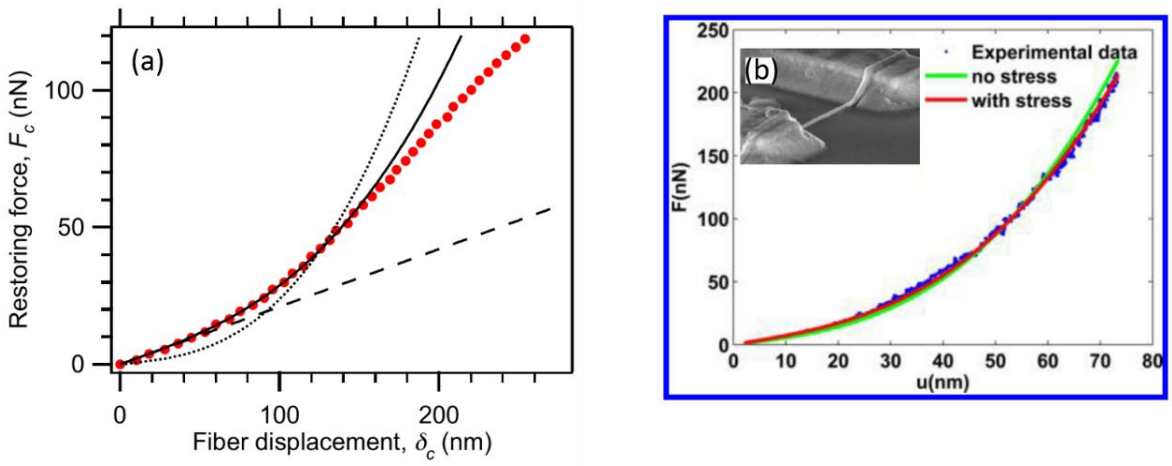

Figure 3.5: (a) Experimental *F–d* curve for a single spider silk under an initial tension. Fits are shown for Euler-Bernoulli beam mechanics which accounts purely for bending (Linear Fit), the Heidelberg model which accounts for bending and tensile stresses (Poor Fit) and a residual tension adjusted model which accounts for bending and tensile stresses along with an initial tension[39] (Good Fit). (b) Experimental *F-d* curve (blue dots) for a doubly-clamped SiNW fitted to both the Heidelberg model (Green Fit) and tension-adjusted model (Red Fit)[41], inset shows an SEM image of a doubly-clamped SiNW.

In this chapter, the difference in adhesion between a SiO_2 substrate with AgNWs and SiNWs deposited using either solvent or dry deposition methods was investigated. Subsequently, NWs of both types and using both deposition methods were suspended over trenches, mechanically clamped, and a 3-point bending measurement was performed.

3.6 Experimental Approach

Adhesion measurements were performed by depositing NWs onto a clean blank SiO_2 substrate using both solvent and dry deposition methods. The adhesion was determined either as weak or strong depending on whether the wire was mobile under lateral manipulation by an AFM tip. The procedure for manipulating the NWs is the same as for the 3-point bending experiment except that the tip is positioned to sit just above the surface in line with the NW as opposed to being below the plane of the NW, as is the case for the 3-point bending experiment. Mechanical measurements were then performed using the lateral 3-point bending technique described in chapter 2. Details of the substrate preparation can also be found in chapter 2.

3.6.1 Solvent Deposition

AgNWs dispersed in IPA were dropcast over the blank SiO_2 and trenched substrates and suitable wires were identified under dark field imaging in an optical microscope. For solvent dispersal of SiNWs the growth wafer was placed in a small vial with 3 ml IPA and sonicated at 80 kHz for 5 seconds, or until the NWs had been removed from the growth wafer; this was identifiable by an observed colour change. 5 µL of the dispersion was then dropcast on the desired substrate.

3.6.2 Dry Deposition

To dry transfer the AgNWs a PDMS stamp was used. The PDMS stamp was comprised of a mixture of silicone elastomer:resin (10:1). The mixture was degassed in a desiccator for 5 minutes and placed on a glass slide where it was cured on a hotplate at 80° C. 5 µL of a concentrated AgNW solution (2 mg/ml) was dropcast on a piece of unpatterned SiO_2. The PDMS stamp was then placed on the SiO_2 to remove the NWs and transfer them to the desired substrate. The SiNWs were synthesised on a growth wafer as described previously. They were dry transferred directly from the growth wafer to the desired substrate using the PDMS

stamp. For the 3-point bending measurement NWs were optically inspected to identify wires that spanned trenches and were suitable to measure mechanically.

3.6.3 Platinum Electron Beam Induced Deposition

NW samples positioned over patterned trenches for 3-point mechanical loading in a doubly-clamped beam configuration were inserted into the Auriga crossbeam FIB/SEM with EBID capabilities to pin the wires to the substrate. This clamping process prevents the wires from sliding during the mechanical AFM experiment and defines an accurate pinning length, *L*. The electron beam accelerating voltage used was 5 kV with a 30 µm aperture. Each wire to be pinned was located in the SEM. The appropriate area on each side of the trench for Pt deposition was defined using the SEM design software. The Pt precursor gas was switched on, allowing Pt to be electron beam deposited for 10-15 seconds. The Pt precursor gas was then switched off. The chamber pressure was allowed to return to its initial level before the beam was switched back on. This was to ensure all the Pt precursor gas was removed from the chamber to prevent contamination of the wire of interest. The same procedure was used for both the AgNWs and SiNWs. An example of a pinned wire is shown in Figure 3.7 (a). Wires of both types were also left unclamped so that a comparison could be made.

3.6.4 Mechanical Measurement

For the 3-point AFM measurement, the NW was oriented in the AFM so that its long axis was parallel to the long axis of the cantilever. A 3x3 µm AFM image of the NW was acquired followed by tapping mode imaging along the desired manipulation path. The AFM tip was then lowered into the trench below the xy plane of the wire, the AFM feedback loop switched off and the loading and unloading of the wire was performed with the change in lateral signal on the photodetector being recorded. This procedure was repeated several times so that consistent and reproducible loading could be verified. The AFM tip was then calibrated using the procedures outlined in chapter 2. The cantilever stiffness was obtained from this calibration which allowed the *F-d* response of the NW to be acquired.

3.7 Results

3.7.1 Adhesion of AgNWs and SiNWs to a SiO_2 Substrate

The adhesion of AgNWs and SiNWs to a SiO_2 substrate was investigated. Both NW types were deposited using the solvent and dry deposition methods described above. As can be

observed in Figure 3.6 when AgNWs are solvent deposited and manipulated they are strongly adhered to the substrate. This can be observed in the inset of Figure 3.6 (d) where the AFM tip fractures the NW due to its strong adhesion to the surface. However, when the AgNWs are deposited using a dry transfer process the NWs are weakly adhered to the substrate. This can be observed in Figure 3.6 (b) where multiple NWs are shown to move freely on the SiO_2 surface when manipulated by the AFM tip. This result indicates that the adhesion between NWs and surfaces is dependent on the deposition process used. In contrast, the adhesion of the SiNWs showed no apparent dependence of the wire-substrate adhesion on the deposition method used.

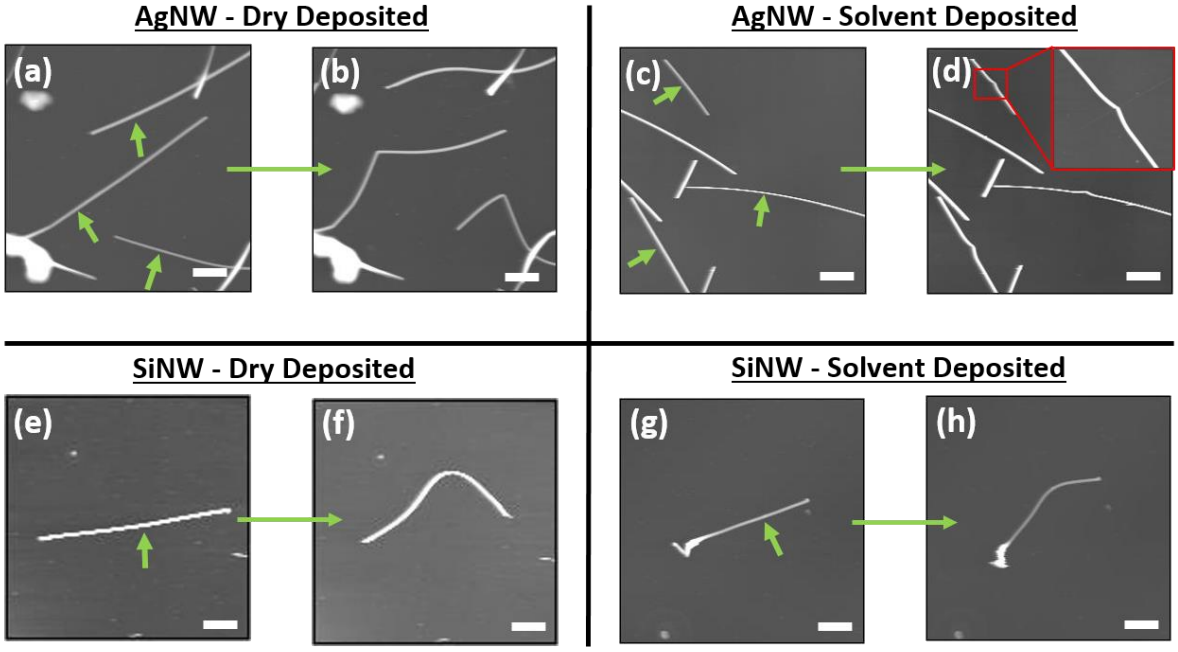

Figure 3.6: AFM images of AgNWs and SiNWs on SiO_2 before and after being manipulated with an AFM tip. NWs were deposited using different deposition methods. Images (a),(c),(e),(g) are wires before manipulation with the green arrows defining the loading path. (a),(c) AgNWs deposited by dry and solvent methods respectively, scale bars 1 μm. (b),(d) The corresponding wires after manipulation with the inset in (d) showing a reduced scan image of a fractured AgNW, scale bars 1 μm. (e),(g) SiNWs deposited by dry and solvent methods respectively with (f) and (h) showing the same wires after having being loaded with the AFM tip, scale bars 500 nm.

As shown in Figure 3.6 (f) and (h), the SiNWs are free to move on the SiO_2 substrate regardless of the deposition method used to deposit them. We now investigate if the mechanical response of these wires in a doubly-clamped beam configuration varies due to the deposition method used.

3.7.2 Doubly-Clamped Beam Analysis of Solvent and Dry Deposited AgNWs

AgNWs were deposited using both solvent and dry transfer methods so that the force response of both could be compared. Figure 3.7 (a) shows a SEM image of a AgNW that has been dropcast on to a SiO_2 substrate. The substrate was pre-patterned with trenches and the NW was clamped at the trench edges via Pt-EBID. The NW was then manipulated using the 3-point bending AFM technique described in chapter 2. Figure 3.7 (b) shows the *F-d* response of the NW repeatedly loaded and unloaded at its centre point. Based on the way subsequent *F–d* curves overlap it can be concluded that the AgNW was pinned to the SiO_2 surface. If a wire was not correctly pinned it would move, resulting in a sudden decrease in the slope of the *F-d* response.

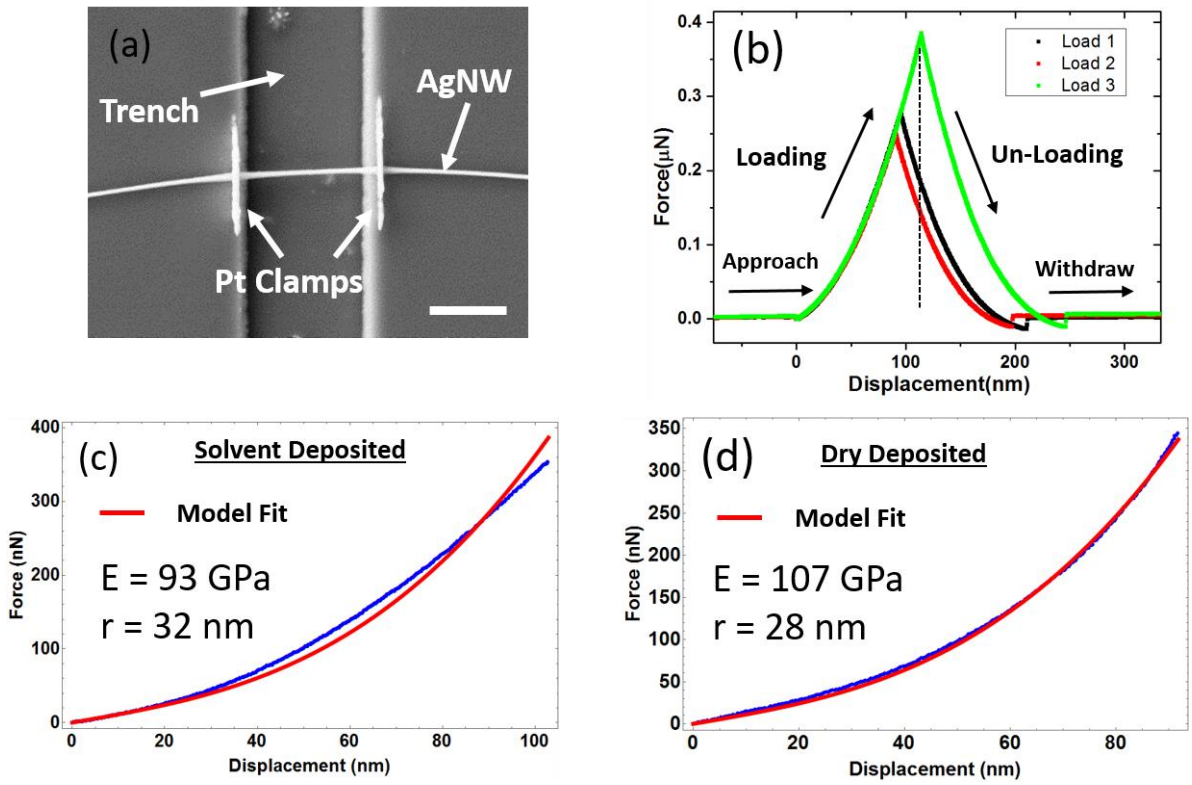

Figure 3.7: (a) SEM image of a AgNW suspended over a trench with Pt clamps pinning the wire to the substrate, scale bar 1 μm. (b) Repeatable *F-d* curves for the loading of the AgNW in (a). (c) *F-d* response of a solvent deposited AgNW fitted to the Heidelberg model. (d) *F-d* response of a dry deposited AgNW fitted to the Heidelberg model.

A dry deposited AgNW was fabricated and analysed using the same procedure. The force responses are then fit to the generalised model, equation (3.2), (Figure 3.7 (c)) which accounts for both bending and tensile deformation;[40]

$$F_{centre} = \frac{192EI}{L^3} f(\alpha)\Delta z_{centre} \tag{3.2}$$

where F_{centre} is the force applied perpendicular to the NW axis at its central point, Δz_{centre} is the resulting displacement at the load point, E is the Young's modulus of the wire, I is the areal moment of inertia for a cylindrical wire and L is the pinned length. From the fits to the Heidelberg (zero-residual stress) model it is clear that NWs which are dry deposited are accurately described by the model, Figure 3.7 (d). This contrasts with the solvent deposited AgNWs where the fit of the model to the *F-d* response is poor. Upon observation, the *F-d* response is significantly more linear than expected. This is seen over a large displacement range and there is little or no cubic response observed, despite the displacement (105 nm) being approximately three times the radius of the wire (32 nm). At such displacements, there should be a large cubic response observed due to tensile stretching of the wire, which is not evident. Therefore, it appears that there is a contribution to the mechanics that is not being accounted for by the model.

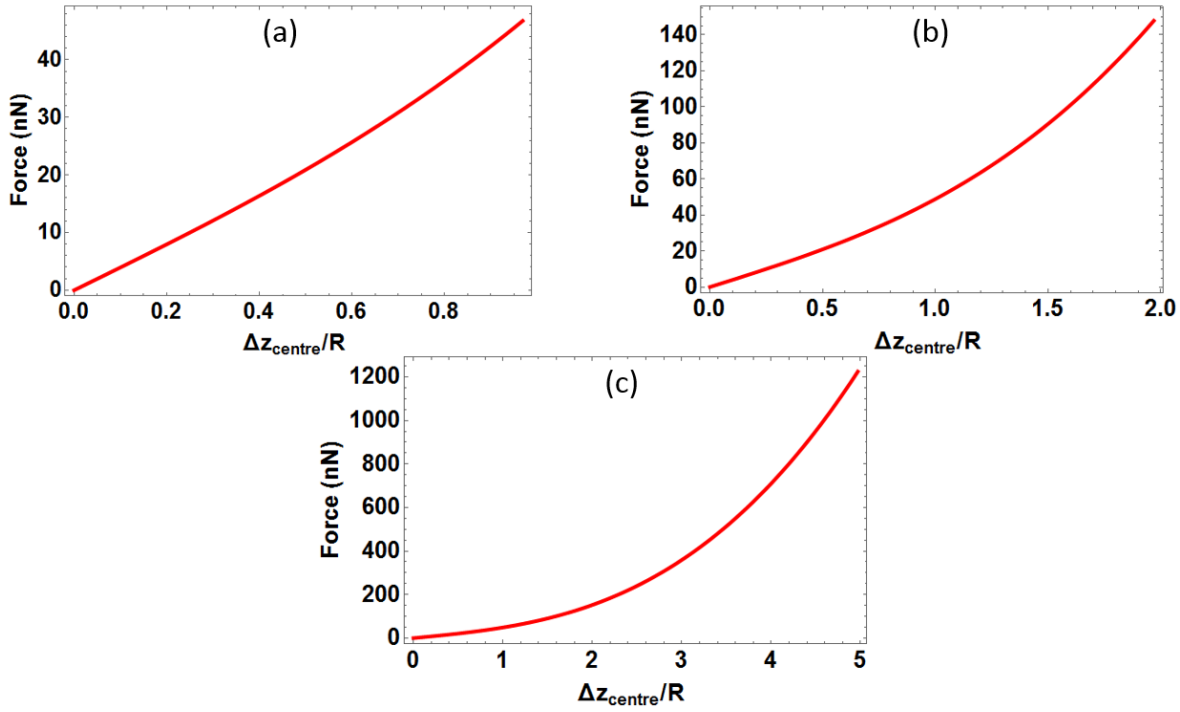

Figure 3.8: (a) Simulated *F-d* curve for a circular cylinder showing the non-linearity for a maximum one radius. (b) Simulated *F-d* curve for a maximum 2 radii. (c) Simulated *F-d* curve for a maximum 5 radii.

This is in contrast to the research paper outlined by Heidelberg *et al.*[40] where it was shown that at displacements larger than one radius the *F-d* response should become non-linear and

at a displacement greater than two radii the non-linearity should have grown considerably. Figure 3.8 (a) – (c) shows the calculated shape of the *F-d* curves for a 32 nm radius wire, (L = 2.2 μm) with a Young's modulus of 83 GPa (Bulk Silver) at varying displacements ranging from one radius to 5 radii. These parameters reflect the dimensions and clamping length used for the wire in Figure 3.7.

It is quite clear that the model cannot accurately account for this behaviour and that there is an additional contribution which is not being considered. It is assumed that before the wire is loaded for the first time there is no residual stress. That is to say, we assume that the wire is suspended over the trench with no forces acting upon it other than gravity. This result also indicates that the residual stress has not been induced by the Pt clamps, if it were, there would be residual stress observed regardless of the deposition method. If the wire is subjected to an initial residual stress the approximated form of the model discussed in chapter 1, and used up to this point becomes;

$$F = \frac{192EI}{L^3}\Delta z_{centre}\left(1 + \frac{A}{24I}\Delta z_{centre}^2 + \alpha_0\right) \tag{3.3}$$

where $\alpha_0 = T_0L^2/40EI$, with T_0 being residual tension in the wire. α_0 represents the ratio of axial stresses due to extension and bending. From the formula in (3.3) it can be observed that if a wire is under an initial residual stress, so that $\alpha_0 > 1$, it will result in an increase in the linear *F-d* response of the wire. This is consistent with the response observed in Figure 3.7 (c). The model as outlined in chapter 1 no longer describes the *F-d* response of a wire that is subjected to a residual stress.

In summary, we have demonstrated that the solvent deposition of 60 nm diameter AgNWs results in an enhanced adhesion to the substrate, and when the solvent deposition method is used in doubly-clamped 3-point bending measurements the wires exhibit a residual stress. To determine if this occurs for other NW systems we now perform a similar analysis on SiNWs.

3.7.3 Doubly-Clamped Beam Analysis of Solvent and Dry Deposited SiNWs

For mechanical adhesion measurements on SiNWs, the procedure is the same as that outlined previously. Firstly, a mechanical measurement is performed on a SiNW that has been solvent deposited but without mechanical clamping. This is to observe the *F-d* curve of an unclamped NW. Following this, mechanical measurements are carried out on both solvent and dry

deposited SiNWs, where Pt-EBID mechanical clamps are used in order to ensure reliable mechanical clamping of the NWs. When a SiNW is solvent deposited over a pre-fabricated trench and loaded, prior to the addition of EBID mechanical clamps, it can be observed that the NW is weakly adhered to the surface.

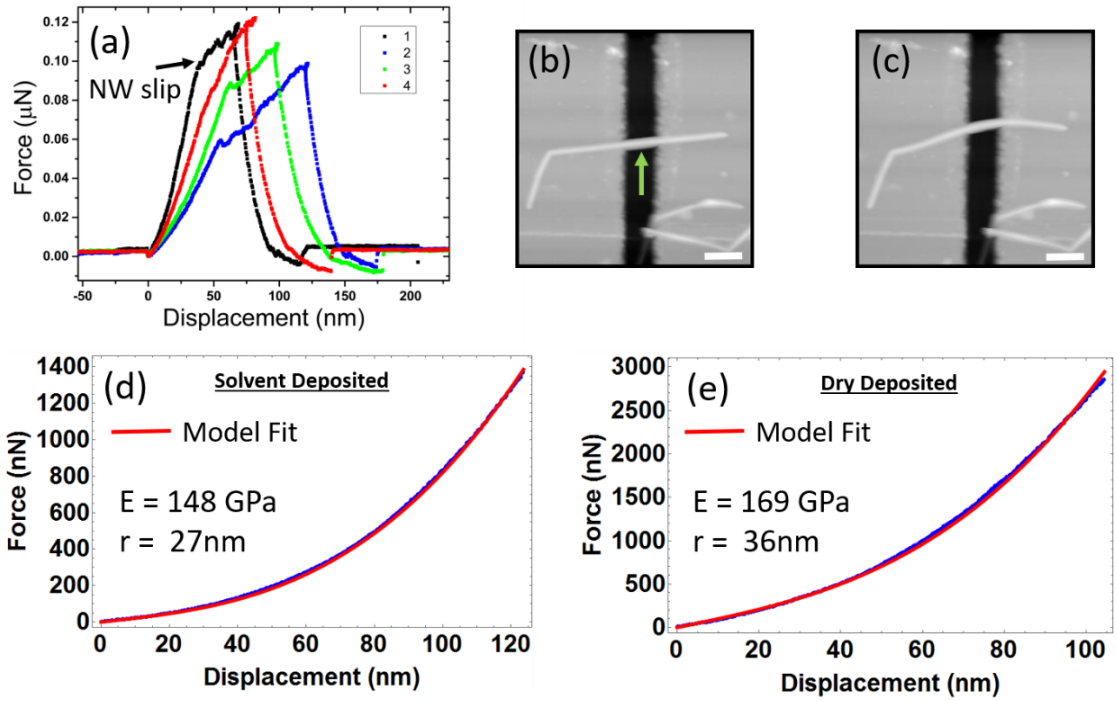

Figure 3.9: (a) *F-d* curves for an unpinned SiNW that has been solvent deposited. (b), (c) Before and after manipulation AFM images showing the AFM tip manipulation path (Green), scale bar 2 μm. (d) *F-d* curve for a solvent deposited SiNW with additional mechanical clamps fitted to the Heidelberg model. (e) *F–d* curve for a dry deposited SiNW with additional mechanical clamps fitted to the Heidelberg model.

Figure 3.9 (a) shows the non-repeatable *F–d* curves in four sequential loading cycles. Additionally, the *F–d* curves show a signature where the NW begins to slide on the surface, detected by an abrupt change in slope of the loading curve. The AFM images in Figure 3.9 (b) and (c), show the NW before and after these loading experiments. It is evident that the position of the NW has changed, confirming that when SiNWs are solvent deposited they are weakly adhered to a SiO_2 surface. Regardless of whether SiNWs are deposited by a solution or dry process, they need to be pinned using Pt-EBID in order for 3-point bending measurements to be correctly performed. Following deposition of clamps the wires are investigated, and Figure 3.9 (d) and (e), clearly shows that both solvent and dry deposited SiNWs fit the Heidelberg (zero-residual stress) model described by equation (3.2). This

indicates that the SiNWs are not subjected to a residual stress. This is not unexpected since, both solvent and dry deposited SiNWs are mobile on the surface prior to pinning indicating that it is not possible for them to be under an initial tension.

When NWs are weakly adhered to the surface, clamped and manipulated they do not exhibit residual stresses. The weak adhesion to the substrate allows the NWs to relax, removing any potentially induced residual stresses. In contrast, solvent deposited AgNWs exhibit a residual stress coupled with a strong adhesion to the surface. This strong adhesion seems to enable any induced residual stresses in the wire during deposition to become fixed within the NW when it is clamped. The origin of this residual stress will be discussed in greater detail in chapter 6. When analysing the adhesion between the NWs and the SiO_2 surface van der Waals interactions must be discussed. Assuming the NWs are perfect cylinders, the force of interaction can be estimated between the NW and the flat surface;[28]

$$F_{vdw} = -\frac{A\sqrt{R}}{8\sqrt{2}D^{\frac{5}{2}}} \tag{3.4}$$

where F_{vdw} is the van der Waals interaction force, A is the Hamaker constant between the two materials, R is the radius of the NW and D is the distance between the NW and the surface. The Hamaker constant describes the interatomic pairwise potential between all the atoms in one body and all the atoms in another body. The Hamaker constant will remain fixed regardless of the deposition process used because the wire and the surface remain the same materials. It's therefore plausible that a capillary force is induced between the AgNW and the surface, that is strong enough to reduce the distance, D, between the NW and the surface therefore increasing the interaction force. These types of capillary forces have been observed before by Liu *et al.*[35] A similar response is not observed for SiNWs but every wire type will have unique Hamaker constants and the cross sections of the NWs deviates from the assumption of being perfectly cylindrical.

3.8 Conclusion

In this chapter, it has been demonstrated that the deposition process used for depositing NWs can have a significant effect on the NW-substrate adhesion. In our experiments the deposition of AgNWs, 60 nm in diameter, in a volatile solvent results in them being strongly adhered to a SiO_2 substrate. This enhanced adhesion allows any induced residual stresses to become fixed in the NW when measured in a doubly-clamped beam configuration. When a doubly-clamped

NW is affected by a residual stress the *F-d* response of the wire is no longer accurately described by the Heidelberg (zero-residual stress) model which has been previously used to describe the mechanical properties of NWs. It is important to determine if a suitable model can be used to robustly extract the Young's modulus of a NW that is affected by a residual stress. This will be the focus of chapter 4.

3.9 References

(1) Li, X.; Gao, H.; Murphy, C. J.; Caswell, K. K. Nanoindentation of Silver Nanowires. *Nano Lett.* **2003**, *3*, 1495–1498.

(2) Sohn, Y.-S.; Park, J.; Yoon, G.; Song, J.; Jee, S.-W.; Lee, J.-H.; Na, S.; Kwon, T.; Eom, K. Mechanical Properties of Silicon Nanowires. *Nanoscale Res. Lett.* **2010**, *5*, 211–216.

(3) Poncharal, P.; Wang, Z. L.; Ugarte, D.; de Heer, W. A. Electrostatic Deflections and Electromechanical Resonances of Carbon Nanotubes. *Science (80-.).* **1999**, *283*, 1513–1516.

(4) Yu, M. Strength and Breaking Mechanism of Multiwalled Carbon Nanotubes Under Tensile Load. *Science (80-.).* **2000**, *287*, 637–640.

(5) Almecija, D.; Blond, D.; Sader, J. E.; Coleman, J. N.; Boland, J. J. Mechanical Properties of Individual Electrospun Polymer-Nanotube Composite Nanofibers. *Carbon N. Y.* **2009**, *47*, 2253–2258.

(6) Wu, B.; Heidelberg, A.; Boland, J. J. Microstructure-Hardened Silver Nanowires. *Nano Lett.* **2006**, *6*, 468–472.

(7) Wu, B.; Heidelberg, A.; Boland, J. J. Mechanical Properties of Ultrahigh-Strength Gold Nanowires. *Nat. Mater.* **2005**, *4*, 525–529.

(8) Chen, C. Q.; Shi, Y.; Zhang, Y. S.; Zhu, J.; Yan, Y. J. Size Dependence of Young's Modulus in ZnO Nanowires. *Phys. Rev. Lett.* **2006**, *96*, 1–4.

(9) Gordon, M. J.; Baron, T.; Dhalluin, F.; Gentile, P.; Ferret, P. Size Effects in Mechanical Deformation and Fracture of Cantilevered Silicon Nanowires. *Nano Lett.* **2009**, *9*, 525–529.

(10) Coskun, S.; Aksoy, B.; Unalan, H. E. Polyol Synthesis of Silver Nanowires : An Extensive Parametric Study. *Cryst. Growth Des.* **2011**, *2*, 2–5.

(11) Chung, J. Y.; Chastek, T. Q.; Fasolka, M. J.; Ro, H. W.; Stafford, C. M. Quantifying Residual Stress in Nanoscale Thin Polymer Films via Surface Wrinkling. *ACS Nano* **2009**, *3*, 844–852.

(12) Maissel L.I., G. R. *Handbook of Thin Film Technology*; McGraw-Hill, **1970**.

(13) Wang, D. H.; Wang, G. F. Surface Effects on the Vibration and Buckling of Double-Nanobeam-Systems. *J. Nanomater.* **2011**, *2011*, 1–7.

(14) Sansa, M.; Fernández-Regúlez, M.; Llobet, J.; San Paulo, Á.; Pérez-Murano, F. High-Sensitivity Linear Piezoresistive Transduction for Nanomechanical Beam Resonators. *Nat. Commun.* **2014**, *5*, 1–9.

(15) Schmid, S.; Hierold, C. Damping Mechanisms of Single-Clamped and Prestressed Double-Clamped Resonant Polymer Microbeams. *J. Appl. Phys.* **2008**, *104*, 1–12.

(16) Verbridge, S. S.; Shapiro, D. F.; Craighead, H. G.; Parpia, J. M. Macroscopic Tuning of Nanomechanics: Substrate Bending for Reversible Control of Frequency and Quality Factor of Nanostring Resonators. *Nano Lett.* **2007**, *7*, 1728–1735.

(17) Wilson, D. J.; Regal, C. A.; Papp, S. B.; Kimble, H. J. Cavity Optomechanics with Stoichiometric SiN Films. *Phys. Rev. Lett.* **2009**, *103*, 1–4.

(18) Karabalin, R. B.; Feng, X. L.; Roukes, M. L. Parametric Nanomechanical Amplification at Very High Frequency. *Nano Lett.* **2009**, *9*, 3116–3123.

(19) Pini, V.; Tamayo, J.; Gil-Santos, E.; Ramos, D.; Kosaka, P.; Tong, H. D.; Van Rijn, C.; Calleja, M. Shedding Light on Axial Stress Effect on Resonance Frequencies of Nanocantilevers. *ACS Nano* **2011**, *5*, 4269–4275.

(20) Lachut, M. J.; Sader, J. E. Effect of Surface Stress on the Stiffness of Cantilever Plates: Influence of Cantilever Geometry. *Appl. Phys. Lett.* **2009**, *95*, 1–4.

(21) Zhao, X.; Munroe, P.; Habibi, D.; Xie, Z. Roles of Compressive Residual Stress in Enhancing the Corrosion Resistance of Nano Nitride Composite Coatings on Steel. *J. Asian Ceram. Soc.* **2013**, *1*, 86–94.

(22) Rudd, R. E.; Lee, B. Mechanics of Silicon Nanowires: Size-Dependent Elasticity from First Principles. *Mol. Simul.* **2008**, *34*, 1–8.

(23) Jing, G. Y.; Duan, H. L.; Sun, X. M.; Zhang, Z. S.; Xu, J.; Li, Y. D.; Wang, J. X.; Yu, D. P. Surface Effects on Elastic Properties of Silver Nanowires: Contact Atomic-Force Microscopy. *Phys. Rev. B - Condens. Matter Mater. Phys.* **2006**, *73*, 1–6.

(24) Zhu, Y.; Qin, Q.; Xu, F.; Fan, F.; Ding, Y.; Zhang, T.; Wiley, B. J.; Wang, Z. L. Size Effects on Elasticity, Yielding, and Fracture of Silver Nanowires: In Situ Experiments. *Phys. Rev. B - Condens. Matter Mater. Phys.* **2012**, *85*, 1–7.
(25) Xu, F.; Qin, Q.; Mishra, A.; Gu, Y.; Zhu, Y. Mechanical Properties of ZnO Nanowires under Different Loading Modes. *Nano Res.* **2010**, *280*, 1–10.
(26) Guckel, H.; Sniegowski, J. J.; Christenson, T. R.; Mohney, S.; Kelly, T. F. Fabrication of Micromechanical Devices from Polysilicon Films with Smooth Surfaces. *Sensors and Actuators* **1989**, *20*, 117–122.
(27) Orpana, M.; Korhonen, A. O. Control of Residual Stress of Polysilicon Thin Films by Heavy Doping in Surface Micromachining. *Solid-State Sensors and Actuators*, **1991**, *5*, 957.
(28) Israelachvilli, J. N. *Intermolecular and Surface Forces*; 3rd Edition; Academic Press, **2011**.
(29) Pawashe, C.; Lin, K.; Kuhn, K. J. Scaling Limits of Electrostatic Nanorelays. *IEEE Trans. Electron Devices* **2013**, *60*, 2936–2942.
(30) Mastrangelo, C. H. Adhesion-Related Failure Mechanisms in Micromechanical Devices. *Tribol. Lett.* **1997**, *3*, 223–238.
(31) Huang, J.; Fan, R.; Connor, S.; Yang, P. One-Step Patterning of Aligned Nanowire Arrays by Programmed Dip Coating. *Angew. Chemie - Int. Ed.* **2007**, *46*, 2414–2417.
(32) Huang, J.; Tao, A. R.; Connor, S.; He, R.; Yang, P. A General Method for Assembling Single Colloidal Particle Lines. *Nano Lett.* **2006**, *6*, 524–529.
(33) Park, B.; Bae, I.-G.; Huh, Y. H. Aligned Silver Nanowire-Based Transparent Electrodes for Engineering Polarisation-Selective Optoelectronics. *Sci. Rep.* **2016**, *6*, 1–9.
(34) Dai, H.; Ding, R.; Li, M.; Huang, J.; Li, Y.; Trevor, M. Ordering Ag Nanowire Arrays by Spontaneous Spreading of Volatile Droplet on Solid Surface. *Sci. Rep.* **2014**, *4*, 1–5.
(35) Liu, Y.; Zhang, J.; Gao, H.; Wang, Y.; Liu, Q.; Huang, S.; Guo, C. F.; Ren, Z. Capillary-Force-Induced Cold Welding in Silver-Nanowire-Based Flexible Transparent Electrodes. *Nano Lett.* **2017**, *17*, 1090–1096.
(36) Rabinovich, Y. I.; Esayanur, M. S.; Moudgil, B. M. Capillary Forces between Two Spheres with a Fixed Volume Liquid Bridge: Theory and Experiment. *Langmuir* **2005**, *21*, 10992–10997.
(37) Ding, W.; Calabri, L.; Chen, X.; Kohlhaas, K. M.; Ruoff, R. S. Mechanics of Crystalline Boron Nanowires. *Compos. Sci. Technol.* **2006**, *66*, 1109–1121.
(38) Zaitsev, S.; Shtempluck, O.; Buks, E. Effects of Electron Beam Induced Carbon Deposition on the Mechanical Properties of a Micromechanical Oscillator. *Sensors Actuators, A Phys.* **2012**, *179*, 237–241.
(39) Hudson, S. D.; Zhurov, V.; Grbić, V.; Grbić, M.; Hutter, J. L. Measurement of the Elastic Modulus of Spider Mite Silk Fibers Using Atomic Force Microscopy. *J. Appl. Phys.* **2013**, *113*, 1–7.
(40) Heidelberg, A.; Ngo, L. T.; Wu, B.; Phillips, M. A.; Sharma, S.; Kamins, T. I.; Sader, J. E.; Boland, J. J. A Generalized Description of the Elastic Properties of Nanowires. *Nano Lett.* **2006**, *6*, 1101–1106.
(41) Calahorra, Y.; Shtempluck, O.; Kotchetkov, V.; Yaish, Y. E. Young's Modulus, Residual Stress, and Crystal Orientation of Doubly Clamped Silicon Nanowire Beams. *Nano Lett.* **2015**, *15*, 2945–2950.

4

RESIDUAL STRESS ANALYSIS IN DOUBLY-CLAMPED BEAMS

4.1 Introduction

Due to their small sizes and large surface areas, nanomaterials are susceptible to external environmental factors that may influence their measured properties. To probe the various material properties of nanowires (NWs) such as electrical, mechanical and optical, it is necessary to fabricate a device to allow these properties to be measured. The potential effects that processing and fabrication steps can have on the measured material properties must be considered. For example, as discussed in chapter 3, the deposition process of NWs can have a significant effect on their intrinsic stress state. It has been demonstrated that for certain wires, such as 60 nm diameter silver nanowires (AgNWs), solvent deposition results in them being subjected to a residual stress. Often, solvent deposition may be the only viable option for depositing NWs. It is also the most cost effective and time effective method.

The force-displacement (*F*-*d*) response for a doubly-clamped NW affected by a residual stress is different than that of a NW that is in a zero-stress state. Therefore, it is important to ascertain if the Young's modulus of a doubly-clamped beam can be robustly determined when the beam is subjected to an initial residual stress. In 2013, Hudson *et al.*[1] whilst using the Heidelberg (zero-residual stress) model[2] observed that the force response of spider silk being measured in a doubly-clamped configuration was influenced by an initial residual stress. They modified the Heidelberg doubly-clamped beam model to account for the initial residual stress. Before the modifications made to the Heidelberg model are introduced, let's first summarise the key aspects of the Heidelberg model used to analyse the *F*-*d* response for a NW that is not affected by an initial residual stress.

4.1.1 Heidelberg Model

The ideal (zero-residual stress) doubly-clamped free suspended wire configuration was first considered by Heidelberg *et al.*[2] The exact analytical solution is expressed as;

$$F_{centre} = \frac{192EI}{L^3} f(\alpha)\Delta z_{centre}, \tag{4.1}$$

where F_{centre} is the force applied perpendicular to the NW axis at its central point, E is the Young's modulus of the wire, I is the areal moment of inertia for a cylindrical wire and L is the pinned length. The function $f(\alpha)$ is defined;

$$f(\alpha) = \frac{\alpha}{48 - \frac{192tanh(\sqrt{\alpha}/4)}{\sqrt{\alpha}}}, \tag{4.2}$$

where α is related to the displacement Δz_{centre} of the wire by (a detailed description of the approach can be found in chapter 1);

$$\alpha = \frac{6\epsilon(140+\epsilon)}{350+3\epsilon}, \quad \epsilon = (\frac{2\Delta z_{centre}}{R})^2, \tag{4.3}$$

This model assumes the wire is not subjected to a residual axial stress. The $f(\alpha)$ function may be approximated so that the force F_{centre} comprises two terms: (i) a bending term that is linear in the displacement Δz_{centre} and (ii) a tensile term that is cubic in the displacement Δz_{centre}^2. We note that residual stress in the wire will enhance the contribution of the first term but not the second. As such, it will affect the transition from the linear to the cubic dependence on Δz_{centre} in equation (4.1). This comprehensive model has been used to analyse the *F-d* response of NWs over the entire elastic regime[3-5] . When a beam is affected by a residual stress, the above set of equations does not hold true. The relationship between α and Δz_{centre} changes when a beam is subjected to an initial residual stress. As mentioned, Hudson *et al.* measured the *F-d* response of spider silk fibers in a doubly-clamped beam configuration and found that they were affected by a residual stress[1]. Therefore, the model as developed by Heidelberg *et al.* cannot be used to analyse the mechanical properties of the spider silks.

4.1.2 Hudson - Tension-Adjusted Heidelberg Model

The original model described by Heidelberg *et al.*[2] describes the *F-d* response of a beam that has not been subjected to an initial residual stress. It is possible for this model to be adapted

to account for such stresses. The approach taken by Hudson *et al.* is similar to the approach taken by Heidelberg *et al*. Equation (4.1) and (4.2) remain valid for a beam that is affected by a residual stress however the relationship between α and Δz_{centre} needs to be modified for a beam affected by a residual stress. Equation (4.3) is obtained by using a Padé approximation to simplify a transcendental equation which is complex in nature and requires a numerical solution. The details of this Padé approximant are covered in detail in chapter 1. Hudson *et al.*[1] adapted the transcendental equation to account for a beam that is affected by an initial residual stress to give;

$$\left(1-\frac{L_0^2 T_0}{\alpha EI}\right)\left(\frac{EA}{T_0+EA}\right)\left[\frac{\alpha\cosh^2\left(\sqrt{\alpha}/4\right)}{2+\cosh\left(\sqrt{\alpha}/2\right)-6\frac{\sinh\left(\sqrt{\alpha}/2\right)}{\sqrt{\alpha}}}\left(1-4\frac{\tanh\left(\sqrt{\alpha}/4\right)}{\sqrt{\alpha}}\right)^2=\frac{A}{I}\Delta z_{centre}^2\right] \tag{4.4}$$

Where T_0 is the residual tension in the beam. It can be observed that when $T_0 = 0$ the transcendental equation used to describe a beam that is not affected by a residual tension is recovered[2]. Hudson chose to solve the transcendental equation in (4.4) numerically rather than to approximate it analytically as in the work of Heidelberg *et al.*[2] The authors used the set of equations (4.1), (4.2) and (4.4) to analyse the *F-d* response of spider silk fibers. Figure 4.1 (a) - (c) shows a schematic of a segment of fiber which has been subjected to a residual stress with the corresponding *F-d* curves shown in Figure 4.1 (d). It can be seen from Figure 4.1 (d) that the Heidelberg model does not describe the experimental data of Hudson accurately whereas, the model adjusted for residual tension fits the data accurately. The Euler-Bernoulli fit to the data is also shown, which accounts only for elastic beam bending. When fitting with the Heidelberg model a modulus of 32 GPa was obtained compared to a modulus of 25.4 GPa when using the tension-adjusted model. This indicates that the Heidelberg model overestimated the Young's modulus of the silk by ~ 20%. For this measurement, the initial tension that the fiber was subjected to was 46 nN, which corresponded to an initial strain of 0.22%.

It is important to note that although the Euler-Bernoulli fit for beam bending fits the linear response at small displacements, it will be largely affected by the residual stress in the beam. Despite this, it has often been used to extract the Young's modulus of NWs[6-9] which have the potential to be erroneous due to the inability to detect residual stresses at small

displacements. These linear responses are generally observed at displacements below that of the radius of the beam under investigation.

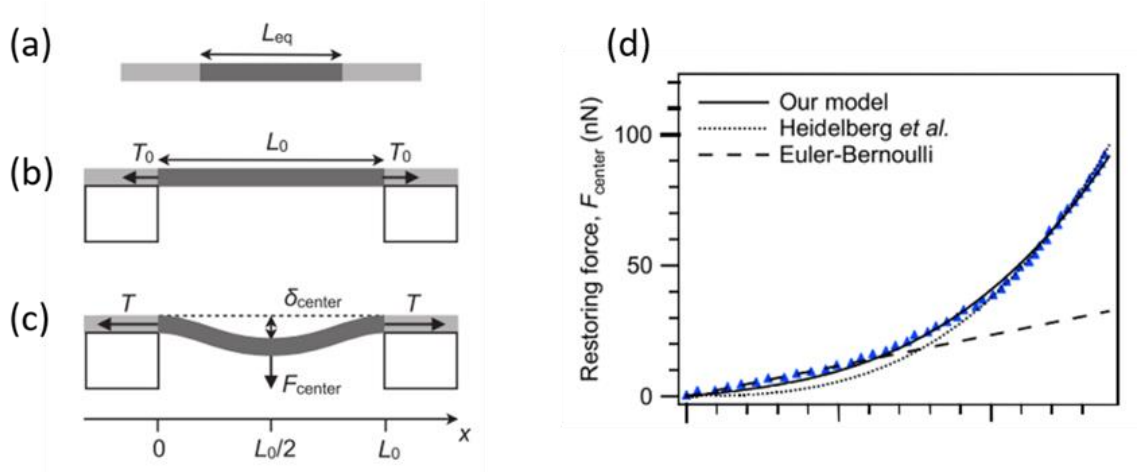

Figure 4.1: Diagram of the segment of fiber under analysis (a) before clamping and without initial tension, (b) after application of initial tension and clamping to grating but before contact with the AFM cantilever tip, and (c) after contact with the AFM cantilever tip. The fiber is shown in light grey, and the segment under analysis in dark grey. L_{eq} is the equilibrium length of the section of fiber stretched by an initial tension T_0 to the distance L_0 between clamping points. When the fiber is deflected by an amount δ_c by a force F_c applied at its midpoint $x = L_0/2$, the total axial tension increases to $T = T_0 + T_s$, the sum of the initial tension and the tension due to elongation of the fiber. (d) Experimental *F–d* curve for a single spider silk affected by an initial tension. Fits are shown for Euler-Bernoulli beam mechanics (linear dashed line) which accounts purely for bending, the Heidelberg model (dotted line) which accounts for bending and tensile stresses and a residual tension-adjusted model (solid line) which accounts for bending and tensile stresses along with an initial tension[1].

Based on this data it might appear that the adjustment of the ideal (zero- residual stress) Heidelberg model allows for the correct analysis of wires that have been affected by a residual stress. However in 2015, Yaish *et al.* proposed that the tension-adjusted model proposed by Hudson can be erroneous and that from the model fit the correct Young's modulus and residual tension cannot always be correctly determined[10]. They proposed that certain approximations of the model work with a greater degree of certainty.

4.1.3 Yaish - Tension-Adjusted Heidelberg Model

Yaish *et al.*[10] adapted the original Heidelberg model[2], similar to that as outlined by Hudson *et al.*[1] The difference here is that instead of using a numerical solution to the transcendental equation, they approximated it analytically using the same Padé approximation implemented

by Heidelberg *et al*.[2] where the solution to equation (4.4) possesses the following asymptotic solutions;

$$\alpha = \begin{cases} \frac{12}{5}\epsilon - \frac{3}{875}\epsilon^2, \epsilon \to 0 \\ 2\epsilon, \qquad\qquad \epsilon \to \infty \end{cases} \tag{4.5}$$

Where $\epsilon = \Delta z_c^2(\frac{A}{I})$, an approximate expression for α is then obtained by constructing a Padé approximation using equation (4.5), giving;

$$\alpha \cong \frac{L^2 T_0}{EI} + \frac{6\epsilon(140+\epsilon)}{350+3\epsilon} \equiv \alpha_{app} \tag{4.6}$$

Where $\frac{L^2 T_0}{EI} = \alpha_0$ which represents the ratio of residual axial stress to the stress generated by bending. The residual stress can occur in the form of tension (positive α_0) or compression (negative α_0). The additional α_0 term in equation (4.6) affects the *F-d* response of the beam in the small (linear) displacement range, as described previously. The authors used the set of equations (4.1), (4.2) and (4.6) to generate synthetic *F-d* curves to analyse the validity of the extracted Young's modulus and residual stress parameters over a large fitting range.

F-d data was generated for a beam of L = 1 µm, R = 20 nm, E = 190 GPa, for two residual stresses, σ_0 = 0 MPa, σ_0 = 500 MPa. They showed that the relative deviation of α_{app} from the exact value is less than 2% for both initial stresses, up to displacements of 10 times the beam radius as shown in Figure 4.2 (a) which validates the use of the approximate analytical expression used in equation (4.6). The authors indicated that by using various approximations of the full analytical model, some approximations showed a dependency on the range over which the data was fit while one approximation appeared to be independent of the fitting range, see Figure 4.2 (b) and (c). The actual approximations are not discussed in detail here because they are an indication that the separation of Young's modulus and residual tension can prove problematic. The fact that making minor changes to the full analytical expression appears to provide more consistent results is an indication of the sensitivity of the tension-adjusted model and that caution must be exercised when using it. Furthermore, the dependency on fitting range as outlined by Yaish *et al.* was only demonstrated for theoretical data. The authors used the approximation they deemed to work best to extract the mechanical

properties for silicon nanowires (SiNWs), however, they do not analyse the experimental data over different fitting ranges[11].

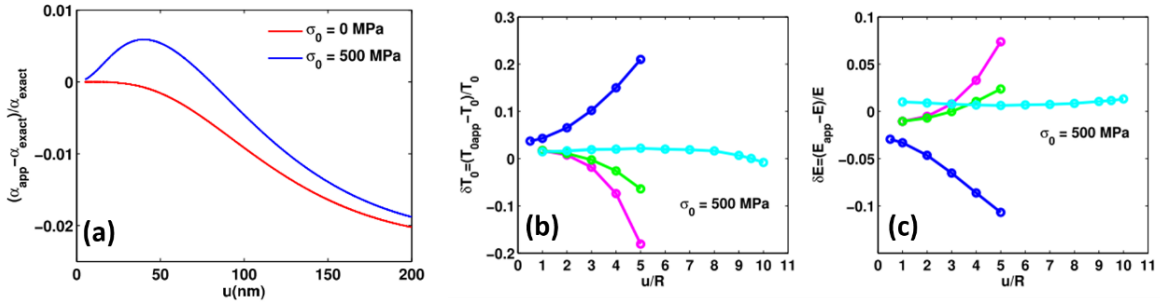

Figure 4.2: (a) Relative difference between α_{app} and α_{exact} vs displacement, for σ_0 = 0 MPa and 500 MPa. α_{exact} being the exact analytical solution and α_{app} being from Eq. (4.6). (b), (c) The relative error in the extracted residual tension (b) and Young's modulus (c) for different fitting ranges measured in beam radius (u/R). The different coloured plots are approximations of the full analytical expression described by Eqns. (4.1), (4.2) and (4.6). The theoretical *F-d* curves were calculated using E = 190 GPa and σ_0 = 500 MPa[10].

In this chapter, we investigate the validity of the full analytical tension-adjusted model for both theoretical and experimental data. It is important to assess the fit range sensitivity of the model for experimental data. Furthermore, we analyse both the Heidelberg (zero-residual stress) model and the tension-adjusted model for a NW that has not been affected by an initial residual stress. If both models work correctly, then the Young's modulus extracted by both models should be consistent as the tension-adjusted model reverts to the original (zero-residual stress) Heidelberg model in cases of zero residual tension.

4.2 Experimental Method

The fabrication techniques for a doubly-clamped beam have been discussed in chapters 2 and 3 along with the 3-point mechanical measurement. Measurements are made on both AgNWs and SiNWs with greater emphasis on the analysis of the data using a Mathematica fitting procedure.

4.2.1 Fitting to the Tension-Adjusted Heidelberg Model

The tension-adjusted model used in this analysis is the expansion of the Heidelberg model[2] described by Yaish *et al.*[10] to account for residual stress. Although Yaish *et al.* claimed that certain approximations appeared to be independent of the fitting range over which the *F-d* curves are fit, we found that there is minimal difference between the assumed best

approximation and the full analytical expression. Therefore, the full analytical expression is used throughout this analysis.

4.2.2 Comparison of Synthetic Data with Tension-Adjusted Heidelberg Model

Synthetic data is generated to determine the ability of the tension-adjusted model to correctly extract the Young's modulus and residual stress in a doubly-clamped NW. This is achieved by inputting parameters such as wire radius, pinning length, Young's modulus and residual tension. With these parameters, a *F-d* curve was generated using the tension-adjusted model described by the set of equations (4.1), (4.2) and (4.6). In Figure 4.3, the parameters chosen for the wire was a radius, *r*, of 27 nm, pinning length, *L*, of 2.2 μm and Young's modulus, *E*, of 83 GPa. The residual stress in the wire was varied from $\alpha_0$values of 0, 20, 50, 150, which corresponds to a residual tension, T_0, in the wire of 0 nN, 143 nN, 358 nN, 1074 nN respectively. As can be observed in Figure 4.3, in all cases the tension-adjusted model correctly extracts both the correct Young's modulus and the correctly inputted α_0 term. The greater the residual stress in the wire the more the values deviate at smaller displacements. The radius of this NW is 27 nm so consistent values are obtained up to 7.5 times the radius. At small displacements, there is potential for erroneous results and this is purely down to the dynamic range of the measurement.

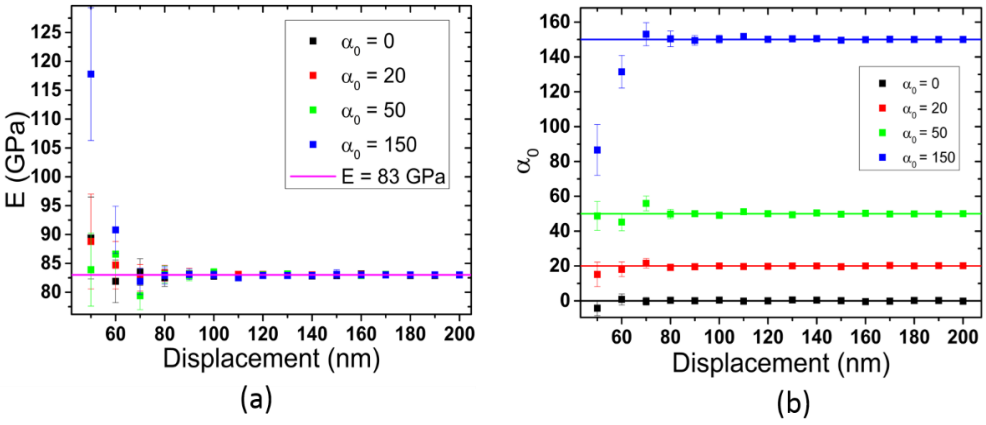

Figure 4.3: Variation of Young's modulus (a) and residual stress (b) with fitting range using the tension-adjusted Heidelberg model. The synthetic data was generated for a 54 nm diameter AgNW with a pinning length of 2.2 μm. The Young's modulus chosen was 83 GPa, with α_0 values of 0, 20, 50 and 150.

An approximate solution for the full analytical model can be obtained by superimposing the small and large deflection limits[2], yielding;

$$F_{center} = \frac{192EI}{L^3}\Delta z_{center}\left(1 + \frac{A}{24I}\Delta z_{center}^2 \pm \frac{T_0 L^2}{40EI}\right) \quad (4.7)$$

From equation (4.7) it can be observed that from the bending term that is linear in displacement Δz_{centre} there are terms containing both Young's modulus, E, and residual tension, T_0. Therefore, it is not possible to extract Young's modulus solely from the linear term. The tensile term which is cubic in displacement Δz_{centre} is independent of tension, T_0, therefore to extract the correct Young's modulus, a significant cubic response is required. If the response is completely linear due to a significant residual stress, the model cannot be used to extract the correct Young's modulus. When there is no residual stress in a wire it is possible to extract Young's modulus from the linear response alone because $E \propto$ slope of the linear response and depends only on the slope, pinning length, L, and moment of inertia, I, which are all precisely measured.

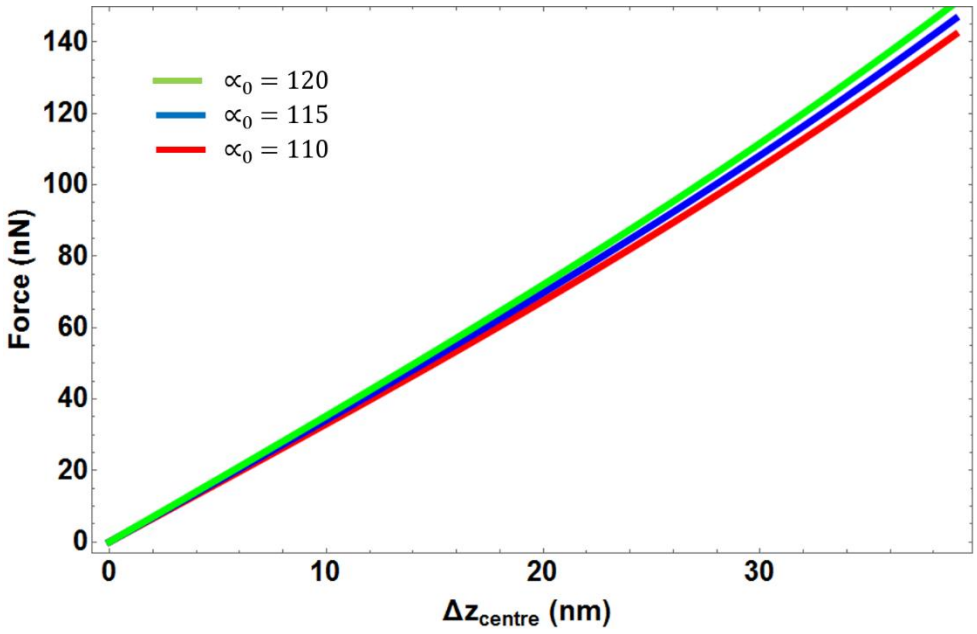

Figure 4.4: Synthetic *F-d* curves for a 60 nm diameter wire with pinning length of 2.2 μm under different initial residual stresses. The Young's modulus value for all three data curves is 83 GPa showing that under the influence of an initial stress the slope becomes a convolution of the Young's modulus and the residual stress/tension.

However, for a wire affected by a residual tension any residual tension in the wire which may arise from fabrication processes, will alter the slope of the linear response. The slope now depends on both Young's modulus and residual tension which cannot be separated as seen in Figure 4.4. If a wire is loaded in the small displacement region so that the *F-d* response is

completely linear then it is not possible to determine if the wire is initially under a residual stress or if the Young's modulus is correct. Therefore, Young's modulus values extracted from a fit to the linear response only, are potentially erroneous. It is therefore essential to obtain a significant cubic response and, as illustrated in Figure 4.3, as the residual stress in the wire increases the uncertainty in Young's modulus and residual stress increases at lower displacements.

The AgNWs and SiNWs measured in this work often plastically deform/fracture at ~ 5 times their radius and depending on the magnitude of initial tension this may not yield a large enough dynamic range to correctly separate the Young's modulus and the residual stress. Figure 4.3 demonstrates that theoretically the tension-adjusted model can separate Young's modulus and residual tension. It is important to determine if the model produces consistent results when applied to real experimental *F-d* curves.

4.2.3 Comparison of Experimental *F-d* Curves with Tension-Adjusted Heidelberg Model

As demonstrated in chapter 3, when AgNWs are solvent deposited onto a SiO_2 substrate they are adhered to the substrate and affected by a residual stress. Therefore, the *F-d* response of these NWs is not accurately described by the original (zero-residual stress) Heidelberg model. Figure 4.5 (a) shows the fit of a 68 nm diameter AgNW to the Heidelberg model. It is clear that the Heidelberg model does not accurately describe the *F-d* data. The Young's modulus of 76 GPa is similar to that expected for silver (83 GPa) however, this comes from what is clearly a poor fit. The *F-d* data is excellently described by the tension-adjusted model as seen in Figure 4.5 (b). However, the Young's modulus value extracted by the model is 54 GPa, which is lower than that expected for these wires. Furthermore, when the data is fit over varying displacement ranges it is clear that the extraction of Young's modulus and residual tension is not independent of the fitting range, see Figure 4.5 (c).

This contrasts with what is predicted theoretically. For this measurement, the model is not able to separate the Young's modulus and residual tension. There is an anti-correlation between the two where for larger Young's modulus values lower residual tension values are extracted and *vice versa*. Theoretically, we have demonstrated that the model can separate the two variables for wires with a residual tension up to 1000 nN which is greater than in this measurement. However, there are differences between theoretical data and experimental data and so caution must be exercised when attempting to extract the Young's modulus of NWs using a modified version of the Heidelberg model.

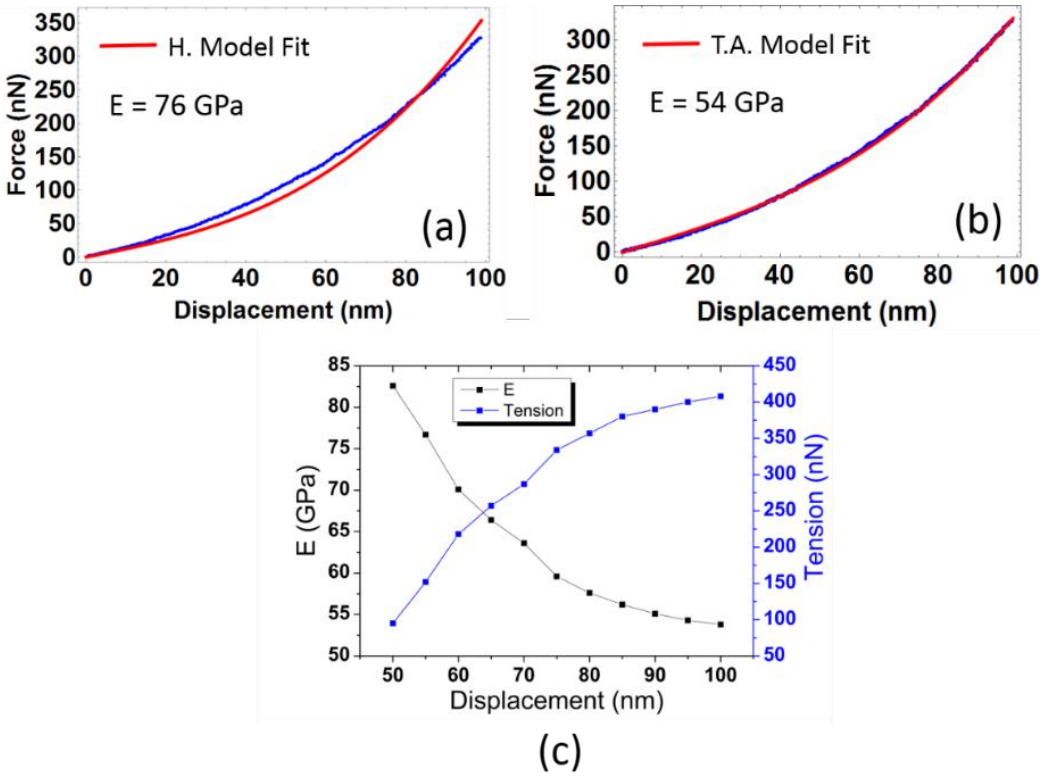

Figure 4.5: Force-displacement curves for a 68 nm diameter AgNW using (a) the Heidelberg model, (b) tension-adjusted model. (c) Anti-correlation between Young's modulus and residual tension when the tension-adjusted model is fitted to different displacements.

4.2.4 Comparison of Heidelberg and Tension-Adjusted Model for Zero-Residual Stress NWs

In chapter 3, we determined that SiNWs are not subjected to a residual stress upon deposition and mechanical clamping. Wires that are not affected by a residual stress are well described by the Heidelberg model[2-4]. Furthermore, they should also be well described by the tension-adjusted model because when wires are not affected by a residual stress (α_0 = 0) the tension-adjusted model reverts to the Heidelberg model. Figure 4.6 shows the *F-d* response for a doubly-clamped SiNW. From Figure 4.6 (a) it can be observed that the *F-d* response for this wire fits the Heidelberg model accurately indicating that the wire has not been subjected to a residual stress. A Young's modulus of 154 GPa is obtained which compares well with the bulk value for silicon of 169 GPa. From Figure 4.6 (b) it can be observed that the tension-adjusted model fits the data accurately with a Young's modulus value of 149 GPa. The values extracted by both models compare well. However, when analysing the dependence of both models on the *F-d* curves fitting range, it is clear that the Heidelberg model is independent of the fitting range, unlike the tension-adjusted model which demonstrates a dependency on the fitting range.

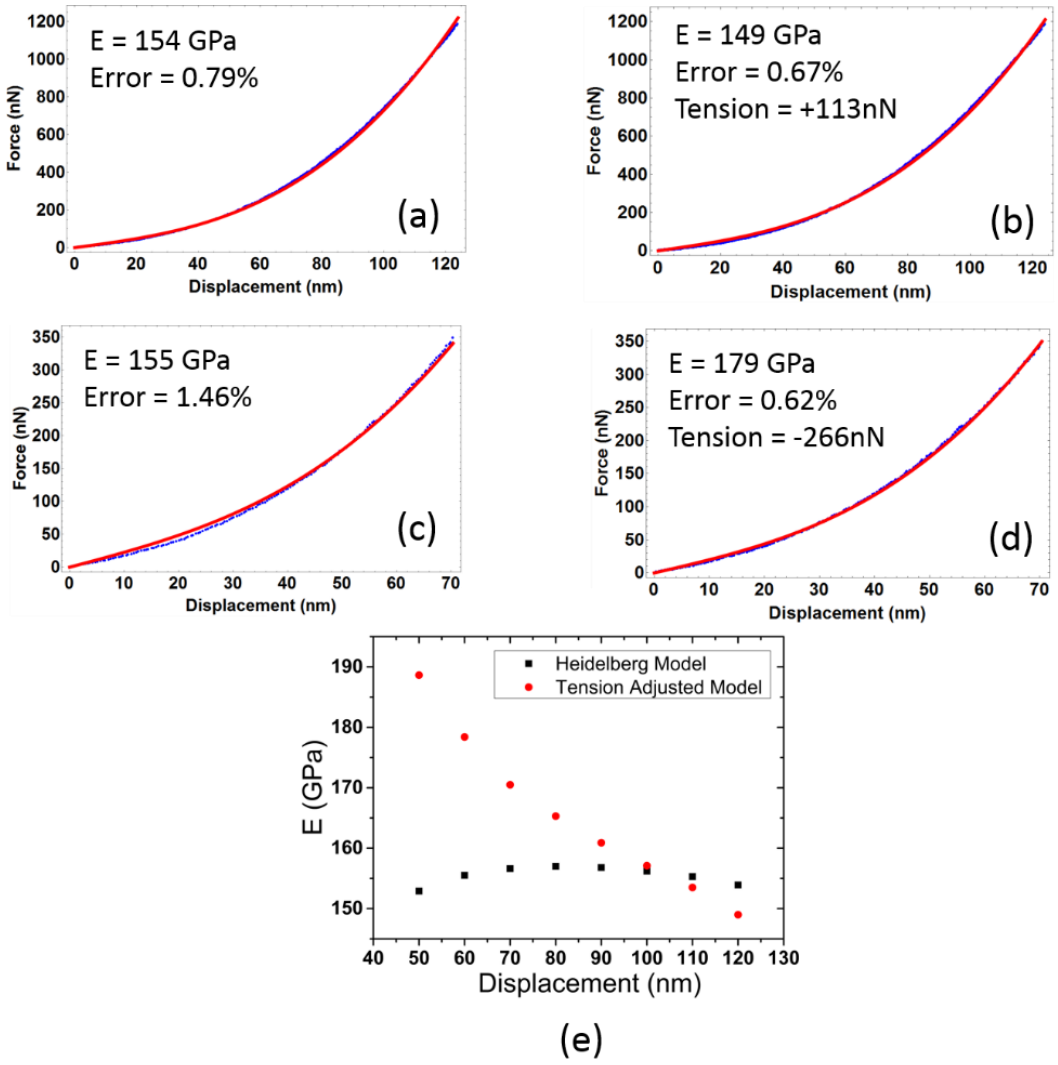

Figure 4.6: (a), (c) Fit of the Heidelberg model to the *F-d* response of a 62 nm diameter SiNW that was not affected by an initial residual stress fit to displacements of 120 nm and 70 nm. (b), (d) Fit of the tension-adjusted model to the same data as (a) and (b). (e) Variation of Young's modulus with fitting range for both the Heidelberg and tension-adjusted models.

Again, it is clear that the tension-adjusted model has difficulties when used to extract Young's modulus and residual tension for a NW affected by a residual stress. Occasionally, it is possible for both the Heidelberg model and the tension-adjusted models to provide consistent results and to be independent of fitting range. As shown in Figure 4.7 (a) and (b), both the Heidelberg model and the tension-adjusted model accurately fit the *F-d* response for this SiNW, indicating that it has not been affected by an initial residual stress. Figure 4.7 (e) shows that for this particular NW the extraction of Young's modulus using both models is independent of fit range. However, for the majority of NWs measured, the Young's modulus extracted from the tension-adjusted model is dependent on the fitting range.

For most cases, the tension-adjusted model does not provide consistent results due to the presence of minor experimental noise in the measurement. In Figure 4.6 (c) it can be observed that the error in the fit of the data to the Heidelberg model at lower displacements (1.46%) is almost a factor of two times greater than the error in the fit at larger displacements (0.79%). This contrasts with the fit of the Heidelberg model in Figure 4.7 (c) where the error in the fit of the data to the model at small displacements (0.67%) is comparable to that at larger displacements (0.51%). The error in the fits are obtained from the residuals of the fit of the model to the *F-d* data.

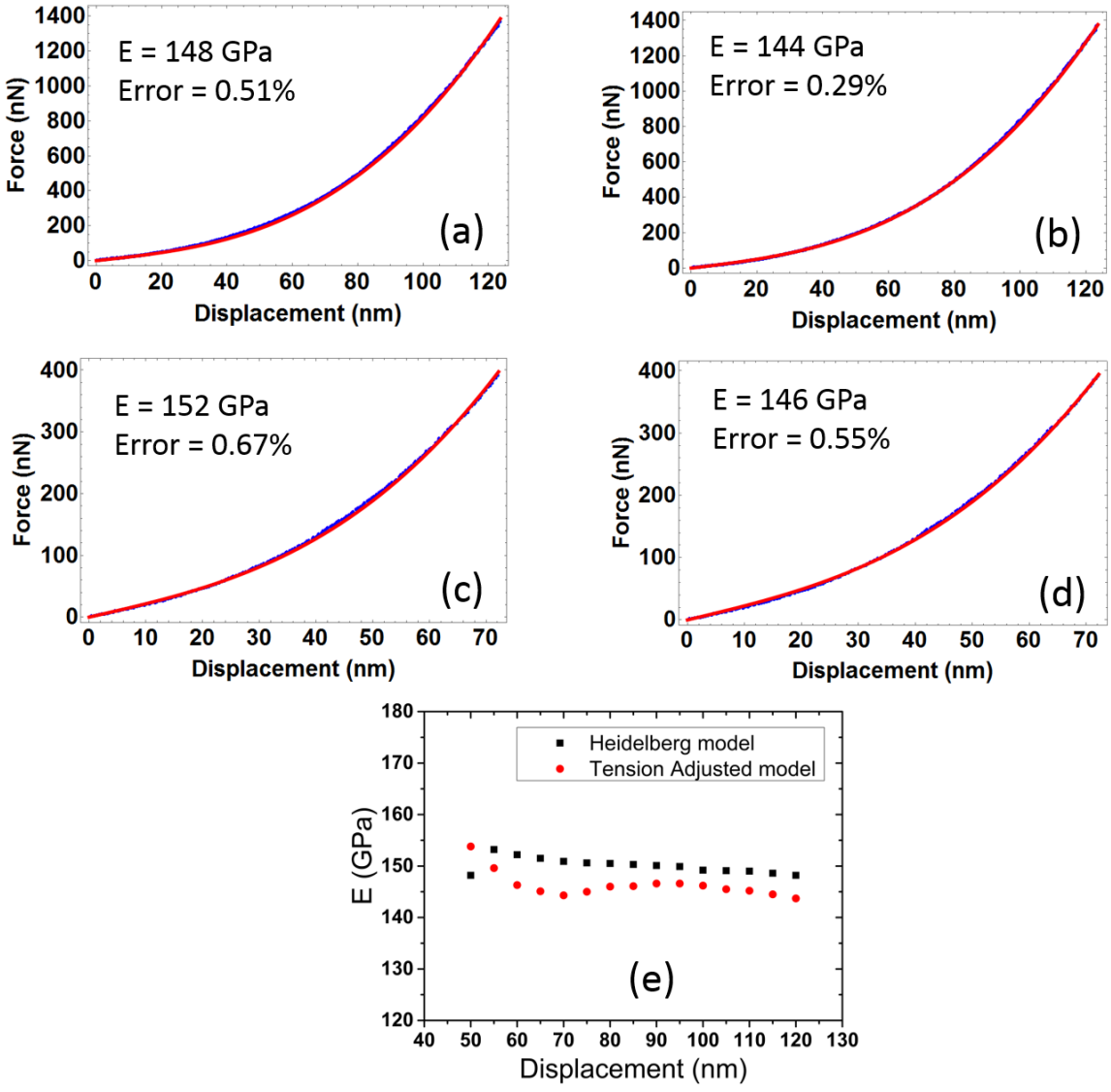

Figure 4.7: (a), (c) Fit of the Heidelberg model to the *F-d* response of a 54 nm diameter SiNW that was not affected by an initial residual stress fit to displacements of 120 nm and 70 nm. (b), (d) Fit of the tension-adjusted model to the same data as (a) and (b) showing the consistency of the fits over varying fitting ranges. (e) Variation of Young's modulus with fitting range for both the Heidelberg and tension-adjusted models.

The tension-adjusted Heidelberg model provides good quality fits with low residuals < 0.8% for the majority of data sets. This is because this model simultaneously fits for two variables, Young's modulus and residual stress. Therefore, these two degrees of freedom allow it more flexibility to fit to the shape of the *F-d* curves. The Heidelberg model however, only has one degree of freedom as it fits only for the Young's modulus. Therefore, it is more constrained in its fitting procedure and any noise in the experiment can be more easily detected. In such cases when there is minor experimental noise the Heidelberg model is a more robust model and is independent of fitting range. This contrasts with the tension-adjusted Heidelberg model which is sensitive to experimental noise making the extraction of Young's modulus problematic. It is difficult to carry out an experiment with 100% accuracy and for these measurements experimental deviations pose problems in the determination of the Young's modulus of NWs affected by residual stress in a doubly-clamped beam configuration. Therefore, it is advised that to correctly determine the material characteristics of doubly-clamped NWs it is important that either; (i) the NW is free of residual stress and analysed using the Heidelberg model, or (ii) a different approach used to determine the NWs mechanical properties.

4.3 Conclusion

It has been demonstrated that when using the doubly-clamped beam model adjusted to account for an initial residual tension caution should be exercised. Despite the tension-adjusted model fitting the experimental data accurately, the extraction of Young's modulus and initial tension can be problematic. This is because there are two parameters; Young's modulus and initial tension that are being fitted for simultaneously which makes the model sensitive to variations in the *F-d* curve. When there is experimental noise in conducting the measurement the tension-adjusted model recognises this incorrectly as a change in Young's modulus and or residual tension. It is difficult to carry out the experiment with close to 100% accuracy as it is likely that there will always be experimental variances. These experimental variations do not impact the original Heidelberg model significantly because it is only fitting for one parameter, the modulus, thus reducing its sensitivity to minor changes in the *F-d* curve. Therefore, when analysing the Young's modulus, it is important to deposit and clamp NWs over trenches without inducing residual stresses and analyse them using the Heidelberg (zero-residual stress) model.

4.4 References

(1) Hudson, S. D.; Zhurov, V.; Grbić, V.; Grbić, M.; Hutter, J. L. Measurement of the Elastic Modulus of Spider Mite Silk Fibers Using Atomic Force Microscopy. *J. Appl. Phys.* **2013**, *113*, 1–7.

(2) Heidelberg, A.; Ngo, L. T.; Wu, B.; Phillips, M. A.; Sharma, S.; Kamins, T. I.; Sader, J. E.; Boland, J. J. A Generalized Description of the Elastic Properties of Nanowires. *Nano Lett.* **2006**, *6*, 1101–1106.

(3) Wu, B.; Heidelberg, A.; Boland, J. J.; Sader, J. E. Microstructure-Hardened Silver Nanowires. *Nano Lett.* **2006**, *6*, 468–472.

(4) Wen, B.; Sader, J. E.; Boland, J. J. Mechanical Properties of ZnO Nanowires. *Phys. Rev. Lett.* **2008**, *101*, 1–4.

(5) Ngo, L. T.; Almecija, D.; Sader, J. E.; Daly, B.; Petkov, N.; Holmes, J. D.; Erts, D.; Boland, J. J. Ultimate-Strength Germanium Nanowires. *Nano Lett* **2006**, *6*, 2964–2968.

(6) Jing, G. Y.; Duan, H. L.; Sun, X. M.; Zhang, Z. S.; Xu, J.; Li, Y. D.; Wang, J. X.; Yu, D. P. Surface Effects on Elastic Properties of Silver Nanowires: Contact Atomic-Force Microscopy. *Phys. Rev. B - Condens. Matter Mater. Phys.* **2006**, *73*, 1–6.

(7) Paulo, A. S.; Bokor, J.; Howe, R. T.; He, R.; Yang, P.; Gao, D.; Carraro, C.; Maboudian, R. Mechanical Elasticity of Single and Double Clamped Silicon Nanobeams Fabricated by the Vapor-Liquid-Solid Method. *Appl. Phys. Lett.* **2005**, *87*, 1–3.

(8) Varghese, B.; Zhang, Y.; Dai, L.; Tan, V. B. C.; Lim, C. T.; Sow, C.-H. Structure-Mechanical Property of Individual Cobalt Oxide Nanowires. *Nano Lett.* **2008**, *8*, 3226–3232.

(9) Ni, H.; Li, X.; Gao, H. Elastic Modulus of Amorphous SiO_2 Nanowires. *Appl. Phys. Lett.* **2006**, *88*, 1–3.

(10) Yaish, Y. E.; Calahorra, Y.; Shtempluck, O.; Kotchetkov, V. Three-Point Bending Analysis of Doubly Clamped Silicon Nanowire Beams; Young's Modulus, Initial Stress, and Crystal Orientation. *J. Appl. Phys.* **2015**, *117*, 1–11.

(11) Calahorra, Y.; Shtempluck, O.; Kotchetkov, V.; Yaish, Y. E. Young's Modulus, Residual Stress, and Crystal Orientation of Doubly Clamped Silicon Nanowire Beams. *Nano Lett.* **2015**, *15*, 2945–2950.

5

CANTILEVER BEAM APPROACH

5.1 Introduction

As discussed in chapter 3, a nanowire (NW) in a doubly-clamped beam configuration can be subjected to an initial residual stress resulting from solvent interactions or other aspects of the fabrication process. Chapter 4 demonstrated that although the Heidelberg (zero-residual stress) model[1] for a doubly-clamped beam can be adjusted to account for residual stresses, the estimation of the Young's modulus (E) and elimination of the influence of the residual stress (α_0) is problematic. It is paramount that the scientific community are aware of these potential difficulties to prevent incorrect application of the tension-adjusted Heidelberg model[2,3] to account for residual stress. In the design of mechanical devices, it is important that the correct Young's modulus can be determined and is not influenced by the presence of residual stresses. The problem of separating the two contributions, Young's modulus and residual stress from the model arises due to their co-dependence on the wire displacement, particularly at small values. This problem is further compounded by the finite range of most data sets. These limitations coupled with minor experimental noise in the data inhibits the separation of Young's modulus and residual stress.

In chapter 4, it has been demonstrated that the tension-adjusted Heidelberg model is highly sensitive to minor noise in the experimental measurement, however this noise does not affect the extraction of Young's modulus when there is no residual stress in the wire and when using the Heidelberg (zero-residual stress) model. However, it can be problematic when it is necessary to extract both parameters E and α_0. Therefore, in order to correctly extract the mechanical properties of a doubly-clamped NW it is necessary that the experiment is not influenced by an initial residual stress in which case an alternative method should be applied.

When a wire is fabricated in a doubly-clamped beam configuration any existing residual stresses can become fixed in the wire[2,4]. It is here where the problem arises. If the

wire was singly-clamped at one end it would not be possible for an axial residual stress to remain in that wire. Once the solvent evaporates the wire should simply relax to a zero-stress state. Take for example an elastic band. If you hold it at both ends (doubly-clamped) and stretch it, you can subject the elastic band to a "residual stress" analogous to what we observe in certain NWs. If the elastic band is released at one end (singly-clamped) the band will return to its original length (provided that it was only stretched elastically) and the "residual stress" will be released. We now explore the possibility of measurements on singly-clamped wires, i.e., cantilever beam structures.

5.2 Cantilever Beam Structures

In 1997 Wong *et al.*[5] used atomic force microscopy (AFM) to measure the mechanical properties of silicon carbide (SiC) nanorods and multiwall carbon nanotubes. In this paper the authors used molybdenum disulphide substrates because of their low coefficient of friction and pinned the nanorods on one end using silicon monoxide (SiO) pads.

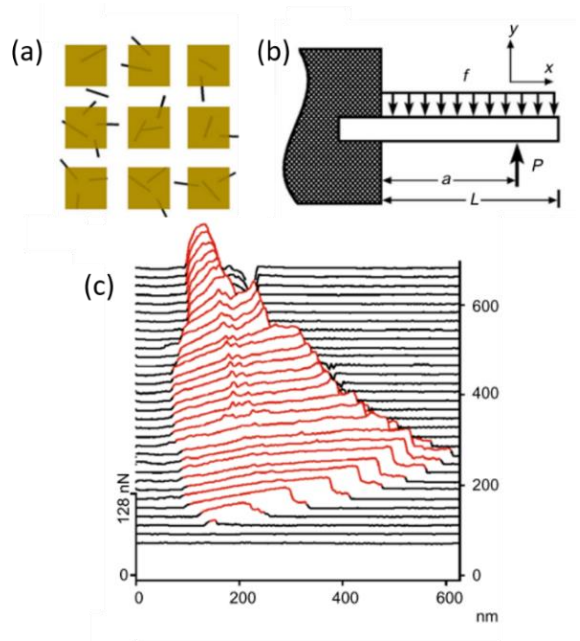

Figure 5.1: (a) Schematic of carbon nanotubes pinned to a MoS_2 substrate using SiO deposited pads. (b) Schematic of a pinned beam with a free end. The beam of length (L) is subjected to a load P at x = a. (c) *F-d* responses for a 32.9 nm diameter carbon nanotube with a normal load of 16.4 nN loaded at multiple locations along its length. The image is tilted 30˚ and displays only 30 of 300 curves for clarity[5].

The nanobeams were laterally loaded at multiple positions along their length, with a force-displacement (*F-d*) curve produced at each point, this allowed Young's modulus to be determined. Figure 5.1 shows a schematic of the experiment and the *F-d* response observed. The beam could also be loaded to fracture to determine the fracture strength of the material. Using this technique, the authors could qualitatively extract the mechanical properties in the absence of residual stress. It was found that the average multiwall carbon nanotube modulus

was 14.2 ± 8 GPa and the largest SiC modulus observed was 53.4 GPa. Since this work, there have been numerous measurements on cantilever beam nanorods/nanowires to extract mechanical properties whether by resonant experiments[6,7] or by AFM techniques[8,9].

In this chapter, we demonstrate that the residual stress in a doubly-clamped beam can be removed. This is accomplished using a focused ion beam (FIB) to section the suspended wire into two singly-clamped cantilevers, each of which is well described by conventional Euler-Bernoulli beam mechanics and yields a modulus that agrees with the expected value. Using this technique, we can also investigate the accuracy of the assumed pinning length for NWs that are adhered to the surface by surface adhesion without the use of Pt-EBID to define mechanical clamps. From this analysis, the importance of physical mechanical clamps to define the beam length in doubly-clamped beam experiments is demonstrated.

5.3 Experimental Method

The fabrication techniques for a doubly–clamped beam have been previously discussed in chapters 2 and 3 along with the 3-point mechanical measurement. Prior to depositing NWs, the SiO_2 surface was coated with 10 nm thermally evaporated gold (Au) metal. The purpose of the metal was to create a conducting substrate which dissipates any charge build up during the FIB experiments. The use of solvent or dry deposited wires was dependant on whether wires with or without an initial residual stress were required. After mechanical measurements were made, the doubly-clamped wires were prepared for sectioning by focused ion beam.

5.3.1 Focused Ion Beam Cutting of Nanowires

The substrate was loaded into the Auriga crossbeam FIB/SEM. The wire was sectioned by defining a path for gallium ions to mill the wire in two parts using the FIB design software. An example of a NW cantilever beam is shown in Figure 5.3 (b). An acceleration voltage of 30 kV was used with a probe current of 2 pA. The substrate was then returned to the AFM and the wire realigned and reimaged. One side of the FIB sectioned wire was loaded at numerous points along its length and the change in lateral signal recorded. The AFM technique used here is similar to that for the 3-point bending experiment used in chapter 3, but differs in that the NW is loaded at different positions along its length and not only at its centre-point. As before, the tip was calibrated to ensure the calibration parameters were established.

5.4 Doubly-Clamped Beam Analysis on an Unclamped AgNW

In chapter 3, it was determined that when AgNWs are solvent deposited they are strongly adhered to a SiO_2 surface. This strong adhesion also allows residual stresses to become fixed in the AgNWs. Therefore, these measurements were performed on NWs which were adhered solely to the SiO_2 substrate by surface adhesion as the fabrication time involved was reduced. As a reminder, Figure 5.2 (b) and (c) shows the *F-d* response observed when a NW is affected by an initial residual stress and illustrates how the data is poorly described by the Heidelberg (zero-residual stress) model.

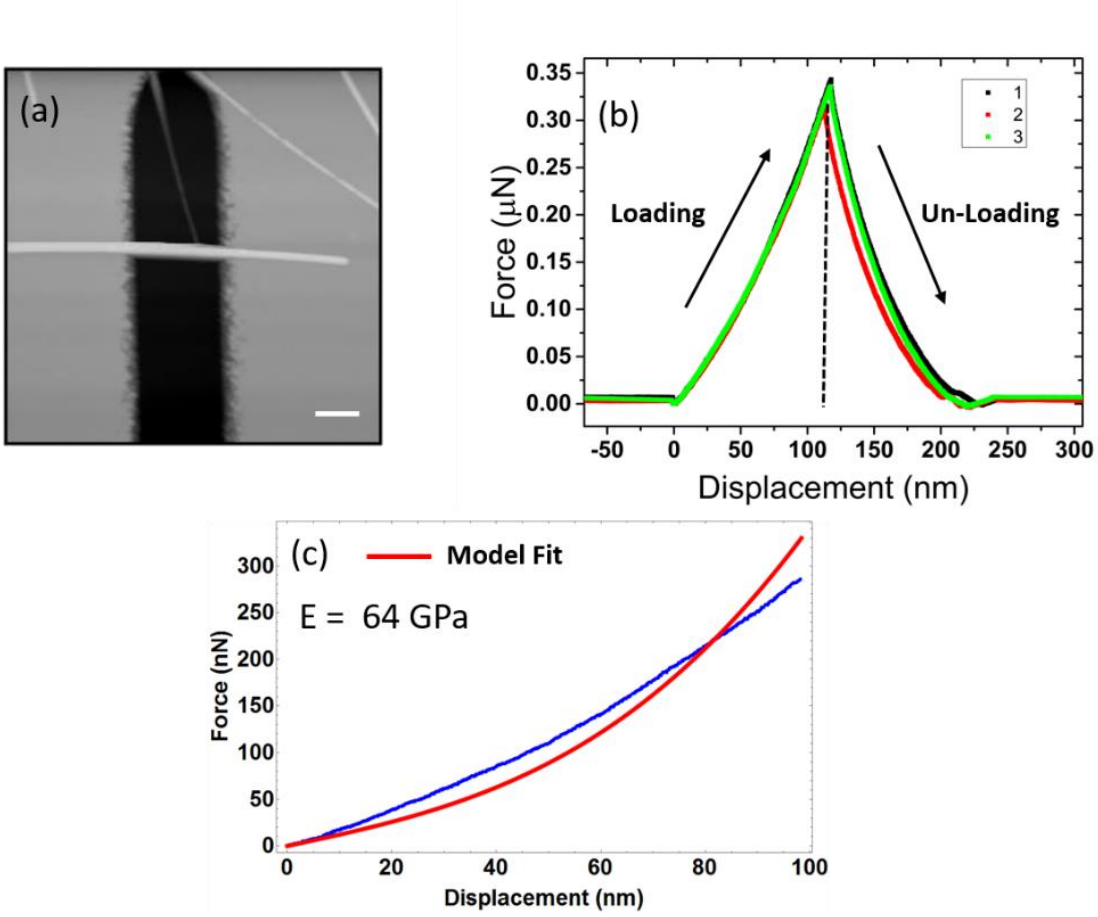

Figure 5.2: (a) AgNW suspended over a trench with substrate adhesion pinning the wire to the substrate. (b) Repeatable *F-d* curves for AgNW in (a). (c) Fit of one of the loading curves in (b) to the Heidelberg doubly-clamped beam model.

As outlined in the previous chapter the tension-adjusted Heidelberg model can be problematic when analysing NWs that are subjected to an initial residual stress. The initial residual stress affects the rigidity of the beam, which results in an enhancement of the beam's apparent stiffness. Figure 5.2 (c) shows that at displacements less than 80 nm a greater force is required to push the beam by a given displacement - compared to the predictions made by the

Heidelberg model. By sectioning the beam the residual stress is removed which allows for a stress-free analysis.

5.5 Removal of Residual Stress and Euler-Bernoulli Cantilever Beam Analysis

One way to remove the residual stress from a doubly-clamped wire is to use a focused ion beam of gallium ions to section the wire in half as shown in Figure 5.3 (b). This creates a singly-clamped cantilever beam, using conventional Euler-Bernoulli beam mechanics, which will now be discussed, the correct modulus of the NW under investigation can be determined.

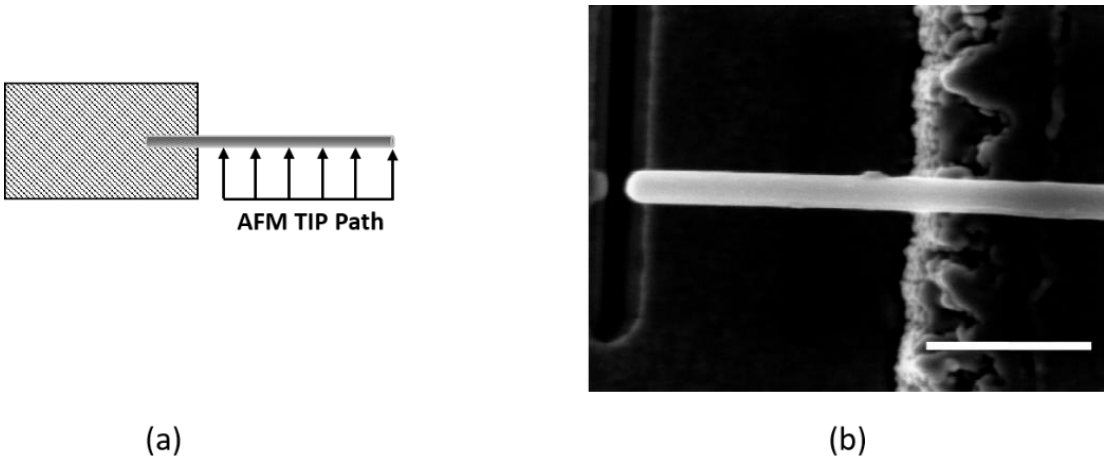

Figure 5.3: (a) Schematic of a singly-clamped NW beam. (b) SEM image of a singly-clamped NW beam, scale bar 500 nm.

5.5.1 Euler-Bernoulli Cantilever Beam Analysis

Euler-Bernoulli cantilever beam analysis has been around since the 18th century[10]. However, it has not been used with the intentions of analysing NWs which have been subjected to residual stresses in a doubly-clamped beam configuration. Figure 5.4 shows the arc of the neutral axis of a beam subjected to bending within the elastic range. The neutral axis is the unique region where the final deformed length is the same as the initial length. The neutral axis does not always have to be at the centre of the beam and indeed can vary if the beam is made up of composite materials[11].

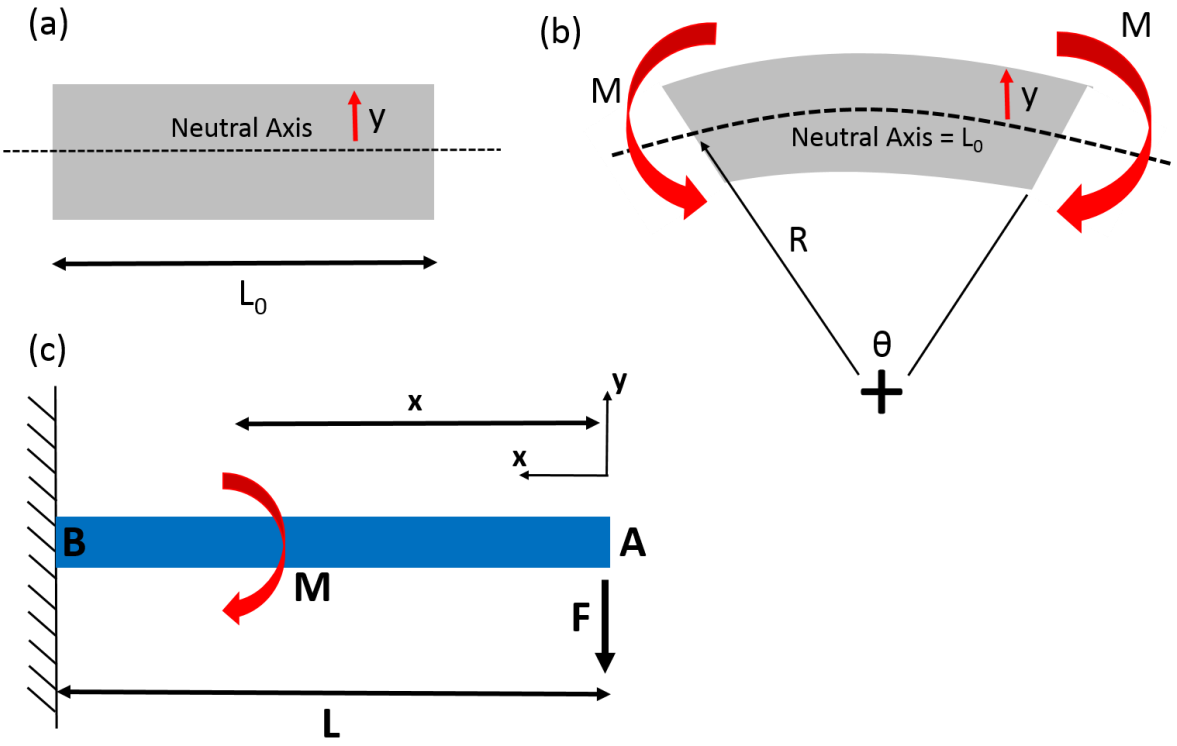

Figure 5.4: Schematic of a beam before (a) and after bending (b) showing the neutral axis in both cases. (c) Cantilever beam with a point load at its free end.

The curvature of the neutral surface may be expressed as;[12]

$$\frac{1}{R} = \frac{M}{EI} \tag{5.1}$$

where R is the radius of curvature, M is the bending moment, E is the Young's Modulus and I is the moment of inertia of the cross section. The bending moment and the radius of curvature vary depending on the position at which the loading occurs, therefore we write;

$$\frac{1}{R} = \frac{M(x)}{EI} \tag{5.2}$$

When we consider a cantilever beam AB, of length L subjected to a concentrated load F at its free end A (see Figure 5.4 (c)). $M(x) = -Fx$, where x denotes the distance from the right end of the beam, so we have;

$$\frac{1}{R} = -\frac{Fx}{EI} \tag{5.3}$$

This shows that the curvature of the neutral axis varies with *x*, from zero at *A* to $-FL/EI$ at *B*.

From elementary calculus, the curvature of a plane curve at a point on a curve may be expressed as;

$$\frac{1}{R} = \frac{\frac{d^2y}{dx^2}}{[1 + (\frac{dy}{dx})^2]^{\frac{3}{2}}} \tag{5.4}$$

Where dy/dx and d^2y/dx^2 are the first and second derivatives of the function $y(x)$ represented by that curve. But, for small beam displacements dy/dx is very small so we can write;

$$\frac{1}{R} = \frac{d^2y}{dx^2} \tag{5.5}$$

Then by substituting $1/R$ from (5.5) into (5.3) we get;

$$\frac{d^2y}{dx^2} = -\frac{Fx}{EI} \tag{5.6}$$

Integrating we get;

$$EI\frac{dy}{dx} = -\frac{Fx^2}{2} + C_1 \tag{5.7}$$

Where C_1 is a constant of integration.

Integrating again we get;

$$EIy = -\frac{Fx^3}{6} + C_1x + C_2 \tag{5.8}$$

The constants of integration can be found from the boundary conditions;

$$\begin{gathered} at\ x = L, y = 0\ (no\ deflection) \\ at\ x = L, \frac{dy}{dx} = 0\ (gradient\ horizontal) \end{gathered} \tag{5.9}$$

Solving for C_1 and C_2; $C_1 = FL^2/2$ and $C_2 = -FL^3/3$ and substituting back in to (5.8) we obtain;

$$y = -\frac{F}{6EI}(x^3 - 3L^2x + 2L^3) \tag{5.10}$$

Deflection at the free end is obtained by setting $x = 0$, to give;

$$y = \frac{FL^3}{3EI} \tag{5.11}$$

Rearranging we find that;

$$F^{-1/3} = (3EId)^{-\frac{1}{3}}.(L_c + \Delta L) \tag{5.12}$$

where L_c+ΔL is the length of the NW from its pinned end to its free end; L_c is the nominal wire length from its pinned end to the load point, and ΔL is the required adjustment to give the true length. The latter length, ΔL, is fixed for any given wire because the wire pinning point remains fixed as the load point is varied along the wire segment. This formula can be used to assess the accuracy of the length, L, used in the doubly-clamped beam experiments. Plotting $F^{\frac{-1}{3}}$ *vs* L_c the true Young's modulus can be obtained from the slope of the linear fit to the data. An additional benefit of analysing the data this way, is that it is not necessary to know the exact pinning length, L_c+ΔL, of the wire. Inaccuracies in the pinning length affects where the data intercepts the x-axis but it does not affect the slope, the parameter used to obtain the modulus.

In circumstances where surface adhesion pins a wire, the wires do not need to be mechanically clamped using Pt-EBID. This eliminates potential contamination of the wire surface during the EBID process. Where a wire is not affected by an initial residual stress both the doubly-clamped and singly-clamped beam methods can be used to obtain Young's modulus and a comparison can be made to evaluate the validity of both approaches.

The 64 nm AgNW examined in Figure 5.2 as a doubly-clamped beam will now be investigated in greater detail. The *F-d* response for this NW after it has been sectioned in half and analysed as a cantilever beam is shown in Figure 5.5. Figure 5.5 (b) shows ten *F-d* curves, recorded at different positions along the left-hand side of the wire in Figure 5.5 (a). The lowest force measured is from the load point furthest from the fixed end, with the force increasing for each load closer to the fixed point. Figure 5.5 (c) shows an individual loading and unloading curve. From the curve, it can be observed that at larger displacements the curve becomes non-linear. This is due to slippage between the AFM tip and the NW, which is unavoidable in a singly-clamped cantilever configuration.

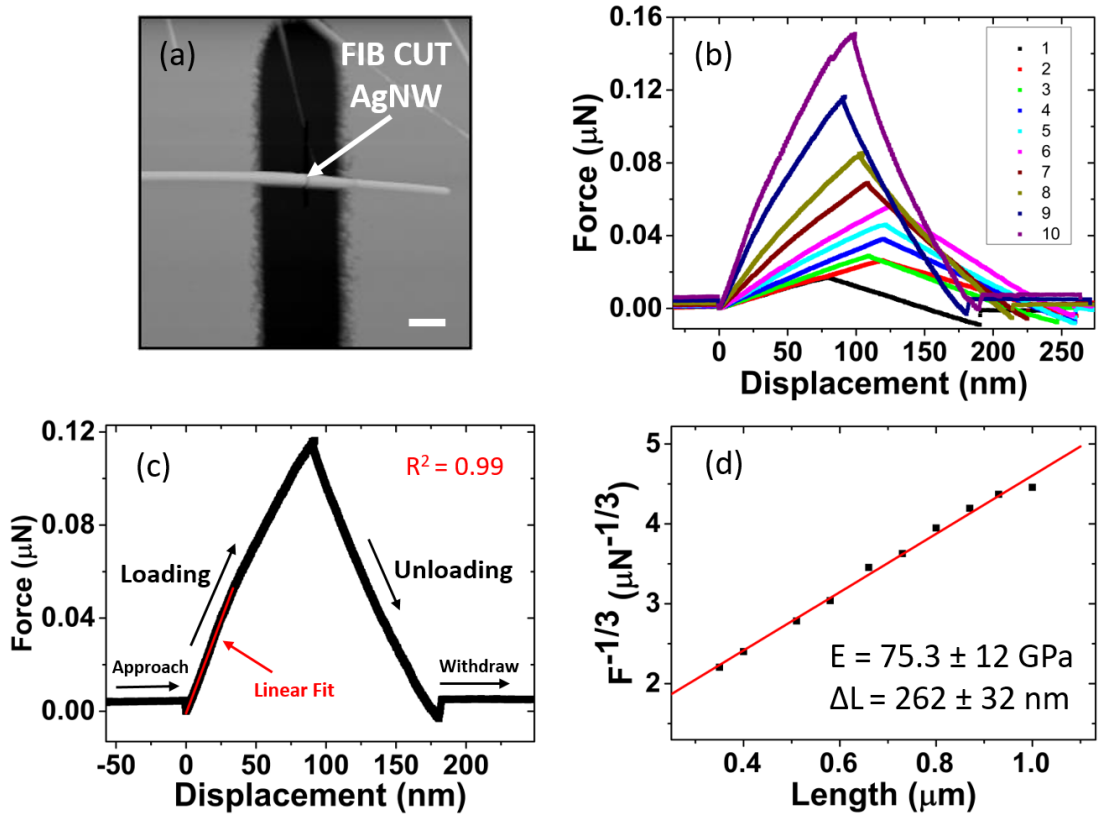

Figure 5.5: (a) AgNW from Figure 5.2 that has been sectioned using a focused beam of gallium ions, scale bar 1 μm. (b) *F–d* response from loading the left-hand side of the AgNW in (a) at different points along the wire. (c) Loading and unloading curve of a cantilevered NW. (d) $F^{-1/3}$ vs *L* for the NW loaded at ten positions along its length.

However, the force measurements used for Figure 5.5 (d) are only recorded from the linear portion of the curves, as shown in Figure 5.5 (c), where the R^2 fit is 0.99. Again, as was the case in the doubly-clamped beam experiments the NWs are loaded and unloaded within their elastic limits in order to prevent plastic deformation. From the slope of the graph in Figure 5.5 (d) the correct Young's modulus of the wire without any residual stress can be extracted. For this wire a Young's modulus of 75 ± 9 GPa was obtained, comparable with the bulk value for silver.

The two largest sources of error in the experiment are the measurement of the radius of the NW and the error in the slope of the plot in Figure 5.5 (d). They scale respectively as $E \propto 1/r^4$, $E \propto 1/m^3$. To ensure an accurate measurement of the wire diameter, the diameter was measured by AFM and verified with SEM measurements as shown in Figure 5.6. Both measurement techniques are in good agreement with one another. Ten measurements were taken along the length of the NW to give an accurate diameter measurement and standard

deviation. For the AFM analysis, it was necessary to measure the diameter of the NW where the NW was directly on top of the Au surface as opposed to over the trench.

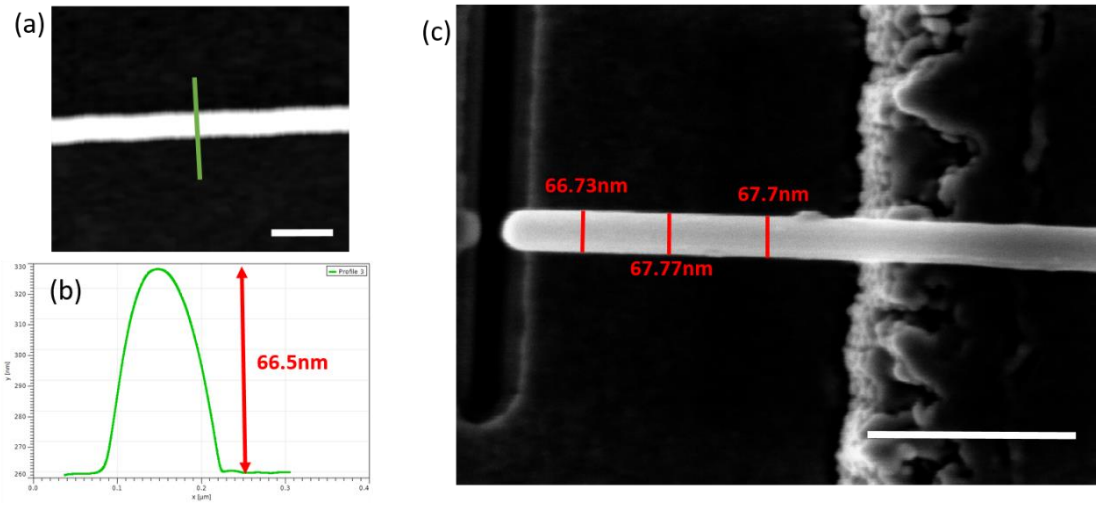

Figure 5.6: (a) AFM image of a AgNW. (b) Line profile of green line in (a), the height of the NW is measured from the accurate z-piezo height. (c) SEM image of the same AgNW in (a) with the NW diameter measured using Image J software. All scale bars 500 nm.

As previously noted, an additional benefit of this method is not requiring a value for the exact pinning point of the NW to the surface. The fitting procedure can account for any inaccuracies due to an incorrect assumption of the pinning length. From the intercept of the linear fit with the x-axis the overestimated/underestimated length (ΔL) can be determined. From the plot intercept in Figure 5.5 (d) it was determined that the pinning length is $L_c+\Delta L = 1362$ nm. The length, L_c, from the edge of the trench to the unpinned end of the cantilevered wire is 1100 nm. The difference between the two values indicates that the wire is pinned a distance 262 nm farther in from the edge of the trench. Note - this only accounts for one side of the doubly-clamped beam, there is also a similar inaccuracy in estimating the pinning length at the other side of the doubly-clamped beam. It is important to note therefore that in the majority of cases the pinning length, L, of a wire without mechanical clamps is greater than the measured length of the wire that extends over the trench. This highlights the importance of physically clamping NWs directly at the edge of a trench using Pt-EBID for doubly-clamped beam experiments. For the doubly-clamped beam experiment $F \propto 1/L^3$ and so inaccuracies in defining the pinning length will introduce large errors into the calculation of Young's modulus. An incorrect estimate of the pinning length only affects the magnitude of the modulus extracted, see Figure 6.5, chapter 6. It does not affect the quality of the fits to the

Heidelberg (zero-residual stress) model[1] and it cannot and does not help to account for or explain the apparent levels of residual stress in the wires.

The NW under study is in fact over 20 μm long and is suspended across several trenches. Figure 5.7 (a) illustrates a different section of the same wire as in Figure 5.5 (a). By analysing this wire using Euler-Bernoulli cantilever beam analysis a Young's modulus of 91 ± 8 GPa is obtained which is within the error limits for the initial measurement on the same wire. In this case the length had been underestimated by 185 nm, as shown in Figure 5.7 (d).

This method was also used to extract the Young's modulus values for silicon nanowires (SiNWs). As was discovered in chapter 3, these wires were not adhered to the substrate so additional EBID clamps were deposited to make them mechanically robust. These SiNWs have a native oxide which varies between 3-7 nm in thickness. This requires the use of a core-shell model (5.13) to correctly extract the Young's modulus of the silicon core. An assumed value of 4 nm is used as the oxide thickness as it is not possible to measure the oxide thickness for each individual wire measured. A TEM image of the oxide on a SiNW can be observed in Figure 5.8. The effective modulus is as follows;[4]

$$E_{eff} = E_{shell} + (E_{core} - E_{shell})(\frac{d_{core}}{d_{total}})^4 \tag{5.13}$$

where E_{shell} = 70 GPa[13]

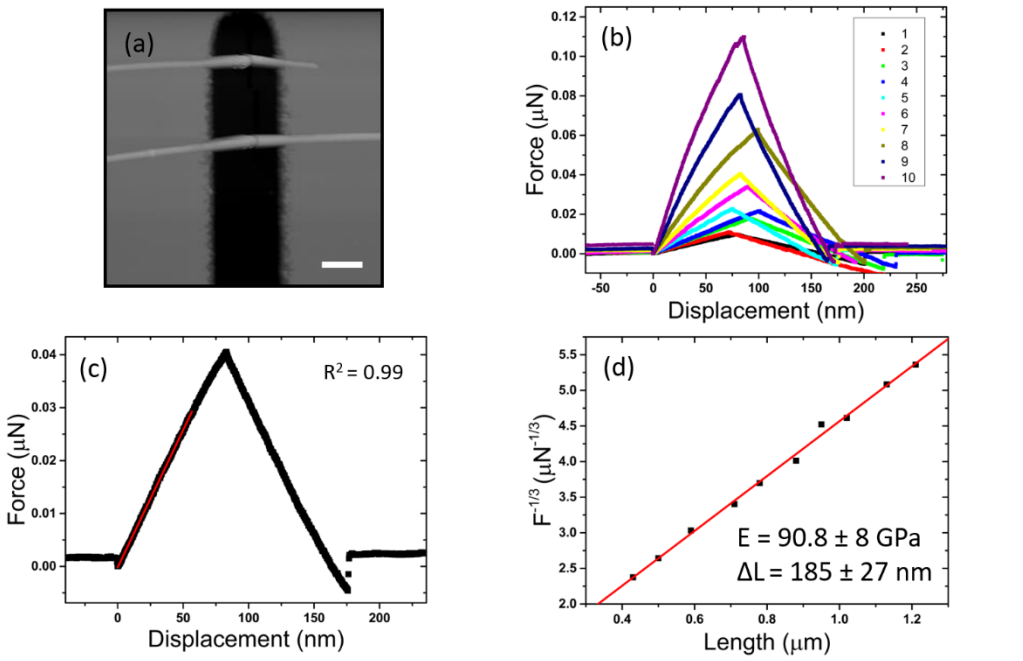

Figure 5.7: (a) AFM image of a FIB sectioned AgNW, scale bar 1 μm. (b) Loading and unloading curves of NW in (a) at different positions along its length. (c) Linear fit to one of the loading curves in (b). (d) Plot of $F^{-1/3}$ vs L to determine Young's modulus.

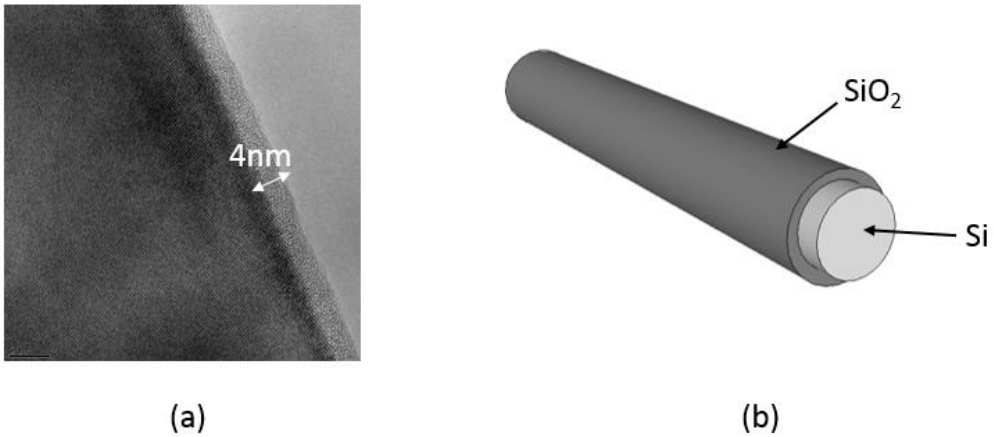

Figure 5.8: (a) TEM image of the oxide thickness on a SiNW. (b) Schematic of the core shell structure of a SiNW with a SiO_2 layer.

Figure 5.9 illustrates the same Euler-Bernoulli cantilever beam experiment carried out for a SiNW and Figure 5.10 shows the collective Young's moduli obtained for 16 AgNWs and 16 SiNWs. The values obtained in this work for both AgNWs[14,15] and SiNWs[1,16,9] are comparable to previous measurements that have been reported in the literature. The scatter in the data for the SiNWs may be attributed to the varying surface oxide thickness. Oxide thicknesses varied from 3-7 nm as shown in Figure 5.11 which will introduce scatter to the data. As mentioned previously in chapter 3 the AgNWs are pentagonally twinned along their axis[17], as shown in Figure 5.11 (a).

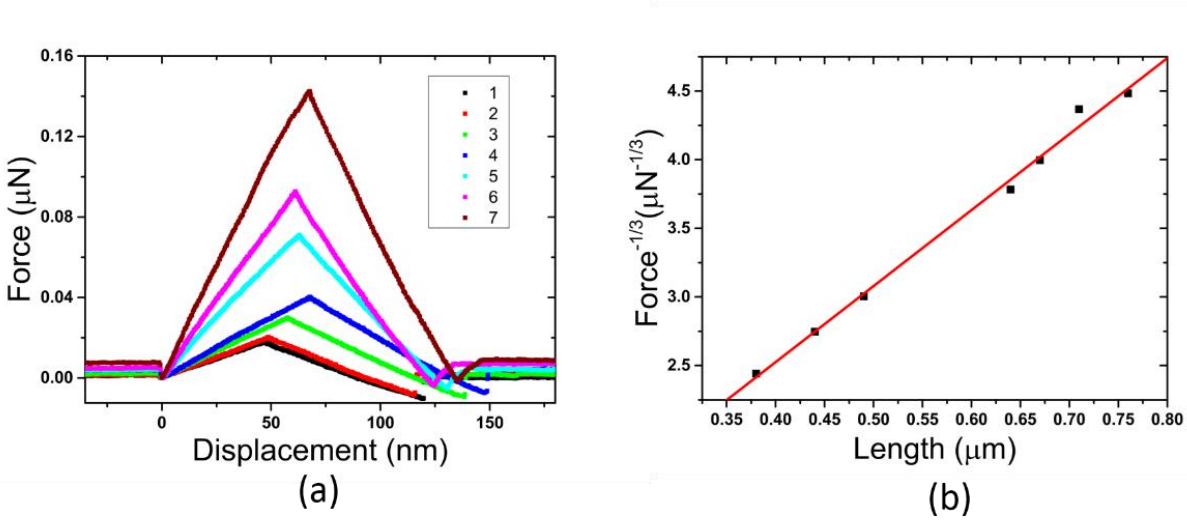

Figure 5.9: (a) *F-d* response for a singly-clamped SiNW. (b) Plot of $F^{-1/3}$ vs L for varying lengths along the length of a SiNW.

A proposed reason for the scatter in the data is that the five twinned facets are unable to bridge the 360 degrees of the wire circumference, as depicted in Figure 5.11 (b). The 7-8° solid angle deficit that results introduces radial strain into the AgNWs. This strain likely varies from wire to wire as pentagonal twins are rarely the same size so that the centre line where the five twins meet is located in a different position for each wire[18].

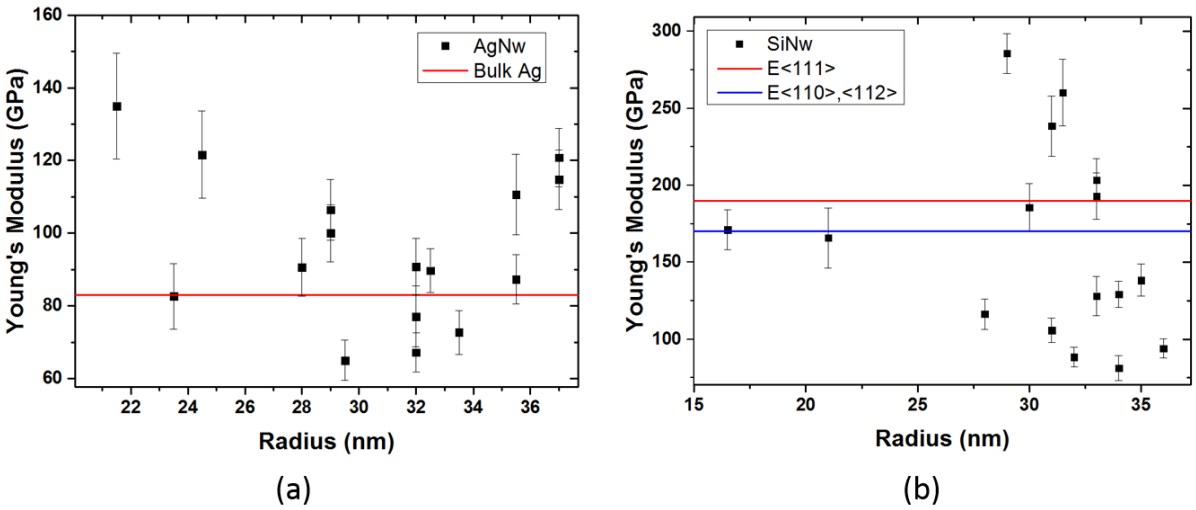

Figure 5.10: Young's modulus values for (a) AgNWs and (b) SiNWs using Euler-Bernoulli cantilever beam analysis.

5.5.2 Determination of Young's Modulus of Tension Free SiNWs using Doubly-Clamped and Cantilever Methods

As shown in chapter 3, SiNWs are not subjected to residual stresses regardless of the deposition method. Therefore, SiNWs represent an excellent system in which to demonstrate that the singly-clamped cantilever and doubly-clamped approaches yield similar results. Note that for these experiments it was essential to clamp the NWs at the edges of the trench so that the wire length (L) was well defined for the doubly-clamped beam experiment. Figure 5.12 (a) and (c), shows fits to the Heidelberg (zero-residual stress) model for two different SiNWs. These wires were pushed to failure using the AFM tip and exhibited brittle fracture, resulting in a clean wire break. The wires also returned to their original position. This allows for the application of Euler-Bernoulli cantilever beam analysis and thus the comparison of both techniques and their ability to extract the correct Young's modulus. Figure 5.12 (b) and (d) show the $F^{-1/3}$ vs L plot for the same SiNWs as in (a) and (c) analysed using Euler-Bernoulli cantilever beam analysis.

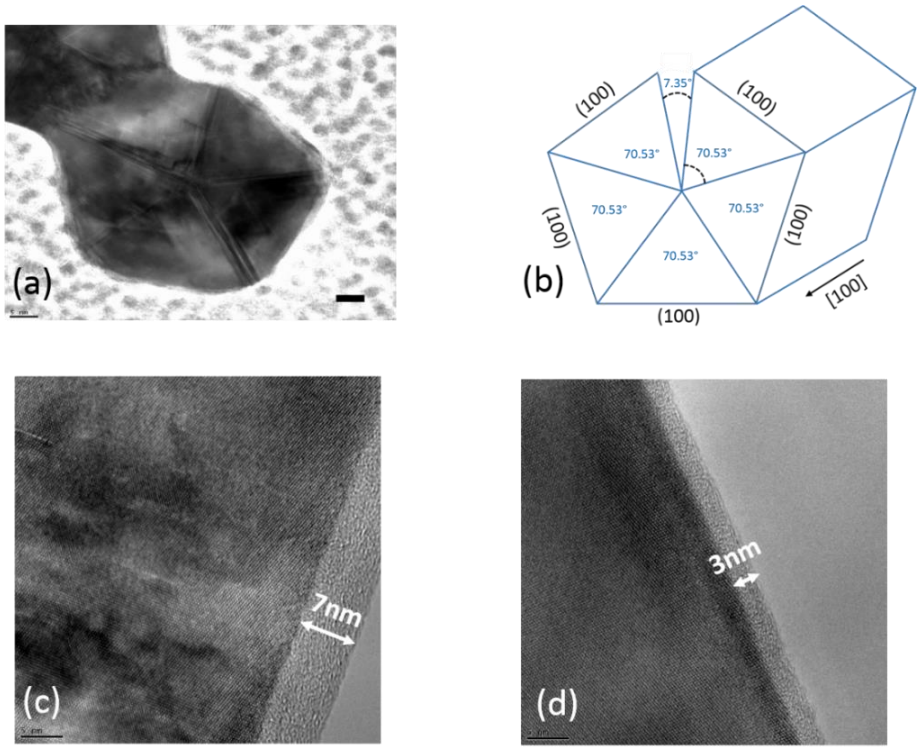

Figure 5.11: (a) TEM cross section of a AgNW displaying pentagonal twinning, scale bar 5 nm. (b) Schematic of the pentagonally twinned NW showing the 7.35° deficiency[19]. (c), (d) TEM images of SiNWs showing surface oxide thicknesses of 7 nm and 3 nm. (TEM courtesy of Dr. Eoin McCarthy).

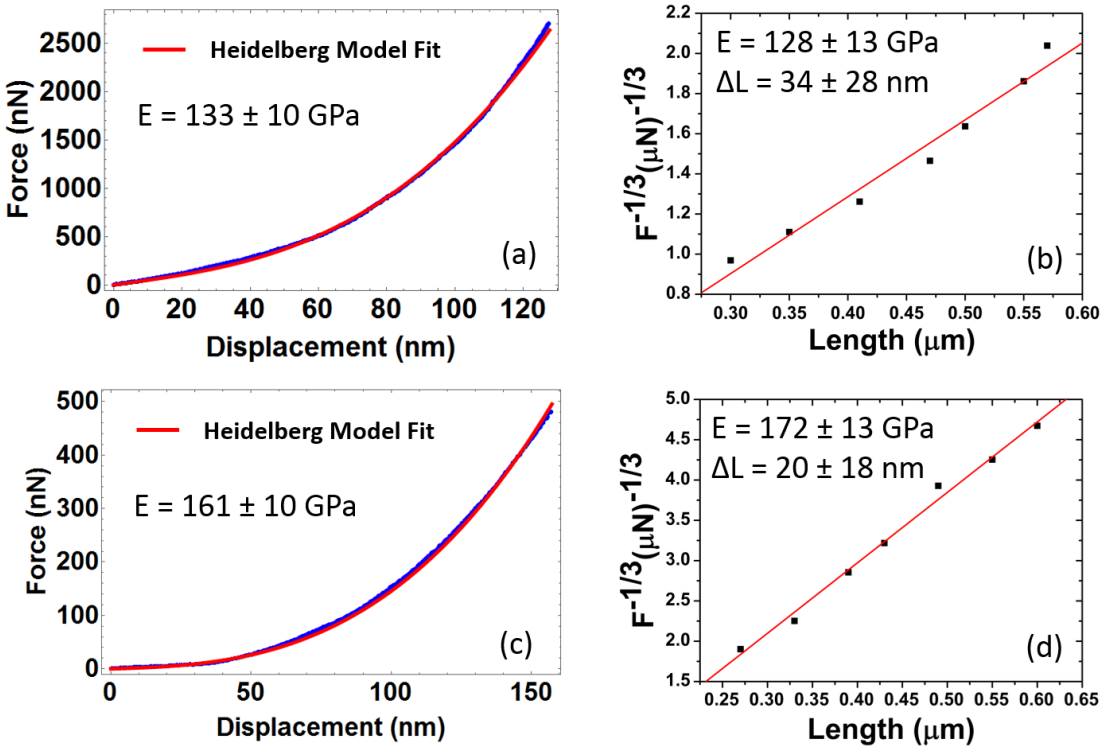

Figure 5.12: (a), (c) Doubly-clamped beam experiment for two different SiNWs that were not affected by an initial residual stress. (b), (d) Cantilever Euler-Bernoulli beam experiment on the same two SiNWs after they had been loaded to fracture.

The Young's modulus obtained by the doubly-clamped beam method for the first SiNW measured was 133 ± 10 GPa. When measured using the cantilever beam method the Young's modulus was 128 ± 13 GPa. The second SiNW had a modulus of 161 ± 10 GPa when measured by the doubly-clamped beam method compared to 172 ± 13 GPa when measured by the cantilever beam method. Both techniques are therefore capable of extracting the same Young's modulus for the same wire within the error. This validates both techniques in their ability to extract reliable values of the Young's modulus for NWs that are not under the influence of an initial residual stress. Furthermore, it shows that the spread in the Young's modulus of the wires is not due to experiment but due to inherent differences in the wires themselves. For the cantilever beam experiments, the inaccuracies in the length, ΔL, were 34 ± 28 nm and 20 ± 18 nm, for the first and second SiNWs respectively. Note - for measurements made without mechanical clamps, inaccuracies were generally > 150 nm. This shows the importance of using EBID clamps to clearly define the correct pinning length, L, for the doubly-clamped beam experiments.

5.6 Conclusion

In previous chapters, it has been outlined how the doubly-clamped analysis of a NW subjected to a residual tension is ill-posed. In order to correctly extract the mechanical properties of a NW, it must be deposited and clamped without the effects of residual tension, or an alternative approach is required to analyse its mechanical properties. It has been demonstrated that the approach taken by Wong *et al.*, can be correctly used on these wires but only after sectioning them with a focused ion beam to create a cantilever structure. Using this approach, Young's modulus values for AgNWs and SiNWs were determined. These were both in good agreement with previous literature results.

The cantilever beam method has an advantage whereby the exact pinning point of the wire to the substrate does not need to be known. From the analysis, it was determined that a NW only adhered to the surface by surface adhesion was not adequately pinned. This emphasised the importance of using physical clamps to clearly define the pinning length for the doubly-clamped beam experiment. Additionally, demonstrated is the validity of the doubly-clamped beam experiment and the cantilever beam experiment. This was achieved by using both techniques on the same individual SiNW which was initially under no residual stress. After analysis, a consistent Young's modulus was obtained by both techniques on the same wire which proves the validity of both methods.

5.7 References

(1) Heidelberg, A.; Ngo, L. T.; Wu, B.; Phillips, M. A.; Sharma, S.; Kamins, T. I.; Sader, J. E.; Boland, J. J. A Generalized Description of the Elastic Properties of Nanowires. *Nano Lett.* **2006**, *6*, 1101–1106.

(2) Hudson, S. D.; Zhurov, V.; Grbić, V.; Grbić, M.; Hutter, J. L. Measurement of the Elastic Modulus of Spider Mite Silk Fibers Using Atomic Force Microscopy. *J. Appl. Phys.* **2013**, *113*, 1–7.

(3) Yaish, Y. E.; Calahorra, Y.; Shtempluck, O.; Kotchetkov, V. Three-Point Bending Analysis of Doubly Clamped Silicon Nanowire Beams; Young's Modulus, Initial Stress, and Crystal Orientation. *J. Appl. Phys.* **2015**, *117*, 1–11.

(4) Calahorra, Y.; Shtempluck, O.; Kotchetkov, V.; Yaish, Y. E. Young's Modulus, Residual Stress, and Crystal Orientation of Doubly Clamped Silicon Nanowire Beams. *Nano Lett.* **2015**, *15*, 2945–2950.

(5) Wong, E. W.; Sheehan, P. E.; Lieber, C. M. Nanobeam Mechanics: Elasticity, Strength, and Toughness of Nanorods and Nanotubes. *Science (80-.).* **1997**, *277*, 1971–1975.

(6) Poncharal, P.; Wang, Z. L.; Ugarte, D.; de Heer, W. A. Electrostatic Deflections and Electromechanical Resonances of Carbon Nanotubes. *Science (80-.).* **1999**, *283*, 1513–1516.

(7) Qin, Q.; Xu, F.; Cao, Y.; Ro, P. I.; Zhu, Y. Measuring True Young's Modulus of a Cantilevered Nanowire: Effect of Clamping on Resonance Frequency. *Small* **2012**, *8*, 2571–2576.

(8) Manoharan, M. P.; Desai, A. V.; Neely, G.; Haque, M. A. Synthesis and Elastic Characterization of Zinc Oxide Nanowires. *J. Nanomater.* **2008**, *2008*, 1–7.

(9) Gordon, M. J.; Baron, T.; Dhalluin, F.; Gentile, P.; Ferret, P. Size Effects in Mechanical Deformation and Fracture of Cantilevered Silicon Nanowires. *Nano Lett.* **2009**, *9*, 525–529.

(10) Vable, M. *Mechanics of Materials*; Second Edi.; Oxford University Press, **2012**.

(11) Eltaher, M. A.; Alshorbagy, A. E.; Mahmoud, F. F. Determination of Neutral Axis Position and Its Effect on Natural Frequencies of Functionally Graded Macro/nanobeams. *Compos. Struct.* **2013**, *99*, 193–201.

(12) Beer, F. P.; Johnston, E. R.; DeWolf, J. T.; Mazurek, D. F. *Mechanics of Materials (Sixth Edition)*; 6th Edition; McGraw-Hill: New York, **2012**.

(13) Ni, H.; Li, X.; Gao, H. Elastic Modulus of Amorphous SiO2 Nanowires. *Appl. Phys. Lett.* **2006**, *88*, 1–3.

(14) Jing, G. Y.; Duan, H. L.; Sun, X. M.; Zhang, Z. S.; Xu, J.; Li, Y. D.; Wang, J. X.; Yu, D. P. Surface Effects on Elastic Properties of Silver Nanowires: Contact Atomic-Force Microscopy. *Phys. Rev. B - Condens. Matter Mater. Phys.* **2006**, *73*, 1–6.

(15) Wu, B.; Heidelberg, A.; Boland, J. J. Microstructure-Hardened Silver Nanowires. *Nano Lett.* **2006**, *6*, 468–472.

(16) Hsin, C. L.; Mai, W.; Gu, Y.; Gao, Y.; Huang, C. Te; Liu, Y.; Chen, L. J.; Wang, Z. L. Elastic Properties and Buckling of Silicon Nanowires. *Adv. Mater.* **2008**, *20*, 3919–3923.

(17) Sun, Y.; Mayers, B.; Herricks, T.; Xia, Y. Polyol Synthesis of Uniform Silver Nanowires: A Plausible Growth Mechanism and the Supporting Evidence. *Nano Lett.* **2003**, *3*, 955–960.

(18) Mayoral, A.; Barron, H.; Estrada-Salas, R.; Vazquez-Duran, A.; José-Yacamán, M. Nanoparticle Stability from the Nano to the Meso Interval. *Nanoscale* **2010**, *2*, 335–342.

(19) McCarthy, E. K.; Bellew, A. T.; Sader, J. E.; Boland, J. J. Poisson's Ratio of Individual Metal Nanowires. *Nat. Commun.* **2014**, *5*, 1–7.

6

THE ORIGIN OF RESIDUAL STRESS IN SOLVENT DEPOSITED NANOWIRES

6.1 Introduction

In the work presented in this thesis up to this point, it has been demonstrated that solvent deposited silver nanowires (AgNWs) can be affected by a residual stress when they adhere strongly to a SiO_2 substrate. When these nanowires (NWs) are analysed in a doubly-clamped beam configuration the residual stress affects the measured mechanical response of the NWs. NWs which do not adhere strongly to the surface are free to relax to a zero-stress state prior to being incorporated into a doubly-clamped beam configuration. It has been demonstrated that the original Heidelberg (zero-residual stress) model[1] used to describe the force-displacement (*F-d*) response for the full elastic range of NWs is not valid for wires that are affected by a residual stress. Furthermore, use of a model[2,3] that incorporates residual stress can lead to ambiguity in the measurement of Young's modulus which exhibits a displacement dependence. This displacement dependence arises due to experimental noise in the measurement.

Based on these observations, it was concluded that either; (i) a different analytical technique must be developed to extract the mechanical properties of NWs that are under stress or (ii) a wire must be deposited without the incorporation of unwanted residual stresses, clamped and analysed using the Heidelberg model for zero tension NWs. For the former, NWs that were in a doubly-clamped beam configuration were sectioned to form stress-free singly-clamped NWs[4]. Conventional Euler-Bernoulli beam mechanics was used to determine the Young's modulus of these NWs without the presence of tension. These cantilever beam measurements were used as a benchmark to analyse the validity of both the Heidelberg (zero-residual stress) model[1] and the tension-adjusted model[3]. However, there are certain experiments for which it is beneficial to have a NW in a doubly-clamped beam configuration,

such as electromechanical measurements[5]. To analyse the effects current flow through a NW can have on its mechanical properties, it is necessary to have electrical contacts on both sides of the wire to act as a source and a drain. Therefore, the Heidelberg (zero-residual stress) model is appropriate to determine any current dependent material properties, but only if we can guarantee that NWs are not subjected to a residual stress prior to mechanical clamping and manipulation. This requirement motivates the research in this chapter where we explicitly investigate the possible origins of the residual stress known to exist in solvent deposited AgNWs.

6.2 Functionalisation of Nanomaterials

Due to their large surface area to volume ratios, nanomaterials have a high surface energy. This results in nanomaterials having an enhanced surface reactivity when compared to their bulk counterparts. It is energetically favourable for nanomaterials to minimise their surface area hence minimise their surface energy. This phenomenon is the reason why isotropically free liquids and solids form spherical droplets as these have the smallest surface area and therefore the lowest surface energy[6]. However, this same high surface energy makes solution synthesised nanomaterials prone to agglomeration. It is thermodynamically favourable for nanomaterials suspended in solution to decrease their surface area to lower their surface energy through agglomeration, which can be problematic during nanowire synthesis and during the subsequent processing of these wires. Therefore, it is often necessary for a stabilising agent, such as a surfactant or a polymer coating, to be used to reduce the surface energy of the nanomaterial and to stabilise them against aggregation. The AgNWs used in these measurements are synthesised via the polyol solution based process which involves polymer functionalisation of the NW surface to prevent agglomeration.

6.2.1 Surface Functionalisation of Nanowires

When synthesising 1-dimensional NWs in a liquid phase it is often necessary to apply anisotropic confinements to promote and maintain 1–dimensional growth. In the case of the AgNWs used in these experiments a polyol synthesis method is used[7]. This involves using polyvinylpyrollidone (PVP) $(C_6H_9NO)_n$ as a polymer capping reagent. Additionally, it is believed to introduce a seeding step[8]. As shown in Figure 6.1, the ends of the AgNW are terminated by {111} facets, and the side surfaces are bounded by {100} facets. There is a strong interaction between the PVP and the {100} facets and a weak interaction between PVP

and the {111} facets. This results in NW growth in the [110] direction in a process known as Oswald ripening. The PVP also serves a second purpose in that it helps stabilise the NWs once they are dispersed in solution[7].

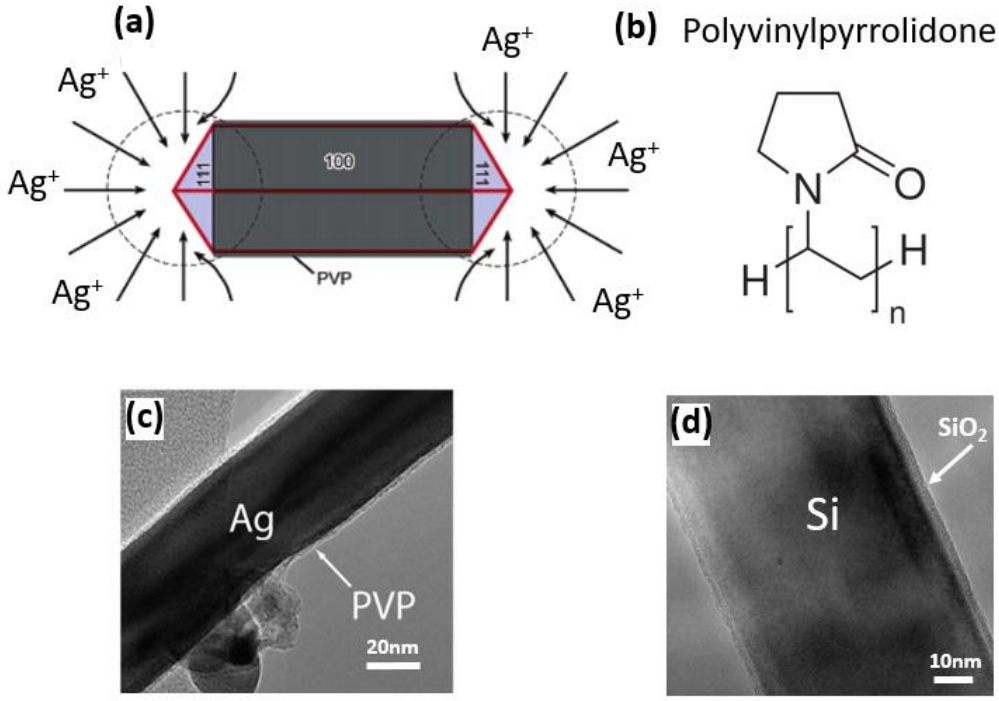

Figure 6.1: (a) Schematic showing the diffusion of liberated Ag atoms to the two ends of a nanorod. The {100} surfaces are passivated by PVP due to strong interactions with the PVP (grey colour) whereas the {111} surfaces are not passivated due to weak interactions with the PVP allowing growth along one axis only[8]. (b) Chemical structure of PVP. (c) TEM image of a AgNW with a PVP coating. (d) TEM image of a SiNW with a native oxide outer shell. (TEM courtesy of Dr. Eoin McCarthy)

In contrast, the SiNWs used in this study were synthesised using chemical vapour deposition as previously outlined. As they are grown on a Si/SiO_2 wafer they do not need to be stabilised against agglomeration. If they are sonicated away from their growth substrate to allow for solvent deposition, the wires will aggregate after 1-2 weeks, therefore only small dilutions are dispersed at a time. As such, the SiNWs have a native oxide as their outer shell and do not have any polymeric stabiliser or surfactants. Polymers and inorganic oxides have very different properties that must be taken into account when considering the adhesion and mechanical response of these NWs. TEM images of the surface coatings on both AgNWs and SiNWs are confirmed in Figure 6.1 (c) and (d).

In this chapter, we investigate how the different coatings on these NWs can result in differences in adhesion between NW types as observed in chapter 3. We also investigate the possibility that these surface coatings interact with solvents to potentially exert a residual stress on NWs. Firstly, we recap the results in the context of those observed in chapter 3.

6.3 Results

6.3.1 Solvent Dependent Adhesion and Mechanical Response of Nanowires

The adhesion of both AgNWs and SiNWs to a SiO_2 substrate was investigated. The level of adhesion was determined by whether the wire was mobile upon manipulation with an AFM tip. The procedure for manipulating the NWs is the same as for the 3-point bending experiment except that the tip is positioned to sit just above the surface in line with the NW as opposed to below the plane of the NW for the 3-point bending experiment. The main findings of the results presented in chapter 3, are shown in Figure 6.2 and show that only solvent deposited AgNWs adhered to the surface. It is noteworthy that only solvent deposited AgNWs were found to be affected by residual stress (see chapter 3). Evidently, other wires did not exhibit residual stress because they were weakly adhered to the substrate therefore they were able to relax following solvent evaporation. Since AgNWs have a PVP coating as their outer shell it is possible that some specific interactions (for example solvent-induced polymer swelling/softening) between the PVP coating and the solvent results in the enhanced adhesion and the incorporation of residual stress.

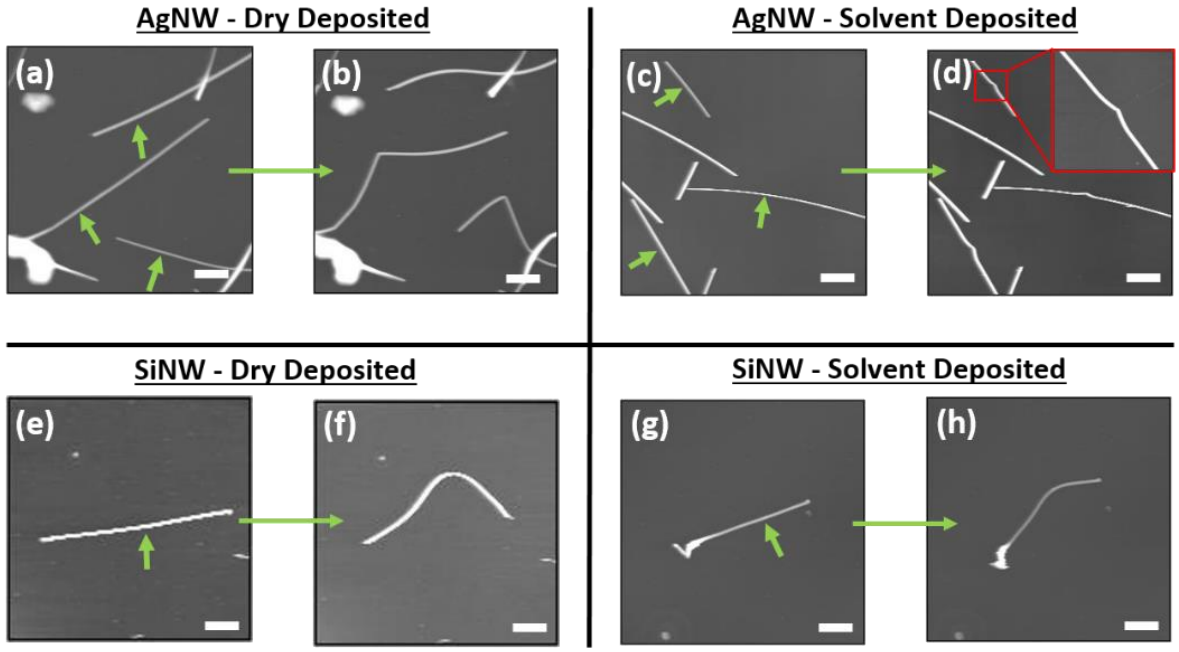

Figure 6.2: AFM images of AgNWs and SiNWs on SiO_2 before and after being manipulated with an AFM tip. NWs were deposited using different deposition methods. Images (a),(c),(e),(g) are wires before manipulation with the green arrows defining the loading path. (a),(c) AgNWs deposited by dry and solvent methods respectively, scale bars 1 μm. (b),(d) Corresponding wires after manipulation with the inset in (d) showing a reduced scan image of a fractured AgNW, scale bars 1 μm. (e),(g) SiNWs deposited by dry and solvent methods respectively with (f) and (h) showing the same wires after having being loaded with the AFM tip, scale bars 500 nm.

6.3.2 Solvent and Dry Deposition of Gold Nanowires

To determine if these interactions are observed in other NW systems which contain surface coatings that may be pervious to solvents, we investigate gold nanowires (AuNWs). The AuNWs used are functionalised with a CTAB coating to stabilise the nanowires against agglomeration. CTAB is a nineteen carbon chain long quaternary surfactant ($C_{19}H_{42}NBr$) whose presence can be observed in the TEM image in Figure 6.3 (e). These wires were analysed in the same way as the AgNWs and SiNWs. First, the adhesion of these wires to a SiO_2 substrate was determined. The wires were subsequently deposited over trenches, clamped and the 3-point bending experiment conducted as before (see chapter 3). The results can be observed in Figure 6.3.

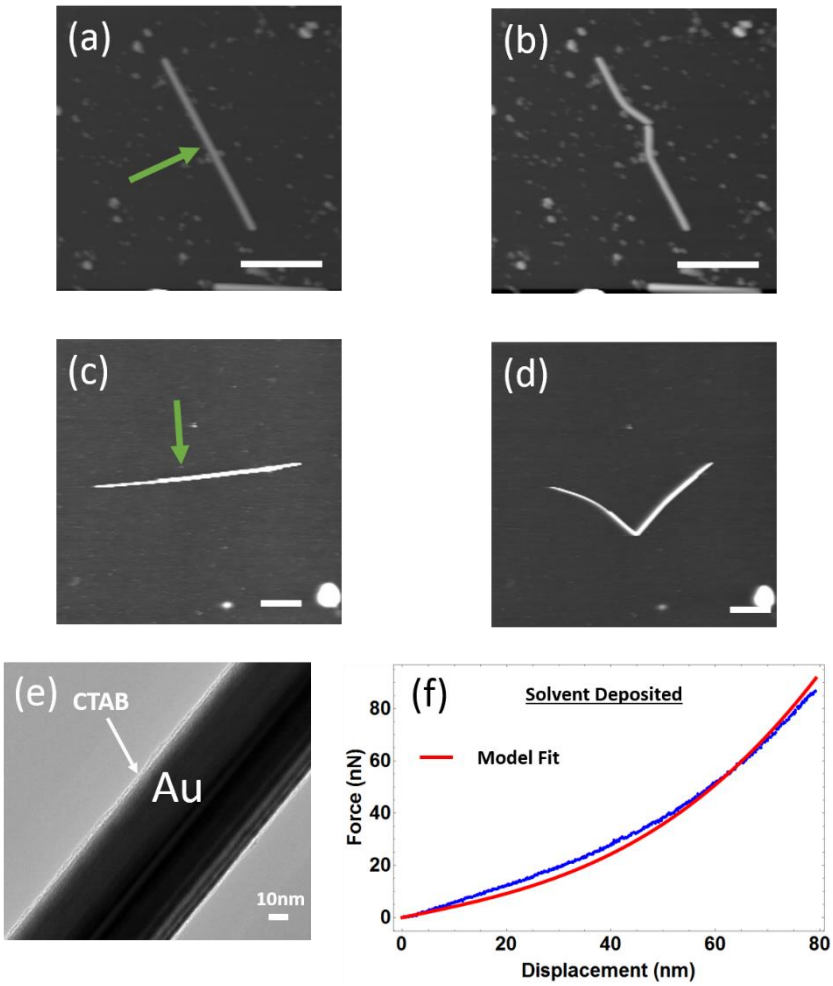

Figure 6.3: AFM images of AuNWs deposited on SiO_2 (a) solvent deposited, (c) dry deposited, with the resulting corresponding AFM images in (b), (d) after AFM manipulation, all scale bars 1 μm. (e) TEM image showing CTAB coating on the shell of the AuNW. (f) *F-d* response of solvent deposited AuNW in doubly-clamped beam configuration fit to the Heidelberg (zero-residual stress) model.

From Figure 6.3 it is clear that the CTAB coating on the AuNWs appears to interact to a similar extent with solvents as the PVP coated AgNWs. When the wires are solvent deposited and manipulated they are strongly adhered to the substrate resulting in wire fracture (Figure 6.3 (b)). When they are dry deposited, they are mobile on the surface when manipulated with an AFM tip (Figure 6.3 (d)). For solvent deposited wires, the fit of the Heidelberg (zero-residual stress) model to the *F-d* response is consistent with a NW that has been subjected to a residual stress (Figure 6.3 (f)). This strengthens the argument that it is solvent - polymer/surfactant interactions that result in an enhanced adhesion to the substrate. In order to determine if these coatings also result in the creation of residual stresses it is necessary to analyse a NW that has a solid outer coating that does not interact with solvents but exhibits strong adhesion to the substrate upon solvent deposition. In this scenario, if the solvent drying process were to induce residual stresses in the wire they would become fixed in the wire due to the strong adhesion to the substrate.

6.3.3 Strongly Adhered Solvent Deposited SiNW

In most cases the SiNWs measured in these experiments are weakly adhered to the substrate when solvent deposited. Under certain circumstances we have observed that these wires are strongly adhered. This may be as a result of a greater contact area between the NW and the SiO_2 substrate or residues on the surface creating a stronger adhesion. In such cases, it is possible to determine if a wire that is solvent deposited, but that does not have a polymeric outer coating, is subjected to the same residual stresses as were evident with the AgNWs.

Figure 6.4 shows a solvent deposited SiNW which is strongly adhered to the SiO_2 surface. From the optical image in Figure 6.4 (a) it can be seen that the SiNW spans four trenches. This allows us to determine if the levels of residual stress are consistent across an individual NW. Three suspended sections of the NW were mechanically clamped using Pt-EBID (Figure 6.4 (b)). The fourth suspended section was left unclamped so that the strong adhesion of the wire to the surface could be demonstrated. From the AFM image in Figure 6.4 (c), it can be observed that upon loading the unclamped SiNW was fractured indicating strong adhesion of the NW to the surface. Therefore, any solvent induced residual tension should remain fixed in the NW. If the wire was weakly adhered it would have moved and NW fracture would not have been observed. The *F-d* response for the 3-point bending measurement on each of the four sections is shown in Figure 6.4 (d) - (g). All *F-d* curves are fit to the Heidelberg model, equation (3.2). For all four *F-d* curves the fits to the model are

excellent indicating that the wire has not been subjected to a residual stress during the drying process of the solvent evaporation. The Young's modulus values obtained by the three physically clamped sections are 127.4 GPa, 125.8 GPa and 128.7 GPa. The excellent agreement between the measurements validates the accuracy of the 3-point bending experiment. The unclamped section of wire yielded a Young's modulus value of 85.4 GPa. This is over 30% lower than the previous measured value. The reason for this discrepancy is that the width of the trench was taken to be the pinning length, *L*, of the wire. However, although the NW is strongly adhered to the substrate the actual pinning length is greater than the width of the trench. This is consistent with the results of the cantilever experiments in chapter 5.

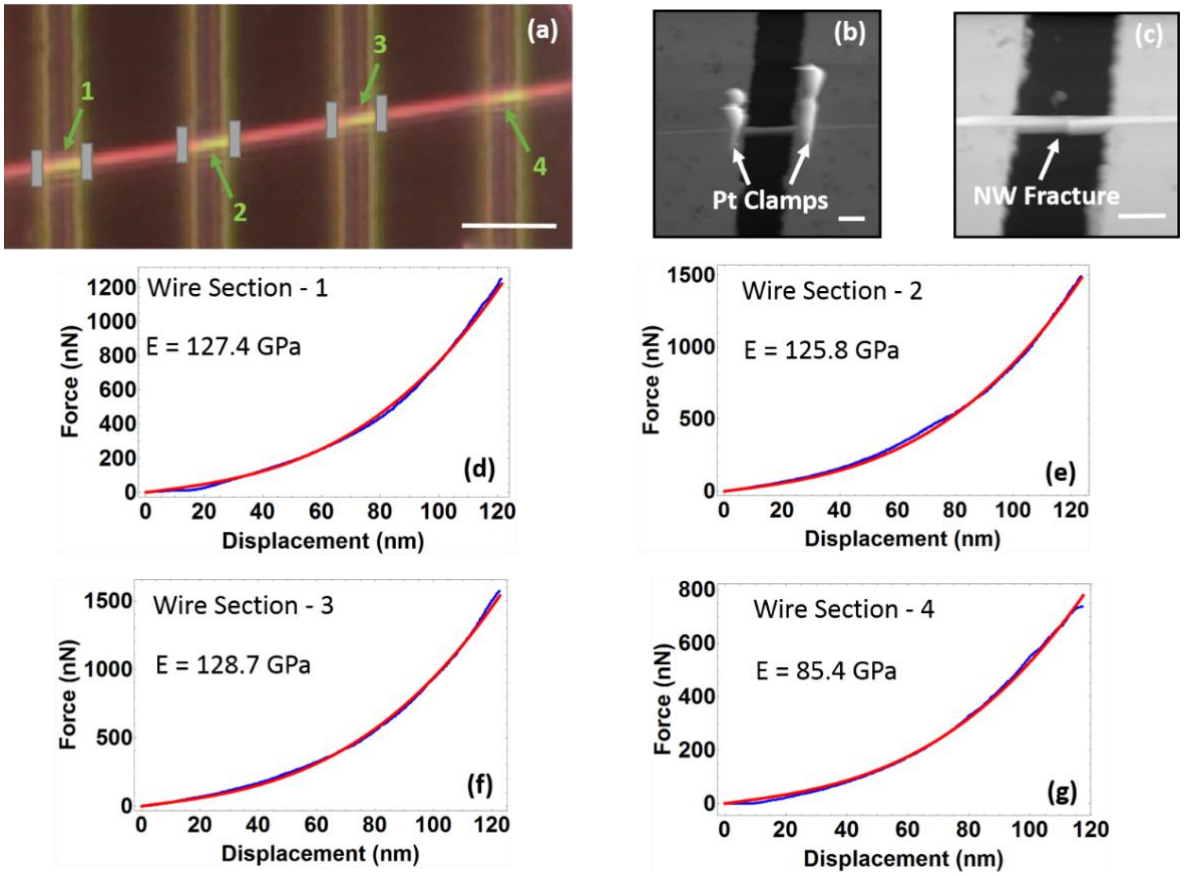

Figure 6.4: (a) Optical image of a SiNW solvent deposited spanning four trenches. Sections 1-3 are physically clamped with Pt-EBID, while section 4 is left unclamped, scale bar 5 µm. (b) AFM image of section 2 with Pt-EBID clamps, scale bar 1 µm. (c) AFM image of section 4 showing brittle fracture of NW after 3-point bending experiment, scale bar 1 µm. (d)-(g) *F-d* curves for the four sections of wire, each curve is fit to the Heidelberg model described in Equation (3.2).

The width of the trench for the section of wire that was not mechanically clamped was 1.9 µm. To obtain the correct modulus for the wire, the correct pinning length is 2.15 µm which

indicates the true pinning length is 250 nm greater than the trench width. This verifies the cantilever beam measurements in that although the NW is strongly adhered to the substrate, that physical clamps are required along the edges of the trench in order to correctly define the pinning length.

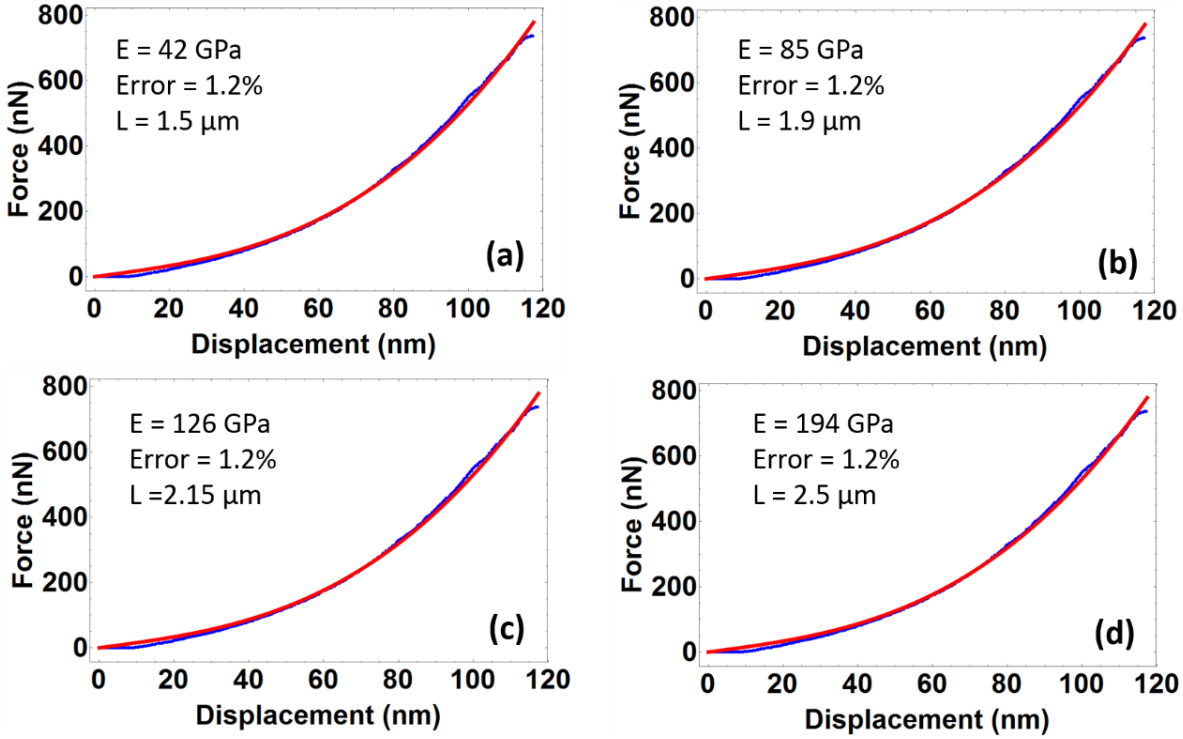

Figure 6.5: Quality of the fit plus extracted Young's modulus when the experimental data is fit to the Heidelberg model (3.2) at different pinning lengths; (a) 1.5 µm, (b) 1.9 µm, (c) 2.15 µm, (d) 2.5 µm.

However, in the Heidelberg (zero-residual stress) model described by Equation (3.2) inaccurate values of L affects only the magnitude of modulus extracted and do not affect the fit to the model. This is demonstrated in Figure 6.5 where the *F-d* response for the unclamped section of the SiNW in Figure 6.4 has been fit to the model using various pinning lengths and the error in the fit to the model remains constant.

From these results, it is apparent that the residual stress that is observed in solvent deposited AgNWs is not because of the solvent drying process. It is a further indication of the presence of a specific interaction between solvent and the PVP coating that subjects the wire to an initial residual stress. It is important to analyse potential interactions between polymer coatings and solvents which could lead to NWs becoming strained.

6.3.4 Interaction between Solvents and PVP Coatings on AgNWs

It is apparent that an interaction occurs between the PVP coating on AgNWs and solvents such as isopropanol. The ability of polymers to swell in solvent media is well known[9,10]. When a dry polymer is exposed to a solvent, the solvent molecules enter the porous polymer molecules and occupy all free available space[11]. Indeed, the swelling of polymers has been used in gas sensors. Typically, cantilever beams are coated with a polymer which swells in the presence of a vapour resulting in the deflection of the beam[12,13]. The deflection occurs due to a bimaterial effect where surface stresses are generated between the sensor material and the cantilever[14].

The extent to which polymers swell depends heavily on the degree of crosslinking between the polymer chains. If the polymer is not crosslinked, then the polymer will dissolve if there is enough solvent present for the solvation process. The fact that the PVP is bound to the AgNW prevents solvation of the PVP. TEM imaging has proved the presence of the PVP coating after being dispersed in solvents for extended periods. If the polymer is heavily crosslinked there will be little or no free space available within the polymer matrix so swelling will be at a minimum. For hydrogels, where polymers are intentionally treated to promote solvent absorption, PVP has been shown to swell to greater than 1000% in volume[15,16]. The polymer on these NWs are not hydrogels, however the degree of swelling could still be sufficient to exert an axial force on the NW as it expands. We can estimate how much a NW can potentially be strained by a swelling polymer. Assuming isotropic swelling of the polymer we can write (see A2 for full derivation);

$$\varepsilon_{wire} = -2\left(\frac{h_{film}}{R_{wire}}\right)\left(\frac{E_{film}}{E_{wire}}\right)\varepsilon_{film} \tag{6.1}$$

where, ε_{wire} and ε_{film} are the strain of the NW and polymer film respectively, h_{film} is the thickness of the polymer coating, R is the wire radius and E is the Young's modulus of the core wire and polymer coating. The thickness of the PVP film is on average 3 nm as can be observed in Figure 6.1 (c). The radius of the AgNWs are on average 30 nm. The Young's modulus for bulk silver is 83 GPa. It is difficult to determine the exact Young's modulus value for the PVP coating on the NWs. The Young's modulus will vary with the crosslinking of the PVP and also with the molecular weight of PVP used. For the polyol synthesis growth of AgNWs the most common molecular weight used is approximately 55,000[17,7]. A study on PVP of a molecular weight of 58,000 found the Young's modulus to be 2.5 GPa[18]. Therefore,

it is an appropriate estimation. As mentioned, PVP has been shown to swell to an extent greater than 1000% its volume, but for a PVP coated NW a reasonable assumption would be in the range of 20 - 40% as the polymer was not specifically treated with the aim of promoting its swelling ability. When the model (6.1) above is used to calculate the strain on a NW using the parameters discussed, an axial strain of roughly 0.33% is obtained when assuming the polymer swells by 40% of its initial volume. Assuming an initial wire length of 10 μm, this would correspond to an axial stress of 0.28 GPa, which would result in a 33 nm extension of the wire.

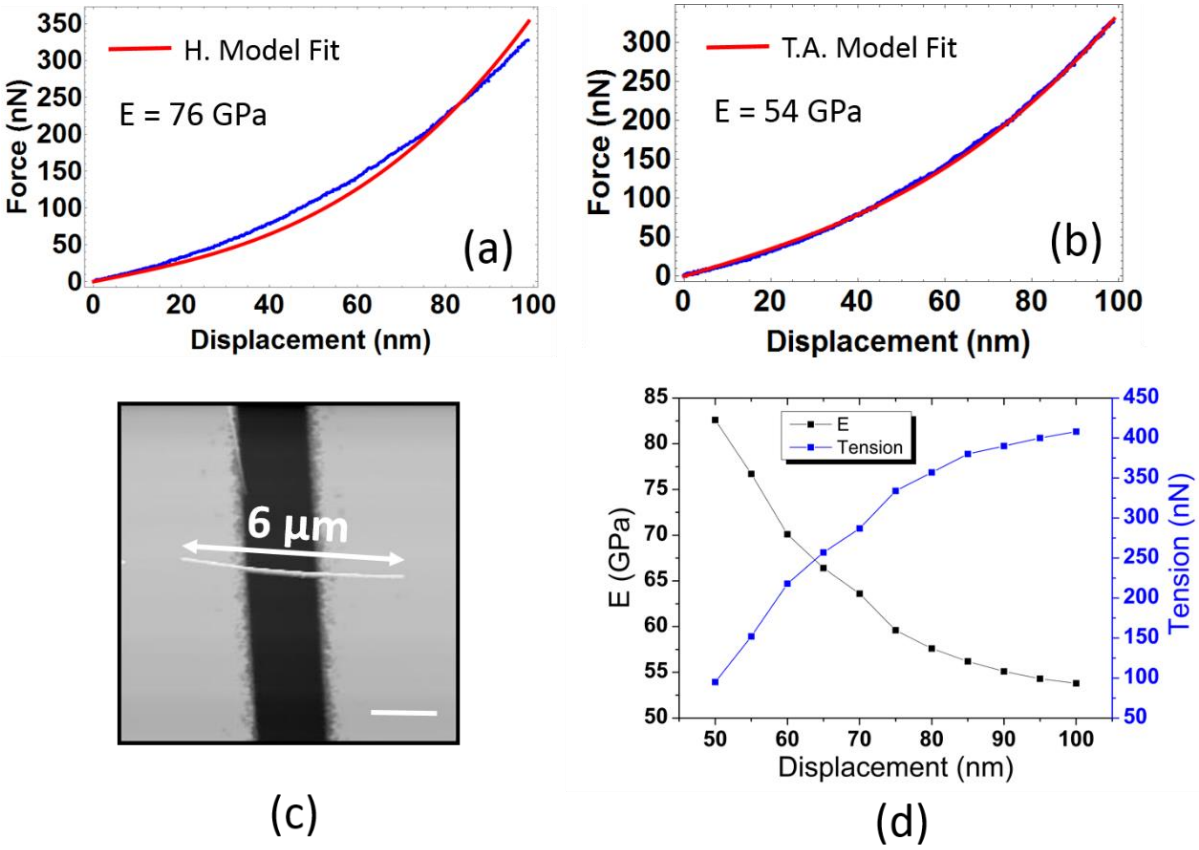

Figure 6.6: *F-d* curves for a 68 nm diameter AgNW fitted to (a) the Heidelberg Model, (b) tension-adjusted model. (c) AFM image of a AgNW suspended over a trench before deposition of mechanical clamps, scale bar 2 μm. (d) Shows an anti-correlation between Young's modulus and residual tension when the tension-adjusted model is fitted to different displacements.

This calculation indicates that the polymer has the potential to exert a considerable stress on the NW consistent with our 3-point bending experiments. Although it has been demonstrated that the separation of Young's modulus and residual stress is ambiguous, we can get an approximate estimate of the latter. Based on the fits of the Heidelberg (zero-residual stress) and tension-adjusted model in Figure 6.6 (a) and (b) to the *F-d* response of the AgNW in

Figure 6.6 (c) at different displacements, tension values can be estimated as ranging from 100 nN - 400 nN. This corresponds to a stress of between 0.03 GPa - 0.11 GPa which corresponds to a strain level of 0.04% - 0.12% for a wire with a Young's modulus of 83 GPa with a 68 nm diameter. Given that this NW is 6 μm long, this strain then corresponds to an extension of the wire of between 2.4 nm - 7.2 nm, which is well within the range of predicted polymer swelling.

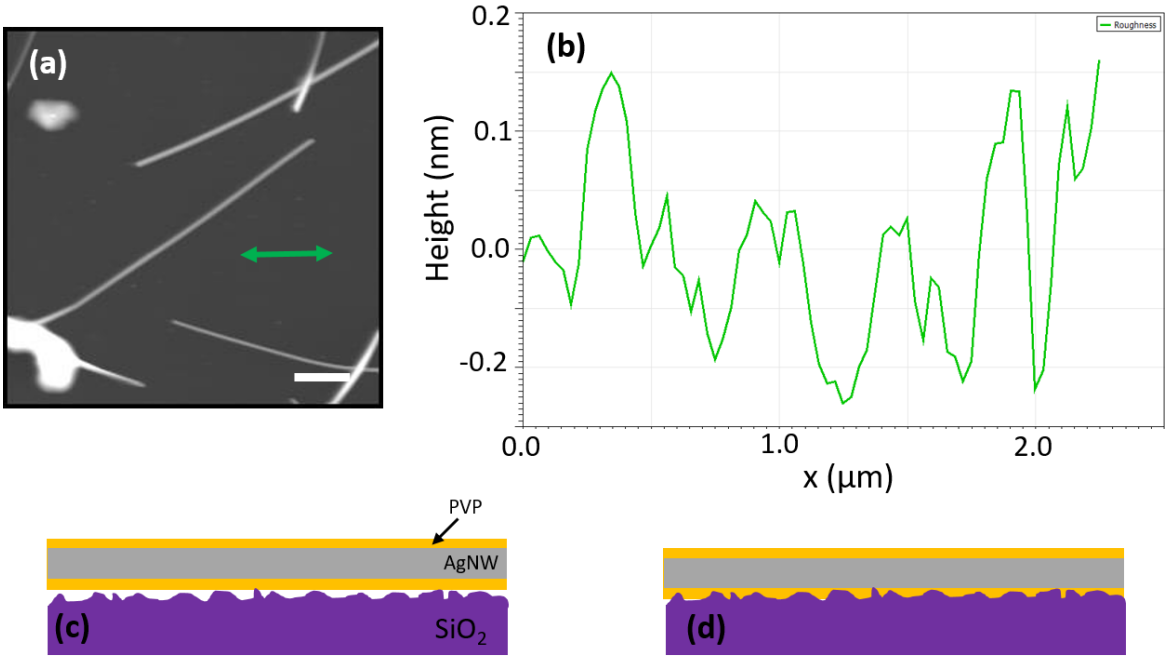

Figure 6.7: (a) AFM image of AgNWs on a SiO_2 substrate, scale bar 2 μm. (b) Line profile of green line in (a) showing the SiO_2 substrate, with a RMS roughness of 0.3 ± 0.1 nm. (c) Schematic of proposed contact area of a dry deposited PVP coated AgNW on a SiO_2 surface. (d) Proposed increased contact area of solvent deposited AgNW. The PVP becomes more compliant when swollen resulting in enhanced adhesion to the substrate.

To postulate why polymer swelling results in an enhanced adhesion to a SiO_2 substrate it is necessary to examine the interface between the two materials. In reality, the surface of the SiO_2 on which the NWs are deposited is not atomically flat[19]. Figure 6.7 (b) shows a line scan of a SiO_2 surface with a root mean square (RMS) roughness value of 0.3 ± 0.1 nm. The RMS roughness values for some of the SiO_2 surfaces used can be as high as 2 ± 1 nm. When polymers swell they become more compliant[20] and this may increase the contact area allowing the softer polymer to conform to surface asperities in contrast to when the wires are dry deposited.

Similar adhesion and residual stress affects are observed when the AgNWs are dispersed in polar solvents in which they can readily swell such as methanol, ethanol and water. However when dispersed in non-polar solvents such as hexane and heptane the adhesion of the AgNWs when deposited on a SiO_2 surface is weaker which prevents residual stress from becoming fixed in the nanowire. This is a further indication that it is swelling of the polymer coating that results in the enhanced adhesion and the incorporation of residual stress.

6.3.5 Investigating the Effect of Solvent on a Dry Deposited AgNW

To further demonstrate the effect that solvent has on the adhesion of polymer coated NWs and on their initial stress state, we examine the effect that solvent has on a AgNW that has been initially dry deposited. For this measurement, a AgNW is dry deposited over a trench and mechanically manipulated to confirm its state of adhesion. Subsequently, a drop of isopropanol is dropcast on the sample, allowed to evaporate and the same NW manipulated again to determine if there is a change in the adhesion to the surface. As expected the AgNW that is dry deposited is weakly adhered to the surface. This can be observed in Figure 6.8 (b) where the position of the NW has changed after manipulation with the AFM tip. Interestingly, when a drop of isopropanol is dropcast onto the substrate and allowed to evaporate, the NW returns close to its original shape as observed in Figure 6.8 (c). When this wire is subsequently manipulated it is found to be strongly adhered to the surface. What is more, the wire is now under stress. This can be seen from the *F-d* curve in Figure 6.8 (e) where the presence of residual tension is evident by the poor fit to the Heidelberg model. This provides further evidence that polymer swelling leads to enhanced adhesion and the incorporation of strain in the NW. The fact that the wire straightens upon the application of IPA can be explained by reduction of the adhesive interaction due to the relative dielectric constants of the SiO_2 and IPA and the intrinsic modulus of the wire that favours a straightened configuration.

Studies of dry deposited wires in an optical microscope, revealed that wires straightened back into their original shapes immediately after the solvent drop was deposited on the substrate. An example of this can be observed in Figure 6.9, where Figure 6.9 (a) and (b) show a dry deposited SiNW before and after manipulation with an AFM tip. In Figure 6.9 (c), a drop of IPA has been deposited on the sample and the wire has instantaneously straightened back to its original position, the blurring of the optical image of the NW is a result of having to focus through the solvent. Figure 6.9 (d) shows the wire after the evaporation of the IPA.

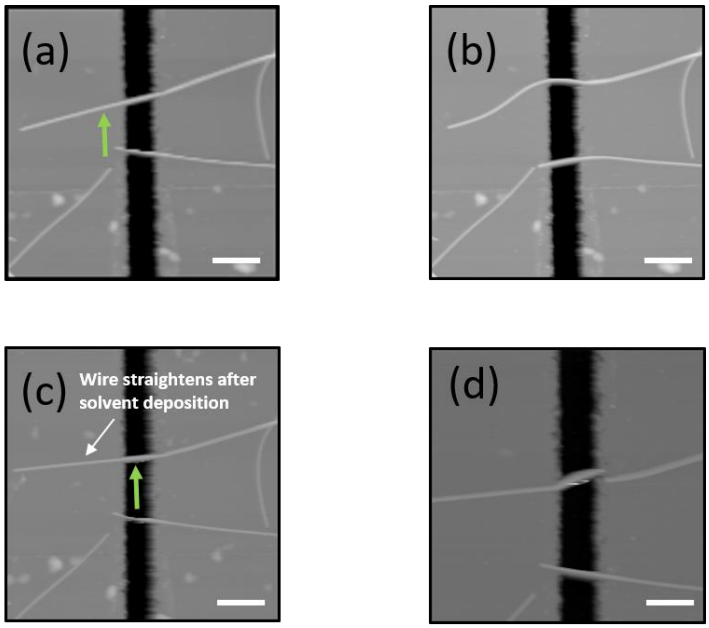

Figure 6.8: (a) AFM image of a dry deposited AgNW showing manipulation path (green arrow) (b) Movement of AgNW indicating wire is weakly adhered to the surface. (c) Subsequent straightening out of the NW upon exposing to solvent drop. (d) Fractured NW after subsequent manipulation showing pinned NW, scale bars 2µm. (e) *F-d* curve with fit to the Heidelberg model of fractured NW, inset shows brittle fracture due to sharp drop in force.

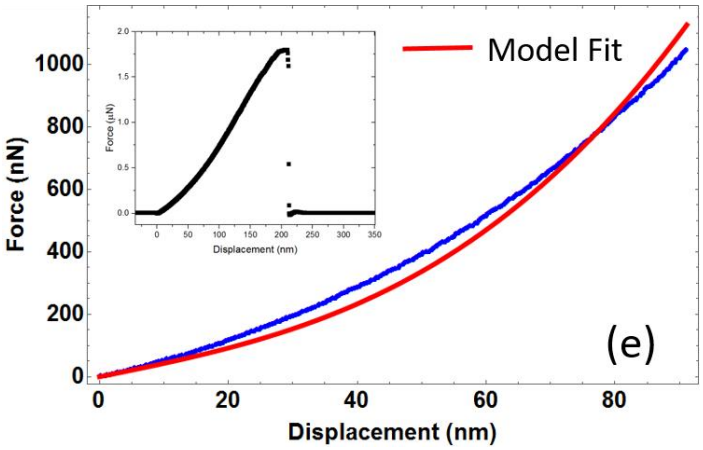

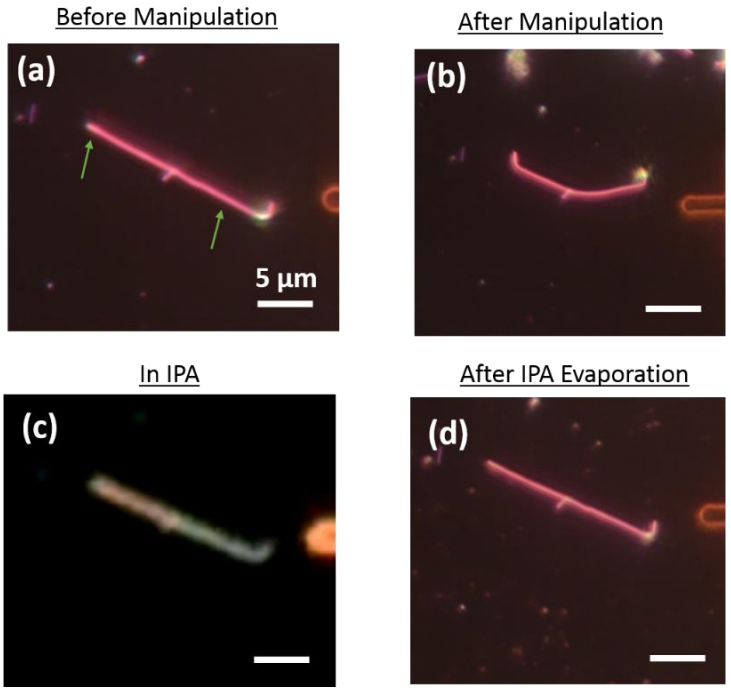

Figure 6.9: (a) SiNW dry deposited on a SiO_2 substrate. (b) SiNW manipulated by an AFM tip in the direction of the green arrows in (a). (c) SiNW immediately after a drop of IPA has been deposited. Note: The apparent blurriness of the wire is as a result of having to focus through the solvent. (d) Final position of the SiNW after evaporation of the IPA.

This straightening action can be explained by considering image charges whereby if a charge *e* is situated near the boundary of two different phases with dielectric constants ε_1 and ε_2, the dielectrics are polarised by its field[21], and the charge experiences an image force *F* given by;

$$F = \frac{QQ'}{4\pi\varepsilon_1\varepsilon_0(2h)^2} \tag{6.2}$$

where the image charge is;

$$Q' = -Q\left(\frac{\varepsilon_{SiO_2} - \varepsilon_{IPA}}{\varepsilon_{SiO_2} + \varepsilon_{IPA}}\right) \tag{6.3}$$

where *h* is the distance between the charge and the boundary. The dielectric constants in our experiment are ε_{SiO_2} = 3.8 and ε_{IPA}=17.9. Using these values gives an image charge of +0.65Q which results in a positive force experienced between the IPA and SiO_2. This indicates that there is a repulsion between the two. When solvent is deposited on a bent NW, this repulsion shields the van der Waals forces that are adhering the wire to the substrate, allowing the wire to relax back to an equilibrium state. This same effect was observed when a solvent drop was deposited on SiNWs that had been manipulated with an AFM tip.

6.4 Conclusion

In this chapter, we have demonstrated that surface coatings on NWs have the potential to induce parasitic residual stresses. Surface coatings such as PVP polymer are often necessary to stabilise NWs against agglomeration and are also required to allow the growth of certain NWs in 1-dimension. Upon being immersed in a solvent medium, polymers can swell when solvent molecules occupy free space within the polymer matrix. We have estimated that the isotropic swelling of the PVP coating on a NW has the potential to strain a nanowire by at least 0.33%, which for a wire of length 10 μm, would result in a 33 nm extension. This may appear like a small strain, but in measuring the *F-d* response this initial residual stress renders the original Heidelberg (zero-residual stress) model invalid. It was shown that SiNWs are not subjected to the same residual stress because they have a solid oxide coating which does not interact with the solvent.

The polymer coatings on the AgNWs also result in an enhanced adhesion to the substrate when solvent processed. The proposed mechanism for this is that as the polymer swells it becomes more compliant which allows it to conform to the asperities of the SiO_2

substrate. This results in an enhanced contact area which improves the adhesion between the NW and the surface. Again, this effect was not observed for the SiNWs and the adhesion properties of those wires were comparable regardless of the deposition method.

Through these experiments, we have demonstrated that polymer coatings on the surface of NWs have the potential to swell in solvent media and induce residual stresses in NWs. These stresses remain fixed in a NW when the wire is strongly adhered to its supporting substrate. When NW-substrate adhesion is weak the wire can relax releasing any induced stresses. This result emphasises the importance of determining the original stress state of a material and its adhesion to its supporting substrate. For strain measurements conducted in a TEM, fabrication induced strains could affect the accurate characterisation of material properties. It is important to minimise strain in nanomaterials prior to these strain measurements. By avoiding solvent use the chances of inducing unwanted residual strains are greatly reduced.

6.5 References

(1) Heidelberg, A.; Ngo, L. T.; Wu, B.; Phillips, M. A.; Sharma, S.; Kamins, T. I.; Sader, J. E.; Boland, J. J. A Generalized Description of the Elastic Properties of Nanowires. *Nano Lett.* **2006**, *6*, 1101–1106.

(2) Hudson, S. D.; Zhurov, V.; Grbić, V.; Grbić, M.; Hutter, J. L. Measurement of the Elastic Modulus of Spider Mite Silk Fibers Using Atomic Force Microscopy. *J. Appl. Phys.* **2013**, *113*, 1–7.

(3) Yaish, Y. E.; Calahorra, Y.; Shtempluck, O.; Kotchetkov, V. Three-Point Bending Analysis of Doubly Clamped Silicon Nanowire Beams; Young's Modulus, Initial Stress, and Crystal Orientation. *J. Appl. Phys.* **2015**, *117*, 1–11.

(4) Wong, E. W.; Sheehan, P. E.; Lieber, C. M. Nanobeam Mechanics: Elasticity, Strength, and Toughness of Nanorods and Nanotubes. *Science (80-.).* **1997**, *277*, 1971–1975.

(5) McCarthy, E. K.; Bellew, A. T.; Sader, J. E.; Boland, J. J. Poisson's Ratio of Individual Metal Nanowires. *Nat. Commun.* **2014**, *5*, 1–7.

(6) Israelachvilli, J. N. *Intermolecular and Surface Forces*; 3rd Edition; Elsevier, **2011**.

(7) Coskun, S.; Aksoy, B.; Unalan, H. E. Polyol Synthesis of Silver Nanowires : An Extensive Parametric Study. *Cryst. Growth Des.* **2011**, *2*, 2–5.

(8) Sun, Y.; Mayers, B.; Herricks, T.; Xia, Y. Polyol Synthesis of Uniform Silver Nanowires: A Plausible Growth Mechanism and the Supporting Evidence. *Nano Lett.* **2003**, *3*, 955–960.

(9) Nandi, S.; Winter, H. H. Swelling Behavior of Partially Cross-Linked Polymers: A Ternary System. *Macromolecules* **2005**, *38*, 4447–4455.

(10) Dušek, K.; Choukourov, A.; Dušková-Smrčková, M.; Biederman, H. Constrained Swelling of Polymer Networks: Characterization of Vapor-Deposited Cross-Linked Polymer Thin Films. *Macromolecules* **2014**, *47*, 4417–4427.

(11) Singh, A.; Mukherjee, M. Effect of Polymer-Particle Interaction in Swelling Dynamics of Ultrathin Nanocomposite Films. *Macromolecules* **2005**, *38*, 8795–8802.

(12) Lang, H.; Hegner, M.; Gerber, C. Cantilever Array Sensors. *Mater. Today* **2005**, *8*, 30–36.

(13) Maute, M.; Raible, S.; Prins, F. E.; Kern, D. P.; Weimar, U.; Göpel, W. Fabrication and Application of Polymer Coated Cantilevers as Gas Sensors. *Microelectron. Eng.* **1999**, *46*, 439–442.

(14) Berger, R.; Delamarche, E.; Lang, H. P.; Gerber, C.; Gimzewski, J. K.; Meyer, E.; Gantherodt, H. J. Surface Stress in the Self Assembly of Alkanethiols on Gold. *Science (80-.).* **1997**, *276*, 2021–2024.

(15) Roy, N.; Saha, N.; Kitano, T.; Saha, P. Novel Hydrogels of PVP-CMC and Their Swelling Effect on Viscoelastic Properties. *J. Appl. Polym. Sci.* **2010**, *117*, 1703–1710.

(16) Jovanović, Ž.; Krklješ, A.; Stojkovska, J.; Tomić, S.; Obradović, B.; Mišković-Stanković, V.; Kacarevic-Popovic, Z. Synthesis and Characterization of silver/poly(N-Vinyl-2-Pyrrolidone) Hydrogel Nanocomposite Obtained by in Situ Radiolytic Method. *Radiat. Phys. Chem.* **2011**, *80*, 1208–1215.

(17) Wiley, B.; Sun, Y.; Xia, Y. Synthesis of Silver Nanostructures with Controlled Shapes and Properties. *Acc. Chem. Res.* **2007**, *40*, 1067–1076.

(18) Chen, W.; Wang, C.; Yan, L.; Huang, L.; Zhu, X.; Chen, B.; Sant, H. J.; Niu, X.; Zhu, G.; Yu, K. N.; *et al.* Improved Polyvinylpyrrolidone Microneedle Arrays with Non-Stoichiometric Cyclodextrin. *J. Mater. Chem. B* **2014**, *2*, 1699–1705.

(19) Rabinovich, Y. I.; Adler, J. J.; Ata, A.; Singh, R. K.; Moudgil, B. M. Adhesion between Nanoscale Rough Surfaces. *J. Colloid Interface Sci.* **2000**, *232*, 10–16.

(20) Cappella, B. *Mehanical Properties of Polymers Measured through AFM Force-Distance Curves*; 1st Edition; Springer International Publishing, **2016**.

(21) Korobeynikov, S. M.; Melekhov, A. V; Furin, G. G.; Charalambakos, V. P.; Agoris, D. P. Mechanism of Surface Charge Creation due to Image Forces. *J. Phys. D. Appl. Phys.* **2002**, *35*, 1193–1196.

7

IRREVERSIBLE CURRENT INDUCED STIFFENING OF Ag AND Au NANOWIRES

7.1 Introduction

Despite the range of novel properties that have emerged over the last decade there is yet no direct method to control the mechanical properties of a given nanoscale object. Materials can be processed to different sizes[1,2], with particular nano/microstructures[3] and with different kinds of surface functionalisation[4], but once formed the mechanical properties are fixed. Previous studies have shown that it is possible to alter the mechanical properties of a material using an external stimulus.

In 2015, Li *et al.*[5] demonstrated that the Young's modulus of 50 nm $BiFeO_3$ (BFO) thin films could be altered by inducing a phase transformation within the films. This phase transition involved a structure change in the material from rhombohedral - tetragonal (R→T). To induce this change, an AFM cantilever was contacted on the film surface with a voltage bias between 0 - 10 V applied between the tip and the surface, Figure 7.1 (a). The voltage required for the phase transition varied depending on the polarity of the applied bias and the initial strain in the film as shown in Figure 7.1 (b). The authors used band-excitation elastic/piezoresponse spectroscopy (BEPS) to probe the sub-MHz elastic dynamics of the surface to monitor the change in resonance frequency of the surface. A change in frequency of ~ 4.5 kHz was observed during a R→T phase transition which corresponded to a Young's modulus decrease of ~ 30%. The phase transition could be reversed by applying a tip bias opposite to the one that induced the initial transition, Figure 7.1 (c). The Young's modulus of the film decreased from 204 GPa to 141 GPa in the area locally to where the AFM tip contacted the surface. In this example the modulation of the Young's modulus is controlled

but involves a structural change that requires an external bias from a point source such as an AFM tip.

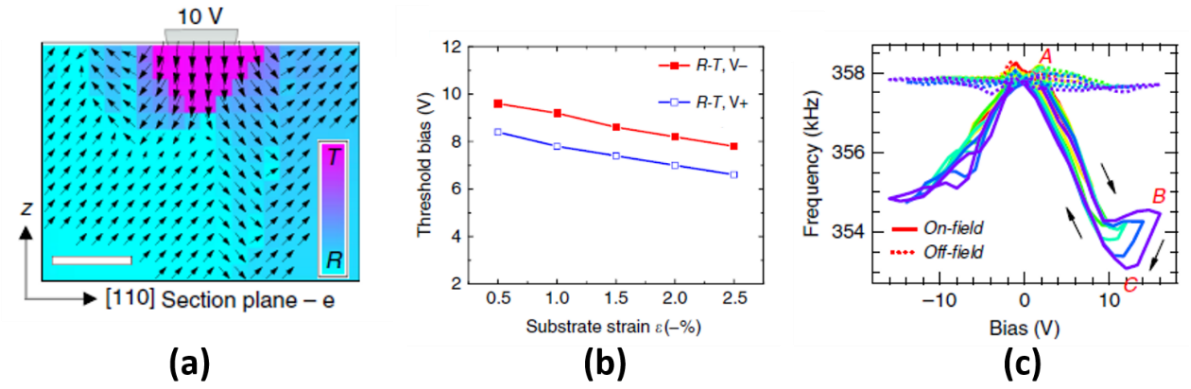

Figure 7.1: (a) Evolution of local polarisation in $BiFeO_3$ under the AFM tip during the application of a positive bias of 10 V. Arrows indicate the direction of the polarisation and scale with its magnitude from rhombohedral (R) to tetragonal (T). (b) Threshold bias required to induce phase change from R→T as a function of substrate strain and direction of applied bias. (c) Change in resonance frequency of the surface detected when sweeping the applied bias from -10 V – +10 V.[5]

For mechanical devices, whose operation may depend on multiple external stimuli, such as optical or electrical, it is important to analyse the potential effects that these stimuli may have on the mechanical properties of the active element in the device. Take for example, a nanoelectromechanical (NEM) switch which works by using electrostatic forces to mechanically deflect an active element such as a NW in to contact with an opposing electrode, allowing the flow of electric charge[6]. The device is now said to be in its 'on' state. When the electrostatic forces are switched off, the NW restoring force will oppose the force of adhesion between the NW and the electrode. If the restoring force is greater than the force of adhesion the NW will break contact with the electrode switching the device to an 'off' state. If the restoring force cannot overcome the force of adhesion, then the NW will remain adhered to the electrode and the device will remain on.

The restoring force of the NW depends on its Young's modulus. Therefore, it is important to determine if the Young's modulus of the NW is affected by the flow of electrical charge when the device is in an 'on' state. If the Young's modulus were to increase during device operation it would cause the beam to stiffen and potentially break contact with the electrode switching the device off unexpectedly. If current flow had the opposite effect and reduced the Young's modulus of the NW, the restoring force would be reduced. This may result in the device becoming permanently fixed in an 'on' state as the force of adhesion may

dominate. Therefore, it is necessary to investigate the effects of external stimulus on the mechanical properties of nanomaterials.

In 2013, Hao *et al.*[7] modelled the potential effects that electric charge residing on the surface of graphene can have on its mechanical properties. The simulations indicated that the Young's modulus decreased for both armchair and zig-zag graphene with increasing net electric charge on the graphene. The reason proposed for the reduced modulus was that the increased electric charge increased the carbon-carbon bond lengths at the edges of the graphene sheet. The mechanism behind this bond length change was not discussed. The bond lengthening induced an in-plane strain in the graphene sheets which reduced their overall strength. The authors believe this reduction in strength is consistent with a simultaneous reduction in the Young's modulus of the graphene sheet. These results indicate that coupling between mechanical properties and external stimulus should be considered.

7.1.1 Current Induced Stiffening in Silver Nanowires

Since the early 1950's[8,9] the effects that strain has on the electrical properties of materials has been widely studied[10]. However, there has been very little research into the reciprocal effect, i.e. the effect that charge flow can have on the mechanical properties of materials. In the 2013 thesis of McCarthy[11], it was demonstrated that the mechanical properties of pentagonally twinned silver nanowires (AgNWs) could be manipulated by the flow of electric charge through the wires. As the current density through the wires was increased the Young's modulus also increased. This contrasted with polycrystalline nickel nanowires (NiNWs) where the Young's modulus showed no correlation with the current density passed through the NWs as shown in Figure 7.2 (b).

The author measured the mechanical properties of these NWs using the doubly-clamped beam approach, as outlined in chapter 2. The AgNW measured in Figure 7.2 (c) exhibited a Young's modulus increase from 93 GPa to 218 GPa at the maximum current density which is a remarkable enhancement in the stiffness of the wire. Similar results were reported for several AgNWs. However, the experiments did not demonstrate if the induced Young's modulus change is reversible or due to a permanent change in the microstructure of the NW. If the Young's modulus change is irreversible it is an indication that the structure of the wire has changed since the Young's modulus is an inherent material property related to the inter-atomic bond length, as discussed in chapter 1.

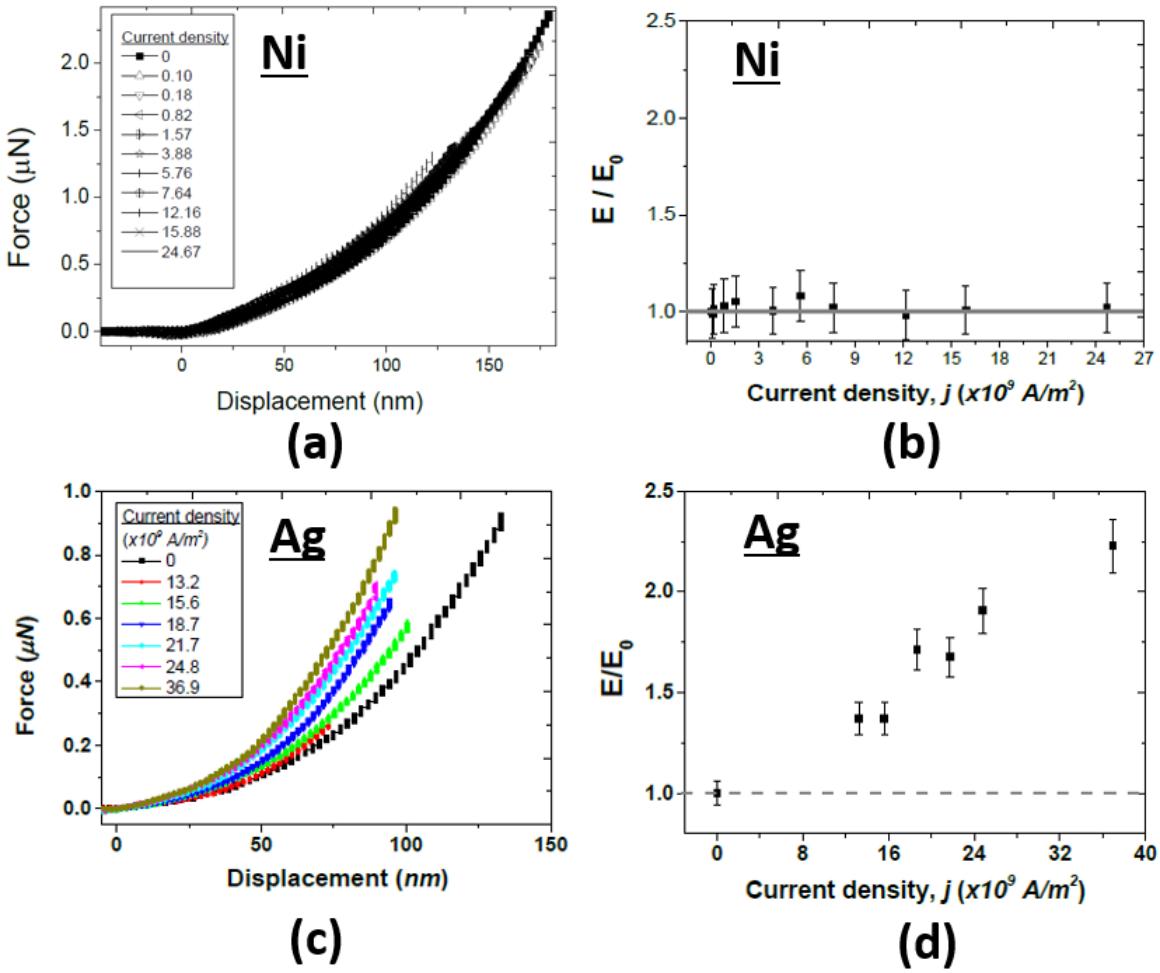

Figure 7.2: (a) *F-d* curves for an 80 nm diameter NiNW with an increasing current density. (b) Corresponding change in Young's modulus as a function of increasing current density. (c) *F-d* curves for a 68 nm diameter AgNW with an increasing current density. (d) Corresponding change in Young's modulus as a function of increasing current density[11].

In this chapter, the experiment conducted by McCarthy on pentagonally twinned AgNWs is repeated with emphasis on determining the reversibility of the measurement. Measurements are also made on another pentagonally twinned NW system, gold nanowires (AuNWs). In an attempt to establish the mechanism that results in the observed stiffening effects, theoretical simulations are performed to examine the behaviour of pentagonally twinned NWs when subjected to a current flow.

7.2 Experimental Method

The 3-point bending experiment used here is the same as that described in chapter 2 and used throughout this thesis. As is also described in chapter 2, there are additional fabrication steps required to electrically contact the NWs for a 4-point electrical measurement. This allows for

the determination of the NW mechanical properties whilst electric charge is passed through the wires. Figure 7.3 (a) shows a AgNW contacted with six silver contacts with the current-voltage (*I-V*) response shown in Figure 7.3 (b). The four outer contacts are used for the 4-point electrical measurement, with the inner two contacts being used as mechanical clamps to clearly define the pinning length, *L*. The electrical contacts and mechanical clamps are all EBL defined, removing the requirement for Pt-EBID clamps, and therefore reducing the fabrication time involved.

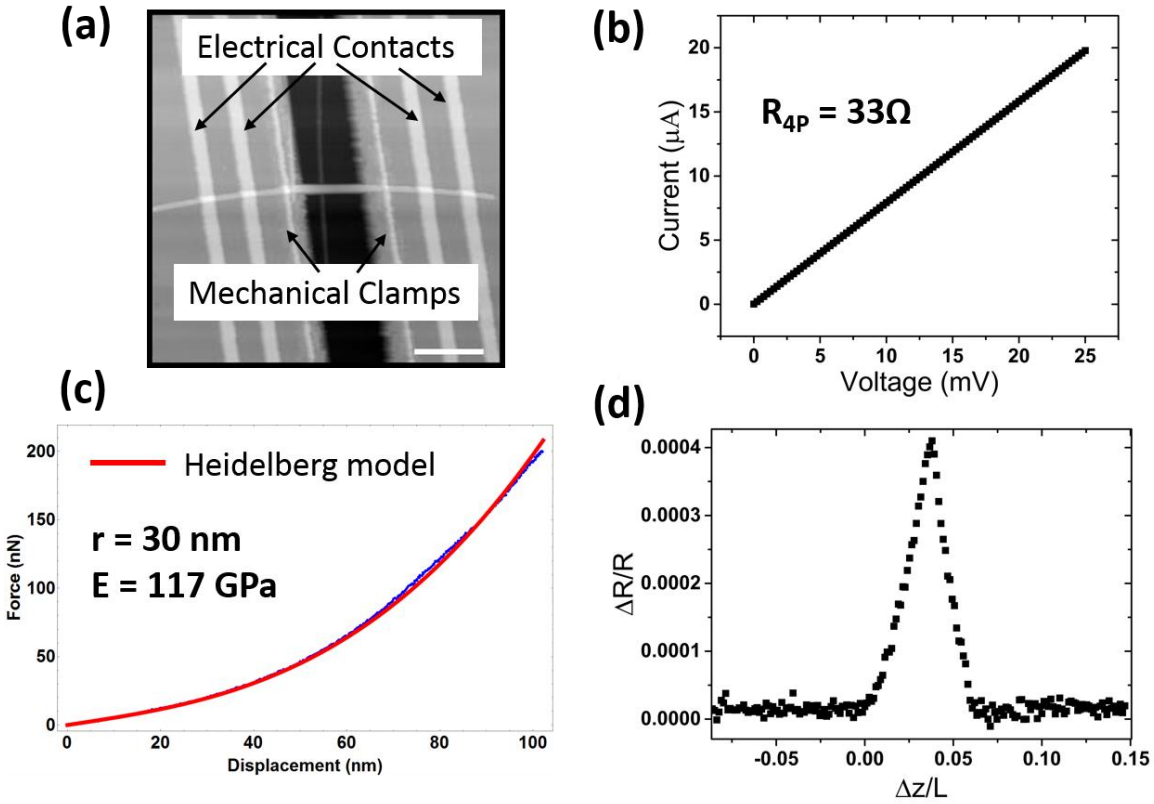

Figure 7.3: (a) 60 nm diameter AgNW with four electrodes for a 4-point electrical measurement and two mechanical contacts, scale bar 2 μm. (b) *I-V* response for a 4-point electrical measurement on the AgNW in (a). (c) *F-d* curve for the 3-point mechanical measurement of the NW in (a) fit to the Heidelberg (zero-residual stress) model. (d) Relative change in resistance as a function of *Δz/L* as the NW in (a) is manipulated.

The measurements on the NWs in this chapter were performed prior to understanding the effects that solvent deposition can have on their initial stress state. As such, NWs in these measurements were solvent deposited, however the *F-d* response of the wires analysed here are accurately described by the Heidelberg (zero-residual stress) model, equation (7.1). The residual stress in these wires is negligible as the e-beam evaporated metal for the electrical and mechanical contacts results in relaxation of the NWs to a near zero residual stress state

as observed in Figure 7.3 (c). The Heidelberg (zero-residual stress) model accounts for both bending and tensile deformation;[12]

$$F_{centre} = \frac{192EI}{L^3} f(\alpha)\Delta z_{centre} \tag{7.1}$$

where F_{centre} is the force applied perpendicular to the NW axis at its central point, Δz_{centre} is the resulting displacement at the load point, E is the Young's modulus of the wire, I is the areal moment of inertia for a cylindrical wire and L is the pinned length.

During the 3-point bending experiment the NW resistance is simultaneously measured using the four Ag electrodes. Current is sourced at the outer contacts by applying a fixed source voltage, while the voltage drop across the wire and current through the wire is measured. The wire resistance increased during the manipulation as can be observed in Figure 7.3 (d). The resistance increases upon loading because the NW cross section decreases and the length of the clamped section of the wire increases upon stretching, therefore resistance increases as $R \propto L/A$. The relative change in NW resistance, $\Delta R/R$, as the wire is displaced can be used to evaluate the Poisson's ratio, v, by the following model;[13]

$$\frac{\Delta\rho}{\rho} = \frac{\Delta R}{R} - 2(1+2v)\left(\frac{\Delta z_{centre}}{L}\right)^2 \tag{7.2}$$

where ρ is the wire resistivity. Equation (7.2) is valid when the displacement is greater than the radius of the wire, consistent with conditions in our experiments. For the metal wires used in these measurements $\Delta\rho$ is expected to be zero and the fit of equation (7.2) can then be used to extract Poisson's ratio. However, the purpose of this work was not to measure Poisson's ratio but to determine the mechanical properties of pentagonally twinned NWs under current flow. The simultaneous measurement of resistance is important however, as any change in resistance can be monitored to determine if the NW is heating during the measurement. Also, if any plastic deformation of a NW occurs during loading the resistance will not return to its original value as the dimensions of the wire will be altered.

7.3 Results

7.3.1 Mechanical Experiment Repeatability

In order to determine whether current flow alters the mechanical properties of NWs, it is necessary to ensure that mechanical measurements are repeatable for consecutive

loading/unloading cycles. Figure 7.4 below shows a AgNW, clamped in a doubly-clamped beam configuration that is elastically manipulated seven times. In each case the *F-d* curves overlap indicating that the force response is repeatable over numerous loading cycles.

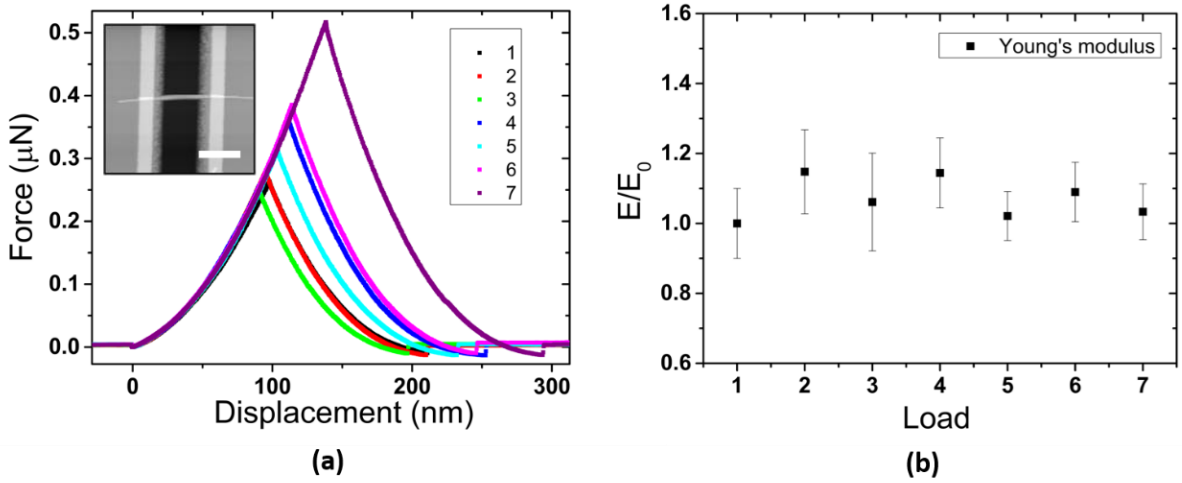

Figure 7.4: (a) Repeatable *F-d* curves for an individual AgNW, inset shows the AgNW suspended over a trench clamped with evaporated Ag metal, scale bar 2 μm. (b) Young's modulus values for each of the *F-d* curves in (a).

This repeatability demonstrates the robustness of the doubly-clamped measurement with Young's modulus varying only by 12% across the seven loads. Therefore, any significant changes in the Young's modulus as a result of current flow through the wire can be detected. In the next section the effects of current flow on the Young's modulus of AgNWs will be investigated.

7.3.2 Irreversible Stiffening of AgNWs

These measurements were conducted on a 60 nm diameter AgNW. Initially the NW was manipulated three times without any current density applied to the wire. This was to ensure a consistent Young's modulus was obtained before applying a voltage bias to the wire. Subsequently, a voltage bias was placed on the outer two electrical contacts, as shown in Figure 7.5 (a), and the corresponding current was recorded. The initial voltage applied was 20 mV, with the resistance change as the wire was manipulated being recorded from the voltage drop across the inner two electrical contacts. Three loads were performed at each current density before the current through the wire was increased again. The sequence of voltage biases applied to the outer contacts was 0 mV, 20 mV, 30 mV, 40 mV, 50 mV, 40 mV, 30 mV. Due to the sheer volume of manipulations involved it is quite common for the

NW to plastically deform before the full completion of the experiment. This wire for example failed after nineteen mechanical manipulations were performed on it. This type of failure has been observed in multiple wires. For each of the voltage bias levels applied to the wire, the Young's modulus was plotted as a function of both load number and current density, Figure 7.5 (d). The current density, *j*, normalises the current with respect to cross sectional area, $j = I/A$. Hence, it allows for the direct comparison of NWs with different radii and electrical resistances under a universal parameter.

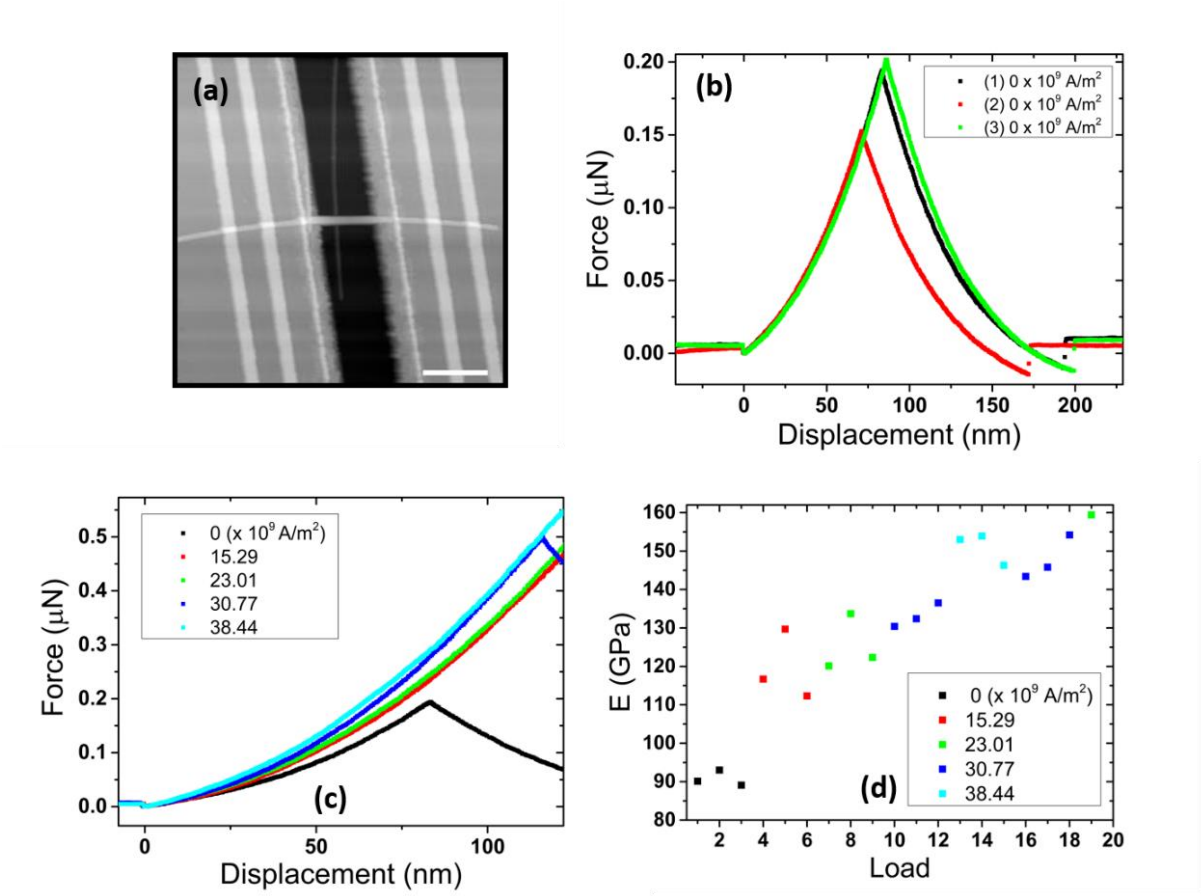

Figure 7.5: (a) AFM image of a 60 nm diameter AgNW suspended over a trench contacted with four Ag electrodes plus two additional Ag mechanical contacts at the edge of the trench, scale bar 2 μm. (b) Three repeatable *F-d* curves with zero current density applied to the NW. (c) Observed stiffening of the *F-d* curves when current density through the wire is systematically increased. (d) Change in Young's modulus as a function of increasing and decreasing current density.

As shown in Figure 7.5 (b) prior to the application of a voltage bias the *F-d* curves exhibit good repeatability, with Young's modulus values of 90 GPa, 94 GPa and 88 GPa having been obtained for three consecutive loads. Figure 7.5 (c) then shows that as the current density through the wire is increased systematically from 15.29 - 38.11 A/m^2, the slope of the *F-d* curves increase indicating an increase in the Young's modulus. By analysing the data with

the model described by equation (7.1), it was established that the Young's modulus was indeed found to increase (Figure 7.5 (d)). However, when the current density was decreased, the Young's modulus of the NW still exhibited an additional stiffening. For this wire under investigation the stiffening was not reversible which is a possible indication that the wire undergoes a permanent change in structure. The Young's modulus of the NW increased to 159 GPa which corresponds to a modulus increase of 70%, comparable to the work of McCarthy (2013)[11]. This measurement was repeated for numerous different AgNWs, to determine if the same effects were observed for all AgNWs.

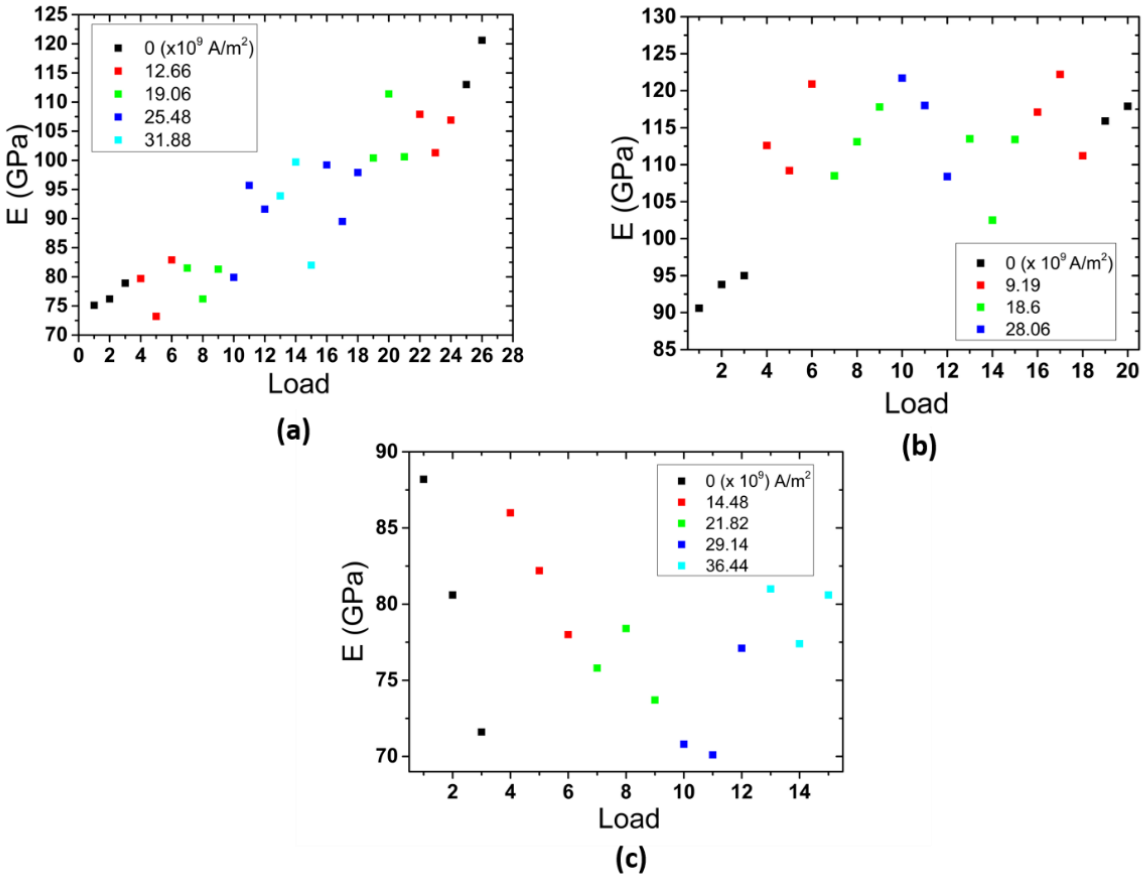

Figure 7.6: Variation in Young's modulus with current density for three different AgNWs with diameters; (a) 62 nm, (b) 56 nm, (c) 62 nm.

For the 64 nm diameter AgNW measured in Figure 7.6 (a) a similar Young's modulus variation with current density was observed. For this wire the Young's modulus increased by 60% and again there was no reversibility observed. Interestingly, the modulus increased even further upon the reduction of the current density. As shown in Figure 7.6 (b), for the three loads at zero current bias the Young's modulus values were consistent (91 GPa, 94 GPa, 95

GPa). Then as a current density of 9.2 A/m^2 was allowed to flow through the wire, the modulus increased by approximately 22%, however, further increases in current density did not increase the stiffness further. Moreover, when the current bias was removed from the wire and the wire manipulated with no current flow, the Young's modulus did not return to its initial value. This indicates that a permanent change in the NW has occurred. Occasionally there were AgNWs where Young's modulus showed no dependence on current density, as shown in Figure 7.6 (c).

Nonetheless, most wires did exhibit a Young's modulus increase with increasing current density. The current densities passed through the wires are remarkably high, up to 38 x 10^9 A/m^2. Therefore, it is important to investigate the potential occurrence of heating effects in these wires.

7.3.3 Joule Heating in Nanowires

Due to the large current densities involved (up to 38 x 10^9 A/m^2) in these measurements, it is important to determine whether there is significant joule heating occurring in these NWs. Considering, $P = I^2R$, where P is the power converted from electrical to thermal energy, the square dependence on the applied current makes it a critical factor in potential heating effects. However, even with the large current densities used, there was no evidence of mechanical softening of the wires which suggests the absence of appreciable current-induced heating under the present conditions. Additionally, there was no increase in the resistance without loading, i.e. any current-induced heating of the NW had no measurable effect on its resistivity and the original resistance of the wire was always recovered after the load (Figure 7.7 (a)), provided the wire was loaded in the elastic regime.

The *IV* response of the NW in Figure 7.7 (a) was analysed at high current densities. Remarkably, the wire could withstand current densities up to 10^{12} A/m^2 at failure, Figure 7.7 (b). The *IV* curve does show a deviation from linear behaviour with the best fitting function of the form $y=Ax+Cx^2$, where the quadratic term was found to be negative indicating that there was an increase in resistance at higher current densities. When analysing the resistance change of the NW, it was found that the resistance of the NW increased by ~5% at the highest current density, as shown in Figure 7.7 (c). This resistance change could be used to estimate the temperature change in the NW. Using the formula, $R = R_o(1 + \alpha\Delta T)$, where α defines the temperature coefficient of resistance which for silver is approximately 4 x 10^{-3} °C^{-1}. As shown in Figure 7.7 (d), the temperature change at the highest current density was

approximately +10°C. However, this current density was approximately three orders of magnitude greater than that used in the electromechanical experiment in which case the temperature change in the wire could be estimated to be ≪ 0.2%, which is a further indication that there is no significant current-induced heating under the present experimental conditions.

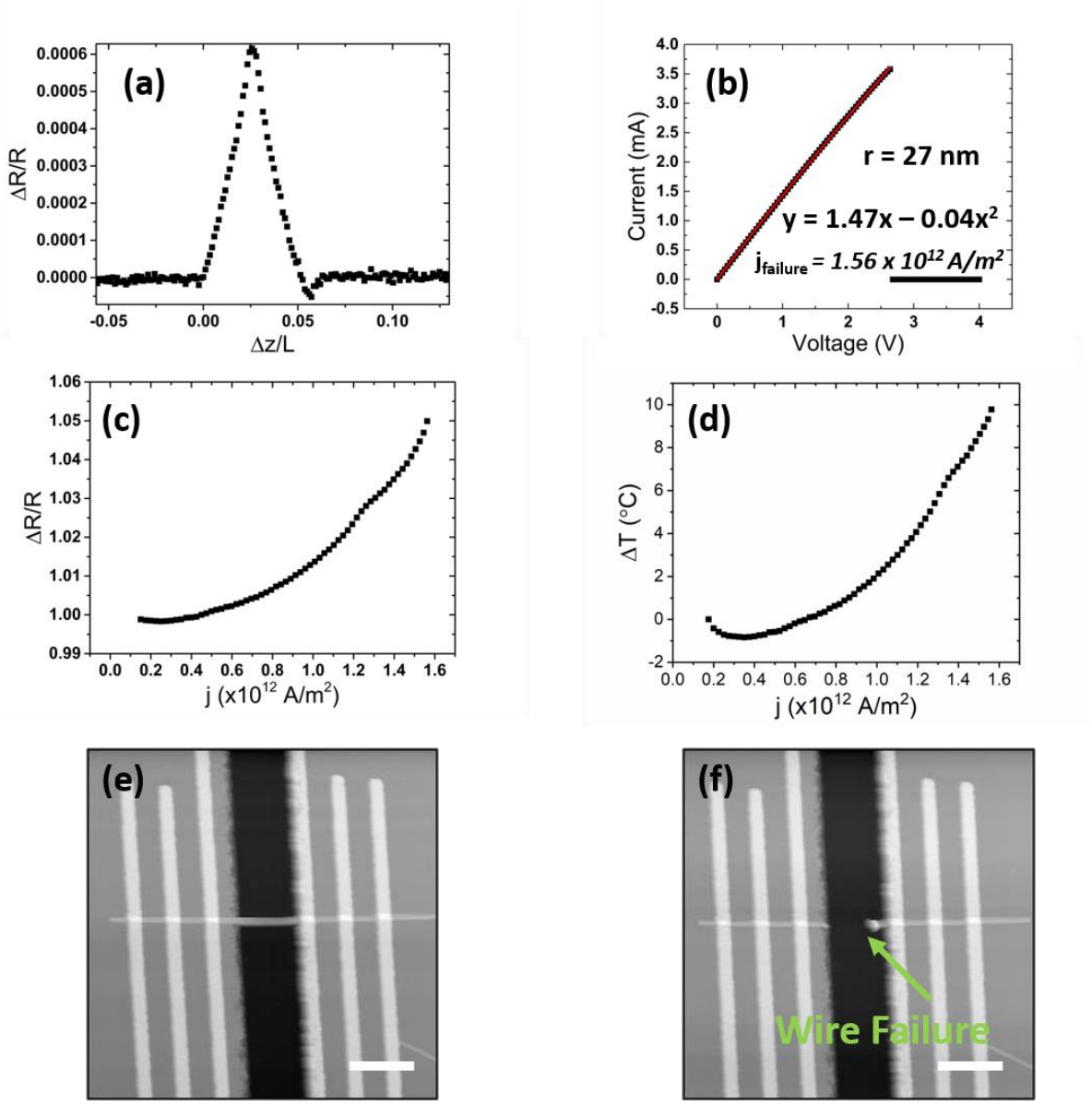

Figure 7.7: (a) Relative change in resistance as a function of *Δz/L* for an individual 54 nm diameter AgNW during mechanical manipulation. (b) Polynomial fit to the *IV* response of the AgNW in (a) up to a current density of 1.56 x 10^{12} A/m^2 at wire failure. (c), (d) Relative change in NW resistance and temperature as a function of current density. (e), (f) AFM images of AgNW before and after failure due to excessive current density, scale bar 2 μm.

Theoretically the heat generated in the wires should be quite large. In the paper of Fangohr *et al.*[14] the heating of NWs was estimated;

$$\frac{dT}{dt} = \frac{j^2}{\rho C \sigma} \tag{7.3}$$

Using material parameters for silver, density (ρ) of 10490 kg/m^3, specific heat capacity (C) of 230 J/kgK and electrical conductivity (σ) of 63 x 10^6 Ωm^{-1}, along with a current density (j) of 38 x 10^9 A/m^2, we find the temperature increase of the wire neglecting any losses should be 95 x 10^5 K/s. The melting point of silver is around 1233 K, so these AgNWs should melt in a fraction of a second. However, we have never observed NW melting. Therefore, it would seem that dissipation at the contacts and through the substrate is sufficient to minimise the temperature rise in the NWs. Therefore, the stiffening effect that is observed occurs due to reasons other than heating effects in these NWs.

From the results shown it appears that the increase in the Young's modulus of these NWs is as a result of the unique pentagonally twinned microstructure of these AgNWs. It had previously been shown that polycrystalline NiNWs do not exhibit any Young's modulus dependence with current density[11]. In order to verify this further we investigate a different wire system with a pentagonally twinned structure. For this, gold nanowires (AuNWs) are used.

7.3.4 Irreversible Current Induced Stiffening of Gold Nanowires

Two AuNWs were measured to determine if their Young's modulus exhibited any dependency on current flow through the wire. The results can be observed in Figure 7.8. For the 56 nm diameter AuNW in Figure 7.8 (a), there was an increase in Young's modulus with an increasing current density. At a current density of 9.32 x 10^9 A/m^2 the Young's modulus had increased by 60%.

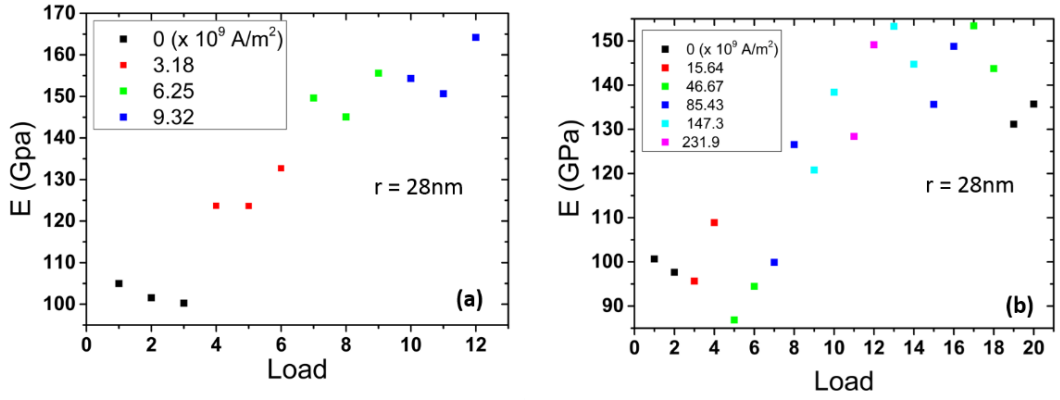

Figure 7.8: Effect of increasing current density on the mechanical properties of two 56 nm diameter AuNWs.

This is comparable with the largest stiffness increase observed for the AgNWs. Unfortunately, this wire plastically deformed before the current density could be stepped back down to zero. In Figure 7.8 (b), the Young's modulus of the 56 nm diameter AuNW increased by approximately 50%, however for this measurement the Young's modulus increase saturated and upon further increase in current density the modulus remained fixed. When the current density was stepped back down to zero the Young's modulus of the wire did not return to its initial value. These AuNWs exhibit the same response as that observed for the AgNWs, indicating that it appears to be changes in the structure of the pentagonally twinned NWs that leads to an increase in the modulus. The pentagonal structure of both wire types can be observed in Figure 7.9.

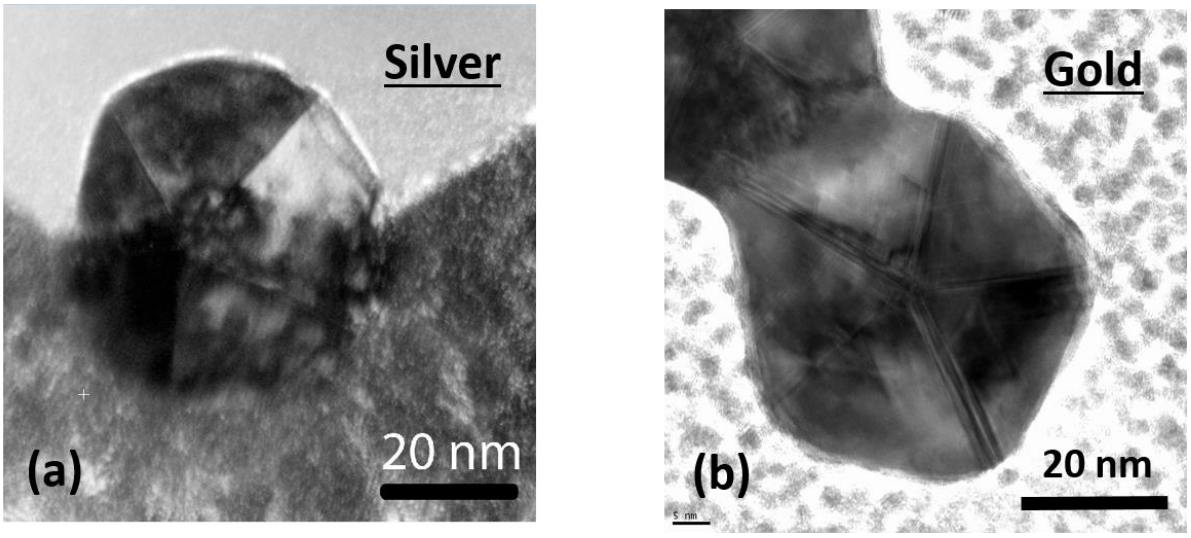

Figure 7.9: Cross sectional TEM images of pentagonally twinned nanowires; (a) Silver[13], (b) Gold. (TEM courtesy of Dr. Eoin McCarthy).

In order to determine why pentagonally twinned NWs stiffen upon application of a current bias, the effects of current flow on the equilibrium state of a pentagonally twinned NW is modelled.

7.3.5 Theoretical Effects of Current Flow on Pentagonally Twinned NWs

The theoretical modelling work detailed in this section has been conducted by the research group of Prof. Stefano Sanvito in Trinity College Dublin. Density Functional Theory (DFT) simulations using the Perdew-Burke-Ernzerhof (PBE) form of the generalised gradient approximation (GGA) of the exchange and correlation function are used as implemented in SIESTA[15] and CP2K[16] codes. Simulations were conducted on a NW with a pentagonal cross

section oriented along the [110] direction, which was constructed by joining the {111} faces of five smaller crystalline wires, as shown in Figure 7.10 (c). Due to the computational complexity of the problem, the wire diameter chosen was approximately 20 Å.

To model a NW of infinite length a slab with two bi-layers of 51 Ag atoms was periodically replicated along the z-direction (along the axis of the wire). Fictitious periodic boundary conditions were imposed along x and y, by using a 56 x 56 Å supercell. The equilibrium geometry of the NW under strain was obtained by relaxing the structure for slightly different inter-planer distances along z (δz), until a maximum component of all forces was smaller than 0.005 eV/Å (this was equivalent to introduce strain along the NW axis). The equilibrium inter-planar distance (δz = 1.442 Å, interatomic spacing (c) = 4.078 Å) then corresponded to the zero-stress condition along z. The σ_{xx} and σ_{yy} components of the stress tensor were evaluated at different fixed cell lengths, L, using the relaxed forces acting on the wire at every constrained condition. When compared to the equilibrium lattice parameter of bulk Ag (c = 4.160 Å), a core radial compression of the order of 1 - 2% and a surface tension due to core compression was observed in pentagonal NWs. This reflects in a densification (shorter interatomic distances) of the {111} internal surfaces and of the regions nearby the five corners. Additionally, there is softening of the cores of the triangular units.

To simulate current flow through the NW, the electrodes were held at different chemical potentials μ_1 and μ_2 as shown in Figure 7.10 (a). As the current is applied an increase of both σ_{xx} and σ_{yy} is observed, which gets larger as the current becomes more intense as shown in table 7.1. This indicates the tendency of the NW cross section to shrink under the application of a current. The calculations of the stress tensor along the z-direction is somewhat more complicated since an artificial contribution to the forces appears at the boundary between the scattering region and the electrodes, due to the abrupt potential drop imposed by the boundary conditions. In this case a local pseudo-stress tensor $\bar{\sigma}_{zz}$ defined as $\bar{\sigma}_{zz} = \sum_i \frac{F_z z_i}{V}$ is evaluated where V is the volume of the region considered and F_z is the z-component of the force acting on the atom with z_j co-ordinates. These quantities were calculated at different fixed wire lengths at finite bias. Not only does the NW contract axially due to an increase in σ_{xx} and σ_{yy} under current flow but, for every fixed cell's length an increased current flow always corresponded to a larger $\bar{\sigma}_{zz}$ as well.

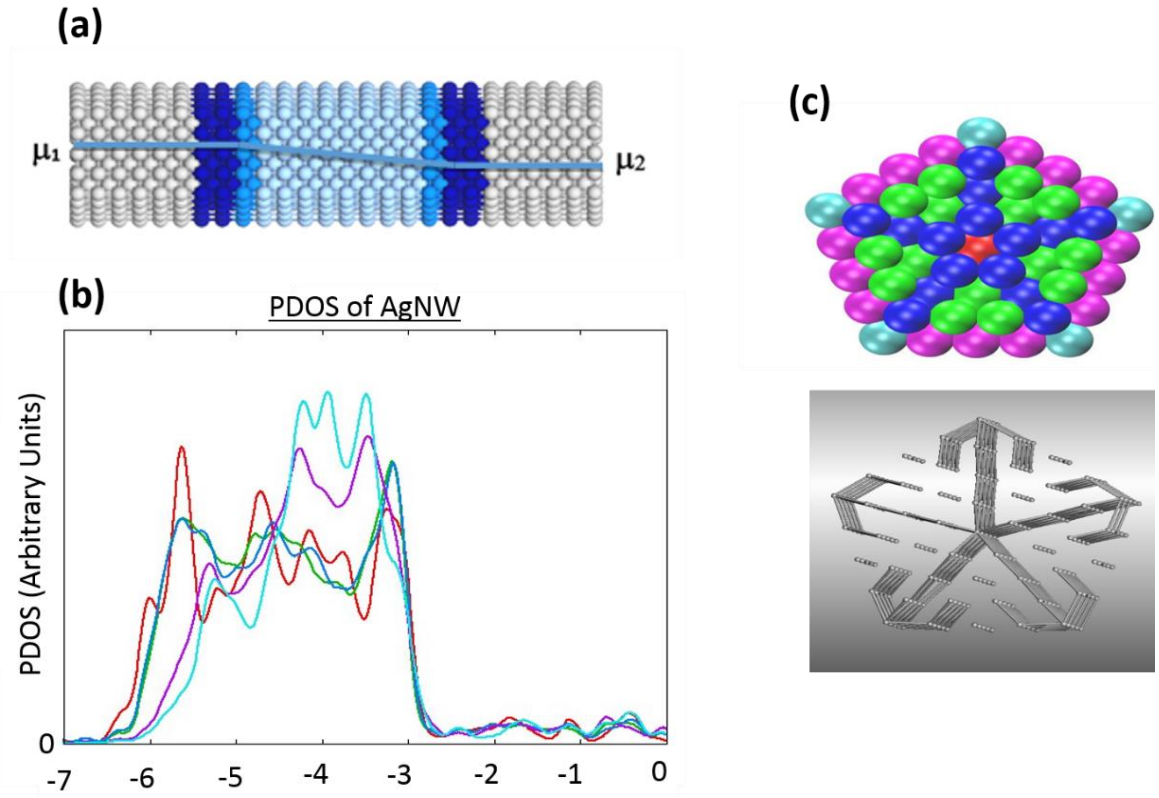

Figure 7.10: (a) Geometry of AgNW simulated in this work, with pentagonal cross section and alignment along the [110] direction. The wire is constructed by joining the {111} faces of five smaller crystalline wires with triangular cross section. The Ag atoms colour code is as following; dark blue: leads; blue: constrained atoms within the scattering region; light blue: atoms in the scattering region allowed to relax in the presence of the current; light grey: the semi-infinite leads. A potential bias is applied to the leads keeping the electrodes at two different chemical potentials, μ_1 and μ_2. The blue line along the wire represents the potential drop. (b) Projected density of states (PDOS) of the Ag pentagonal NW on different atoms (colour code as in (c)). (c) Top: cross section of the pentagonal wire and colour code of PDOS. Bottom: cross section of the pentagonal wire with the shortest bond lengths highlighted in grey.

Table 7.1: Increase in the stress tensor as a function of applied voltage.

Bias potential (Volt)	σ_{xx}
0 (bulk)	$-1.2\cdot10^{-5}\pm7\cdot10^{-6}$
0	$-1.3\cdot10^{-5}\pm7.1\cdot10^{-6}$
0.1	$-0.6\cdot10^{-5}\pm0$
0.2	$2.45\cdot10^{-5}\pm7\cdot10^{-6}$
0.3	$5.05\cdot10^{-5}\pm5\cdot10^{-7}$

The computational results suggest that the wires also shrink longitudinally when a current is applied and that the mechanical properties of these pentagonally twinned AgNWs and AuNWs can be altered by current flow through the wire. However, for our experimental results the stiffening is not reversible which is not consistent with theoretical modelling at the present level.

In addition to the geometrical changes of these pentagonally twinned AgNWs under current flow, the projected density of states (PDOS) provide interesting insights into the actual current flow. As shown in Figure 7.10 (b), the PDOS projected on atoms belonging to different regions (edges, central axis, external surfaces, internal {111} boundaries and core of each triangular unit) are different. The PDOS on the outside {100} surfaces is more intense and peaked in the energy region between -3 eV and -5 eV below the Fermi energy. The PDOS on the atoms belonging to the wire axis also present a broad peak at approximately - 5.8 eV. The PDOS on the core of the triangular units is qualitatively very similar to that of bulk silver. The electronic charge of the system shadows the atomic distribution, alternating higher values on the more tightly packed {111} internal surfaces and lower density in the cores of each triangular subshell, where interatomic distances are longer. This novel 5-fold modulation of the atomic and charge density might be at the origin of the electromechanical properties of these pentagonally twinned wires.

These theoretical results demonstrate that the unique pentagonally twinned structure of these NWs behave differently under current flow than polycrystalline NWs such as the NiNWs previously measured. The fact that the stiffening increase is irreversible suggests that there is a change in structure occurring in these pentagonally twinned NWs. Further experimental measurement is required to determine if a structure change is occurring. An in-situ TEM electrical stage would be required to directly observe a structural change under current flow. Due to the varying nature of the pentagonal structure in different NWs it would also be necessary to examine an individual NW before and afterwards. Unfortunately, at the time of writing, the TEM used in these studies did not have those capabilities. Regardless, the results shown here demonstrate that it is possible to engineer the mechanical properties of pentagonally twinned NWs, with increases in the Young's modulus of up to 70%, beyond that of normal silver. This may have important implications for future electromechanical devices.

7.4 Conclusion

In conclusion, individual AgNWs were elastically loaded, at their centre point, under increasing current densities. It was demonstrated that for the majority of NWs measured the Young's modulus of the NWs increased with increasing current density. However, the original Young's modulus was not recovered upon the removal of the current source. The same observations were made on pentagonally twinned AuNWs. Previous work demonstrated that the Young's modulus of polycrystalline NiNWs was not affected by the flow of charge through the wire.

DFT modelling indicated that upon the application of a current bias pentagonally twinned NWs experience a densification axially and contract longitudinally. This is consistent with experimental results that indicate an increase in the modulus at increasing current densities. Theoretical calculations also indicate that there is a distribution of density of states across the wire, with the corners of the pentagon's having the highest and the central section of each of the triangular units having the lowest. This complex 5-fold mass and charge distribution in pentagonally twinned NWs is proposed to be at the origin for the increasing Young's modulus with increasing current density through the wires. However, unlike the theory the experimental data shows that this effect is not reversible. This is likely due to a structural change in the wire that results from the complicated nature of the pentagonal twins. Further research is required to determine the exact mechanism behind the increase in Young's modulus, but it is an exciting prospect that shows the potential to tune the mechanical properties of pentagonally twinned NWs.

7.5 References

(1) Zhu, Y.; Qin, Q.; Xu, F.; Fan, F.; Ding, Y.; Zhang, T.; Wiley, B. J.; Wang, Z. L. Size Effects on Elasticity, Yielding, and Fracture of Silver Nanowires: In Situ Experiments. *Phys. Rev. B - Condens. Matter Mater. Phys.* **2012**, *85*, 1–7.

(2) Qiao, L.; Zheng, X. Effect of Surface Stress on the Stiffness of Micro/nanocantilevers: Nanowire Elastic Modulus Measured by Nano-Scale Tensile and Vibrational Techniques. *J. Appl. Phys.* **2013**, *113*, 1–9.

(3) Fatahalla, N.; Hafiz, M.; Abdulkhalek, M. Effect of Microstructure on the Mechanical Properties and Fracture of Commercial Hypoeutectic Al-Si Alloy Modified with Na, Sb and Sr. *J. Mater. Sci.* **1999**, *34*, 3555–3564.

(4) Pu, Z.; Zheng, P.; Jia, K.; Liu, X. Effect of Surface Functionalisation on the Properties (Rheological, Mechanical, and Dielectric) and Microtopography of PEN/CPEN-F-CNTs Nanocomposites. *Polym. Compos.* **2008**, *37*, 2622–2631.

(5) Li, Q.; Cao, Y.; Yu, P.; Vasudevan, R. K.; Laanait, N.; Tselev, A.; Xue, F.; Chen, L. Q.; Maksymovych, P.; Kalinin, S. V; *et al.* Giant Elastic Tunability in Strained BiFeO3 near an Electrically Induced Phase Transition. *Nat. Commun.* **2015**, *6*, 1–9.

(6) Loh, O. Y.; Espinosa, H. D. Nanoelectromechanical Contact Switches. *Nat. Nanotechnol.* **2012**, *7*, 283–295.

(7) Hao, P.; Gao, Y.; Zhou, Y. The Effect of Electric Charge on the Mechanical Properties of Graphene. *Sci. China* **2013**, *56*, 1148–1156.

(8) Hall, H.; Bardeen, J.; Pearson, G. L. The Effects of Pressure and Temperature on the Resistance of P-N Junctions in Germanium. *Phys. Rev.* **1951**, *84*, 129–132.

(9) Smith, C. S. Piezoresistance Effect in Germanium and Silicon. *Phys. Rev.* **1954**, *94*, 42–49.

(10) Zhao, W.; Seabaugh, A.; Winstead, B.; Jovanovic, D.; Adams, V. Influence of Uniaxial Tensile Strain on the Performance of Partially Depleted SOICMOS Ring Oscillators. *Ieee Electron Device Lett.* **2006**, *27*, 52–54.

(11) McCarthy, E. K. The Electromechanical Properties of Individual Nanowires, Trinity College Dublin, **2013**.

(12) Heidelberg, A.; Ngo, L. T.; Wu, B.; Phillips, M. A.; Sharma, S.; Kamins, T. I.; Sader, J. E.; Boland, J. J. A Generalized Description of the Elastic Properties of Nanowires. *Nano Lett.* **2006**, *6*, 1101–1106.

(13) McCarthy, E. K.; Bellew, A. T.; Sader, J. E.; Boland, J. J. Poisson's Ratio of Individual Metal Nanowires. *Nat. Commun.* **2014**, *5*, 1–7.

(14) Fangohr, H.; Chernyshenko, D. S.; Franchin, M.; Fischbacher, T.; Meier, G. Joule Heating in Nanowires. *Phys. Rev. B - Condens. Matter Mater. Phys.* **2011**, *84*, 1–12.

(15) Soler, J. M.; Artacho, E.; Gale, J. D.; Garcia, A.; Junquera, J.; Ordejon, P.; Sanchez-Portal, D. The SIESTA Method for Ab Initio Order-N Materials Simulation. *J. physics. Condens. matter* **2002**, *14*, 1–22.

(16) Vandevondele, J.; Krack, M.; Mohamed, F.; Parrinello, M.; Chassaing, T.; Hutter, J. Quickstep: Fast and Accurate Density Functional Calculations Using a Mixed Gaussian and Plane Waves Approach. *Comput. Phys. Commun.* **2005**, *167*, 103–128.

8

CONCLUSIONS

This thesis has demonstrated for the first time the importance of the initial stress state of NWs (~ 60 nm in diameter) prior to mechanical testing. Over the past twenty years, different measuring techniques have been utilised to measure the mechanical properties of individual NWs, ranging from in-situ electron microscopy techniques to AFM based bending measurements. Sample preparation for these different techniques tends to vary considerably, from the growth process used to synthesise the NWs, to the deposition method used to deposit the NWs onto the testing substrate. One of the most critical processing steps used in the fabrication of devices involves the use of solvents, therefore the effects of solvent processing needs to be well understood. Additionally, nanowire surface passivation is often required to promote growth and to prevent agglomeration. The potential for these surface coatings to interact with solvent media must be considered.

In this work, comparisons were made between the adhesion of AgNWs with a PVP polymer surface coating, and SiNWs with a native oxide surface coating, both with a SiO_2 surface. The adhesion of the different wires was compared using both solvent and dry deposition methods and was estimated by manipulating the NWs with an AFM tip. The results showed that when AgNWs were deposited on a SiO_2 surface using a solvent deposition method, they were strongly adhered to the surface. Furthermore, when these wires were solvent deposited over a trench, clamped using Pt-EBID and laterally manipulated using a 3-point bending technique, it was observed that the wires were affected by an initial residual stress. However, when the same AgNWs were deposited using a dry transfer technique, the NWs were mobile on the surface indicating a much weaker adhesion to the SiO_2 surface and that they were not affected by a residual stress. In contrast, there was no variation in the adhesion of SiNWs to a SiO_2 surface with the deposition method used. The SiNWs were generally always weakly adhered to the surface and did not exhibit residual stress. This is an indication that when solvent processing is employed, the interaction between the solvent and

polymer surface coatings results in an enhanced adhesion to the surface. To confirm this AuNWs which contained a surfactant (CTAB) surface coating were analysed in the same way. When solvent processed these AuNWs also demonstrated enhanced adhesion to the surface and exhibited residual stress.

To determine whether the residual stress observed in AgNWs and AuNWs occurred as a result of the drying process associated with evaporating solvent or due to the potential swelling of the polymer coating, it was necessary to establish if an oxide coated NW exhibited residual stress when strongly adhered to the surface. Occasionally, when SiNWs were solvent deposited they were strongly adhered to the surface. When they were deposited over a trench, clamped and manipulated using the 3-point bending technique they were not affected by residual stress. This is a further indication that the observed stress in AgNWs and AuNWs resulted from interactions between solvents and their surface coatings and was not a drying effect or due to the formation of pinning contacts. Using a strain model for a coaxial wire it was estimated that the polymer coating on AgNWs can swell to strain NWs by up to 0.33% which is comparable to that measured experimentally. The swelling of the polymer also supports the enhanced adhesion observed for the AgNWs. Swelling polymers become more compliant, therefore increasing the contact area between the NW and the SiO_2 surface, which in turn enhances the adhesion and prevents relaxation of the elongated strained wire. These results emphasise the importance of analysing the initial stress state of nanowires prior to measuring their mechanical properties. The residual stresses outlined here may also have implications for TEM analysis of nanowire microstructures which may inadvertently be in a non-zero stress state.

This thesis also informs the science community of the caution that is required when analysing the Young's modulus of NWs in a doubly-clamped beam configuration affected by a residual stress. Adaptions made to the (zero-residual stress) model developed by Heidelberg *et al*. to account for residual stresses have proven to be problematic. It was shown that theoretically it is possible to adapt the Heidelberg model to account for residual stress. However, when the tension-adjusted model was applied to experimental data it was observed that the Young's modulus and residual stress extracted by the model were dependent on the fitting range. An anti-correlation between Young's modulus and residual stress was observed. It was determined that this was due to minor experimental noise when conducting the 3-point bending experiment which prevented the unambiguous extraction of Young's modulus and residual stress, both of which are very dependent on the linear response in *F-d* curves. This is

an important result as it confirms that to unambiguously ascertain the Young's modulus of NWs in a doubly-clamped beam configuration, it is necessary that; (i) the NWs are deposited without the effects of residual stress and (ii) the original model developed by Heidelberg *et al*. is used to extract the material properties.

To remove residual stress, AgNWs were sectioned in half using a focussed ion beam. This created a cantilever beam structure which could be analysed using conventional Euler-Bernoulli cantilever beam theory. These measurements were then used as a benchmark to compare the doubly-clamped beam measurements of both the Heidelberg and tension-adjusted models. SiNWs were deposited over a trench, mechanically clamped and manipulated using the 3-point bending technique. Subsequently the wires were FIB sectioned and analysed using Euler-Bernoulli cantilever beam analysis. For two SiNWs measured, the Young's modulus obtained from the 3-point bending experiment and the Heidelberg model compared well with the Young's modulus obtained from the cantilever beam experiment. In contrast, the tension-adjusted model continued to show a dependence on fitting range, even though the wires did not contain a residual stress, further emphasising the problematic nature of this model. Through the cantilever beam experiments, it was determined that the clamping points for a nanowire that is adhered solely by surface adhesion is greater than the width of the trench. This result emphasises the importance of clearly defining the pinned length of nanowires for doubly-clamped beam experiments.

Using a previously devised electromechanical technique, the effects that electrical charge flow has on the Young's modulus of NWs was investigated. Of particular interest was an irreversible stiffening effect that was observed in single crystal pentagonally twinned AgNWs under current flow. The majority of AgNWs exhibited a stiffening effect with some wires showing an increase in Young's modulus of up to 70%. This same effect was observed in AuNWs consisting of the same pentagonally twinned microstructure. Theoretical calculations indicated that pentagonally twinned NWs contract axially and longitudinally upon the application of a current bias which is consistent with an increase in Young's modulus. However, the stiffening effect was determined to be irreversible. Further research is required to determine the exact mechanism behind the increase in Young's modulus. This is an exciting observation as it has not been previously demonstrated that the Young's modulus of nanowires can be permanently altered by current flow.

Overall the work in this thesis, has provided a greater insight into the interactions between solvents and polymer coated nanowires as well as the potential for parasitic residual

stresses to become incorporated in NWs. These effects have not been studied before and could have significant impacts on many solvent processed polymer coated nanomaterials. Additionally, a novel irreversible current induced stiffening in pentagonally twinned silver and gold nanowires has also been reported.

A

APPENDICES

A1: Young's Modulus Determination for a Doubly-Clamped Beam

The following proof was provided in Heidelberg, 2006.

Young's modulus, *E*, is normally obtained from a measurement of the beam displacement as a function of the applied load. For a doubly-clamped beam used here, the resulting curve is described by the following well-known equation;

$$F_{centre} = \frac{192EI}{L^3}\Delta z_{centre} \tag{A.1}$$

where F_{centre} is the load applied to the centre of the beam. Δz_{centre} is the resulting displacement of the beam at the load point, *E* is the Young's modulus of the beam and $I = \pi R^4/4$ is the moment of inertia for a cylindrical beam, and *L* is the beam length. The equation predicts a linear relationship between the applied load and the resulting displacement and thus requires that measurements exhibit this property. However, as the beam is displaced, an axial tensile force is inherently induced due to stretching of the beam. This force affects the total stress experienced by the beam, which leads to an enhancement in the rigidity. A simple closed form solution which enables the Young's modulus to be determined irrespective of applied load is described. To begin we note that the governing beam equation, which includes the effects of axial forces, is;

$$EI\frac{d^4w}{dx^4} - T\frac{d^2w}{dx^2} = F_{centre}\delta(x - \left(\frac{l}{2}\right)) \tag{A.2}$$

where *w* is the deflection of the beam, *x* is the spatial coordinate along the beam length, *T* is the tension along the beam, and δ is the Dirac delta function. Note that $\Delta z_{centre} = w(L/2)$. The tension *T* is determined from the strain along the axis of the beam, and is given by;

$$T = \frac{EA}{2L}\int_0^L (\frac{dw}{dx})^2 dx \tag{A.3}$$

Equation (A.2) and (A.3) are solved subject to the usual clamped boundary conditions at both ends of the beam, i.e.

$$w = \frac{dw}{dx} = 0 \quad at \quad x = 0 \; and \; L \tag{A.4}$$

Solving equations (A.2-A.4) gives the required solution;

$$F_{centre} = \frac{192EI}{L^3} f(\alpha)\Delta z_{centre} \tag{A.5}$$

where

$$f(\alpha) = \frac{\alpha}{48 - \frac{192\tanh(\sqrt{\alpha}/4)}{\sqrt{\alpha}}} \tag{A.6}$$

where α is related to the maximum deflection Δz_{centre} by the following transcendental equation;

$$\frac{\alpha cosh^2(\frac{\sqrt{\alpha}}{4})}{2 + cosh(\sqrt{\alpha}/2) - 6\frac{sinh\left(\frac{\sqrt{\alpha}}{2}\right)}{\sqrt{\alpha}}}(1 - 4\frac{tanh(\frac{\sqrt{\alpha}}{4})}{\sqrt{\alpha}})^2 = \Delta z_{centre}^2(\frac{A}{I}) \tag{A.7}$$

We note that $f(\alpha) \geq 1$, so that inclusion of the tensile force increases the effective rigidity of the beam. Also, α is directly connected to the tension in the rod via the relation;

$$\alpha = \frac{TL^2}{EI} \tag{A.8}$$

and represents the ratio of axial stresses due to extension and bending.

While equations (A.5 - A.8) present an exact analytical solution, it is complex in nature, requiring the numerical solution of a transcendental equation. To overcome this limitation, we note that the solution to equation (A.7) possesses the following asymptotic solutions;

$$\alpha = \begin{cases} \frac{12}{5}\epsilon - \frac{3}{875}\epsilon^2, \epsilon \to 0 \\ 2\epsilon, \qquad\qquad \epsilon \to \infty \end{cases} \tag{A.9}$$

where

$$\epsilon = \Delta z_{centre}^2 (\frac{A}{I}) \tag{A.10}$$

An approximate and explicit expression for α is then obtained by constructing a Padé approximant using equation (A.9), i.e.

$$\alpha = \frac{6\epsilon(140 + \epsilon)}{350 + 3\epsilon} \tag{A.11}$$

which exhibits a maximum error of only 2.1% over the entire range of ϵ. Equations (A.5), (A.6) and (A.11) give the generalized form we seek and enable the applied force to be determined for any beam displacement.

Equation (A.10) indicates that the solution, equation (A.1) is valid provided the maximum displacement Δz_{centre} is less than the radius of the beam. As Δz_{centre} is increased to a value larger than the beam radius, the solution becomes progressively non-linear with respect to the displacement, leading finally to a cubic dependence on Δz_{centre}. Thus, an approximate solution can be obtained by superimposing the small and large deflection limits, namely;

$$F_{centre} = \frac{192EI}{L^3}\Delta z_{centre}(1 + \frac{A}{24I}\Delta z_{centre}^2) \tag{A.12}$$

a result which exhibits a maximum error of 18%. This approximate solution was not used for any of the analysis in this thesis. Only the full generalized model was used unless stated.

A2: Estimation of the Strain Exerted on a NW by a Swelling Polymer Coating

This derivation, allows the strain in a polymer coated NW upon isotropic swelling of the polymer coating to be estimated.

Assuming that prior to polymer expansion, there is no net strain on the wire, we can write;

$$\sigma_{net} = \sigma_w + \sigma_f = 0 \tag{A.13}$$

where σ_{net} is the net stress in the entire wire, σ_w and σ_f are the stress in the core wire and the outer polymer respectively.

Using $\sigma = E\varepsilon$ and $F = \sigma/A$ the net force, F_{net}, in the core-shell wire system can be written as;

$$F_{net} = E_w \pi R_w^2 \varepsilon_w + E_f \pi((h_f + R_w)^2 - R_w^2)(\varepsilon_f + \varepsilon_w) = 0 \tag{A.14}$$

where E_w and E_f, are the Young's modulus of the core wire and outer polymer respectively, R_w is the radius of the core wire, h_f is the thickness of the polymer coating, ε_w is the strain in the wire and ε_f is the residual strain in the polymer due to swelling.

Simplifying, we obtain the expression;

$$\varepsilon_w = \frac{-\varepsilon_f}{\frac{E_w R_w}{2E_f h_f} + 1} \tag{A.15}$$

If $E_f h_f \ll E_w R_w$ which is always true, we can write;

$$\varepsilon_w = -2\left(\frac{h_f}{R_w}\right)\left(\frac{E_f}{E_w}\right)\varepsilon_f \tag{A.16}$$

Equation (A.16) allows the strain induced in a NW by the swelling of an outer polymer coating to be estimated.